Liquid crystal phase behaviour of colloidal mixtures

Vloeibaar-kristallijn fasegedrag van colloïdale mengsels

(met een samenvatting in het Nederlands)

Proefschrift

ter verkrijging van de graad van doctor aan de
Universiteit Utrecht op gezag van de Rector Magnificus,
Prof. dr. W.H. Gispen, ingevolge het besluit van het
College voor Promoties in het openbaar te verdedigen
op maandag 14 juni 2004 des namiddags te 16.15 uur

door

Henricus Herman Wensink

geboren op 31 januari 1976 te Lichtenvoorde

Universiteit Utrecht

Promotor:	Prof. dr. H. N. W. Lekkerkerker
Co-promotor:	Dr. G. J. Vroege

Beiden verbonden aan de Faculteit Scheikunde van de Universiteit Utrecht

Aan mijn vader

This thesis is based on the following publications:

Chapter 2:
   H. H. Wensink, G. J. Vroege and H. N. W. Lekkerkerker,
   Isotropic-nematic density inversion in a binary mixture of thin and thick hard platelets,
   J. Phys. Chem. B **105**, 10610 (2001).

Chapter 3:
   H. H. Wensink, G. J. Vroege and H. N. W. Lekkerkerker,
   Isotropic-nematic phase separation in asymmetric rod-plate mixtures,
   J. Chem. Phys. **115**, 7319 (2001).

Chapter 4:
   H. H. Wensink, G. J. Vroege and H. N. W. Lekkerkerker,
   Biaxial versus uniaxial nematic stability in asymmetric rod-plate mixtures,
   Phys. Rev. E **66**, 041704 (2002).

Chapter 5:
   H. H. Wensink and G. J. Vroege,
   Demixing in binary mixtures of anisometric colloids,
   J. Phys.; Condens. Matt. **16**, S2015 (2004).

Chapter 6:
   H. H. Wensink and G. J. Vroege,
   Isotropic-nematic phase behaviour of length-polydisperse hard rods,
   J. Chem. Phys. **119**, 6868 (2003).

Chapter 7:
   H. H. Wensink and G. J. Vroege,
   Phase equilibria in systems of hard disks with thickness polydispersity,
   Phys. Rev. E **65**, 031716 (2002).

Chapter 9:
   H. H. Wensink and H. N. W. Lekkerkerker,
   Sedimentation and multi-phase equilibria in mixtures of platelets and ideal polymer,
   Europhys. Lett. **66**, 125 (2004).

Contents

1

General introduction

ABSTRACT

In this Chapter we introduce the concept of lyotropic liquid crystals, both from a practical and statistical mechanical point of view. We also establish the aim of this thesis in relation to recent experimental work on colloidal mixtures.

1.1. PHENOMENOLOGICAL BACKGROUND

Among the states of matter encountered in daily life the gas, liquid and solid states are probably best known. Common examples ubiquitous in nature are air, water and ice. From a microscopic point of view the low-density (ideal) gas state can be represented by a collection of disordered spherical particles diffusing freely through space and colliding only with the wall of the container. The collisions of the particles with each other are neglected. The only distinction between a gas and a liquid is the higher density of the latter. Due to this, the particles do not only collide with the wall but also with each other thereby leading to strong correlations between the particles' motions. Despite their steric hindering, the particles are still allowed to move through the entire volume, i.e. the liquid is disordered. Contrary to the liquid, a solid is represented by an ordered arrangement of particles occupying sites in a specific lattice. The only possible motions which are then allowed are the vibrations of the particles about their lattice positions. The solid phase is therefore characterized by a long-range order of the particles in all three directions of the system.

Interesting enough, many materials in practical life are composed of *anisometric* (nonspherical) building blocks. For instance, optical displays and switching devices are usually composed of rod-shaped molecules. Many *colloidal* dispersions consist of particles (within the size range 1-1000 nm) with a distinct anisometric shape, such as blood (containing toroidal red blood cells) or clay (which consists of layer-shaped colloids). All these systems may display additional states of matter which are intermediate between the dilute gas and the crystalline solid state at low and high densities, respectively. These are referred to as *liquid crystalline* phases. The very existence of these states is related to the additional *orientational* degrees of freedom anisometric particles have compared to spherical ones. From a practical point of view, the term 'liquid crystal' indicates that these systems possess some of the characteristics of a disordered liquid, evidenced by the ease of flow, and of an ordered solid, evidenced for instance by diffraction of X-rays or light. We will now illustrate some examples of liquid crystalline phases in detail below. Corresponding graphic impressions of these phases are depicted in Fig. 1.1.
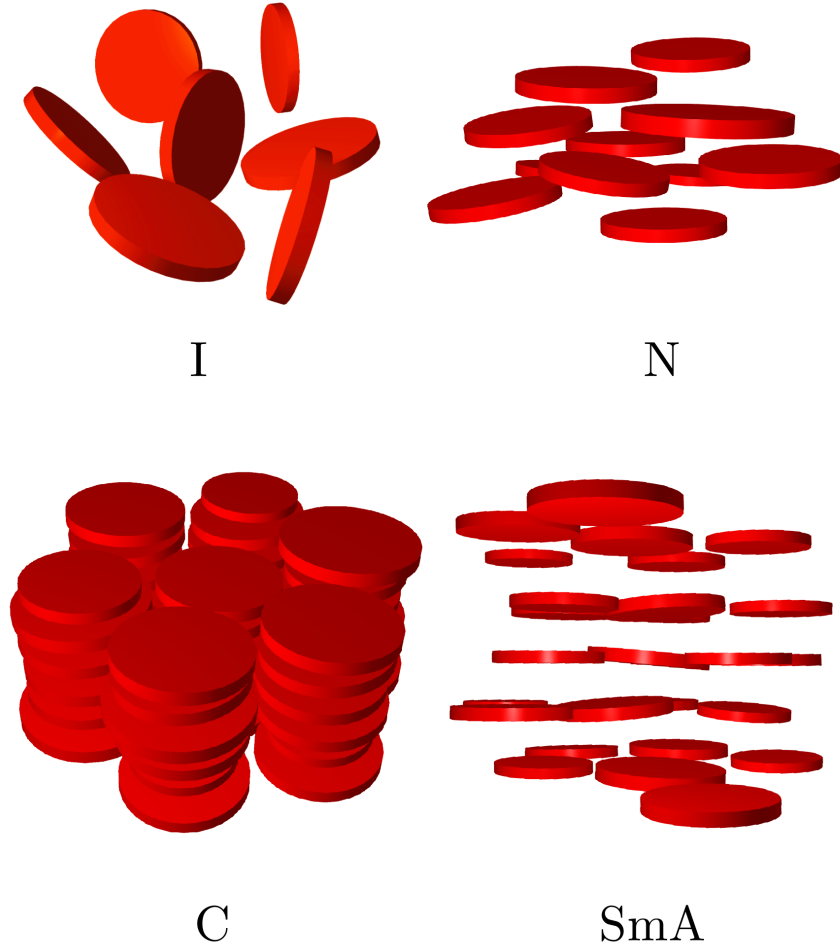
FIGURE 1.1. Schematic representations of the various (liquid crystal) phases
for platelike particles.

The *isotropic* (I) fluid phase is very similar to the gas and liquid phases for spheri-
cal particles and is characterized by a complete absence of positional and orientational
order. In the *nematic* (N) phase the orientations of the particles are largely "frozen"
such that the particles point on average in the same direction. Their centres of masses
are however still distributed homogeneously over the entire system volume, i.e. there
is no long-range positional order. At high densities the systems may form *inhomoge-
neous* liquid crystal states which possess both orientational order and *partial long-range
positional order* in one or two dimensions of the system. Examples are the *smectic-A*
(SmA) phase, characterized by a one-dimensional ordering of layers along the preferred
orientational direction whereas in the other two directions, i.e. within each layer, the
system is spatially disordered and therefore behaves like a liquid*.

In the *columnar* (C) state, the particles are ordered into a two-dimensional hexagonal
lattice perpendicular to the preferred orientational direction. In the direction along the

---

*Unlike the columnar phase, the smectic phase sketched in Fig. 1.1 has not yet been observed in
colloidal systems of platelets, on which we will focus in part of this thesis.

columns their arrangement is disordered and hence there are no long-range spatial correlations.

It is well-known from everyday experience that, under certain conditions, matter can transform from one state to the other by a *phase transition*. For instance, increasing the temperature may lead to boiling and evaporation of water or the melting of ice, nitrogen gas can be liquefied at low temperatures and high pressures. As to the liquid crystals we discuss here, phase transitions among the different states may be brought about in two different ways; one by varying the temperature and the other by changing the concentration of particles in solution. The variety of systems characterized by the former is qualified as 'thermotropic' and consists mainly of systems of anisometric low molecular weight constituents (and also certain polymers). In this thesis we shall however restrict ourselves to the latter class of systems; the *lyotropic* liquid crystals. These are composed of high-molecular weight colloidal particles, polymers or surfactants in a solvent such that the formation of these liquid crystals occurs upon increasing the *concentration* of the solute particles.

Historically, lyotropic liquid crystals were first recognised in the 1920s by Zocher [1] who investigated nematic textures in solutions of rodlike inorganic vanadiumpentoxide (V_2O_5) particles. Later, similar observations were reported by Langmuir [2] for clay platelets and Bawden *et al.* [3,4] for Tobacco Mosaic Virus (TMV) rods. At present, there are many other examples of lyotropic liquid crystals to be found in a wide variety of dispersions of (mainly rodlike) colloidal particles and solutions of stiff polymers (see e.g. Refs. [5,6] for an overview). In the last decade much of the experimental effort in colloid science was focussed on the development and characterization of colloidal *model systems* comprising particles with a well-defined size and shape. The effective interactions between the particles can often be tailored either by chemically altering the surface of the particles or by changing the solvent conditions through variation of the ionic strength or the addition of non-adsorbing polymer. As to anisometric colloids, two important examples of these model systems are the Boehmite (AlOOH) rods [7,8] and the plate-shaped Gibbsite ($Al(OH)_3$) particles [9]. These particles can be stabilised for instance by grafting a layer of polymer onto the particle surface [10,11]. If the particles are subsequently dispersed in a suitable solvent, the polymer layer acts as a steric stabilizer which gives rise to short-ranged repulsive interactions, closely resembling so-called *hard* interactions, i.e. the particles repel each other when they touch (they are impenetrable) but do not interact otherwise. Owing to their simple hard-body interactions the sterically stabilized systems are particularly suitable for studying the influence of *particle shape*, explored by either changing the intrinsic shape of the particles or by mixing particles with distinctly different sizes and shapes, on the liquid crystalline phase behaviour of anisometric colloids [12].

1.1.1. Entropic phase transitions

On the theoretical side, the field of statistical mechanics of lyotropic liquid crystals was opened up by Lars Onsager in the 1940s. He recognized that the transition from an isotropic to a nematic state in solutions containing sufficiently anisometric particles

can be described successfully within a virial expansion of the free energy truncated after the second virial term, an approach which could not be used to explain the gas-liquid transition for spherical particles. One of the crucial insights of Onsager was that the transition can be explained by hard-body repulsions only, thereby dismissing the widespread notion that attractive forces between particles must be responsible for the formation of aligned configurations. The theory of Onsager will be described comprehensively in Sec. 1.3.

About a decade after Onsager's work, Alder, Wainwright and others [13, 14] first showed by means of computer simulations that a similar disorder-order transition, albeit of the positional degrees of freedom, occurs in a fluid of hard spheres. Subsequent work by Hoover and Ree [15] established that if the hard-sphere packing fraction exceeds $\phi = 0.494$ a fluid spontaneously freezes into a crystalline solid phase with a packing fraction $\phi = 0.545$. Much later, computer simulations by Frenkel *et al.* revealed the stability of smectic and columnar liquid crystals which appear upon densifying systems of respectively hard rods [16] and hard platelets [17,18], without attractive interactions between the particles. The transitions of matter mentioned here share an important characteristic; they are driven purely by *entropy*, i.e. there are no energetic effects involved. For this reason these ordering phenomena are nowadays often referred to as *entropic phase transitions* [19]. The notion that spontaneous ordering of particles corresponds to an increase of the total entropy may seem counter-intuitive at first sight, since an increase of order is usually connected to a decrease of entropy. Yet, the general mechanism behind these transitions can be understood as follows. Although the particles lose entropy because the density –in terms of orientations or positions– is no longer uniform, this loss is more than offset by the simultaneous gain of translational entropy, i.e. the available space per particle increases as the particles align or freeze into a crystal lattice.

1.1.2. Mixtures

So far we have implicitly assumed that all particles which build up a gas, liquid (crystal) or solid phase are identical. Many systems in nature are however *mixtures* containing a number of different types of particles or molecules. In this respect we may roughly distinguish between mixtures of chemically distinct moieties on the one hand and so-called *polydisperse* mixtures on the other. Examples of the first are blood (containing red and white blood cells, plasma etcetera), mayonnaise (a mixture of oil and vinegar) and milk (consisting of dispersed fat globules, casein micelles and whey proteins). Polydisperse mixtures are characterized by a large (potentially infinite) number of species –all belonging to a *single* family of particles– with continuously varying properties such as particle shape, size or possible surface charge. Common examples of these are colloidal model systems , where the particles usually have the same basic shape (e.g. spheres, rods or plates) but a *range* of radii, lengths, diameters, etcetera. Of course, in reality many systems share characteristics of both classes; they may comprise a number of distinct species each with some degree of polydispersity with respect to one or more properties of the particle family.

It is not surprising that the phase behaviour of mixtures is richer than that of pure systems –if only for the additional *entropy of mixing*– and that mixing different species may lead to phenomena not encountered in one-component systems. In particular, depending on the miscibility of the species involved, mixing may sometimes lead to a destabilization of a homogeneous state causing a phase separation into two or more phases, each with a different density and/or composition. The associated segregation of species among the coexisting phases, called *fractionation*, is inherent to mixtures and may sometimes give rise to surprising phenomena, as shown in the next Chapter. Mixing particles with distinctly different sizes or shapes may also cause the formation of "new" phases whose structures are not observed in pure systems of the constituent species. For instance, in a two-component (or binary) mixture of rod- and platelike colloids we may encounter the so-called *biaxial* nematic phase, in which both particles types are aligned in mutually perpendicular directions. Similarly, mixing spheres of two (or more) different sizes may give rise to the formation of various solid states with intricate lattices structure not encountered in pure solids [20].

1.2. SCOPE OF THIS THESIS

The central aim of this thesis is to theoretically investigate the effects of *mixing* particles with different shapes on their liquid crystal phase behaviour. Many of the studies to be described in the remainder of this thesis have been triggered off by recent experimental observations in mixtures of colloids with well-controlled shapes and inter-actions. In particular, we mention the experimental work of Van der Kooij [12] who investigated a vast number of mixtures which display many interesting phenomena left open for theoretical interpretation. One of our primary goals in this work is to account for these experimental observations by constructing simple, yet realistic, models for the colloidal systems under consideration and by scrutinizing relevant aspects of their phase behaviour.

The first part of this thesis will be devoted to binary mixtures of anisometric parti-cles. In Chapter 2 a simple model is proposed that allows to qualitatively explain the recently observed isotropic-nematic density inversion in polydisperse systems of col-loidal platelets. In the next two chapters we shall be concerned with mixtures of rods and platelets and provide a theoretical underpinning for the low-concentration part of the experimental phase diagram. We also assess the possible stability of the disputed biaxial nematic phase in experimentally realizable mixtures. In Chapter 5 we conclude the first part with an overview on demixing transitions within the isotropic and nematic phases of binary mixtures of particles whose size differs only in one particle dimension. Previously published results for rodlike particles will be combined with new results for platelets to compare phase diagram topologies and demixing mechanisms pertaining to the various mixtures.

In the second part of this thesis we address the more challenging issue of calculat-ing phase equilibria in polydisperse mixtures of anisometric particles. In Chapter 6 we present a study of isotropic-nematic phase coexistence in systems of length-polydisperse

hard rods, focussing in particular on fractionation effects and the possibility of a demixing of the nematic phase. Chapter 7 deals with polydisperse systems of thickness-polydisperse platelets. The binary model, introduced in Chapter 2, is extended to a polydisperse one which allows us to provide a more realistic, albeit still qualitative, description of the experimental observations. In Chapter 8 we provide a preliminary calculation on the competition between smectic and columnar ordering in systems of polydisperse hard rods. As a first-order approximation we consider an artificial model system of *perfectly aligned* cylinders. The possibilities of extending the approach towards a more realistic one will be discussed.

The contents of Chapter 9 of this thesis differ somewhat from the rest because of the introduction of an *external field*. Inspired by recent experimental observations of a significant sedimentation in dispersions of platelets we illustrate the drastic effect of gravity on the phase behaviour of colloidal mixtures. As an example we consider a system of sedimenting platelets mixed with non-sedimenting ideal polymers, as studied experimentally by Van der Kooij. Also here, the results of the calculations reveal an improved description of the experimentally observed behaviour.

Finally, in Chapter 10 we present a free-volume theory for a columnar state of hard platelets by combining the traditional cell model with an appropriate fluid description which accounts for the rotational freedom of the particles in the (one-dimensional) direction of the phase. Excellent quantitative agreement is found with recent computer simulation results.

1.3. Statistical mechanical background

In this section we introduce the statistical mechanical framework of Onsager's second virial theory [5, 21, 22] to describe the thermodynamic properties of a spatially homogeneous fluid of hard colloidal rods or platelets. The theory is then modified to account for higher virial terms by means of a decoupling approximation as devised by Parsons [23]. Finally, we introduce a bifurcation analysis to verify the stability of the fluid with respect to the spatially *inhomogeneous* liquid crystalline states.

1.3.1. Fluids of hard anisometric particles

We start from an (imperfect) gas of N identical cylindrically symmetric particles in a volume V. Assuming a pairwise additive interaction potential we can express the total potential energy U_N as a summation over pairs

$$U_N = \sum_{i<j} u(\mathbf{r}_{ij}; \Omega_i, \Omega_j), \tag{1.1}$$

where $\mathbf{r}_{ij} = \mathbf{r}_j - \mathbf{r}_i$ is the vector connecting the centres of mass of particles i and j; Ω_i and Ω_j represent the solid angles describing the orientations of the respective particles with respect to some space-fixed coordinate system. For hard-core interactions the pair potential explicitly reads

$$u(\mathbf{r}_{ij}; \Omega_i, \Omega_j) = \begin{cases} \infty & \text{if } i \text{ and } j \text{ overlap;} \\ 0 & \text{otherwise.} \end{cases} \tag{1.2}$$

The description can be applied analogously to dispersions of colloidal particles but the direct pair potential u should then be replaced by the potential of mean force $w(\mathbf{r}_{ij}; \Omega_i, \Omega_j)$ describing the interaction between the particles i and j dispersed in a solvent with a fixed chemical potential [24, 25]. This procedure involves a configurational average of the solvent molecules accounting for their mutual interactions and the interactions with the dispersed particles.

The configurational partition function Q_N for the system reads

$$Q_N = \frac{1}{\mathcal{V}^N N!} \int d\mathbf{r}^N \int d\Omega^N \exp\left[-\beta U_N(\mathbf{r}^N; \Omega^N)\right], \tag{1.3}$$

with $\beta = 1/k_B T$ and $\mathcal{V}$ the (de Broglie) thermal volume, arising from integrations over the translational and rotational momenta of the anisometric particles. The positional and orientational degrees of freedom of the particles are collectively denoted by $\{\mathbf{r}^N; \Omega^N\}$. If we assume that there are no *a priori* restrictions on the particle orientations we may approximate the angular integrations to arbitrary accuracy by dividing the orientational phase space, i.e. the surface of a unit sphere, into s arbitrarily small equal sections with a surface $\Delta\Omega = 4\pi/s$ and summing over all possible orientation distributions $\{N_1, N_2, \ldots, N_s\}$, where N_k is the number of particles with its solid angle Ω in the k-th section centered about Ω_k such that

$$\sum_{k=1}^{s} N_k = N. \tag{1.4}$$

The partition function Eq. (1.3) then becomes

$$Q_N = \frac{1}{\mathcal{V}^N N!} \left(\frac{\Delta\Omega}{4\pi}\right)^N \sum_{N_1=0}^{N} \cdots \sum_{N_s=0}^{N} \frac{N!}{\prod_{k=1}^{s} N_k!}$$
$$\times \int d\mathbf{r}^N \exp\left[-\beta U_N(\mathbf{r}^N; N_1, N_2, \ldots, N_s)\right], \tag{1.5}$$

where the summations need to be carried out under the condition of Eq. (1.4). For large N it is justified to replace the sum by its maximum term [25]. Denoting the set (i.e. orientation distribution) which maximizes $\ln Q_N$ (and hence Q_N) by $\{\tilde{N}_1, \tilde{N}_2, \ldots, \tilde{N}_s\}$ we obtain

$$Q_N \approx \frac{1}{\mathcal{V}^N N!} \left(\frac{\Delta\Omega}{4\pi}\right)^N \frac{N!}{\prod_{k=1}^{s} \tilde{N}_k!} \int d\mathbf{r}^N \exp\left[-\beta U_N(\mathbf{r}^N; \tilde{N}_1, \tilde{N}_2, \ldots, \tilde{N}_s)\right]. \tag{1.6}$$

The partition function can be expressed in a more convenient form after some rearranging. This yields

$$Q_N = \underbrace{\frac{V^N}{\mathcal{V}^N N!}}_{Q_N^{\text{trans}}} \underbrace{\left(\frac{\Delta\Omega}{4\pi}\right)^N \frac{N!}{\prod_{k=1}^{s} \tilde{N}_k!}}_{Q_N^{\text{orient}}} \underbrace{\left\langle \exp\left[-\sum_{i<j} \beta w(\mathbf{r}_{ij}; \tilde{N}_i, \tilde{N}_j)\right]\right\rangle_{\{\tilde{N}_1, \tilde{N}_2, \ldots, \tilde{N}_s\}}}_{Q_N^{\text{int}}}, \tag{1.7}$$

where the brackets denote a (normalized) configurational average over all positional and orientational coordinates under the condition that the particles obey an orientational distribution according to the set $\{\tilde{N}_1, \tilde{N}_2, \ldots, \tilde{N}_s\}$. The first terms Q_N^{trans} and Q_N^{orient} are

identified as the translational (ideal gas) and orientational contributions, respectively, whereas the bracketed one accounts for the hard-body interactions between the particles. The Helmholtz free energy is obtained from the standard relation $\beta F = -\ln Q_N$. Applying this to Q_N^{trans} gives the common ideal free energy $\beta F_{\text{id}} = N[\ln(\rho \mathcal{V}) - 1]$, with $\rho = N/V$ the number density. For the orientational part we obtain

$$\beta F_{\text{orient}} = N \left\{ \ln \left[\frac{4\pi}{\Delta\Omega} \right] + \sum_{k=1}^{s} \tilde{n}_k \ln \tilde{n}_k \right\}, \tag{1.8}$$

in terms of the number fractions $\tilde{n}_k = \tilde{N}_k/N$ with $\sum_{k=1}^{s} \tilde{n}_k = 1$. Introducing the normalized *orientational distribution function* (ODF) $f(\Omega_k)$ we may write $\tilde{n}_k = f(\Omega_k)\Delta\Omega$. Using this in Eq. (1.8) and taking the limit $\Delta\Omega \to 0$ for a *continuous* distribution in Ω we obtain the following expression for the orientational free energy

$$\frac{\beta F_{\text{orient}}}{N} = \int f(\Omega) \ln[4\pi f(\Omega)] \, d\Omega. \tag{1.9}$$

The configurational partition function Q_N^{int} can be approximated systematically by a *virial expansion* in terms of the density variable ρ [26]. At low densities it is justified to make a second virial approximation by taking each of the $N(N-1)/2$ pair interactions independent from all others so that

$$Q_N^{\text{int}} = \left\langle \prod_{i<j} \exp\left[-\beta w(\mathbf{r}_{ij}; \Omega_i, \Omega_j)\right] \right\rangle_f \approx \prod_{i<j} \left\langle \exp\left[-\beta w(\mathbf{r}_{ij}; \Omega_i, \Omega_j)\right] \right\rangle_f$$

$$\approx \langle 1 + \Phi_{12} \rangle_f^{N(N-1)/2}. \tag{1.10}$$

The subscript f indicates the condition that the orientational distribution is given by $f(\Omega)$. Furthermore, Φ_{12} is the Mayer function, defined as

$$\Phi_{12} \equiv \exp\left[-\beta w(\mathbf{r}_{12}; \Omega_1, \Omega_2)\right] - 1. \tag{1.11}$$

Applying the hard-core pair potential Eq. (1.2) we see that this function is equal to -1 if two particles 1 and 2 overlap and zero otherwise. Spatially integrating the Mayer function yields the so-called pair cluster integral β_1:

$$\beta_1(\Omega_1, \Omega_2) \equiv \frac{1}{V} \int d\mathbf{r}_1 d\mathbf{r}_2 \Phi(\mathbf{r}_{12}; \Omega_1, \Omega_2) = -v_{\text{excl}}(\Omega_1, \Omega_2), \tag{1.12}$$

which is equal to minus the *excluded volume* v_{excl} of two anisometric particles at fixed solid angles Ω_1 and Ω_2. Using this in Eq. (1.10) yields

$$Q_N^{\text{int}} \approx \left[1 - \frac{1}{V} \iint d\Omega_1 d\Omega_2 f(\Omega_1) f(\Omega_2) v_{\text{excl}}(\Omega_1, \Omega_2) \right]^{N(N-1)/2}$$

$$\approx \exp\left[-N\frac{\rho}{2} \iint d\Omega_1 d\Omega_2 f(\Omega_1) f(\Omega_2) v_{\text{excl}}(\Omega_1, \Omega_2) \right]. \tag{1.13}$$

Collecting results we obtain the following expression for the free energy of a fluid of hard anisometric particles in the second virial approximation:

$$
\begin{aligned}
\frac{\beta F}{N} =& \beta\mu_0 + \ln\left[\mathcal{V}\rho\right] - 1 + \int f(\Omega)\ln\left[4\pi f(\Omega)\right]d\Omega \\
&+ \frac{\rho}{2}\iint d\Omega d\Omega' f(\Omega)f(\Omega')v_{\text{excl}}(\Omega,\Omega').
\end{aligned}
\tag{1.14}
$$

with μ_0 a reference chemical potential of the dispersed particles depending only on the solvent conditions. Higher order contributions in the virial expansion of the free energy –involving clusters of three, four, etcetera particles– can be derived using similar arguments as in Eq. (1.10) [27]. In the *third virial* approximation for example we encounter the triplet cluster integral $\beta_2(\Omega_1,\Omega_2,\Omega_3)$

$$
\beta_2(\Omega_1,\Omega_2,\Omega_3) \equiv \frac{2}{V}\iiint d\mathbf{r}_1 d\mathbf{r}_2 d\mathbf{r}_3 \Phi_{12}\Phi_{13}\Phi_{23},
\tag{1.15}
$$

which is nonzero only if three particles overlap simultaneously. Eq. (1.15) and higher order cluster integrals are notoriously difficult to calculate because this requires knowledge of the excluded volume of a multi-particle cluster as a function of the orientations of all particles involved. In practice, other methods are adopted to include higher virial terms, albeit approximately, such as 'scaled particle' [22,28] and density functional theories (see [5,29] for a review). In this thesis we shall often use the so-called decoupling approximation, to be described in Sec. 1.3.3.

The next step is to minimize the free energy, at a given density ρ, with respect to the non-conserved orientational degrees of freedom. In practice, there are two different ways to find this minimum; a formal approach and a trial function method which we both shall discuss briefly here. The formal way is to apply a functional differentiation of the free energy with respect to the ODF $f(\Omega)$. This yields the stationarity condition:

$$
\frac{\delta}{\delta f(\Omega)}\left[\frac{\beta F}{N} - \lambda'\int f(\Omega)d\Omega\right] = 0,
\tag{1.16}
$$

where λ' is a Lagrange multiplier to be determined from the normalization condition for the ODF:

$$
\int f(\Omega)d\Omega = 1.
\tag{1.17}
$$

Inserting the free energy Eq. (1.14) gives a nonlinear integral equation

$$
\ln[4\pi f(\Omega)] = \lambda - \rho\int f(\Omega')v_{\text{excl}}(\Omega,\Omega')d\Omega',
\tag{1.18}
$$

with $\lambda = \lambda' - 1$. A trivial solution to Eq. (1.18) is the constant $f(\Omega) = 1/4\pi$ describing an *isotropic* fluid in which all particle orientations are equally probable. The thermodynamic equilibrium ODF for a *nematic* state –which will be a peaked function– can however only be obtained numerically e.g. in terms of a series expansion in Legendre polynomials [30–32] or by means of a discretization scheme [33]. It is important to realize that for *uniaxial* particles the ODF satisfies both azimuthal symmetry around the nematic director and inversion symmetry. The former implies that the ODF depends

only on the polar angle θ between the particle orientation vector and the nematic direc-tor[†], so that $f(\Omega) = f(\theta)$. The latter implies the angles θ and $\pi - \theta$ being equivalent, thus $f(\theta) = f(\pi - \theta)$.

To avoid the necessity of solving the nonlinear integral equation Eq. (1.18) one may choose the trial function approach instead. The ODF $f(\Omega)$ in Eq. (1.14) is then replaced by a *fixed functional form* depending on one or more variational parameters and the free energy is subsequently minimized with respect to these parameters. This approach was first employed by Onsager in his original paper [21] where he used the following trial form:

$$f_O(\cos\theta) = \frac{\alpha \cosh(\alpha \cos\theta)}{4\pi \sinh\alpha}, \tag{1.19}$$

in terms of the variational parameter α. Although this trial function gives reasonable results for the isotropic-nematic phase transition the analysis involved is quite com-plicated. In this thesis we shall therefore often use the simpler Gaussian trial ODF, introduced by Odijk [34]:

$$f_G(\theta) \cong \begin{cases} Z\exp[-\frac{1}{2}\alpha\theta^2] & \text{if } 0 \leq \theta \leq \frac{\pi}{2} \\ \\ Z\exp[-\frac{1}{2}\alpha(\pi-\theta)^2] & \text{if } \frac{\pi}{2} \leq \theta \leq \pi \end{cases} \tag{1.20}$$

The normalization constant $Z = Z(\alpha)$ can be calculated analytically by means of an asymptotic expansion for large α. Noting that $f_G(\theta)$ is then a rapidly decaying function we may expand as follows

$$Z = \left[\int_0^{2\pi} d\phi \int_0^{\pi} \exp\left[-\frac{1}{2}\alpha\theta^2\right]\sin\theta d\theta\right]^{-1} \sim \left[4\pi\int_0^{\infty} \exp\left[-\frac{1}{2}\alpha\theta^2\right]\left\{\theta - \frac{1}{6}\theta^3 + \ldots\right\}d\theta\right]^{-1}$$

$$\sim \frac{\alpha}{4\pi}\left(1 + \frac{1}{3\alpha} + \ldots\right), \tag{1.21}$$

where the error introduced by extending the θ-integration to infinity is $\mathcal{O}(\mathrm{e}^{-\alpha})$. Retain-ing the leading order term in Eq. (1.21) we see that the Gaussian ODF, unlike $f_O(\cos\theta)$, does *not* give the correct isotropic ODF $1/4\pi$ in the limit $\alpha \to 0$, since $f_G(\theta)$ vanishes in this limit. Using the Gaussian ODFs we can calculate the *typical* or root-mean-square polar angle, which is related to the variational parameter via $\langle\theta^2\rangle^{1/2} \propto \alpha^{-1/2}$, showing that it will be small for large α. We shall use this relation implicitly in Chapter 5 where an alternative description of the trial function approximation will be presented entirely in terms of these typical angles.

A benefit of using the Gaussian trial ODF is that it renders the Onsager theory analytically tractable. The free energy minimization can be carried out entirely ana-lytically, which reveals that $\alpha \propto \rho^2$, whereas approximate asymptotic expressions can be derived for the orientational and excess parts of the free energy Eq. (1.14) [5, 34]. Although the Gaussian ODF is *not* a solution of the the exact stationarity condition

---

[†]An exception to this case is a mixture of uniaxial rods and plates, where the ODF may depend on the azimuthal angle as well due to a possible *biaxial* symmetry of the nematic phase. This will become clear in Chapter 4.

Eq. (1.16) it does satisfy an exact high-density scaling relation for the ODF, as was shown by Van Roij [35], owing to the abovementioned quadratic density-dependence of the variational parameter. This in turn implies that the Gaussian ODF is particularly suitable for strongly ordered nematic phases. As to mixtures of rods with different lengths, the Gaussian ODF has so far been successful in explaining the generic features of the isotropic-nematic phase behaviour such as a fractionation effect, a widening of biphasic gap [34] and the existence of triphasic and nematic-nematic equilibria [36].

As is clear from Eq. (1.12) the key ingredient in the Onsager theory is the excluded volume of two particles which depends essentially on the shape of the particles under consideration. In this thesis we shall model the particles as cylinders with length L and D; slender rods are then characterized by $L/D \gg 1$ whereas thin platelets have $L/D \ll 1$. Henceforth, we will use the ratio of the largest to the shortest dimension of the particle, the *aspect ratio*, to quantify the anisometry of the particle. The general expression for the excluded volume of two different cylinders with lengths L_1 and L_2 and diameters D_1 and D_2 at mutual angle γ has been derived in closed form by Onsager in a remarkable appendix to his paper [21]. The result is

$$v_{\text{excl}}(L_1, D_1; L_2, D_2; \gamma) = \frac{\pi}{4} D_1 D_2 (D_1 + D_2) |\sin\gamma| + L_1 L_2 (D_1 + D_2) |\sin\gamma|$$
$$+ L_2 \left[\frac{\pi}{4} D_2^2 + D_1 D_2 E(\sin\gamma) + \frac{\pi}{4} D_1^2 |\cos\gamma| \right]$$
$$+ L_1 \left[\frac{\pi}{4} D_1^2 + D_1 D_2 E(\sin\gamma) + \frac{\pi}{4} D_2^2 |\cos\gamma| \right], \tag{1.22}$$

with $E(x)$ the complete elliptic integral of the second kind. For sufficiently anisometric particles characterized by a large aspect ratio, we may neglect the $\mathcal{O}(LD^2)$-contributions arising from the particles' finite thicknesses[‡] and retain only the leading order contribution, given by the first term (in case of thin platelets) or the second one (for slender rods). To assess the influence of multi-particle correlations Onsager gave some geometric arguments to estimate the following scaling behaviour of the triplet cluster integral Eq. (1.15) for *isotropically oriented* thin rods

$$\frac{\beta_2}{\beta_1^2} \sim \mathcal{O}\left(\frac{D}{L} \ln \frac{L}{D} \right), \tag{1.23}$$

which clearly vanishes for $L/D \rightarrow \infty$. The decrease has been verified by means of Monte-Carlo simulations on hard spherocylinders by Frenkel [37,38] showing that higher order virial coefficients can be neglected only if $L/D \gg 100$. The situation is much different for thin platelets for which Onsager estimated

$$\frac{\beta_2}{\beta_1^2} \sim \mathcal{O}(1), \tag{1.24}$$

which is also true for spheres. This important result shows that the third and higher virial terms cannot be neglected for thin platelets (not even in the limit $L/D \rightarrow 0$) [18].

[‡]Strictly, this is only justified if the orientational order in the nematic state is such that the typical mutual angles $\langle\langle \gamma \rangle\rangle$ are large compared to D/L (rods) or L/D (platelets).

In the concentrated *nematic* state the interactions between the aligned particles are much stronger due to steric hindering. For slender rods Onsager showed that the third virial coefficient in the aligned state remains vanishingly small only if the typical angle between the particles $\langle\langle\gamma\rangle\rangle$ is much larger than the so-called *internal* angle $\gamma_{\text{int}} \sim D/L$ of the rod. If $\langle\langle\gamma\rangle\rangle$ is of the order D/L the rods are nearly parallel and the triplet cluster is always finite, as in Eq. (1.24), irrespective of L/D. However, it turns out that the latter situation is not encountered for thin rods since the ratio of the typical and internal angles $\langle\langle\gamma\rangle\rangle/\gamma_{\text{int}}$ can be shown to scale as $\sim L/D$, indicating that higher virial terms vanish in the nematic phase for $L/D \to \infty$ [5]. We can therefore conclude that Onsager's second virial theory for the isotropic-nematic transition is an *exact* theory for rods in the limit $L/D \to \infty$ whereas only qualitative results can be expected for short rods (say $L/D \ll 100$) and platelike particles.

1.3.2. Mixtures

In this thesis we shall be concerned with mixtures of anisometric particles comprising either two distinctly different species (binary mixtures) or a large number of particles with a continuously varying size parameter (polydisperse mixtures). Introducing mole fractions $x_j = N_j/N$ of species j, the free energy of a mixture is given by a simple generalization of Eq. (1.14):

$$\frac{\beta F}{N} \sim \ln[\rho\bar{\mathcal{V}}] - 1 + \sum_j x_j \ln x_j + \sum_j x_j \int f_j(\Omega) \ln\left[4\pi f_j(\Omega)\right] d\Omega$$

$$+ \frac{\rho}{2} \sum_j \sum_k x_j x_k \iint d\Omega d\Omega' f_j(\Omega) f_k(\Omega') v_{\text{excl}}^{jk}(\Omega, \Omega'), \tag{1.25}$$

with $\bar{\mathcal{V}} = \prod_j \mathcal{V}_j^{x_j}$. The contribution following the ideal entropy is an *entropy of mixing* due to the fact that we are dealing with different species. Although the free energy for mixtures is easily established, the implications of Eq. (1.25) are quite drastic. In particular, each species j now has its own ODF which must be normalized according to $\int f_j(d\Omega) d\Omega \equiv 1$. Formally minimizing the free energy with respect to all ODFs then gives a *coupled* set of nonlinear equations:

$$\ln[4\pi f_j(\Omega)] = \lambda_j - \rho \sum_k x_k \int f_k(\Omega') v_{\text{excl}}^{jk}(\Omega, \Omega') d\Omega', \tag{1.26}$$

which is progressively difficult to solve if the number of components increases. A similar set of coupled equations, albeit not in integral form, can be obtained from the Gaussian trial function approximation by inserting $f_G(\alpha_j; \theta)$ from Eq. (1.20) and minimizing with respect to all α_j. Moreover, in case of a phase coexistence between e.g. an isotropic (I) and a nematic (N) phase, the conditions for mechanical and chemical equilibria require equal osmotic pressure Π and chemical potentials μ_j for *all* species involved. Hence, the coexistence equations are

$$\Pi^I = \Pi^N$$
$$\mu_j^I = \mu_j^N \qquad \text{for } all \ j, \tag{1.27}$$

where we must realise that the composition $\{x_j\}$ may be different in each phase due to fractionation effects. These considerations indicate that the calculation of phase transition in mixtures is, in general, a difficult task. For the binary mixtures to be considered in Part I in this thesis, the equations are still manageable, in particular when the Gaussian approximation is used. However, for the polydisperse systems treated in Part II, the situation is usually much worse so that special numerical techniques have to be devised to solve the coupled minimization equations along with the coexistence conditions, as we shall see in Chapter 6.

1.3.3. Parsons' theory

Parsons [23] showed that the orientational degrees of a system of anisometric particles may be decoupled from the translational ones if the *pair correlation function* is assumed to obey a certain scaling form. Before discussing the full details of the approach let us first state the basic equations needed. We start from the generalized virial equation for a homogeneous system of monodisperse anisometric particles, which reads [26]:

$$\beta\Pi = \rho - \frac{\rho^2}{6} \int d\Delta\mathbf{r} \iint d\Omega d\Omega' f(\Omega) f(\Omega') \left[\Delta r \nabla_r \beta w(\Delta\mathbf{r}; \Omega, \Omega')\right] g(\Delta\mathbf{r}; \Omega, \Omega'; \rho), \quad (1.28)$$

with Π the osmotic pressure of the fluid. The gradient ∇_r acts only on the spatial coordinate $\Delta\mathbf{r} = \mathbf{r} - \mathbf{r}'$ of the pair interaction w. Eq. (1.28) is difficult to use in practice because of the unknown pair correlation function g describing the possibility to find, at a given density ρ, two particles with respective orientations Ω and Ω' at a distance $\Delta\mathbf{r}$. Using the standard relation

$$\beta\Pi = \left(\frac{\partial \beta F}{\partial V}\right)_{N,T,f(\Omega)} = \rho^2 \left(\frac{\partial \beta F/N}{\partial \rho}\right)_{N,T,f(\Omega)}, \quad (1.29)$$

and integrating over ρ yields a formal expression for the excess free energy:

$$\frac{\beta F_{\text{excess}}}{N} = -\frac{1}{6} \int d\Delta\mathbf{r} \iint d\Omega d\Omega' f(\Omega) f(\Omega')$$
$$\times \int_0^\rho d\rho' \left[\Delta r \nabla_r \beta w(\Delta\mathbf{r}; \Omega, \Omega')\right] g(\Delta\mathbf{r}; \Omega, \Omega'; \rho'), \quad (1.30)$$

As before we can approximate this expression by applying a virial expansion up to first order in the density. In the second virial approximation the pair correlation function is written as $g \approx \exp[-\beta w]$ and the integration over ρ becomes trivial. Furthermore, an integration by parts on the $d\Delta\mathbf{r}$ integral gives

$$\frac{\beta F_{\text{excess}}}{N} = -\frac{\rho}{2} \iint d\Omega d\Omega' f(\Omega) f(\Omega') \int d\Delta\mathbf{r} \left(\exp\left[-\beta w(\Delta\mathbf{r}; \Omega, \Omega')\right] - 1\right)$$
$$= -\frac{\rho}{2} \iint d\Omega d\Omega' f(\Omega) f(\Omega') \beta_1(\Omega, \Omega'), \quad (1.31)$$

Clearly, with Eq. (1.12), this expression is equivalent to the Onsager excess free energy Eq. (1.14), as should be the case.

To account for spatial correlations at higher densities Parsons suggested the following scaling Ansatz for the pair correlation function:

$$g(\Delta\mathbf{r};\Omega,\Omega';\rho) = g\left(\frac{\Delta r}{\sigma(\hat{\mathbf{r}};\Omega,\Omega')};\rho\right), \tag{1.32}$$

where $\sigma(\hat{\mathbf{r}};\Omega,\Omega')$ is the (centre-to-centre) distance of nearest approach of two particles along the unit vector $\hat{\mathbf{r}}$ connecting their centres of mass. Eq. (1.32) basically represents a mapping of the pair correlation function for anisometric particles onto the radially symmetric $g(\Delta r/\sigma_{\mathrm{HS}};\rho)$ for spheres with the sphere diameter σ_{HS} replaced by an orientation-dependent collision diameter $\sigma(\hat{\mathbf{r}};\Omega,\Omega')$. An implication of Eq. (1.32) is that the contact value of the correlation function $g(1;\rho)$ will be the same regardless of the particle orientations. The quality of the decoupling approximation is difficult to assess precisely but it is expected to become worse for higher particle anisometry and densities. The quantitative value of the approach will be discussed below.

When we apply the Ansatz in Eq. (1.30) the $\Delta\mathbf{r}$ integral can be split into a positional and orientational part. Using $\int d\Delta\mathbf{r} = \int d\hat{\mathbf{r}} \int \Delta r^2 d\Delta r$ we obtain after some algebra

$$\int d\Delta\mathbf{r} \int_0^\rho d\rho' \Delta r \frac{\partial\beta w}{\partial\Delta r} g\left(\frac{\Delta r}{\sigma(\hat{\mathbf{r}};\Omega,\Omega')}\right) = \int_1^\infty dy\, y^3 \int_0^\rho d\rho' \frac{\partial\beta w}{\partial y} g(y;\rho') \int \sigma^3(\hat{\mathbf{r}};\Omega,\Omega') d\hat{\mathbf{r}}$$

$$= \int_0^\rho d\rho'\, g(1;\rho') \int \sigma^3(\hat{\mathbf{r}};\Omega,\Omega') d\hat{\mathbf{r}}$$

$$= J(\rho) \int \sigma^3(\hat{\mathbf{r}};\Omega,\Omega') d\hat{\mathbf{r}}, \tag{1.33}$$

with $y = \Delta r/\sigma(\hat{\mathbf{r}};\Omega,\Omega')$ the rescaled interparticle distance. Here, we have also used that $\partial\beta w/\partial y = \delta(y-1)$ for hard-body interactions. The function $J(\rho)$ arises from integrating the contact value of the pair distribution function $g(1;\rho)$ over the density ρ. The integration over the unit vector $\hat{\mathbf{r}}$ represents the excluded volume, i.e.

$$v_{\mathrm{excl}}(\Omega,\Omega') = \frac{1}{3}\int d\hat{\mathbf{r}}\,\sigma^3(\hat{\mathbf{r}};\Omega,\Omega') \tag{1.34}$$

which gives the correct limit $v_{\mathrm{excl}} = 4\pi\sigma_{\mathrm{HS}}^3/3$ for hard spheres with $\sigma(\hat{\mathbf{r}};\Omega,\Omega') = \sigma_{\mathrm{HS}}$. The excess free energy in the decoupling approximation thus becomes

$$\frac{\beta F_{\mathrm{excess}}^{\mathrm{P}}}{N} = \frac{1}{2}J(\rho)\iint d\Omega d\Omega'\, f(\Omega)f(\Omega')v_{\mathrm{excl}}(\Omega,\Omega'), \tag{1.35}$$

Going back to $J(\rho)$ we may now use the results for a hard-sphere fluid to express it in explicit form. First of all we notice from the virial equation Eq. (1.28) that the equation of state for hard spheres is given by

$$\frac{\beta\Pi V}{N} = 1 - 4\phi \int dy\, y^3 \frac{\partial\beta w(y)}{\partial y} g(y;\rho)$$

$$= 1 - 4\phi g(1;\rho) \tag{1.36}$$

with $y = \Delta r/\sigma_{\text{HS}}$ and $\phi = \rho\pi\sigma_{\text{HS}}^3/6$ the volume fraction. Using the Carnahan-Starling equation of state [39]

$$\frac{\beta\Pi_{\text{HS}}V}{N} = \frac{1 + \phi + \phi^2 - \phi^3}{(1-\phi)^3}, \tag{1.37}$$

which represents a very good fit to the simulation data for a hard-sphere fluid up to the freezing volume fraction $\phi = 0.494$, $J(\rho)$ is obtained by straightforward integration via

$$J(\rho) = \int_0^\rho \frac{1}{4\phi}\left[1 - \frac{\beta\Pi_{\text{HS}}V}{N}\right]d\rho'$$
$$= \rho\frac{4-3\phi}{4(1-\phi)^2}, \tag{1.38}$$

Gathering results and comparing with Eq. (1.14) we see that the decoupling approximation boils down to a *rescaling* of the Onsager second-virial free energy according to

$$\frac{\rho}{2}\langle\langle v_{\text{excl}}(\Omega, \Omega')\rangle\rangle_{f(\Omega)} \rightarrow \frac{\rho}{2}\tilde{f}_{\text{CS}}\langle\langle v_{\text{excl}}(\Omega, \Omega')\rangle\rangle_{f(\Omega)}, \tag{1.39}$$

with

$$\tilde{f}_{\text{CS}}(\phi) = \frac{1 - (3/4)\phi}{(1-\phi)^2}. \tag{1.40}$$

Noting that $\tilde{f}_{\text{CS}}(\phi) \rightarrow 1$ for ϕ going to zero we see that the second virial coefficient is unaffected by the rescaling, as it should. Alternatively, one might regard Parsons' approach as a generalization of the Carnahan-Starling excess free energy to anisometric particles. Considering the Carnahan-Starling excess free energy for hard spheres

$$\frac{\beta F_{\text{excess}}^{\text{CS}}}{N} = \frac{4-3\phi}{(1-\phi)^2}, \tag{1.41}$$

obtained by standard integration of Eq. (1.37), the Parsons excess free energy can be expressed as

$$\frac{\beta F_{\text{excess}}^{\text{P}}}{N} = \frac{\langle\langle v_{\text{excl}}(\Omega, \Omega')\rangle\rangle}{8v_0}\frac{\beta F_{\text{excess}}^{\text{CS}}}{N}, \tag{1.42}$$

where the orientation dependent prefactor reduces to 1 for spheres (v_0 is the particle volume). Parsons' method thus allows us to incorporate many-body effects –albeit in an average way– while requiring only explicit knowledge of the two-particles interactions embodied in the excluded volume. For this reason, the method is much easier to implement than the straightforward option of direct inclusion of higher virial terms [40, 41]. Extending the approach to binary and polydisperse mixtures does not pose serious difficulties as we shall see in Chapter 2 and 7. It is important to note that Parsons' method does not affect the free energy (and hence the phase behaviour) of platelets in the limit $L/D \rightarrow 0$. The reason for this is that infinitely thin platelets have a *zero* volume, according to Eq. (1.22) and hence a zero packing fraction. This in turn implies that $f_{\text{CS}} = 1$ for all densities.
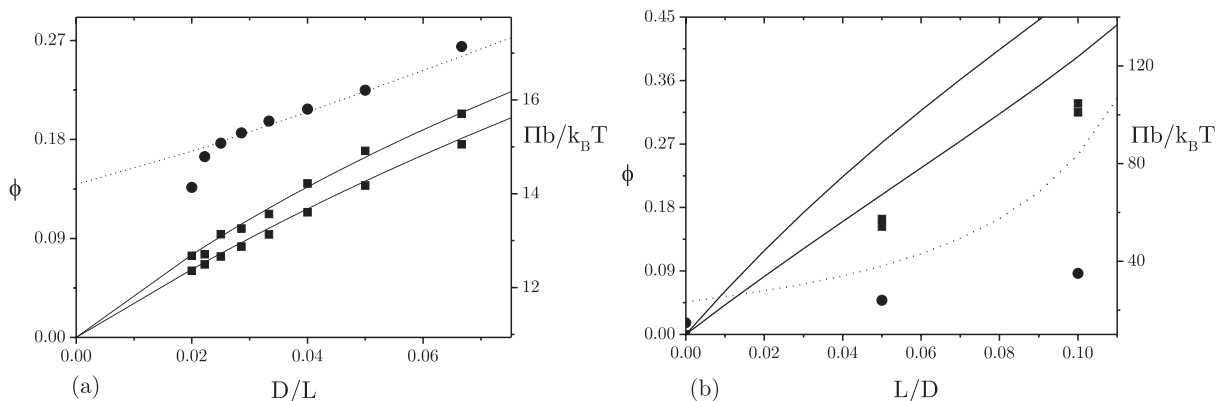
FIGURE 1.2. Isotropic-nematic coexistence volume fractions and osmotic pressure obtained from the Onsager-Parsons free energy compared with simulation results. (a) Hard spherocylinders. The solid and dotted lines are theoretical results for the transition densities and the coexistence pressure, respectively. Squares and circles denote corresponding results from Monte-Carlo simulations [42]. We have plotted the *inverse* aspect ratio on the horizontal axis. The pressure is rendered dimensionless using the excluded volume $b = \frac{\pi}{4}L^2 D$ for thin rods. (b) Same for hard disklike cylinders using simulation results from [43]. Here, $b = D^3$.

The quantitative success of Parsons' approach has initially been confirmed by Lee [44, 45] for hard rodlike particles. The $I - N$ transition densities calculated for a system of hard ellipsoidal particles with aspect ratio $L/D = 5$ were found in close agreement with results from computer simulations. More extensive comparisons between the Onsager-Parsons theory and simulations were made by Mc Grother *et al.* [46] for short hard spherocylinders ($L/D < 5$) and by Camp *et al.* [47] for hard prolate ellipsoids ($5 \leq L/D \leq 20$). In both cases, the transition densities as found from the theory agreed very well with the simulation results. In a similar study, Camp *et al.* [48, 49] showed that Parsons' approach also worked well for mixtures of rod- and platelike ellipsoids, showing improved quantitative agreement with computer simulations over the Onsager theory and the y-expansion approach. The latter method, which is due to Barboy and Gelbart [50], provides direct inclusion of higher virial terms by a recasting of the free energy in terms of a new density variable y. The results of Camp and co-workers motivated us to apply Parsons' method to the mixtures of rods and plates discussed in Chapter 3.

Unlike hard rods, no systematic comparative study has been reported so far on the effect of the Parsons rescaling on the $I - N$ transition in systems of hard platelike particles. For this reason we have combined in Fig. 1.2 the results for spherocylinders and platelets. The theoretical calculations were based on the Onsager-Parsons free energy using a formal minimization procedure [33]. The rods were modeled as spherocylinders and the platelets were represented by flat cylinders. These are compared with Monte Carlo simulations results for spherocylinders performed by Bolhuis [42] and cut spheres by Zhang [43]. The latter are platelike objects obtained by slicing two caps off a sphere

of diameter D, at two planes parallel to the equatorial plane with equal distance $L/2$. Although the shape of a cut sphere is different from a cylindrical disk used in the calculations, the discrepancy is expected to be marginal for sufficiently anisometric platelets. The agreement between theory and simulations is surprisingly good for spherocylinders (as already noted by Lee) but unfortunately quite poor for the platelets. In particular, Parsons' approach tends to overestimate both the transition densities and the width of the coexistence region $\phi_N - \phi_I$. The coexistence pressure is also predicted much larger compared to the simulation. As to platelike particles we must therefore conclude that although Parsons' approach constitutes a significant improvement over the original second virial theory (the results of which are not shown here), there is a considerable lack of quantitative agreement with computer simulations.

1.3.4. Inhomogeneous liquid crystal phases

So far we have restricted ourselves to systems where the particle density is homogeneously distributed throughout the system. As already alluded to before, a homogeneous nematic fluid may become smectic or columnar at higher densities leading to modulatory spatial density profiles. Spatial inhomogeneity is also present for example near an interface separating two coexisting phases with different densities, or it may be induced by a wall –which gives rise to local structuring of the homogeneous fluid– or an external gravitational, electromagnetic or flow field leading e.g. to gradients in the density. All of these cases can be formally described within the framework of *density functional theory* (DFT) which was introduced in the field of classical fluids in the late 1970s to study freezing of hard spheres [51, 52] and the nature of the liquid-gas interface [53]. Although DFT has been widely and successfully used to describe phase transitions and other phenomena in systems of spherical particles [54,55], its application to lyotropic liquid crystals is at present much less developed [5, 29].

In the following we will not describe the formal background of DFT nor shall we treat the inhomogeneous liquid crystal phases in full. Instead, we merely show how an *instability* of the homogeneous nematic phase with respect to these phases can be established starting from the rescaled second virial approximation explained above. Introducing the generalized density distribution $\rho(\mathbf{r}; \Omega)$ the expression for the Onsager-Parsons free energy for a monodisperse system can be recast into the following density functional

$$
\begin{aligned}
\beta F[\rho] =& \beta \mu_0 + \iint d\mathbf{r}\, d\Omega\, \rho(\mathbf{r}; \Omega) \left\{ \ln[\mathcal{V}\rho(\mathbf{r}; \Omega)] - 1 \right\} \\
& - \tilde{f}_{\mathrm{CS}}(\phi)\frac{1}{2} \iint d\mathbf{r}\, d\Omega \iint d\mathbf{r}'\, d\Omega'\, \Phi(\Delta\mathbf{r}; \Omega, \Omega')\rho(\mathbf{r}; \Omega)\rho(\mathbf{r}'; \Omega').
\end{aligned}
\tag{1.43}
$$

For a homogeneous fluid we may substitute $\rho(\mathbf{r}; \Omega) = \rho f(\Omega)$ which immediately gives back the original Onsager result Eq. (1.14) (ignoring $\tilde{f}_{\mathrm{CS}}(\phi)$) as we expect. Formally,

the second virial approximation represents the simplest density functional one can construct. It corresponds to the *direct correlation function* $c(\Delta\mathbf{r};\Omega,\Omega')$ [26] being proportional to the Mayer function for all densities, i.e.

$$c(\Delta\mathbf{r};\Omega,\Omega') \equiv -\frac{\delta^2\beta F_{\text{excess}}}{\delta\rho(\mathbf{r})\delta\rho(\mathbf{r}')} = \tilde{f}_{\text{CS}}(\phi)\Phi(\Delta\mathbf{r};\Omega,\Omega'). \tag{1.44}$$

This correlation function has also been tested *directly* against results from computer simulations –at least for hard ellipsoids– showing that its quality compares very well with more complicated density functional approaches [56].

We will now determine the limit of stability of the spatially homogeneous nematic state by means of a *bifurcation analysis*. This technique which was introduced in the field of liquid crystals by Kayser and Raveché [30] and later elaborated by Mulder [57] in general involves probing the stability of a homogeneous phase with respect to infinitesimal density perturbations pertaining to "new" inhomogeneous states. The analysis can also be applied to the stationarity condition Eq. (1.18) to locate the state point where inhomogeneous (i.e. nematic) solutions for the ODF branch off from the homogeneous isotropic ODF [30]. This will be done in Chapter 4. For the smectic and columnar state the following density modulations are proposed

$$\rho(\mathbf{r};\Omega) = \rho f(\Omega) + \delta\rho(\mathbf{q};\Omega)\cos(\mathbf{q}\cdot\mathbf{r}) \qquad \text{(smectic)}$$

$$\rho(\mathbf{r};\Omega) = \rho f(\Omega) + \delta\rho(\mathbf{q};\Omega)\sum_{i=1}^{3}\cos(\mathbf{q}_i\cdot\mathbf{r}) \qquad \text{(columnar)}, \tag{1.45}$$

which obey the condition of inversion symmetry for the wave vector (i.e. $\mathbf{q} = -\mathbf{q}$). Defining the nematic director $\hat{\mathbf{n}} = \{0,0,1\}$ along in the z-director of the Cartesian frame, we may write $\mathbf{q} = q_{\text{SmA}}\{0,0,1\}$ for the smectic phase, resembling the one-dimensional density modulation along the director. In the columnar state the six-fold rotational symmetry of the hexagonal lattice perpendicular to the director can be described by a combination of three wave vectors: $\mathbf{q}_1 = q_{\text{C}}\{1, 1/\sqrt{3}, 0\}$, $\mathbf{q}_2 = q_{\text{C}}\{1, -1/\sqrt{3}, 0\}$, $\mathbf{q}_3 = q_{\text{C}}\{0, 2/\sqrt{3}, 0\}$. The magnitude of the wave vectors is related via $q = 2\pi/\lambda$ to the typical *spacing* λ corresponding to the smectic and columnar density modulations.

Inserting Eq. (1.45) into the free energy and performing a Landau-type expansion up to quadratic order in the amplitude $\delta\rho(\mathbf{q};\Omega)$ we obtain the following condition for marginal stability of the homogeneous nematic phase:

$$\beta\delta^2 F = \iint d\Omega d\Omega' \left\{ \frac{\delta(\Omega,\Omega')}{\rho f(\Omega)} - \hat{c}(\mathbf{q};\Omega,\Omega') \right\} \delta\rho(\mathbf{q};\Omega)\delta\rho(\mathbf{q};\Omega') > 0, \tag{1.46}$$

where the caret denotes a cosine transform of the direct correlation function:

$$\hat{c}(\mathbf{q};\Omega,\Omega') \equiv \int d\Delta\mathbf{r}\cos(\mathbf{q}\cdot\Delta\mathbf{r})c(\Delta\mathbf{r};\Omega,\Omega'). \tag{1.47}$$

For the columnar symmetry this leads to superposition of three transforms corresponding to $\mathbf{q}_1,\mathbf{q}_2$ and $\mathbf{q}_3$. The amplitude of the perturbation may be factorized according to $\delta(\mathbf{q};\Omega) = \delta\rho(\mathbf{q})f_{(1)}(\Omega)$ with $f_{(1)}(\Omega)$ the new ODF pertaining to the periodic density fluctuation. If we assume that *only spatial* density fluctuations are responsible for

the loss of nematic stability we may set $f_{(1)}(\Omega) = f(\Omega)$ and the bifurcation condition $(\beta\delta^2 F = 0)$ then becomes equivalent to a divergence of the nematic structure function $S(\mathbf{q}; \rho)$:

$$S^{-1}(\mathbf{q}; \rho) = \left[1 - \iint d\Omega d\Omega' f(\Omega) f(\Omega') \hat{c}(\mathbf{q}; \Omega, \Omega')\right] = 0. \tag{1.48}$$

However, the rigorous method of locating the bifurcation point assumes both spatial and orientational fluctuations. Recasting Eq. (1.46) then gives the following self-consistency equation for the unknown orientation distribution $f_{(1)}(\Omega)$

$$f_{(1)}(\Omega) = \rho f(\Omega) \int d\Omega' f_{(1)}(\Omega') \hat{c}(\mathbf{q}; \Omega, \Omega'). \tag{1.49}$$

The bifurcation from the nematic to smectic or columnar state is given by the smallest number density ρ^* (and corresponding ODF $f^*(\Omega)$) that gives rise to a non-trivial solution $f_{(1)}(\Omega) = f_{(1)}^*(\Omega)$ of Eq. (1.49).

The key point in the analysis is finding an appropriate expression for the transformed direct correlation function $\hat{c}(\mathbf{q}; \Omega, \Omega')$. Within the rescaled second virial approximation it is related via Eq. (1.44) to a cosine transform of the *excluded volume body* of two anisometric particles:

$$\hat{c}(\mathbf{q}; \Omega, \Omega') = \tilde{f}_{\mathrm{CS}}(\phi) \int d\Delta\mathbf{r} \cos(\mathbf{q} \cdot \Delta\mathbf{r}) \Phi(\Delta\mathbf{r}; \Omega, \Omega')$$

$$= -\tilde{f}_{\mathrm{CS}}(\phi) \int_{v_{\mathrm{excl}}(\Omega, \Omega')} d\Delta\mathbf{r} \cos(\mathbf{q} \cdot \Delta\mathbf{r}). \tag{1.50}$$

Determining this quantity is a non-trivial task since it requires detailed knowledge of the shape of the excluded-volume body. For spherocylinders an explicit result for the transform was provided by Van Roij [58]. However, doing a similar calculation for a cylindrical plate with finite thickness does not seem worthwile due to the complex shape of its excluded volume body [59].

In Chapter 8 of this thesis we shall treat the much simpler case of *parallel* hard cylinders for which the transformed excluded volume can be easily calculated. Moreover, assuming perfectly aligned particles allows us to extend the present description to a *polydisperse* one. We will show that the approach leads to bifurcation equations which are completely *analogous* to the ones presented here, the basic distinction being the fact that the thermodynamic state is now characterized by a *length* distribution rather than an ODF. Although the neglect of orientational freedom is a serious approximation –even in the high-density regime where the particles are strongly aligned– the model still allows us to make a qualitative assessment of the stability of smectic and columnar structures in polydisperse systems.

Part I

Binary mixtures of anisometric particles

2

Isotropic-nematic density inversion in mixtures of thin and thick hard platelets

ABSTRACT

We study the phase behaviour of a binary mixture of thin and thick hard platelets, using Onsager's second virial theory for binary mixtures in the Gaussian approximation. Higher virial terms are included indirectly by means of a rescaling of the free energy (Parsons' approach). Our calculations provide a simple explanation for the isotropic-nematic density inversion, as experimentally observed in systems of polydisperse gibbsite platelets by Van der Kooij [60]. In these systems, a nematic upper phase was found to coexist with an isotropic bottom phase. We confirm the original conjecture of the authors, which states that the phenomenon originates from a pronounced fractionation in thickness between the phases, such that the thick platelets are largely expelled from the nematic phase and preferentially occupy the isotropic phase. Our calculations show that the inverted state is found in a major part of the $I - N$ coexistence region. We also locate a nematic-nematic demixing transition for any thickness ratio $L_2/L_1 > 1$. At small ratios, the $N - N$ coexistence region is bounded by a lower critical point which shifts towards lower osmotic pressures as the thickness ratio is increased. At high ratios ($L_2/L_1 > 3.3$), a triphasic coexistence is encountered at which two nematic phases coexist with an isotropic phase. We show that the demixing transition is driven by a small $\mathcal{O}(L/D)$-contribution to the excluded volume entropy.

2.1. INTRODUCTION

Contrary to dispersions of colloidal rods, there is little experimental evidence of the isotropic-to-nematic phase transition in systems of platelike colloids. The first observations date back to 1938 in aqueous suspensions of clay particles by Langmuir [2]. However, many later observations in other clay systems have been obscured by gelation effects. In particular, macroscopic phase separation seems to be inhibited by the formation of a rigid gel network [61,62]. Recently, a novel model system for platelike colloids has been developed, consisting of sterically stabilized gibbsite platelets [11]. This system unambiguously shows a macroscopic phase separation into an isotropic and a birefringent nematic phase. The densities of these phases are in reasonable agreement with computer simulation results for hard platelets [63,64].

An important feature of the gibbsite platelets is their polydispersity, i.e. the particles differ in size and shape. The influence of polydispersity on the phase behaviour of
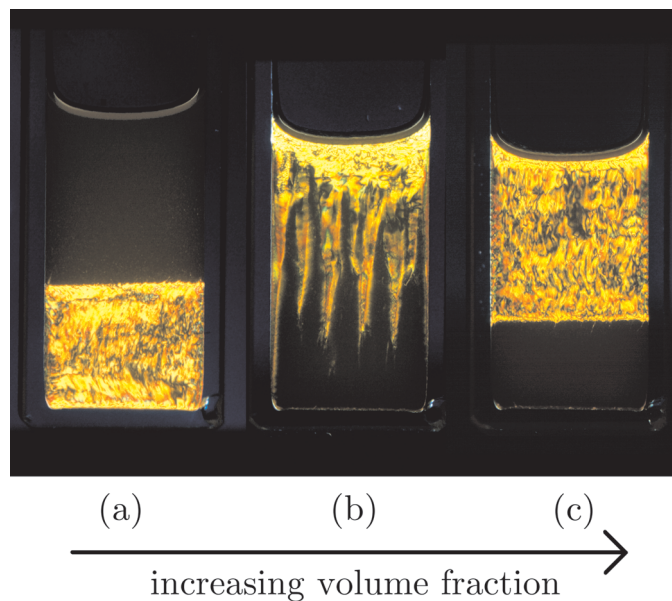
FIGURE 2.1. Samples of sterically stabilized gibbsite platelets after $I - N$ phase separation as observed between crossed polarizers. Volume fraction of the samples vary from (a) $\phi = 0.22$, (b) $\phi = 0.24$, to (c) $\phi = 0.25$. Picture taken from [60].

rod- and platelike colloids is an important factor in the interpretation of experimental results, as already pointed out by Onsager in his original paper [21]. Calculations on binary mixtures of long and short rods [65] within Onsager's approach have revealed some interesting phenomena like the fractionation effect (with the longer rods going preferentially to the nematic phase), a widening of the biphasic gap, a reentrant phenomenon and the possibility of triphasic and nematic-nematic equilibria [66].

The gibbsite systems, developed by Wierenga *et al.* [9], display a very broad size distribution in both diameter and thickness. The polydispersity σ was found to be approximately 25 % for both diameter and thickness [11]. Until recently, the effect of polydispersity in the platelets' thickness was considered to be far less important than the polydispersity in diameter, since the thickness hardly contributes to the excluded volume between two platelets and thus cannot have a significant influence on the phase behaviour. However, a recent experimental study by van der Kooij *et al.* [60] has shown that polydispersity in thickness can have considerable implications for the phase behaviour of platelike colloids.

In these experiments, the phase behaviour of suspensions of gibbsite platelets with a particularly broad distribution in thickness was investigated [60]. The polydispersity in thickness, although difficult to determine accurately, was estimated to be about 50 %. The high polydispersity is caused by the presence of a significant number of very thick platelets, as observed on the transmission electron microscopy (TEM) micrograph of the gibbsite samples. The suspensions show an $I - N$ phase separation over a wide range of particle concentrations. However, a remarkable phenomenon was observed;

in a major part of the coexistence region a nematic *upper* phase was found to coexist with an isotropic *bottom* phase (Fig. 2.1), which implies that the nematic phase has a lower mass density than the coexisting isotropic phase. Henceforth, we will refer to this phenomenon as the $I - N$ *density inversion.* It is argued that this anomalous behaviour is related to the platelets' considerable polydispersity in thickness. To explain the underlying mechanism, two aspects are mentioned by the authors [60]. On the one hand, the difference between the number densities of the coexisting phases; the total number density of platelets in the nematic phase will in general be higher than that in the coexisting isotropic phase and, consequently, the nematic phase will be more dense than the isotropic phase. On the other hand there is a clear evidence of fractionation in thickness between the coexisting phases, such that the thick platelets (i.e. the largest particles) accumulate in the isotropic phase, thereby increasing the mass density of the isotropic phase relative to that of the nematic phase. The authors conjecture that an $I - N$ density inversion may occur if the fractionation effect is strong enough to overcome the difference between the number densities of the coexisting phases.

Our objective in this Chapter is to study the phase behaviour of a simple binary mixture of thin and thick hard platelets starting from Onsager's theory. We show that our calculations indeed account for a significant fractionation effect as well as a density inversion in the $I - N$ coexistence region, thus confirming the conjecture of van der Kooij *et al.*

Within our theoretical approach, we also locate a nematic-nematic demixing transition. We show that a stable demixing transition occurs irrespective of the thickness ratio. At high ratios, an associated triphasic equilibrium is found. Recently, a similar demixing transition was found in binary mixtures of thin and thick rods [67–69], although only at sufficiently high thickness ratios ($\gtrsim 4$). There, even a stable isotropic-isotropic demixing transition could be located (see also [70]). This issue will be discussed in Chapter 5.

2.2. Onsager formulation

We consider a binary mixture of hard platelets of species $j = 1, 2$ with length (thickness) L_j and common diameter D in a macroscopic volume V. For the sake of definiteness we denote the thicker platelets by subscript 2, so that the composition variable $x = N_2/(N_1 + N_2)$ is the mole fraction of the thick platelets. Note that, contrary to a slender rod, the length-to-diameter ratio L/D of a thin platelet is a *small* parameter.

A nematic phase in a dilute solution of platelets is characterized by an ODF, $f_j(\theta)$, describing the distribution of the polar angle θ between the normal to the platelet of type j and the nematic director. The ODF must be normalized according to $\int f_j(\Omega)d\Omega \equiv 1$, with Ω the solid angle of the platelet's normal vector.

The formation of an isotropic state (with f_j constant) or a nematic state (with f_j a peaked distribution) is caused by a competition between orientational entropy (favouring the isotropic state) and the excluded volume entropy (favouring the nematic state). Onsager [21] defined the quantity σ_j as a measure for the (negative of the)

orientational entropy

$$\sigma_j \equiv \int f_j(\theta) \ln[4\pi f_j(\theta)] d\Omega, \qquad\qquad j = 1, 2, \tag{2.1}$$

which has its minimum ($\sigma_j = 0$) in the isotropic state, whereas $\sigma_j > 0$ in the nematic state. In the second virial approximation, the interactions between hard particles are expressed as an excluded volume entropy depending on the orientation-dependent excluded volume between two particles. The excluded volume between two platelets (i.e. circular disks) with thicknesses L_j and L_k as a function of their mutual angle γ is given by

$$v_{\text{excl}}^{jk}(\gamma) = \frac{\pi}{2} D^3 \sin\gamma + (L_j + L_k)D^2 \left\{ \frac{\pi}{4} + E(\sin\gamma) + \frac{\pi}{4} |\cos\gamma| \right\} + \mathcal{O}(L^2 D), \tag{2.2}$$

where $E(k)$ is the complete elliptic integral of the second kind. Note that the leading order term does not depend on the thickness L so that the $\mathcal{O}(L/D)$-term must be included to account for different plate thicknesses. In the isotropic phase, the excluded volume can be readily calculated using the isotropic averages $\langle\langle \sin\gamma \rangle\rangle_{\text{iso}} = \pi/4$ and $\langle\langle E(\sin\gamma) \rangle\rangle_{\text{iso}} = \pi^2/8$ [21]

$$v_{\text{excl,iso}}^{jk} = \frac{\pi^2}{8} D^3 + (L_j + L_k)D^2 \left\{ \frac{\pi^2}{8} + \frac{3\pi}{8} \right\} + \mathcal{O}(L^2 D). \tag{2.3}$$

A measure for the average excluded volume interaction between platelets of type j and k is given by the average of its angular dependence [21]

$$\rho_{jk} \equiv \iint \frac{v_{\text{excl}}^{jk}(\gamma)}{v_{\text{excl,iso}}^0} f_j(\theta) f_k(\theta') d\Omega d\Omega', \tag{2.4}$$

with $v_{\text{excl,iso}}^0 = D^3\pi^2/8$, the average excluded volume between two randomly orientated platelets with zero thickness. Substituting Eq. (2.3) into Eq. (2.4) yields for the isotropic phase*

$$\rho_{jk}^{\text{iso}} = 1 + \frac{L_j + L_k}{D} \left(1 + \frac{3}{\pi} \right) + \mathcal{O}(L^2/D^2). \tag{2.5}$$

where the second contribution is of the order L/D smaller than the leading order term. The total Helmholtz free energy (in units $k_B T$ per particle) of a binary mixture within the second virial approximation can now be expressed in terms of σ_j and ρ_{jk}

$$\frac{\beta F}{N} \sim \text{cst} - 1 + \ln c + (1 - x)\ln(1 - x) + x\ln x + (1 - x)\sigma_1 + x\sigma_2$$
$$+ c\left[(1 - x)^2 \rho_{11} + 2x(1 - x)\rho_{12} + x^2 \rho_{22} \right], \tag{2.6}$$

---

*The definition of ρ_{jk} is slightly different from the one originally used by Onsager [21], since we only retain the leading order term $v_{\text{excl,iso}}^0$ in the denominator instead of the full expression Eq. (2.3). This leads to $\rho_{jk}^{\text{iso}} = 1 + \mathcal{O}(L/D)$ whereas in [21] $\rho^{\text{iso}} \equiv 1$, by definition. Both definitions are equivalent up to leading order.

equivalent to Eq. (1.25) for $j = 1, 2$. Here, c is the total number density of platelets rendered dimensionless by relating it to $v^0_{\text{excl,iso}}$ in the following way

$$c = \frac{1}{2} v^0_{\text{excl,iso}} \frac{N}{V} = \frac{\pi^2}{16} D^3 \frac{N}{V}. \tag{2.7}$$

The last term in Eq. (2.6) can be identified as the (dimensionless) *second virial coefficient* $\tilde{B}_2$ multiplied by the concentration c. Note that $c\tilde{B}_2$ constitutes the excess part of the free energy which accounts for the interactions between the hard particles. Using Eq. (2.5), together with the isotropic value, $\sigma_j \equiv 0$, we obtain the following expression for the free energy in the isotropic phase

$$\frac{\beta F_{\text{iso}}}{N} \sim \text{cst} + (\ln c - 1) + (1 - x) \ln(1 - x) + x \ln x$$
$$+ c \left\{ 1 + \left(2 + \frac{6}{\pi} \right) \left[(1 - x) \frac{L_1}{D} + x \frac{L_2}{D} \right] \right\}. \tag{2.8}$$

In the nematic phase, matters are more complicated since the ODF is no longer a constant but a sharply peaked function. The excluded volume entropy is now given by

$$\rho_{jk}^{\text{nem}} = \frac{4}{\pi} \iint |\sin \gamma| \, f_j(\theta) f_k(\theta') d\Omega d\Omega'$$
$$+ \frac{2}{\pi} \frac{L_j + L_k}{D} \iint \left[3 - \frac{1}{2} \sin^2 \gamma + |\cos \gamma| \right] f_j(\theta) f_k(\theta') d\Omega d\Omega' + \mathcal{O}[(L/D)^2]. \tag{2.9}$$

Here, the following asymptotic expansion of the elliptic integral has been used [71]

$$E(\sin \gamma) = \frac{\pi}{2} \left\{ 1 - \frac{1}{4} \sin^2 \gamma + \mathcal{O}(\sin^4 \gamma) \right\}, \tag{2.10}$$

valid for small angles γ. Note that this approximation is only justified for strongly aligned states where the ODF is a sharply peaked function. In the following we will use Gaussian trial ODFs with variational parameter α_j to describe the angular distribution of the platelets j in the nematic state [34]

$$f_j(\theta) \equiv \begin{cases} \frac{\alpha_j}{4\pi} \exp[-\frac{1}{2}\alpha_j \theta^2] & \text{if } 0 \leq \theta \leq \frac{\pi}{2} \\[2mm] \frac{\alpha_j}{4\pi} \exp[-\frac{1}{2}\alpha_j(\pi - \theta)^2] & \text{if } \frac{\pi}{2} \leq \theta \leq \pi \end{cases} \tag{2.11}$$

An advantage of using these trial ODFs is that σ_j and ρ_{jk} become analytically tractable. Substituting Eq. (2.11) in Eq. (2.1) gives

$$\sigma_j \sim \ln \alpha_j - 1, \qquad j = 1, 2, \tag{2.12}$$

for the orientational entropy. For the excluded volume entropy in the nematic phase we will only retain the leading order terms of its asymptotic expansion for large α_j

$$\rho_{jk}^{\text{nem}} \sim \sqrt{\frac{8}{\pi} \left(\frac{1}{\alpha_j} + \frac{1}{\alpha_k} \right)} + \frac{8}{\pi} \frac{L_j + L_k}{D} \left[1 + \mathcal{O}(\alpha_j^{-1}, \alpha_k^{-1}) \right]. \tag{2.13}$$

Henceforth, we neglect the $\mathcal{O}(\alpha^{-1})$ contribution in the second term, which is justified for very large values of α. This is a crucial step in our analysis, since the $\mathcal{O}(L/D)$-term now becomes independent of α_j and the shape of $f_j(\theta)$. The orientation of the platelets

in the nematic phase is therefore solely determined by the *diameter* of the platelets, which is identical for both components. As the plate thickness does not enter into the free energy anywhere else than via the $\mathcal{O}(L/D)$-term in Eq. (2.13) we can simplify our calculations considerably by using a single variational parameter, $\alpha = \alpha_j = \alpha_k$, which holds for both components. The above expression then reduces to

$$\rho_{jk}^{\text{nem}} \sim \frac{4}{\sqrt{\pi\alpha}} + \frac{8}{\pi}\frac{L_j + L_k}{D}. \tag{2.14}$$

The thickness contribution to ρ^{nem} is now simply the ratio of the excluded volume between two *parallel* platelets in the nematic phase, $\pi D^2(L_j + L_k)$, and the excluded volume $v_{\text{excl,iso}}^0$ between two randomly oriented platelets with zero thickness in the isotropic phase. Note that this contribution remains constant up to order $\mathcal{O}(\gamma^2)$ as can easily be inferred from Eq. (2.9) by expanding the trigonometric functions in the integrand. Inserting Eq. (2.12) and Eq. (2.14) into the Helmholtz free energy Eq. (2.6) and minimizing with respect to α leads to a simple c^2-dependence of the Gaussian variational parameter [5]

$$\alpha = \frac{4c^2}{\pi}, \tag{2.15}$$

independent of the mole fraction x. Substituting all expressions back into the free energy Eq. (2.6) yields a simple expression for the free energy in the nematic phase

$$\frac{\beta F_{\text{nem}}}{N} \sim \text{cst} + 3\ln c + \ln\frac{4}{\pi} + x\ln x + (1-x)\ln(1-x) + \frac{16}{\pi}c\left[(1-x)\frac{L_1}{D} + x\frac{L_2}{D}\right]. \tag{2.16}$$

To locate phase transitions, we must know the osmotic pressure and chemical potential of both species. These are calculated as standard derivatives of the free energy. In the nematic phase we obtain for the osmotic pressure (in dimensionless notation)

$$\tilde{\Pi}_{\text{nem}} \equiv -\frac{1}{2}\beta v_{\text{excl,iso}}^0 \left(\frac{\partial F_{\text{nem}}}{\partial V}\right)_{N_1,N_2,T} \sim 3c_n + \frac{16}{\pi}c_n^2\left[(1-x_n)\frac{L_1}{D} + x_n\frac{L_2}{D}\right], \tag{2.17}$$

where the subscripts n refer to the concentration and composition of the nematic phase. The (dimensionless) chemical potentials follow from

$$\tilde{\mu}_{j,\text{nem}} \equiv \beta\left(\frac{\partial F_{\text{nem}}}{\partial N_j}\right)_{N_j,V,T}, \qquad j = 1, 2. \tag{2.18}$$

Expressions for the isotropic phase can be obtained likewise from Eq. (2.8).

We can summarize our results so far by focusing on the excess free energy in the nematic phase. Judging from Eq. (2.6) we see that the last term $(c\tilde{B}_2)$ is essentially given by a double mole fraction average of the following quantity

$$c\rho_{jk}^{\text{nem}} \sim 2 + \frac{8}{\pi}c\frac{L_j + L_k}{D}, \tag{2.19}$$

which is easily obtained by combining Eq. (2.14) and Eq. (2.15). From this we conclude that the leading order excess free energy, i.e. for platelets with zero thickness, is simply a constant. The $\mathcal{O}(L/D)$-term gives rise to an additional contribution which is linear in c. As to the osmotic pressure Eq. (2.17), we see that this leads to a quadratic correction

term, implying that the pressure of a (dense) nematic state is influenced considerably by the plate thickness.

We are, in principle, ready to construct the phase diagram by equating the osmotic pressure and the chemical potentials of the isotropic and nematic phases. In the next section we show how we can make a quantitative upgrade of the original Onsager theory in order to make plausible comparisons with the experimental results possible. By means of Parsons' approach we indirectly account for the effect of many-body interactions which play an important role in systems of platelike particles.

2.2.1. Parsons free energy

Implementing Parsons' approach to (binary) mixtures can in principle be carried out in a number of ways. In this thesis we shall use the simplest approach, introduced by Camp and Allen [48], which consists of replacing the orientation-dependent prefactor in Eq. (1.42) by $\langle\langle \bar{v}_{\mathrm{excl}} \rangle\rangle /8\bar{v}_0$ in terms of the following linear combinations:

$$
\begin{aligned}
\langle\langle \bar{v}_{\mathrm{excl}} \rangle\rangle =& v_{\mathrm{excl,iso}}^0 \left[(1-x)^2 \rho_{11} + 2x(1-x)\rho_{12} + x^2 \rho_{22} \right] \\
=& v_{\mathrm{excl,iso}}^0 \tilde{B}_2, \\
\bar{v}_0 =& (1-x)v_{0,1} + x v_{0,2}, \\
\phi =& (1-x)\phi_1 + x\phi_2,
\end{aligned}
\tag{2.20}
$$

with ϕ the total volume fraction of particles, related to the dimensionless concentration and composition via

$$
\phi(c,x) = \frac{4}{\pi}c \left[(1-x)\frac{L_1}{D} + x\frac{L_2}{D} \right].
\tag{2.21}
$$

Recalculation of the osmotic pressure and chemical potentials for the isotropic phase is now straightforward, using the definitions Eq. (2.17) and Eq. (2.18). The resulting expressions however involve additional derivatives of $\tilde{f}_{\mathrm{CS}}$ (Eq. (1.40)) with respect to c and x, due to their relation with ϕ via Eq. (2.21). For the nematic state, minimization of the free energy with respect to α now yields

$$
\alpha \sim \frac{4}{\pi}c^2 \tilde{f}_{\mathrm{CS}}^2(\phi).
\tag{2.22}
$$

The Onsager-Parsons free energy (denoted by superscript P) for the nematic phase thus reads

$$
\begin{aligned}
\frac{\beta F_{\mathrm{nem}}^P}{N} \sim& \mathrm{cst} + 3\ln c + \ln\frac{4}{\pi} + x\ln x + (1-x)\ln(1-x) + 2\ln\tilde{f}_{\mathrm{CS}}(\phi) \\
& + \frac{16}{\pi}c\tilde{f}_{\mathrm{CS}}(\phi) \left[(1-x)\frac{L_1}{D} + x\frac{L_2}{D} \right].
\end{aligned}
\tag{2.23}
$$

where the additional $\ln\tilde{f}$ contribution arises from the orientational entropy Eq. (2.12). To compare with Eq. (2.17) we explicitly give the Onsager-Parsons osmotic pressure of the nematic phase

$$
\tilde{\Pi}_{\mathrm{nem}}^P \sim c_n + \left[2c_n + \frac{16}{\pi}c_n^2 \tilde{f}_{\mathrm{CS}} \left\{ (1-x_n)\frac{L_1}{D} + x_n\frac{L_2}{D} \right\} \right] \left[1 + c_n\frac{\partial \ln\tilde{f}_{\mathrm{CS}}}{\partial c} \right].
\tag{2.24}
$$

D (nm)	$L_1(nm)$	$L_2(nm)$	D/L_1	D/L_2
180	20	45	**9**	**4**

Table 2.1. Typical dimensions and aspect ratios of the thick and thin platelets used in the present calculations [72].
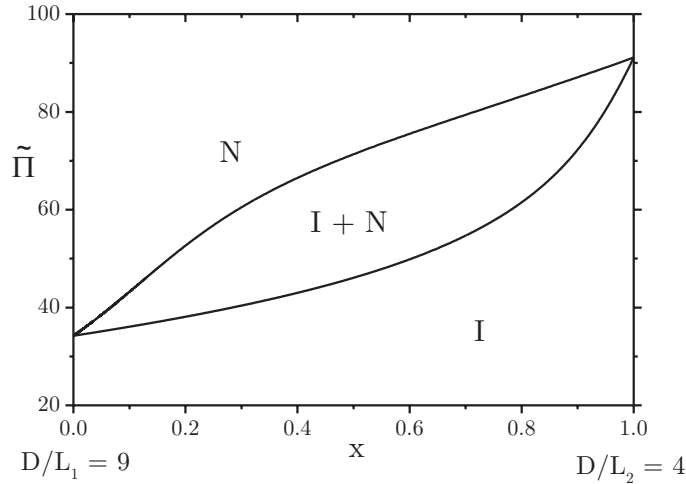
Figure 2.2. Phase diagram in the $\tilde{\Pi} - x$ plane of a binary mixture of thin platelets ($D/L_1 = 9$) and thick platelets ($D/L_2 = 4$), calculated from the Onsager-Parsons free energy. Note the significant degree of fractionation between the phases.

Note that the linear contribution $3c_n$ is retained but the presence of $\tilde{f}$ and its derivatives leads to a more complicated c -dependence. Similar expressions for the chemical potentials can be obtained by straightforward derivation.

2.3. Isotropic-nematic phase coexistence: density inversion

We can now construct phase diagrams by imposing the standard conditions of equal pressure and chemical potentials in the two coexisting phases. However, we are still left with two important, yet unspecified parameters, namely the typical aspect ratio of the thin and thick platelets, D/L_1 and D/L_2 respectively. Since it is our primary aim to account for the experimentally observed features, we restrict ourselves to a single combination of aspect ratios, rather than scanning the entire parameter space. We have chosen a particular combination of dimensions for the platelets under consideration, shown in Table 2.1. These values should resemble the experimental system, studied by van der Kooij *et al.* [60], in a reasonable way. The corresponding phase diagram is depicted in Fig. 2.2. The diagram clearly reveals a considerable degree of fractionation between the coexisting phases. The thick platelets are expelled from the nematic phase and prefer the isotropic phase. Moreover, the strong increase of the equilibrium osmotic
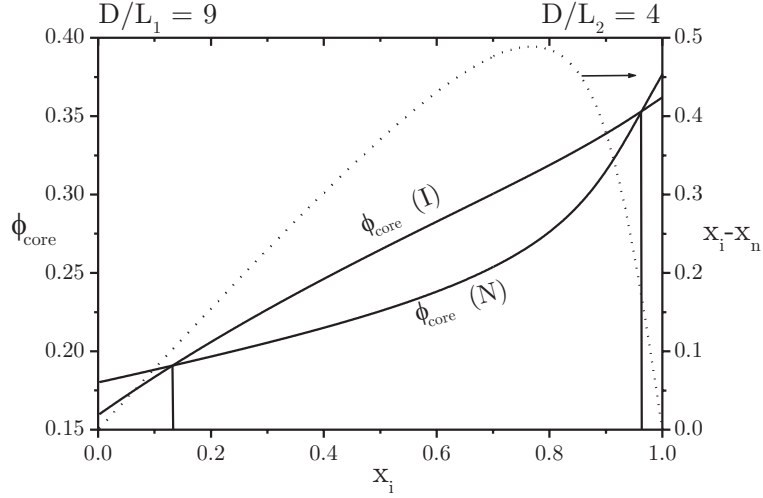
FIGURE 2.3. Core volume fraction ϕ_{core} of the coexisting phases versus x_i. In the area between the vertical lines the phase densities are inverted. On the right vertical axis, the extent of fractionation $(x_i - x_n)$ is plotted versus x_i.

pressure as a function of mole fraction indicates an upward shift of the $I - N$ transition densities in a *pure* system at increasing plate thickness.

When we want to study the possibility of an $I - N$ density inversion, we should calculate the total mass density of the isotropic and the nematic phases. The mass density is linearly proportional to the effective core volume fraction of the platelets

$$\phi_{\text{core}} = \frac{4}{\pi} c \left[(1-x) \frac{L_1}{D} \frac{v_1^{\text{core}}}{v_1} + x \frac{L_2}{D} \frac{v_2^{\text{core}}}{v_2} \right], \tag{2.25}$$

which is related to the fact that, experimentally, the colloidal platelets consist of a (dense) gibbsite (Al(OH)_3) core surrounded by a grafted polymer layer. The density of the polymer layer is approximately the same as that of solvent in which the platelets are immersed, so that the layer does not contribute to the total plate density. However, the polymer layer does contribute to the mutual excluded volume between two platelets. The dimensions given in Table 2.1 therefore apply to the *grafted* gibbsite platelets. The thickness of the polymer layer has been estimated at 4 nm [60] and the ratio of the core volume v_{core} to the total volume v of the platelet can be calculated using the values from Table 2.1, giving $v_1^{\text{core}}/v_1 \approx 0.55$ and $v_2^{\text{core}}/v_2 \approx 0.75$.

Fig. 2.3 reveals that a density inversion indeed takes place during the $I - N$ phase separation. Remarkably, the area in which the isotropic and nematic phase densities are inverted appears to cover a major part of the phase diagram. Only when the overall mole fraction is close to zero or one, i.e. in case of an almost pure system of either thin or thick platelets, fractionation is apparently not strong enough to accomplish a density inversion. In these situations, an isotropic upper phase will be found as in the regular cases. Equal phase densities are found at coexisting mole fractions $(x_i, x_n) = (0.13, 0.03)$ and $(0.96, 0.79)$, corresponding to $\tilde{\Pi} = 36.7$ and 82.7, respectively.

We can also represent the phase diagram by plotting the core volume fraction versus the concentration, as shown in Fig. 2.4. Recall that the core volume fraction is directly
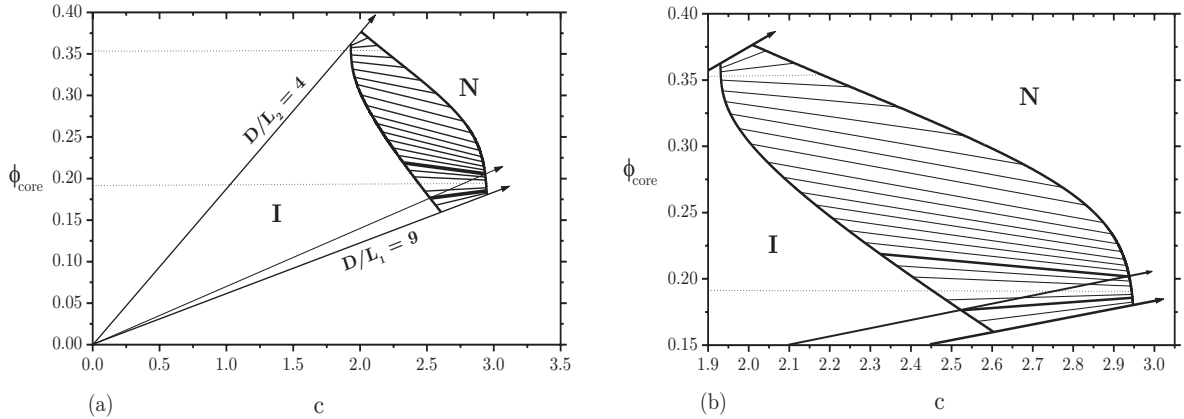
FIGURE 2.4. (a) Phase diagram in the phase density - concentration ($\phi_{core} - c$) plane. The outer dilution lines correspond to the pure systems. Thick lines indicate phase boundaries; thin lines represent tie lines connecting coexisting phases. The horizontal tie lines (dotted lines) denote equal phase densities. In the area between the dotted lines the tie lines have negative slopes, indicating inverted states. (b) Magnification of the biphasic area.

proportional to the mass density of the phases. In this phase diagram, we can draw dilution lines, i.e. straight lines radiating from the origin, along which the overall composition x of the parent system remains constant. This representation clearly shows that the total plate number density in the nematic phase is always higher than that in the isotropic phase, irrespective of mole fraction (i.e. the slope of the dilution line). The density inversion therefore cannot be caused by an inversion of coexistence densities and hence must be driven solely by fractionation effects.

The slope of the tie lines are directly related to the density of the coexisting isotropic and nematic phases, i.e. a positive slope indicates a regular state (isotropic top and nematic bottom phase) whereas a negative one corresponds to an inverted state. The evolution of the tie lines give the impression of a "spiral staircase" with slope signs changing gradually from positive, to negative and back to positive upon increasing mole fractions. Finally, we remark from Fig. 2.4 that there is a distinct widening of the biphasic gap. The widening of the $I - N$ coexistence region is a generally established feature for bidisperse (and polydisperse) mixtures of anisometric particles, both in experiment [73–75] and theory [5, 34, 65] as will become clear in the rest of this thesis.

2.4. Nematic-nematic phase coexistence

As mentioned earlier in this Chapter, the thickness of the platelets has a considerable influence on the osmotic pressure of a nematic phase at high concentrations (see Eq. (2.17). One may ask whether this can cause the nematic phase of a binary mixture of thin and thick platelets to demix into two nematic phases at sufficiently high concentrations.
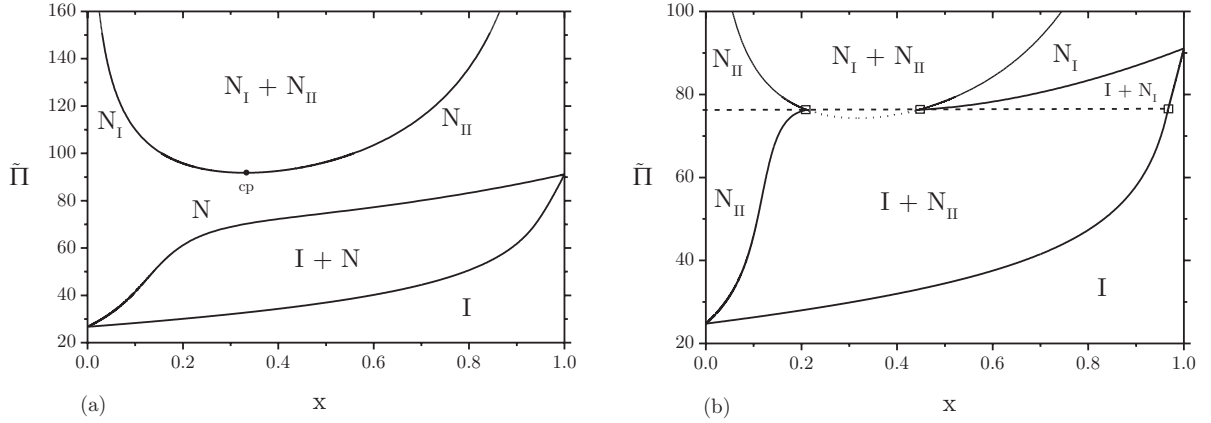
FIGURE 2.5. (a) Phase diagram in the $\tilde{\Pi} - x$ plane of a binary mixture of thin platelets, $D/L_1 = 13$, and thick platelets, $D/L_2 = 4$, $(L_2/L_1 = 3.25)$. The nematic-nematic coexisting region is bounded by a lower critical point (cp). (b) As (a), for $D/L_1 = 15$ and $D/L_2 = 4$, $(L_2/L_1 = 3.75)$. Full curves denote stable phase boundaries, while the dotted curve represents a metastable one. The $I - N_I - N_{II}$ triple point is indicated by $\square$.

In this section we study the relation between the thickness bidispersity, quantified by the thickness ratio L_2/L_1, and the topology of the phase diagram, in particular the existence of a nematic-nematic coexistence region. The occurrence of a demixing transition at a particular osmotic pressure can easily be identified by the presence of an instability region (or van der Waals-loop) in the chemical potential curve (plotted versus the mole fraction), for which $\partial\mu_j/\partial x_j < 0$.

In case of a nematic-nematic coexistence, there must be two states, denoted by N_I and N_{II}, with different c_n and/or x_n, having the same osmotic pressure and chemical potentials. We have investigated this possibility for mixtures with a fixed aspect ratio $D/L_2 = 4$ for the thick species. This means that we increase the degree of bidispersity by making the thin platelets thinner while keeping the thickness of the thick platelets fixed. In Fig. 2.5, the resulting phase diagrams are depicted for two different values of D/L_1.

A remarkable result is that the nematic-nematic transition is always present, irrespective of the thickness ratio $L_2/L_1(> 1)$. Even near monodisperse systems (with L_2/L_1 close to 1) exhibit a nematic-nematic demixing transition, albeit at very high osmotic pressures. In our experimentally considered system $(D/L_1 = 9, D/L_2 = 4)$ we locate a nematic-nematic critical point at a coexistence pressure $\tilde{\Pi} = 208$. Note that the nematic phases are probably metastable with respect to inhomogeneous liquid crystal phases (e.g. smectic, columnar etc.) at these pressures. Obviously, increasing the thickness ratio stabilized the demixing transition in terms of a decrease of the critical pressure. At $L_2/L_1 \approx 3.3$, the $N - N$ binodals overlap with the $I - N$ coexistence region which gives rise to a triple coexistence between two nematic phases (N_I and N_{II}) and an isotropic phase I (Fig. 2.5(b)).

Let us now elaborate on the nematic-nematic demixing transition by trying to gain more insight in the underlying mechanism. A convenient way to study the mechanism behind a demixing transition is to construct the Gibbs free energy and investigate the behaviour of its individual entropic contributions. For the sake of simplicity, we will use the Onsager free energy Eq. (2.16) here, rather than the elaborate expressions obtained via Parsons rescaling. The Gibbs free energy (in units $k_B T$ per particle) is given by

$$g(\tilde{\Pi}, x) \equiv \frac{\beta F}{N} + \tilde{\Pi} c^{-1}(\tilde{\Pi}, x). \tag{2.26}$$

The concentration $c(\tilde{\Pi}, x)$ is obtained by inverting the osmotic pressure in the nematic state Eq. (2.17), which is simply quadratic in c. The individual entropic contributions are given by

$$g_{\text{mix}} \sim (1 - x)\ln(1 - x) + x\ln x, \tag{2.27}$$

$$g_{\text{or}} \sim 2\ln c(\tilde{\Pi}, x) + \ln\frac{4}{\pi} + 1, \tag{2.28}$$

$$g_{\text{ex}} \sim 2 + \frac{32}{\pi}c(\tilde{\Pi}, x)\left[(1 - x)\frac{L_1}{D} + x\frac{L_2}{D}\right], \tag{2.29}$$

where the subscripts refer to the mixing, orientational and excluded-volume entropies, respectively. The subscripts for the nematic phase are left out for notational convenience. The ideal (translational) entropy is omitted here, since it has the same c-dependence as the orientational part.

It is advantageous to rescale the Gibbs free energy by subtracting the chemical potentials of the pure components, weighed by their mole fractions

$$g'(\tilde{\Pi}, x) \equiv g(\tilde{\Pi}, x) - \left[(1 - x)\mu_1^0(\tilde{\Pi}) + x\mu_2^0(\tilde{\Pi})\right]. \tag{2.30}$$

Obviously, the same rescaling procedure can be applied to the individual entropic contributions. The motivation behind the rescaling of g is to uncover the concave/convex curvature of the free energy by subtracting the dominant linear trend. Fig. 2.6 clearly shows that the demixing transition originates from a competition between mixing entropy and orientational entropy on the one hand (all favouring the mixed state) and excluded volume entropy on the other hand (favouring demixing). At sufficiently high osmotic pressures, the latter contribution becomes dominant and demixing occurs.

2.5. Discussion

Our calculations based on the Gaussian approximation provide us with a fairly simple interpretation of the isotropic-nematic density inversion, as observed in experimental systems of polydisperse gibbsite platelets. It appears that this phenomenon indeed originates from a pronounced fractionation with respect to thickness between the isotropic and the nematic phase, as already suggested by van der Kooij et al. [60]. An isotropic-nematic density inversion can only be accomplished when the fractionation is strong enough to overrule the difference between the coexistence number densities of the isotropic and the nematic phase, for which $c_i < c_n$, irrespective of the overall composition.

FIGURE 2.6. Rescaled Gibbs free energy g'_{tot} of the nematic phase (in units $k_B T$ per particle) versus mol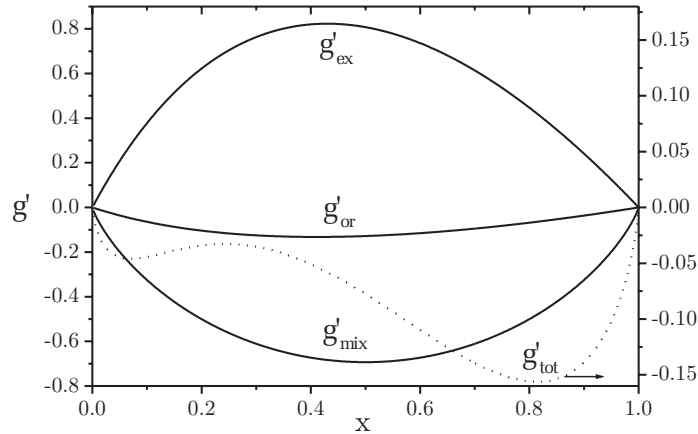e fraction x of a binary mixture of thin platelets, $D/L_1 = 13$, and thick platelets, $D/L_2 = 4$, $(L_2/L_1 = 3.25)$, at coexistence pressure $\tilde{\Pi} = 140$ (dotted curve). The solid curves depict the contributions from the individual entropies; excluded volume (g'_{ex}), orientation (g'_{or}) and mixing (g'_{mix}). The local minima in g'_{tot} indicate a demixing transition.

In this respect, we would like to stress the importance of the Parsons' approach. The possibility of a density inversion strongly depends on the difference between the isotropic and nematic coexistence densities, i.e. the width of the coexistence region. It is a known feature that the Onsager theory overestimates both the coexistence densities and the width of the coexistence region. The theory predicts a strong first order transition $(\Delta(ND^3/V) > 1)$ whereas Monte Carlo simulations only show a weak density jump [18]. It turns out that Parsons' approach constitutes a significant quantitative improvement over the original Onsager theory since it both lowers the coexistence densities and narrows the density gap. It is therefore not surprising that our preliminary calculations solely based on the Onsager theory, could not establish a density inversion at any point in the phase diagram; the density jump was simply too large to be overruled by fractionation and hence an $I - N$ density inversion was not possible.

As pointed out earlier in this Chapter, we intend to compare our results with the experimental observations obtained by van der Kooij [60]. For this purpose, we have drawn a particular dilution line in Fig. 2.4 which resembles the experimental observations in a reasonable way. The "experimental" dilution line corresponds to a mole fraction $x = 0.07$. If a dilute system is concentrated along this dilution line, phase separation starts to occur at an overall volume fraction $\phi = 0.305$. The slope of the initial tie line is positive, indicating that an isotropic upper phase is formed initially. At $\phi = 0.32$ the dilution line and the equal density tie line intersect, indicating that both phases are equally dense at that point. At higher volume fractions, the slope of the tie lines becomes negative, indicating that the densities of the phases are inverted and a nematic upper phase will be formed. At $\phi = 0.351$ the system is fully nematic. The experimental phase boundaries are found to be somewhat lower ($\phi = 0.18$ and

$\phi = 0.30$) [60]. Equal phase densities are found at a volume fraction of approximately 0.24 (Fig. 2.1(b)).

We finally discuss a peculiar observation in relation with the aforementioned dilution experiments. Van der Kooij performed an additional fractionation experiment in which a suspension was brought to a volume fraction $\phi = 0.29$ close to the nematic phase boundary ($\phi = 0.30$) and left to phase separate. The nematic upper phase was separated from the isotropic bottom phase and subsequently diluted. A remarkable observation was that this system did not exhibit a density inversion at any point in the isotropic-nematic coexistence region. This striking observation however cannot be explained by the present model. Fig. 2.4 shows that any dilution line close to the experimental dilution line must cross the horizontal tie line denoting equal phase densities. This means that, according to our phase diagram, splitting off the nematic phase from a system close to the nematic phase boundary should always give rise to a density inversion after dilution. We believe that this particular experimental observation is a clear manifestation of the *polydisperse* nature of a colloidal system of gibbsite platelets. This means that the system essentially comprises infinitely many platelike species with a continuous variation in thickness (and diameter), rather than a finite number of distinct species. Although the present binary model captures most of the experimental features it remains a serious simplification of a real colloidal system. In Chapter 7 we extend the binary model to a polydisperse one and show that this allows us to qualitatively account for the observations of the dilution experiment.

Acknowledgement

3

Asymmetric rod-plate mixtures (I) : Isotropic - uniaxial nematic phase separation

ABSTRACT

Recent experiments on mixtures of rodlike and platelike colloidal particles have uncovered the phase behaviour of strongly asymmetric rod-plate mixtures. In these mixtures, in which the excluded volume of the platelets is much larger than that of the rods, an extended isotropic (I) - plate-rich nematic (N^-) - rod-rich nematic (N^+) triphasic equilibrium was found. In this Chapter, we present a theoretical underpinning for the observed phase behaviour starting from the Onsager-Parsons theory in the Gaussian approximation. We find good qualitative agreement between our results and the low concentration part of the experimental phase diagram.

3.1. INTRODUCTION

The phase behaviour of mixtures of rodlike and platelike particles is intrinsically richer than that of rods and platelets separately. Depending on the concentration and composition, a number of distinctly different nematic liquid crystal phases may be encountered. First, there are two nematic phases of *uniaxial* symmetry, characterized by a single nematic director. For later reference, we distinguish between a rod- and plate-dominated uniaxial nematic phase and denote them by N^+ and N^-, respectively. In addition to these, there is the so-called *biaxial* nematic phase (B) in which both rods and plates are orientationally ordered along mutually perpendicular directions. The stability of the biaxial nematic phase with respect to the uniaxial nematic ones has been subject to debate in a number of theoretical studies [48, 76–80]. However, until recently, no experimental studies on mixtures on well-defined hard rod- and platelike particles had been reported.

The experimental work by van der Kooij *et al.* [73, 74] on mixtures of hard boehmite rods ($L/D \cong 10$) and gibbsite platelets ($D/L \cong 15$) shed some light on the phase behaviour of *asymmetric* rod-plate mixtures. These mixtures are characterized by a large excluded volume difference between the rods and the plates, the excluded volume of the platelets being much larger than that of the rods. Rather than forming a single (biaxial) nematic phase at increasing particle concentrations these systems show a strong tendency to phase separate into two fractionated nematic phases, one containing predominantly rods and the other strongly enriched in platelets. The experimental results
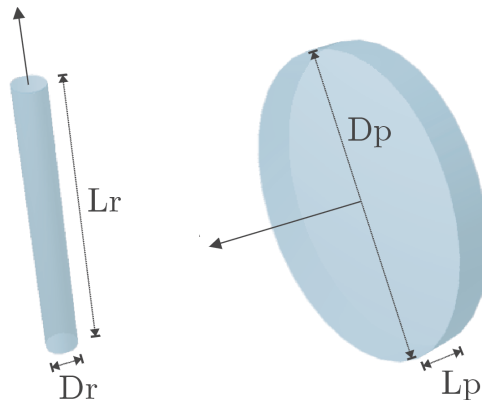
Figure 3.1. Generic shape and orientation axes of the rod- and platelike particles.

therefore seem to point towards an instability of the biaxial nematic phase with respect to demixing into the uniaxial nematic phases in case of strongly asymmetric mixtures.

In this Chapter, we shall attempt to reproduce the isotropic- nematic phase behaviour of asymmetric rod-plate mixtures as studied experimentally in [74], starting from the Onsager-Parsons theory. To retain an analytically tractable theory we will use Gaussian trial ODFs to describe the particle alignment in the different nematic phases. We consider mixtures of cylindrical rods and platelets with equal aspect ratios and equal long dimensions, i.e. rod length equal to plate diameter, such that the excluded volume of the plates is larger than that of the rods. In view of the aforementioned experimental results, we shall focus on the *uniaxial* nematic phases, without taking into account possible biaxiality. The stability of the biaxial phase in these asymmetric mixtures will be considered in Chapter 4.

3.2. Onsager formulation

We consider a binary mixture of hard rods and hard platelets in a macroscopic volume V. The particles involved are characterized by four parameters: the length L_r and the diameter D_r of the rods (with $L_r > D_r$) and the diameter D_p and length (thickness) L_p of the platelets (with $D_p > L_p$). The generic shape of the particles is depicted in Fig. 3.1. The details of the exact shape of the particles are found to be irrelevant for the general argument, provided that the particles are sufficiently anisometric, i.e. $L_r/D_r \gg 1$ and $D_p/L_p \gg 1$. When considering the symmetry of the uniaxial nematic phases, we should realize that one species is aligned in a *polar* fashion, i.e. along a nematic director (say the z-axis), while the other particles tend to orient their axis randomly in the xy-plane perpendicular to the director (*planar* alignment). Throughout this Chapter, we will use subscript 1 to refer to the former species and subscript 2 to the latter. The composition variable, defined as $x = N_2/(N_1 + N_2)$, thus represents the

mole fraction of the species with planar orientations, which will be the platelets in case of the uniaxial N^+ phase and the rods for the N^- phase:

Using the considerations above we propose the following expressions for the (normalized) Gaussian trial ODFs which describe the particle orientations in the uniaxial nematic phases. For particles with polar alignment we write

$$f_1(\theta) \equiv \begin{cases} \frac{\alpha_1}{4\pi} \exp\left[-\frac{1}{2}\alpha_1\theta^2\right] & 0 \le \theta \le \frac{\pi}{2} \\ \\ \frac{\alpha_1}{4\pi} \exp\left[-\frac{1}{2}\alpha_1(\pi-\theta)^2\right] & \frac{\pi}{2} \le \theta \le \pi \end{cases}, \qquad (3.1)$$

In case of planar alignment the Gaussian ODF reads

$$f_2(\theta) \equiv \sqrt{\frac{\alpha_2}{(2\pi)^3}} \exp\left[-\frac{1}{2}\alpha_2\left(\frac{\pi}{2}-\theta\right)^2\right] \qquad 0 \le \theta \le \pi. \qquad (3.2)$$

Note that $f_1(\theta)$ is peaked around the nematic director ($\theta = 0$ or $\theta = \pi$) whereas $f_2(\theta)$ attains its maximum value in the plane perpendicular to the nematic director ($\theta = \pi/2$).

Using these forms in Onsager's definition for the orientational entropy

$$\sigma_j \equiv \int f_j(\theta)\ln[4\pi f_j(\theta)]d\Omega, \qquad j = 1,2, \qquad (3.3)$$

and straightforward integration allows us to obtain the following asymptotic expressions for the orientational entropy in the nematic phases

$$\sigma_1 \sim \ln\alpha_1 - 1,$$
$$\sigma_2 \sim \frac{1}{2}\left(\ln\alpha_2 + \ln\frac{2}{\pi} - 1\right). \qquad (3.4)$$

Recall that, by definition, $\sigma_j \equiv 0$ in the isotropic state. To describe interactions between hard anisometric particles in the second virial approach we need the excluded volumes between two platelets (i.e. circular disks), a platelet and a (cylindrical) rod and two rods as a function of the angle γ between the particles' axes. These are

$$v_{\text{excl}}^{\text{pp}}(\gamma) = \frac{\pi}{2}D_p^3\,|\sin\gamma| + \mathcal{O}(D_p^2 L_p),$$
$$v_{\text{excl}}^{\text{rp}}(\gamma) = \frac{\pi}{4}L_r D_p^2\,|\cos\gamma| + \mathcal{O}(L_r D_p D_r),$$
$$v_{\text{excl}}^{\text{rr}}(\gamma) = 2L_r^2 D_r\,|\sin\gamma| + \mathcal{O}(L_r D_r^2). \qquad (3.5)$$

Note that we restrict ourselves to the leading order contributions, which is justified if the particles are sufficiently anisometric. Using the isotropic averages $\langle\langle\sin\gamma\rangle\rangle_{\text{iso}} = \pi/4$ and $\langle\langle\cos\gamma\rangle\rangle_{\text{iso}} = 1/2$ we obtain the average excluded volume between two randomly orientated particles in the isotropic phase

$$v_{\text{excl,iso}}^{\text{pp}} = \frac{\pi^2}{8}D_p^3,$$
$$v_{\text{excl,iso}}^{\text{rp}} = \frac{\pi}{8}L_r D_p^2,$$
$$v_{\text{excl,iso}}^{\text{rr}} = \frac{\pi}{2}L_r^2 D_r. \qquad (3.6)$$

The average excluded-volume interaction between two particles is quantified by the average of its angular dependence

$$\rho_{jk} \equiv \iint \frac{v_{\text{excl}}^{jk}(\gamma)}{v_{\text{excl,iso}}^{jk}} f_j(\theta) f_k(\theta') d\Omega d\Omega', \tag{3.7}$$

which implies $\rho_{jk} \equiv 1$ for the isotropic phase. Substituting Eq. (3.5) for the nematic phase we obtain the following excluded-volume integrals corresponding to two rods or plates oriented either along the director (polar alignment) or perpendicular to the director (planar alignment)

$$\rho_{jj} = \frac{4}{\pi} \iint |\sin \gamma(\Omega, \Omega')| f_j(\theta) f_j(\theta') d\Omega d\Omega', \qquad j = 1, 2. \tag{3.8}$$

Similarly, for a rod and a plate with mutually perpendicular orientations we have

$$\rho_{12} = 2 \int \int |\cos \gamma(\Omega, \Omega')| f_1(\theta) f_2(\theta') d\Omega d\Omega'. \tag{3.9}$$

Unlike the orientational entropy Eq. (3.3), these excluded-volume integrals cannot be calculated straightforwardly since the integrands depend on the interparticle angle $\gamma(\Omega, \Omega')$. We can make headway by performing an asymptotic expansion of the integrals for small angles θ and/or $\psi = \pi/2 - \theta'$. Clearly, these asymptotic expansions are only justified if both α_j are sufficiently large, i.e. the Gaussian ODFs must be sharply peaked around their maximum values. For ρ_{11} the leading order term of the asymptotic expansion reads

$$\rho_{11} \sim \frac{4}{\sqrt{\pi \alpha_1}} + \mathcal{O}(\alpha_1^{-3/2}), \tag{3.10}$$

which was already found by Odijk [34]. The excluded volume integral for a rod and a plate with mutual perpendicular orientations ρ_{12} requires a bit more effort (see Appendix A for a detailed analysis). The result is as follows

$$\rho_{12} \sim \sqrt{\frac{8}{\pi} \left(\frac{1}{\alpha_1} + \frac{1}{\alpha_2} \right)} + \mathcal{O}(\alpha_1^{-3/2}, \alpha_2^{-3/2}). \tag{3.11}$$

The leading order term of this expansion is the same as the one obtained for rods with two different lengths [34]. Finally, the averaged excluded volume between two particles with planar alignment is given by

$$\rho_{22} \sim \rho_{22,0} \left[1 + \mathcal{F}(\alpha_2) \right], \tag{3.12}$$

Here, the leading order term $\rho_{22,0}$ is simply the average excluded volume between two particles j randomly orientated in the xy plane ($\psi = \psi' = 0$) relative to $v_{\text{excl,iso}}^{22}$, i.e.

$$\rho_{22,0} = (4/\pi) \left[\int_0^\pi d\gamma \right]^{-1} \int_0^\pi d\gamma \sin \gamma$$
$$= \frac{8}{\pi^2}. \tag{3.13}$$

The α_2-depending correction term $\mathcal{F}$ is rather difficult to obtain. It reads

$$\mathcal{F}(\alpha_2) \sim \frac{1}{\alpha_2} \left(\frac{1}{2} \ln \alpha_2 + K \right) + \mathcal{O}(\alpha_2^{-2} \ln \alpha_2), \tag{3.14}$$

where $K = \ln 4 + \frac{1}{2}\gamma_E - \frac{3}{2}$ and $\gamma_E \approx 0.577$ Euler's constant. We will elaborate on its derivation in Appendix A. It is important to note that $\mathcal{F}$ scales as $\alpha_2^{-1} \ln \alpha_2$ whereas ρ_{11} and ρ_{12} both scale as $\alpha^{-1/2}$. Consequently, $\mathcal{F}$ decays much more rapidly than ρ_{11} and ρ_{12} and is therefore a small contribution for large α_2.

The total Helmholtz free energy F of the rod-plate mixture (in units $k_B T$ per particle) reads

$$\frac{\beta F}{N} \simeq \text{cst} + \ln c - 1 + (1 - x)\ln(1 - x) + x \ln x + (1 - x)\sigma_1 + x\sigma_2$$
$$+ c\left[(1 - x)^2\rho_{11} + 2x(1 - x)q_{12}\rho_{12} + x^2 q_{22}\rho_{22}\right], \tag{3.15}$$

where, c is the total dimensionless number density related to $v^{11}_{\text{excl,iso}}$ via

$$c = \frac{1}{2}v^{11}_{\text{excl,iso}}\frac{N_1 + N_2}{V} = \begin{cases} \frac{\pi}{4}L_r^2 D_r \frac{N}{V} & N^+\text{-phase} \\[2ex] \frac{\pi^2}{16}D_p^3 \frac{N}{V} & N^-\text{-phase} \end{cases} \tag{3.16}$$

Furthermore, q_{jk} denote the *isotropic* excluded-volume ratios

$$q_{12} = v^{12}_{\text{excl,iso}}/v^{11}_{\text{excl,iso}},$$
$$q_{22} = v^{22}_{\text{excl,iso}}/v^{11}_{\text{excl,iso}}. \tag{3.17}$$

Obviously, $q_{11} \equiv 1$. Using the expressions for σ_j and ρ_{jk} in Eq. (3.15) and minimizing with respect to α_1 and α_2 yields

$$\alpha_1^{1/2} = 2\pi^{-1/2}\left[(1 - x) + 2^{1/2}xq_{12}h(Q)\right]c, \tag{3.18}$$
$$\alpha_2^{1/2} = \left[2^{5/2}\pi^{-1/2}(1 - x)q_{12}g(Q) - \mathcal{H}(x, \alpha_2)\right]c, \tag{3.19}$$

with the definitions

$$Q \equiv \alpha_2/\alpha_1, \tag{3.20}$$

$$h(Q) \equiv Q^{1/2}g(Q) \equiv \left(\frac{Q}{Q + 1}\right)^{1/2}, \tag{3.21}$$

Furthermore, $\mathcal{H}$ is the contribution arising from $\mathcal{F}(\alpha_2)$

$$\mathcal{H}(x, \alpha_2) = \frac{8}{\pi^2}xq_{22}\alpha_2^{-1/2}\left[1 - 2K - \ln \alpha_2\right], \tag{3.22}$$

which again is small for large α_2. To simplify matters, we set $\mathcal{F}$ (and $\mathcal{H}$) equal to zero for the moment, so that $\rho_{22} = \rho_{22,0} = 8/\pi^2$. Henceforth, this will be referred to as the *zeroth order* problem, denoted by subscripts 0. Within this approximation, it is possible to combine both minimization equations in order to obtain an expression only involving the ratio of both αs. Taking the ratio of Eqs. (3.18) and (3.19) gives

$$Q_0^{1/2} = \frac{2^{3/2}(1 - x)q_{12}g(Q_0)}{(1 - x) + 2^{1/2}xq_{12}h(Q_0)}, \tag{3.23}$$

which is an implicit equation for $Q_0(x)$ only involving the mole fraction x. A similar equation was obtained by Odijk [34]. Fortunately, Eq. (3.23) can be solved analytically, unlike the one obtained for bidisperse rods. After rearranging terms, Eq. (3.23) can be

rewritten as a simple quadratic equation in Q_0, which is easily solvable. In practice, it is convenient to rewrite the excluded volume terms ρ_{jk} in terms of Q_0, x and c using the minimization equations Eqs. (3.18), (3.19) and then substitute $Q_0(x)$ as found from Eq. (3.23). The free energy of the uniaxial nematic phase is then written explicitly in terms of the composition and dimensionless concentration of the phase.

The osmotic pressure and chemical potentials of both species follow from the standard derivatives of the free energy. The osmotic pressure of the nematic phase reads in dimensionless notation

$$\tilde{\Pi}_{\text{nem}} \sim (3-x)c + \frac{8}{\pi^2}q_{22}x^2c^2, \tag{3.24}$$

The chemical potentials are given by

$$\tilde{\mu}_{1,\text{nem}} \sim \ln c + \ln(1-x) + \sigma_1 + 2c\left[(1-x)\rho_{11} + xq_{12}\rho_{12}\right],$$
$$\tilde{\mu}_{2,\text{nem}} \sim \ln c + \ln x + \sigma_2 + 2c\left[(1-x)q_{12}\rho_{12} + xq_{22}\rho_{22}\right]. \tag{3.25}$$

Similarly, we obtain for the isotropic phase using the isotropic values $\sigma_j \equiv 0$ and $\rho_{jk} \equiv 1$

$$\tilde{\Pi}_i \simeq c + c^2\tilde{B}_{2,i},$$
$$\tilde{\mu}_{1,i} \simeq \ln c + \ln(1-x) + 2c\left[(1-x) + xq_{12}\right],$$
$$\tilde{\mu}_{2,i} \simeq \ln c + \ln x + 2c\left[(1-x)q_{12} + xq_{22}\right], \tag{3.26}$$

with $\tilde{B}_{2,i} = \left[(1-x)^2 + 2x(1-x)q_{12} + x^2q_{22}\right]$ the dimensionless second virial coefficient for the isotropic state.

The results obtained thus far apply to the zeroth order problem. When we invoke Eqs. (3.14) and (3.22), the analysis becomes considerably more complicated since the implicit equation for the nematic phase becomes dependent on the concentration as well. Consequently, an analytic solution for Q is no longer possible. To make headway, we will account for $\mathcal{F}(\alpha_2)$ in a perturbative way. Since $\mathcal{F}$ is only a small contribution, the "new" quantities α_j, σ_j and ρ_{jk} are expected to marginally differ from the ones obtained from the case $\mathcal{F} = 0$. We may therefore consider $\mathcal{F}$ as a *perturbation* to the parameters obtained from the zeroth order problem. The perturbation analysis will be discussed in Appendix B.

3.2.1. Parsons rescaling

It has been mentioned in Chapter 1 that although Onsager's second virial approximation works well for sufficiently elongated rods, it does not give quantitative results for platelike particles. Therefore, in case of rod-plate mixtures, many-body interactions involving platelets will undoubtedly play a role in the regime where nematic phases appear. In order to make quantitative progress, we account for the effect of higher virial terms by means of Parsons' approach. The general implementation of the approach for binary mixtures of anisometric particles has been outlined in Sec. 2.2.1 of Chapter 2 so we will only give the results here and refer the reader to Chapters 1 and 2 for details.

Applying a rescaling of the free energy according to Eq. (1.42) and minimizing with respect to α_j now yields (for the *zeroth order problem*, $\mathcal{F} = 0$)

$$\alpha_1^{1/2} = 2\pi^{-1/2}\left[(1-x) + 2^{1/2}xq_{12}h(Q_0)\right]c\tilde{f}_{\mathrm{CS}}(\phi),$$

$$\alpha_2^{1/2} = 2^{5/2}\pi^{-1/2}q_{12}(1-x)g(Q_0)c\tilde{f}_{\mathrm{CS}}(\phi), \tag{3.27}$$

The implicit equation in $Q_0(= \alpha_2/\alpha_1)$ is left unchanged since the concentration dependent part $c\tilde{f}_{\mathrm{CS}}(\phi)$ cancels. The total volume fraction ϕ of rods and platelets is related to the dimensionless concentration c and the mole fraction x via

$$\phi(c,x) = 2c\left[(1-x)\frac{v_{0,1}}{v_{\mathrm{ex,iso}}^{11}} + x\frac{v_{0,2}}{v_{\mathrm{ex,iso}}^{11}}\right]. \tag{3.28}$$

Within the Onsager-Parsons approach the osmotic pressure of the nematic phase reads

$$\tilde{\Pi}_{\mathrm{nem}}^P \sim c_n + \left[(2-x_n)c_n + \frac{8}{\pi^2}c_n^2x_n^2q_{22}\tilde{f}_{\mathrm{CS}}\right]\left[1 + \frac{\partial \ln \tilde{f}_{\mathrm{CS}}}{\partial \ln c_n}\right], \tag{3.29}$$

and the chemical potentials

$$\tilde{\mu}_{1,\mathrm{nem}}^P = \tilde{\mu}_{1,n} + 2\ln \tilde{f}_{\mathrm{CS}} + \left[(2-x_n) + c_n\tilde{f}_{\mathrm{CS}}x_n^2q_{22}\frac{8}{\pi^2}\right]\frac{\partial \ln \tilde{f}_{\mathrm{CS}}}{\partial(1-x_n)},$$

$$\tilde{\mu}_{2,\mathrm{nem}}^P = \tilde{\mu}_{2,n} + \ln \tilde{f}_{\mathrm{CS}} + \left[(2-x_n) + c_n\tilde{f}_{\mathrm{CS}}x_n^2q_{22}\frac{8}{\pi^2}\right]\frac{\partial \ln \tilde{f}_{\mathrm{CS}}}{\partial x_n}. \tag{3.30}$$

Recall that these expressions only hold for the zeroth order problem (i.e. $\rho_{22} = \rho_{22,0}$). Using the full expression Eq. (3.12) gives rise to additional terms from the perturbation analysis (see Appendix B). These contributions are omitted here for the sake of simplicity, but can be obtained after tedious but straightforward derivations. For the isotropic phase the Onsager-Parsons expressions become

$$\tilde{\Pi}_{\mathrm{iso}}^P = c_i + c_i^2\tilde{f}_{\mathrm{CS}}\tilde{B}_{2,i}\left[1 + c_i\frac{\partial \ln \tilde{f}_{\mathrm{CS}}}{\partial c_i}\right], \tag{3.31}$$

$$\tilde{\mu}_{1,\mathrm{iso}}^P = \ln c_i + \ln(1-x_i) + c_i\tilde{f}_{\mathrm{CS}}\left[\tilde{B}_{2,i}\frac{\partial \ln \tilde{f}_{\mathrm{CS}}}{\partial(1-x_i)} + 2(1-x_i) + 2x_iq_{12}\right],$$

$$\tilde{\mu}_{2,\mathrm{iso}}^P = \ln c_i + \ln x_i + c_i\tilde{f}_{\mathrm{CS}}\left[\tilde{B}_{2,i}\frac{\partial \ln \tilde{f}_{\mathrm{CS}}}{\partial x_i} + 2(1-x_i)q_{12} + 2x_iq_{22}\right]. \tag{3.32}$$

3.3. Phase Diagrams

The coexistence binodals were calculated numerically by equating osmotic pressure and chemical potentials in the coexisting phases. The phase diagrams were constructed as follows. The $I - N^-$ and $I - N^+$ binodals were computed separately using $(q_{11}, q_{22}) = (q_{pp}, q_{rr})$ and $(q_{11}, q_{22}) = (q_{rr}, q_{pp})$. A triphasic equilibrium is located at the intersection point (triple pressure) of the two isotropic branches. At this pressure there is an isotropic phase in coexistence with two uniaxial nematic phases, each with a different mole fraction and number density. The location of the triple point (in terms of x and c) is subsequently used as a starting point for the calculation of the $N^+ - N^-$
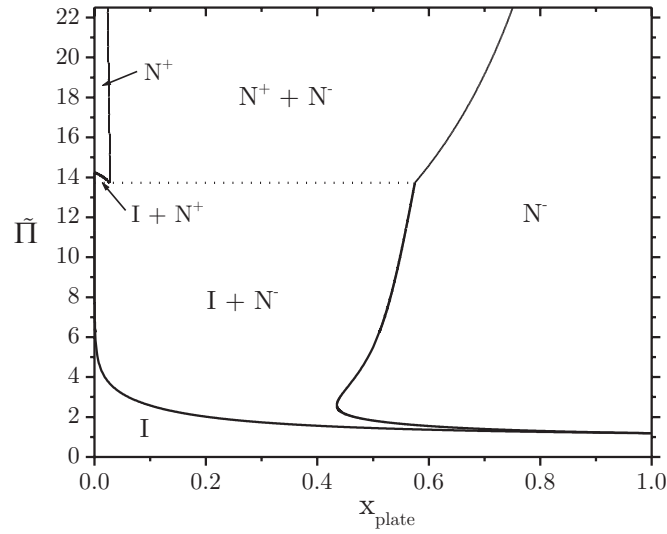
FIGURE 3.2. Phase diagram calculated from the perturbation analysis in the osmotic pressure - composition $(\tilde{\Pi} - x)$ plane for a mixture of rods and plates $(L_r/D_r = D_p/L_p = 15)$ with equal dimensions $(L_r = D_p$ and $D_r = L_p)$. Note the reentrant phenomenon near $x_{\text{plate}} = 0.44$.
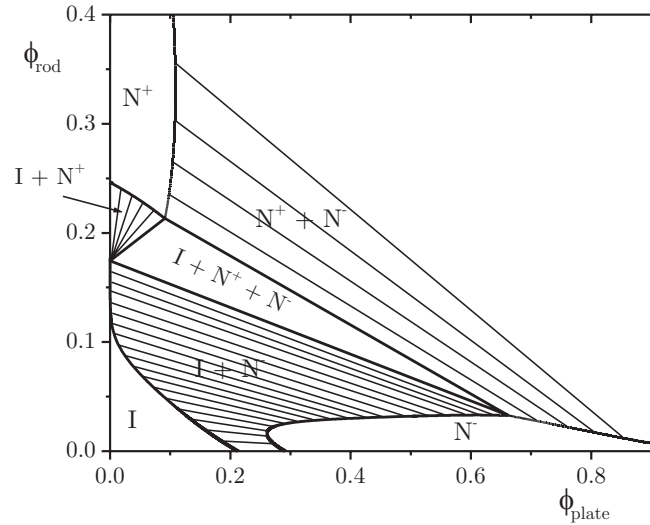
FIGURE 3.3. Phase diagram in the $\phi_{\text{rod}} - \phi_{\text{plate}}$ representation corresponding to Fig. 3.2. Thick lines indicate phase boundaries; thin lines represent tie lines connecting coexisting phases.

binodals.   To give a graphic representation of the results, a $\tilde{\Pi} - x$ diagram is shown in Fig. 3.2 and a diagram in terms of volume fractions, obtained via Eq. (3.28), in Fig. 3.3. The latter may be more convenient from an experimental standpoint. Tie lines connecting coexisting phases are given by horizontal lines in Fig. 3.2 (due to the equal osmotic pressures) and by tilted, straight lines in the volume fraction representation [81]. We can also draw dilution lines along which the overall mole fraction x of the

parent system remains constant. In Fig. 3.3 these are given by straight lines radiating from the origin whereas in a $\tilde{\Pi} - x$ representation the dilution lines run vertically.

To facilitate comparison with experimental results we have matched the dimensions of the particles under consideration to the average size of the boehmite and gibbsite particles used in experiment [74]. Accordingly, we have chosen equal aspect ratios for the rods and platelets, i.e. $L_r/D_r = D_p/L_p = 15$ and equal long and short dimensions of the particles, so that $L_r = D_p$ and $D_r = L_p$. The ratios of the excluded volumes are then given by

$$q_{rr} = 1, \qquad q_{rp} = 3.75, \qquad q_{pp} \approx 11.78, \tag{3.33}$$

indicating that the isotropic excluded volume of two platelets is almost 12 times larger than that of two rods. The mixture is therefore strongly *asymmetric*.

Several features are notable from Figs. 3.2 and 3.3. First, there is a reentrant transition at mole fractions x_p between 0.44 and 0.58. Experimentally, this would imply that a dilute sample containing 50% platelets undergoes numerous phase transitions upon concentration, going from the isotropic state I to $I+N^-$, N^-, $I+N^-$, $I+N^-+N^+$ and finally N^-+N^+. A similar reentrant transition was found in binary mixtures of rods with different lengths [34,65]. Furthermore, the triphasic equilibrium, represented by a triple line in the $\tilde{\Pi} - x$ representation, clearly manifests itself in the volume fraction representation as a triphasic triangle which covers a fair part of the phase diagram. Accordingly, a large range of compositions will pass through the three-phase area. It appears that a very small mole fraction of platelets in the isotropic phase already leads to a three-phase equilibrium upon increasing the overall concentration.

To verify the effect of the excluded-volume asymmetry on the phase diagram in more detail we will now investigate the behaviour a less asymmetric mixture, characterized by smaller excluded-volume ratios. For that, we consider a mixture with aspect ratio $L_r/D_r = D_p/L_p = 50$ and size ratio $L_r = 2D_p$, $D_r = 2L_p$. So, again, both species are equally anisometric but the size of the platelets is now reduced to half the size of the rods. This leads to the following excluded-volume ratios

$$q_{rr} = 1, \qquad q_{rp} \approx 3.13, \qquad q_{pp} \approx 4.91. \tag{3.34}$$

Note that q_{pp} is much smaller compared to Eq. (3.33). The corresponding phase diagrams are shown in Figs. 3.4 and 3.5.

Again, we observe a reentrant transition around $x_{\text{plate}} = 0.5$, albeit less prominent than in Fig. 3.2. A remarkable difference with Fig. 3.2 however is the presence of an *azeotropic* point at $x_{\text{plate}} = 0.718$ in the plate-rich ("tail") part of the $\tilde{\Pi} - x$ diagram (see Fig. 3.4(b)). This implies that a mixture containing 71.8 % platelets (with $L_r = 2D_p$) does not fractionate during phase separation, i.e. the coexisting I and N^- daughter phases have the same mole fraction as the parent sample.

By recalculating the phase diagram for various ratios L_r/D_p on the interval $1 < L_r/D_p < 2$ one can show that the azeotropic point, which corresponds to a *minimum* in $\tilde{\Pi}$, shifts towards higher mole fractions as the ratio L_r/D_p is lowered. Obviously, noting its absence in Fig. 3.3, the azeotropic point must leave the scene at some point on
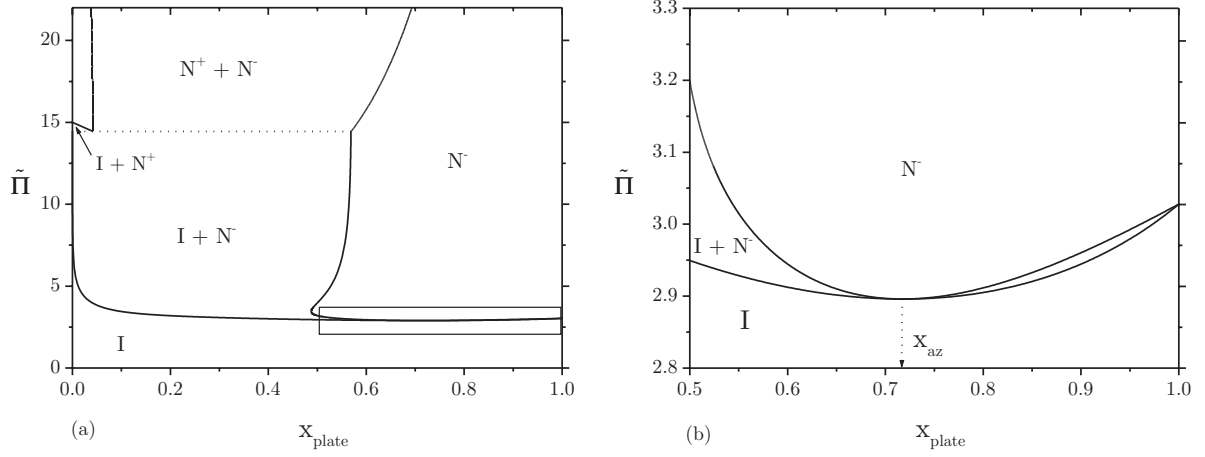
FIGURE 3.4. (a) Phase diagram calculated from the perturbation analysis in the $\tilde{\Pi} - x$ plane for $L_r/D_r = D_p/L_p = 50$. The platelets are half the size of the rods ($L_r = 2D_p$ and $D_r = 2L_p$). A reentrant phenomenon near $x_{\text{plate}} = 0.5$ is evident. (b) Magnification of the tail part of the diagram. Note the azeotropic point at $x_{\text{az}} = 0.718$.
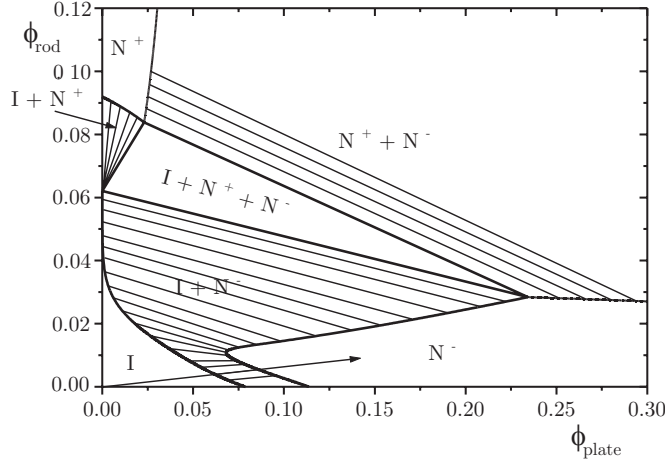
FIGURE 3.5. Phase diagram in the $\phi_{\text{rod}} - \phi_{\text{plate}}$ representation corresponding to Fig. 3.4(a). Thick lines indicate phase boundaries; thin lines represent tie lines connecting coexisting phases. A particular dilution line corresponding to the azeotropic point is drawn.

this interval. This, "critical" ratio can be determined by calculating, for instance, the initial fractionation, which we define as $x_{\text{p}}^I - x_{\text{p}}^N$ for x_{plate} infinitesimally close to 1, as a function of the ratio L_r/D_p. In case of an azeotropic point, the initial fractionation must be positive since the coexistence pressure decreases upon lowering $x_{\text{plate}} = 1$. In case of no azeotropic point, the coexistence pressure increases and the initial fractionation is therefore negative. At the critical ratio the initial fractionation must obviously be zero. From these considerations we obtain a critical ratio $L_r/D_p = 1.54$, *independent* of the aspect ratio $L_r/D_r = D_p/L_p$. Therefore, we may expect an azeotropic point if the rods are sufficiently larger than the platelets, *viz.* $L_r > 1.54D_p$.
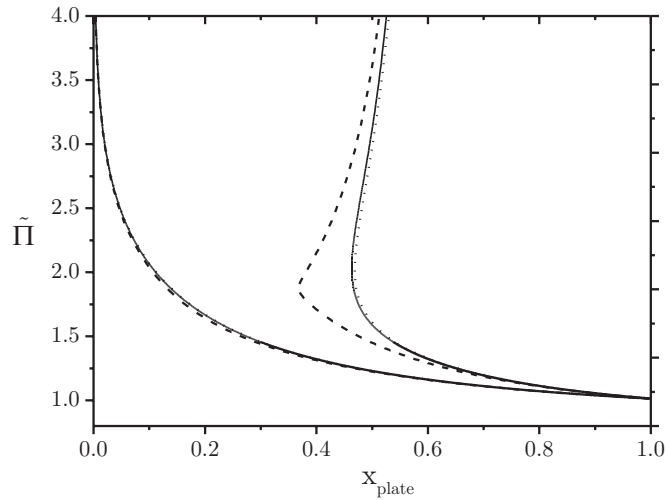
FIGURE 3.6. $I-N^-$ binodals for $L_r/D_r = D_p/L_p = 18$ and $L_r = D_p$, $D_r = L_p$ calculated from several approaches; zeroth order approximation (dashed line), perturbation analysis (dotted line) and full numerical solution (solid line).

3.4. DISCUSSION

We have scrutinized the isotropic-uniaxial nematic phase behaviour of rod-plate mixtures with strongly asymmetric excluded volumes ($v_{\text{ex}}^{\text{plate}} \gg v_{\text{ex}}^{\text{rod}}$) starting from the Onsager-Parsons free energy. Gaussian ODFs with adjustable parameters α_j were used to describe the distribution of angles in the uniaxial nematic phases. In the present calculations, we have set up a perturbation analysis to account for the $\ln \alpha_2/\alpha_2$ - contribution (Eq. (3.14)) in the asymptotic expansion of the excluded volume integral ρ_{22}. To check the validity of the analysis, we may compare it with a full numerical approach, in which the minimization equations are solved numerically along with the coexistence equations. As an example, we have collected some $I - N^-$ binodals obtained from several approaches in Fig. 3.6.

First, agreement between the perturbation analysis and the full numerical solution is very good. In fact, it remains surprisingly good at low aspect ratios (below 15). At high ratios (> 20) the curves almost become indistinguishable. A second conclusion is that the result from the zeroth order approximation (i.e. retaining only the leading order constant in ρ_{22}) clearly deviates from the other curves. The discrepancy increases for lower ratios and, crucially, the approximation completely breaks down at approximately $L_r/D_r = 18$ giving unphysical binodals. This breakdown is not encountered within the perturbation analysis or the numerical treatment. Therefore, we conclude that the second order contribution $\mathcal{F}$ to ρ_{22} is an essential ingredient in our calculations, since it enables us to calculate the phase behaviour of mixtures with aspect ratios comparable to that of experimental systems (i.e. L_r/D_r roughly between 10 and 15).

Let us now compare our calculated phase diagram with the experimental one as constructed in [82] and reproduced in Fig. 3.7. This diagram can be compared directly with the volume fraction representation in Fig. 3.3. From a qualitative point of view,
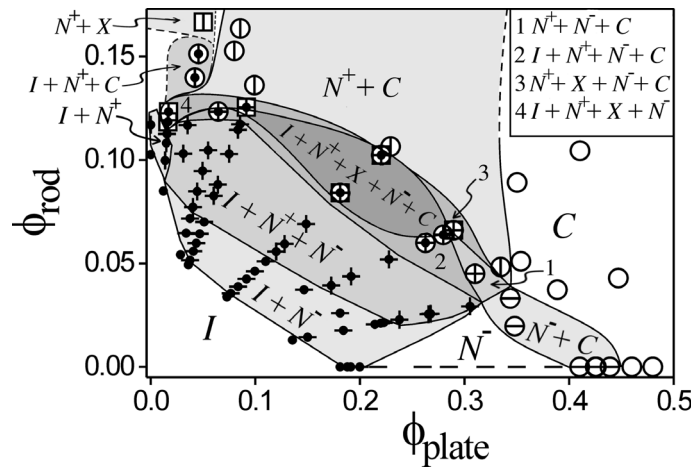
Figure 3.7. Experimental phase diagram for mixtures of colloidal boehmite rods ($L_r/D_r \sim 10$) and gibbsite platelets ($D_p/L_p \sim 15$). Picture taken from [82]. The phase behaviour becomes considerably complicated beyond the triphasic area due to the presence of additional $N - C$ and $N - X$ transitions.

both diagrams agree very well *at low concentrations*; the phase behaviour is largely dominated by coexistence between the isotropic phase and the plate-rich nematic (N^-) phase whereas $I - N^+$ coexistence is only visible in a small area close to the rod axis. Concomitantly, fractionation seems to be much stronger between the I and N^- phases than between the I and N^+ phases, particularly at high osmotic pressures. Both features are direct manifestations of the asymmetric excluded volumes in these mixtures. Another striking similarity between both diagrams is a large $I - N^- - N^+$ triphasic area covering a significant part of the diagrams. A generic feature that does not seem to appear in the experimental diagram is the reentrant transition. However, a detailed investigation of the lower part of the experimental phase diagram is probably required to detect this phenomenon.

The high concentration part of the experimental phase diagram is essentially different from the calculated one because other liquid crystal phases –with long-range crystalline order, such as the columnar (C) phase and the not yet identified rod-rich phase X [74]– come into play which are not taken into account theoretically. Most importantly, the theoretically predicted $N^+ - N^-$ demixing beyond the triphasic area is not observed experimentally. Its absence is probably caused by additional phase transitions from nematic to the (spatially inhomogeneous) C and X phases. As a result, the $N^+ - N^-$ demixing is disrupted by several multiphase equilibria involving more than three phases, in particular, the remarkable 5-phase equilibrium (see Fig. 3.7).

These observations are very striking since they are in conflict with Gibbs phase rule, which states that only bi- and triphasic equilibria can be expected for an effective two-component system of hard particles. One possible explanation for these phenomena would be the polydispersity of the colloidal species. Since both species have a fairly high polydispersity (around 30 %) the resulting mixture effectively contains almost

infinitely many components, which may lead to coexistence between arbitrarily many phases. A second possibility is the effect of sedimentation. Owing to the particles considerable buoyant mass, sedimentation is expected to play an important role in these systems. The presence of multiple phases may therefore be induced by a considerable concentration gradient inside the test tube. In Chapter 9 of this thesis, we will explicitly illustrate this notion for mixtures of plates and nonadsorbing ideal polymer.

APPENDIX A: EXCLUDED VOLUME INTEGRALS

In this Appendix, we give approximate analytical results for ρ_{12} and ρ_{22} by performing asymptotic expansions of the integrals.

Calculation of ρ_{12}

Inserting the Gaussian ODFs Eqs. (3.1) and (3.2) into Eq. (3.9) yields

$$\rho_{12} = \sqrt{\frac{\alpha_1^2 \alpha_2}{(2\pi)^3}} \int_{-\pi/2}^{\pi/2} \int_{-\pi/2}^{\pi/2} \int_{0}^{2\pi} |\cos\gamma| \exp\left[-\frac{1}{2}(\alpha_1 \theta^2 + \alpha_2 \psi^2)\right] d\phi \, d(\cos\theta) \, d(\sin\psi). \quad (3.35)$$

Here, θ is the polar angle between the particle axis and the z-axis and $\psi = \pi/2 - \theta'$ is the meridional angle between the particle vector and its projection onto the xy plane. Furthermore, ϕ is the azimuthal angle between the projections of the particle vectors onto the xy plane. Recall that the ODFs are sharply peaked around $\psi = 0$ and $\theta = 0$. Using the relation

$$|\cos\gamma| = |\cos\theta\sin\psi + \sin\theta\cos\psi\cos\phi|, \quad (3.36)$$

and expanding the trigonometric functions for small polar and meridional angles, we can approximate Eq. (3.35)

$$\rho_{12} \sim 4\sqrt{\frac{\alpha_1^2 \alpha_2}{(2\pi)^3}} \int_{0}^{\pi/2} \int_{0}^{\pi/2} \int_{0}^{2\pi} |\psi + \theta\cos\phi| \exp\left[-\frac{1}{2}(\alpha_1 \theta^2 + \alpha_2 \psi^2)\right] d\phi \, d\theta \, d\psi, \quad (3.37)$$

In order to get rid of the absolute value sign in the integrand we must split the integral into parts. Noting that

$$
\begin{aligned}
\psi + \theta\cos\phi &< 0 \quad \text{if} \quad \theta < \psi \\
\psi + \theta\cos\phi &> 0 \quad \text{if} \quad \psi < \theta \quad \text{and if} \quad -\phi_G < \phi < \phi_G \\
\psi + \theta\cos\phi &< 0 \quad \text{if} \quad \psi < \theta \quad \text{and if} \quad |\phi| > \phi_G,
\end{aligned}
\quad (3.38)
$$

(with $\cos\phi_{\mathrm{G}} = -\psi/\theta$) we split Eq. (3.37) into three separate integrals

$$\rho_{12} \sim 4\sqrt{\frac{\alpha_1^2 \alpha_2}{(2\pi)^3}} \left\{ \int_0^{\pi/2} \int_0^{\pi/2} \int_{-\pi}^{\pi} (\psi + \theta\cos\phi) \exp\left[-\frac{1}{2}(\alpha_1\theta^2 + \alpha_2\psi^2)\right] d\phi\theta d\theta d\psi \right.$$

$$- 4\int_0^{\pi/2} \int_\psi^{\pi/2} \int_{\phi_{\mathrm{G}}}^{\pi} \psi \exp\left[-\frac{1}{2}(\alpha_1\theta^2 + \alpha_2\psi^2)\right] d\phi d\theta d\psi$$

$$\left. -4\int_0^{\pi/2} \int_\psi^{\pi/2} \int_{\phi_{\mathrm{G}}}^{\pi} \theta\cos\phi \exp\left[-\frac{1}{2}(\alpha_1\theta^2 + \alpha_2\psi^2)\right] d\phi d\theta d\psi \right\},$$

$$\rho_{12} \sim 4\sqrt{\frac{\alpha_1^2 \alpha_2}{(2\pi)^3}} \left\{ I_1 + I_2 + I_3 \right\} \tag{3.39}$$

We can extend the (θ,ψ)-integrations up to infinity since the exponential function is expected to decay rapidly to zero for large α_j. The first integral is then easily calculated and yields $I_1 = 2\pi(\alpha_1\alpha_2)^{-1}$. For the second one, it is convenient to reverse the order of integration. Hence, we write

$$I_2 = -4\int_{\pi/2}^{\pi} \int_0^{\pi/2} \int_0^{-\theta\cos\phi} \exp\left[-\frac{1}{2}(\alpha_1\theta^2 + \alpha_2\psi^2)\right] \psi d\psi\theta d\theta d\phi,$$

$$\sim -4\int_{\pi/2}^{\pi} \int_0^{\infty} \exp\left(-\frac{1}{2}\alpha_1\theta^2\right) \alpha_2^{-1} \left[1 - \exp\left(-\frac{1}{2}\alpha_2\theta^2\cos^2\phi\right)\right] \theta d\theta d\phi, \tag{3.40}$$

which can be worked out straightforwardly to give

$$I_2 \sim \frac{2\pi}{\alpha_1\alpha_2} \left[\left(\frac{\alpha_1}{(\alpha_1 + \alpha_2)}\right)^{1/2} - 1\right]. \tag{3.41}$$

For the third integral we use the relation $\int_{\phi_{\mathrm{G}}}^{\pi} \theta\cos\phi d\phi = -(\theta^2 - \psi^2)^{1/2}$ to write

$$I_3 = 4\int_0^{\pi/2} \int_\psi^{\pi/2} \sqrt{\theta^2 - \psi^2} \exp\left[-\frac{1}{2}(\alpha_1\theta^2 + \alpha_2\psi^2)\right] \theta d\theta d\psi, \tag{3.42}$$

substituting $y = \frac{1}{2}\alpha_1(\theta^2 - \psi^2)$ gives

$$I_3 \sim 2^{5/2}\alpha_1^{3/2} \int_0^{\pi/2} \exp\left[-\frac{1}{2}(\alpha_1 + \alpha_2)\psi^2\right] d\psi \int_0^{\infty} y^{1/2}\exp(-y)dy,$$

$$\sim 2\pi/\sqrt{\alpha_1^3(\alpha_1 + \alpha_2)}. \tag{3.43}$$

Putting all contributions back into Eq. (3.39) yields the following asymptotic result for ρ_{12}

$$\rho_{12} \sim \sqrt{\frac{8}{\pi}\left(\frac{1}{\alpha_1} + \frac{1}{\alpha_2}\right)} + \mathcal{O}\left(\alpha_1^{-3/2}, \alpha_2^{-3/2}\right), \tag{3.44}$$

Calculation of ρ_{22}

Inserting the Gaussian ODFs (3.2) into Eq. (3.8) yields

$$\rho_{22} = \frac{4}{\pi}\frac{\alpha_2}{(2\pi)^2} \int_{-\pi/2}^{\pi/2} \int_{-\pi/2}^{\pi/2} \int_0^{2\pi} |\sin\gamma| \exp\left[-\frac{\alpha_2}{2}(\psi^2 + \psi'^2)\right] d\phi d(\sin\psi)d(\sin\psi'), \tag{3.45}$$

which we can approximate, similar to ρ_{12}, as

$$\rho_{22} \sim \frac{16}{\pi} \frac{\alpha_2}{(2\pi)^2} \int_0^\infty \int_0^\infty K(\psi, \psi') \exp\left[-\frac{\alpha_2}{2}(\psi^2 + \psi'^2)\right] d\psi d\psi'. \tag{3.46}$$

Here, $K(\psi, \psi')$ is the azimuthally integrated kernel

$$K(\psi, \psi') \equiv \int_0^{2\pi} |\sin\gamma|\, d\phi$$

$$= \int_0^{2\pi} \sqrt{1 - \cos^2\gamma}\, d\phi, \tag{3.47}$$

We can expand K around $\psi = 0$ since the particle vectors, on average, only marginally deviate from the xy plane. Here, γ is the angle between the two particle vectors $\mathbf{u}(\psi)$ and $\mathbf{u}'(\psi, \phi)$,

$$\mathbf{u} = \begin{pmatrix} \cos\psi \\ 0 \\ \sin\psi \end{pmatrix}, \qquad \mathbf{u}' = \begin{pmatrix} \cos\psi'\cos\phi \\ \cos\psi'\sin\phi \\ \sin\psi' \end{pmatrix}.$$

Taking the square of the inner product of the two vectors and substituting the asymptotic expressions (up to second order in ψ) yields

$$\cos^2\gamma = (\cos\psi\cos\psi'\cos\phi + \sin\psi\sin\psi')^2$$

$$\approx \left[(1 - \frac{1}{2}\psi^2)(1 - \frac{1}{2}\psi'^2)\cos\phi + \psi\psi'\right]^2. \tag{3.48}$$

Using cylindrical coordinates ($\psi = R\sin\chi$ and $\psi' = R\cos\chi$) and expanding up to second order in R gives

$$\cos^2\gamma = (1 - R^2)\cos^2\phi + 2R^2\cos\phi\sin\chi\cos\chi + \mathcal{O}(R^4), \tag{3.49}$$

and

$$|\sin\gamma| = \sqrt{1 - \cos^2\gamma}$$

$$\sim \sqrt{1 - (1 - R^2)\cos^2\phi}\left[1 + \frac{R^2\cos\phi\sin\chi\cos\chi}{1 - (1 - R^2)\cos^2\phi} + \cdots\right]. \tag{3.50}$$

The kernel K now reads*

$$K(R, \chi) = \int_0^{2\pi} \sqrt{1 - (1 - R^2)\cos^2\phi}\, d\phi + \int_0^{2\pi} \frac{R^2\cos\phi\sin\chi\cos\chi}{\sqrt{1 - (1 - R^2)\cos^2\phi}}\, d\phi + \cdots. \tag{3.51}$$

The second integral is zero, since the integrand is an odd periodic function. Likewise, all higher contributions depending on odd powers of $\cos\phi$ are zero. The first integral in Eq. (3.51) can be rewritten as a complete elliptic integral of the second kind $E(\kappa)$

$$\int_0^{2\pi} \sqrt{1 - (1 - R^2)\cos^2\phi}\, d\phi = 4\int_0^{\pi/2} \sqrt{1 - \kappa\sin^2\phi}\, d\phi = 4E(\kappa), \tag{3.52}$$

---

*The higher order terms denoted by $\ldots$ involve integrals of type $\int_0^{2\pi} \frac{R^4\cos^2\phi}{\sqrt{1-(1-R^2)\cos^2\phi}}d\phi$ and $\int_0^{2\pi} \frac{R^4\cos^2\phi}{[1-(1-R^2)\cos^2\phi]^{3/2}}d\phi$ which can be rewritten in terms of complete elliptic integrals of the second and third kind [83].

where $\kappa = 1 - R^2$. This integral can be expanded up to second order around $R = 0$ [83]

$$
\begin{aligned}
E(\kappa) &= 1 + \frac{1}{2}\left[\ln\left(\frac{4}{R}\right) - \frac{1}{2}\right]R^2 + \frac{3}{16}\left[\ln\left(\frac{4}{R}\right) - \frac{13}{12}\right]R^4 + \dots. \\
&= 1 + \frac{1}{2}\left[\ln 4 - \ln R - \frac{1}{2}\right]R^2 + \mathcal{O}(R^4).
\end{aligned}
\tag{3.53}
$$

We now have the following expansion for the azimuthally integrated kernel

$$
K(\psi, \psi') = 4 + 2\left[\ln 4 - \frac{1}{2}\ln(\psi^2 + \psi'^2) - \frac{1}{2}\right](\psi^2 + \psi'^2) + \mathcal{O}(\{\psi^4 \ln \psi\}),
\tag{3.54}
$$

valid for small ψ and ψ'. Substituting this into Eq. (3.46) gives

$$
\rho_{22} \sim \frac{32}{\pi}\frac{\alpha_2}{(2\pi)^2}\int_0^\infty \int_0^{2\pi}\left\{1 + \frac{1}{2}\left[\ln 4 - \ln R - \frac{1}{2}\right]\right\}\exp\left[-\frac{\alpha_2}{2}R^2\right]R d\chi dR,
\tag{3.55}
$$

in terms of the cylindrical coordinates (χ, R). The integral can be solved straightforwardly

$$
\rho_{22} \sim \frac{8}{\pi^2}\left[1 + \frac{1}{2}\frac{\ln \alpha_2}{\alpha_2} + \frac{\ln(2\sqrt{2}) + \frac{1}{2}\gamma_E - 1}{\alpha_2}\right] + \mathcal{O}(\alpha_2^{-2}\ln \alpha_2),
\tag{3.56}
$$

where $\gamma_E = 0.5772156649\dots$ denotes Euler's constant. Note that the $\ln \alpha_2/\alpha_2$ term is the leading order α_2-dependent term in this expansion.

The next step is to work out the higher order integrals contributing to the kernel Eq. (3.51). It can be shown that these integrals give additional $\mathcal{O}(\alpha_2^{-1})$ contributions to ρ_{22}. After tedious derivations we obtain the following final asymptotic expression for ρ_{22}

$$
\begin{aligned}
\rho_{22} &\sim \frac{8}{\pi^2}\left[1 + \frac{1}{2}\frac{\ln \alpha_2}{\alpha_2} + \frac{\ln 4 + \frac{1}{2}\gamma_E - 3/2}{\alpha_2}\right] + \mathcal{O}(\alpha_2^{-2}\ln \alpha_2) \\
&\sim \frac{8}{\pi^2}\left[1 + \mathcal{F}(\alpha_2)\right] + \mathcal{O}(\alpha_2^{-2}\ln \alpha_2),
\end{aligned}
\tag{3.57}
$$

which now contains all contributions up to order $\mathcal{O}(\alpha_2^{-1})$

Appendix B: Perturbation analysis

Let $\alpha_{1,0}$ and $\alpha_{2,0}$ be the solutions of the minimization equations Eqs. (3.18) and (3.19) for the zeroth order problem ($\mathcal{F} = \mathcal{H} = 0$)

$$
\begin{aligned}
\alpha_{1,0}^{1/2} &= 2\pi^{-1/2}\left[(1-x) + 2^{1/2}xq_{12}h(Q_0)\right]c, \\
\alpha_{2,0}^{1/2} &= 2^{5/2}\pi^{-1/2}q_{12}(1-x)g(Q_0)c.
\end{aligned}
\tag{3.58}
$$

When $\mathcal{F}$ is nonzero and $\mathcal{H}$ is represented by Eq. (3.22) the solutions will only be marginally affected, since $\mathcal{H}$ is a small contribution. Hence, we can write

$$
\begin{aligned}
\alpha_1 &= \alpha_1^0 + \delta\alpha_1, \\
\alpha_2 &= \alpha_2^0 + \delta\alpha_2,
\end{aligned}
\tag{3.59}
$$

where $\delta\alpha_1$ and $\delta\alpha_2$ are the perturbations, such that $\delta\alpha_1/\alpha_1^0$ and $\delta\alpha_2/\alpha_2^0$ are small variables. We can linearize $Q(= \alpha_2/\alpha_1)$ with respect to these perturbation variables

$$Q = \frac{\alpha_2^0 + \delta\alpha_2}{\alpha_1^0 + \delta\alpha_1} \simeq Q_0 \left[1 + \frac{\delta\alpha_2}{\alpha_2^0} - \frac{\delta\alpha_1}{\alpha_1^0} \right], \tag{3.60}$$

and, accordingly

$$g(Q) \simeq (1 + Q_0)^{-1/2} \left[1 - \frac{1}{2} \frac{Q_0}{Q_0 + 1} \left(\frac{\delta\alpha_2}{\alpha_2^0} - \frac{\delta\alpha_1}{\alpha_1^0} \right) \right],$$

$$h(Q) \simeq (1 + Q_0^{-1})^{-1/2} \left[1 + \frac{1}{2} \frac{1}{Q_0 + 1} \left(\frac{\delta\alpha_2}{\alpha_2^0} - \frac{\delta\alpha_1}{\alpha_1^0} \right) \right], \tag{3.61}$$

Similarly, we get

$$\alpha_1^{1/2} \simeq \alpha_{1,0}^{1/2} \left[1 + \frac{\delta\alpha_1}{2\alpha_1^0} \right],$$

$$\alpha_2^{1/2} \simeq \alpha_{2,0}^{1/2} \left[1 + \frac{\delta\alpha_2}{2\alpha_2^0} \right]. \tag{3.62}$$

To find solutions for $\delta\alpha_1$ and $\delta\alpha_2$ we substitute the above expressions into the minimization equations (with $\mathcal{H}$ nonzero). All zeroth order terms cancel out, by construction, leaving an inhomogeneous set of linear equations in $\delta\alpha_1$ and $\delta\alpha_2$

$$x\delta\alpha_2 = \left[2(1-x)(1+Q_0) + Q_0 x \right] \delta\alpha_1,$$

$$\delta\alpha_2 = -\frac{Q_0}{1 + Q_0} \left[\delta\alpha_2 - Q_0 \delta\alpha_1 \right] - 2\alpha_{2,0}^{1/2} c\mathcal{H}(x, \alpha_{2,0}), \tag{3.63}$$

where the term involving $\mathcal{H}$ is the inhomogeneous term ensuring nonzero solutions for $\delta\alpha_1$ and $\delta\alpha_2$. The solutions $\delta\alpha_1$ and $\delta\alpha_2$ (not shown here) can be rewritten as explicit functions of $Q_0(x)$, x and c, with the aid of Eq. (3.58). It can be shown that the perturbations scale with concentration as $\delta\alpha_j \sim K_j(x)c + c\ln c$, where $K_j(x)$ are functions of the mole fraction only. Hence, the perturbation $\mathcal{F}$ leads to a $c\ln c$ correction (up to leading order) to the c^2-dependence of $\alpha_{1,0}$ and $\alpha_{2,0}$ (Eq. (3.58)).

The final step is to linearize the expressions σ_j and ρ_{jk}. Substituting Eq. (3.59) in Eq. (3.4) and expanding up to first order in $\delta\alpha_1$ and $\delta\alpha_2$ thus yields for the orientational entropy

$$\sigma_1 = \sigma_{1,0} + \delta\sigma_1 = \ln\alpha_{1,0} - 1 + \frac{\delta\alpha_1}{\alpha_{1,0}}, \tag{3.64}$$

$$\sigma_2 = \sigma_{2,0} + \delta\sigma_2 = \frac{1}{2} \left[\ln\alpha_{2,0} + \ln\frac{2}{\pi} - 1 \right] + \frac{\delta\alpha_2}{2\alpha_{2,0}}. \tag{3.65}$$

Similarly, we get for the excluded volume entropy

$$\rho_{11} = \rho_{11,0} + \delta\rho_{11}$$

$$= 4\pi^{-1/2} \left[\alpha_{1,0}^{-1/2} - \frac{\delta\alpha_1}{2\alpha_{1,0}^{3/2}} \right], \tag{3.66}$$

and

$$\rho_{12} = \rho_{12,0} + \delta\rho_{12}$$

$$= 2^{3/2}\pi^{-1/2}\left\{\left(\frac{1}{\alpha_{1,0}} + \frac{1}{\alpha_{2,0}}\right)^{1/2} - \left[\frac{h(Q_0)\delta\alpha_1}{2\alpha_{1,0}^{3/2}} + \frac{g(Q_0)\delta\alpha_2}{2\alpha_{2,0}^{3/2}}\right]\right\}. \tag{3.67}$$

Note that ρ_{22} Eq. (3.12) remains unchanged, since $\mathcal{F}$ already constitutes the direct perturbation. The leading order terms in Eqs. (3.64), (3.65) and Eqs. (3.66), (3.67) are given by the expressions for σ_j and ρ_{jk} in Sec. 3.2. After some algebra we obtain the following corrections (denoted by δ) to the osmotic pressure and chemical potentials of the nematic phase

$$\delta\tilde{\Pi}_n \sim -c\left[Q_0(1-x)\frac{\delta\alpha_1}{\alpha_{2,0}} + \frac{1}{2}x\frac{\delta\alpha_2}{\alpha_{2,0}}\right] + \frac{1}{2}cx\mathcal{W}(x,c,Q_0), \tag{3.68}$$

$$\delta\tilde{\mu}_{1,n} \sim \frac{x}{2(1-x)}\left[Q_0^2\frac{\delta\alpha_1}{\alpha_{2,0}} - \frac{\delta\alpha_2}{\alpha_{2,0}}\right] - Q_0\frac{\delta\alpha_1}{\alpha_{2,0}}, \tag{3.69}$$

$$\delta\tilde{\mu}_{2,n} \sim -\frac{1}{2}Q_0^2\frac{\delta\alpha_1}{\alpha_{2,0}} + \mathcal{W}(x,c,Q_0), \tag{3.70}$$

with

$$\mathcal{W}(x,c,Q_0) = \frac{1}{4\pi c}\frac{xq_{22}}{q_{12}^2(1-x)^2}(1+Q_0)\left(\ln\alpha_{2,0} + 2K\right). \tag{3.71}$$

These contributions are simply added to the leading order expressions given in Sec. 3.2. Note that the terms depending on $\mathcal{W}$ are the direct perturbations (arising from $\delta\rho_{22}$).

4

Asymmetric rod-plate mixtures (II) : Biaxial versus uniaxial nematic stability

ABSTRACT

The isotropic-nematic phase behaviour of rod-plate mixtures is studied within Onsager's second virial theory using the numerically exact equilibrium orientational distribution functions for both uniaxial and biaxial nematic phases. We concentrate on asymmetric mixtures in which the excluded volume between the plates v_{ex}^{PP} is larger than that between the rods v_{ex}^{RR}. Starting from the symmetric case ($v_{ex}^{PP}/v_{ex}^{RR} = 1$) and increasing the rod-plate excluded volume ratio we scrutinize the phase behaviour, in particular focussing on the stability of the biaxial nematic phase. We observe that, at a certain asymmetry, the characteristic bicritical point is replaced by a two-phase region marking first order isotropic-biaxial transitions. Increasing the asymmetry even further leads to several demixing scenarios. First, there is a uniaxial-biaxial ($N^+ - B$) demixing scenario with an associated isotropic-uniaxial-biaxial ($I - N^+ - B$) triple equilibrium. Second, a uniaxial-uniaxial ($N^+ - N^-$) demixing transition occurs in case of strongly asymmetric mixtures indicating that the biaxial nematic phase may become fully metastable. Since all predicted demixing scenarios lie in the experimentally accessible regime, there is a possibility of finding biaxial nematic structures in lyotropic colloidal rod-plate mixtures.

4.1. INTRODUCTION

Previous theoretical studies on rod-plate mixtures have mainly focussed on *symmetric* mixtures, characterized by equal excluded volumes for both species ($v_{excl.}^{PP}/v_{ex}^{RR} = 1$). The theoretical approaches can roughly be subdivided into two groups. On the one hand, Onsager-type theories [48, 78–80, 84] were adopted which allow for a continuous treatment of both the positional and orientational degrees of freedom. On the other hand, mean-field lattice models [76, 85] were used in which the positional and/or orientational coordinates are discretized, such as the Zwanzig theory [86] where the particle orientations are restricted to lie on one of the Cartesian axes. All theories predict the same qualitative behaviour for the symmetric case; a stable *biaxial* nematic phase exists in between the rod- and plate-dominated uniaxial phases, and meets the isotropic phase in a bicritical point. The phase diagrams for these mixtures are always symmetric about mole fraction $x = 1/2$ (i.e. equal portions of rods and plates) at least within a second virial approximation.

Van Roij and Mulder [85] showed that the biaxial nematic phase in a mixture of rectangular rod- and platelike blocks, treated within a Zwanzig second virial theory, may become unstable with respect to demixing into the uniaxial nematic phases at some critical rod-plate excluded volume ratio. Computer simulations by Camp *et al.* [49] on symmetric mixtures of hard prolate and oblate ellipsoids confirmed that demixing can occur. Their phase diagrams, which were not symmetric due to the effect of higher order particle interactions, essentially revealed a two-step demixing scenario where the biaxial nematic phase demixes into the uniaxial phases upon compression via a transitional uniaxial nematic-biaxial nematic coexistence region.

Experiments [73] on strongly *asymmetric* mixtures ($v_{ex}^{PP}/v_{ex}^{RR} \gg 1$) using rod- and plate-shaped colloids confirmed the presence of a demixing transition involving two fractionated rod- and plate-dominated nematic phases, both probably having a uniaxial symmetry. In the previous Chapter, it was shown that many features of the experimental phase behaviour could be reproduced satisfactorily within the Onsager-Parsons theory using Gaussian trial functions to describe the equilibrium particle orientations in the nematic phases. However, the possibility of biaxial solutions was not explored there as we focussed solely on the uniaxial nematic symmetries.

In this Chapter, we include the possibility of biaxial nematic ordering in the original Onsager treatment. The possibility of biaxial solutions is incorporated explicitly by performing the exact free energy minimization with respect to the orientational degrees of freedom and solving the resulting integral equations exactly, using numerical schemes. In this way we obtain the numerically exact orientational distribution functions for the aligned phases without having to rely on approximations such as using trial forms with a predescribed form [87], discretized orientation models [76, 85], or the so-called L2-model [79, 80, 84]. In the latter case, the excluded volumes are represented as a series expansion in terms of spherical harmonics truncated after the first term, which is only reliable for very weakly aligned nematic phases.

We assess the effect of the asymmetry, induced by increasing the rod-plate excluded volume ratio from unity, on the phase behaviour of rod-plate mixtures focussing on the stability of the biaxial nematic phase. Since our primary goal in this Chapter is to provide qualitative scenarios for the phase diagrams we shall not apply Parsons' approach here for the sake of simplicity.

4.2. Starting equations

We start this section with a brief recapitulation of the basic ingredients described in the previous Chapter. The Helmholtz free energy of a binary mixture in the Onsager treatment reads

$$\frac{\beta F}{N} = \text{cst} + \ln c - 1 + \sum_{j=1,2} x_j \left[\ln x_j + \sigma_j \right] + c\tilde{B}_2, \tag{4.1}$$

in terms of the second virial coefficient

$$\tilde{B}_2 = x_1^2 \rho_{11} + 2x_1 x_2 q_{12} \rho_{12} + x_2^2 q_{22} \rho_{22}. \tag{4.2}$$

Henceforth, $x_2 = x$ will be defined as the mole fraction of *the platelets* and c denotes the total dimensionless concentration, $c = bN/V$, with $b = \pi L_R^2 D_R/4$ the average excluded volume between two randomly oriented thin rods. The parameters q_{12} and q_{22} in Eq. (4.2) quantify the excluded volume between two *randomly oriented* particles (a rod and a platelet and two platelets, respectively) relative to that between two rods (see Eq. (3.17)). They can be expressed explicitly in terms of the particle size ratios

$$q_{12} = \frac{1}{4}\left(\frac{D_P}{D_R}\right)^2\left(\frac{D_R}{L_R}\right), \quad q_{22} = \frac{\pi}{4}\left(\frac{D_P}{D_R}\right)^3\left(\frac{D_R}{L_R}\right)^2. \tag{4.3}$$

These parameters determine the *(a)symmetry* of the rod-plate mixture. Setting q_{22} equal to unity renders the free energy symmetric about $x = 0.5$ in our second virial approach as we see from Eq. (4.2). Consequently, all phase diagrams must be symmetric about the dilution line corresponding to equal mole fractions [48, 80, 85]. In our case, q_{22} will be larger than unity (i.e. the isotropic excluded volume of the plates is larger than that of the rods) which implies that the symmetry is lost and all phase diagrams are asymmetric.

Our final ingredients are σ_j and ρ_{ij}, which represent the integrals pertaining to the orientational and excluded-volume entropy, respectively

$$\sigma_j \equiv \int f_j(\Omega)\ln[4\pi f_j(\Omega)]d\Omega, \tag{4.4}$$

$$\rho_{jj} = \frac{4}{\pi}\iint |\sin\gamma(\Omega,\Omega')|\, f_j(\Omega)f_j(\Omega')d\Omega d\Omega',$$

$$\rho_{12} = 2\iint |\cos\gamma(\Omega,\Omega')|\, f_1(\Omega)f_2(\Omega')d\Omega d\Omega'. \tag{4.5}$$

To allow possible biaxial solutions for the normalized ODFs $f_j(\Omega) = f_j(\theta,\phi)$ they must depend on both the *polar* angle θ between the particle orientation vector and the nematic director and the *azimuthal* angle ϕ describing the orientation of the particle in the plane perpendicular to that director.

The shape of the thermodynamic equilibrium ODF is obtained by minimizing the free energy with respect to the orientational degrees of freedom. Formally minimizing the free energy with respect to f_j by means of a functional differentiation under the constraint of the normalization condition for the ODF yields

$$\frac{\delta}{\delta f_j(\Omega)}\left\{\frac{\beta F}{N} + \lambda_j\left[1 - \int f_j(\Omega)d\Omega\right]\right\} = 0, \quad j = 1, 2, \tag{4.6}$$

where λ_j are the Lagrange undetermined multipliers which follow from the normalization conditions. This results in the following coupled set of Euler-Lagrange equations

$$\lambda_1 = \ln\left[4\pi f_1(\Omega)\right] + \frac{8c}{\pi}(1-x)\int |\sin\gamma(\Omega,\Omega')|\, f_1(\Omega')d\Omega'$$

$$+ 4cxq_{12}\int |\cos\gamma(\Omega,\Omega')|\, f_2(\Omega')d\Omega', \tag{4.7}$$

$$\lambda_2 = \ln\left[4\pi f_2(\Omega)\right] + 4c(1-x)q_{12}\int |\cos\gamma(\Omega,\Omega')|\, f_1(\Omega')d\Omega'$$

$$+ \frac{8c}{\pi}xq_{22}\int |\sin\gamma(\Omega,\Omega')|\, f_2(\Omega')d\Omega'. \tag{4.8}$$

These stationarity conditions constitute the starting expression for the calculations. Since there is no exact solution to the equations above we must adopt numerical techniques to obtain the equilibrium ODF for the nematic phase at a given x and c. This will be explained in the next section. Once the minimization problem has been solved, the compositions and concentrations of the coexisting phases are found in the usual way by imposing the standard conditions of equal osmotic pressure and chemical potentials.

4.3. Solution of the stationarity equations

4.3.1. Series expansion solution

A systematic way to tackle the integral equations Eq. (4.8) is to expand the kernels $|\sin\gamma|$ and $|\cos\gamma|$ in terms of Legendre polynomials P_n. Following Refs. [30] and [80] we write

$$|\sin\gamma| = \frac{\pi}{4} + \sum_{n=1}^{\infty} d_{2n}P_{2n}(\cos\gamma),$$

$$|\cos\gamma| = \frac{1}{2} + \sum_{n=1}^{\infty} c_{2n}P_{2n}(\cos\gamma), \tag{4.9}$$

with coefficients [32]

$$d_{2n} = -\frac{\pi(4n+1)(2n-3)!!(2n-1)!!}{2^{2n+2}n!(n+1)!},$$

$$c_{2n} = \frac{(-1)^{n+1}(4n+1)(2n-3)!!}{2^{n+1}(n+1)!}. \tag{4.10}$$

For symmetry reasons only even Legendre polynomials need be retained [48]. To include the possibility of biaxial symmetry we use the addition theorem of spherical harmonics to rewrite $P_{2n}(\cos\gamma)$ in terms of a bilinear expansion in $P_{2n}(\cos\theta)$ and its associated Legendre functions $P_{2n}^m(\cos\theta)$ [71]:

$$P_{2n}(\cos\gamma) = P_{2n}(\cos\theta)P_{2n}(\cos\theta') + 2\sum_{m=1}^{2n}\frac{(2n-m)!}{(2n+m)!}P_{2n}^m(\cos\theta)P_{2n}^m(\cos\theta')\cos m(\phi-\phi'), \tag{4.11}$$

Substituting Eqs. (4.9) and (4.11) into the integral equations Eq. (4.8) and some rearranging leads to

$$f_j(\theta,\phi) = Z_j^{-1}\exp\left[\sum_{n=1}^{\infty}\alpha_{2n}^{(j)}P_{2n}(\cos\theta)\right]\exp\left[\sum_{n=1}^{\infty}\sum_{m=1}^{n}k_{nm}\beta_{2n}^{2m\,(j)}P_{2n}^{2m}(\cos\theta)\cos 2m\phi\right], \tag{4.12}$$

with $k_{nm} = 2(2n-2m)!/(2n+2m)!$ and Z_j a normalization factor. For symmetry reasons, only even$-m$ associated Legendre functions need be included and all $\sin m\phi$

arising from the addition theorem vanish [48]. The coefficients $\alpha_{2n}^{(j)}$ and $\beta_{2n}^{2m\,(j)}$ are given by

$$\alpha_{2n}^{(1)} = -\frac{8}{\pi}c(1-x)d_{2n}\langle P_{2n}\rangle_{f_1} - 4cxq_{12}c_{2n}\langle P_{2n}\rangle_{f_2},$$

$$\alpha_{2n}^{(2)} = -4c(1-x)q_{12}c_{2n}\langle P_{2n}\rangle_{f_1} - \frac{8}{\pi}cxq_{22}d_{2n}\langle P_{2n}\rangle_{f_2}, \tag{4.13}$$

and

$$\beta_{2n}^{2m\,(1)} = -\frac{8}{\pi}c(1-x)d_{2n}\left\langle P_{2n}^{2m}\cos 2m\phi\right\rangle_{f_1} - 4cxq_{12}c_{2n}\left\langle P_{2n}^{2m}\cos 2m\phi\right\rangle_{f_2},$$

$$\beta_{2n}^{2m\,(2)} = -4c(1-x)q_{12}c_{2n}\left\langle P_{2n}^{2m}\cos 2m\phi\right\rangle_{f_1} - \frac{8}{\pi}cxq_{22}d_{2n}\left\langle P_{2n}^{2m}\cos 2m\phi\right\rangle_{f_2}. \tag{4.14}$$

The values of these coefficients are found by numerically solving the following coupled consistency equations

$$\langle P_{2n}\rangle_{f_j} = \int f_j(\Omega)P_{2n}(\cos\theta)d\Omega, \quad n=1,2,\ldots,N, \tag{4.15}$$

$$\left\langle P_{2n}^{2m}\cos 2m\phi\right\rangle_{f_j} = \int f_j(\Omega)P_{2n}^{2m}(\cos\theta)\cos 2m\phi d\Omega, \quad n,m=1,2,\ldots,N \quad (m\le n). \tag{4.16}$$

with $d\Omega = d(\cos\theta)d\phi$. Assuming the expansion in Eq. (4.12) to converge after a finite number of terms, we truncate the series after the Nth term. In case of uniaxial symmetry, the biaxial coefficients $\beta_{2n}^{2m\,(j)}$ are zero which means that we only have to solve the set of $2N$ consistency equations Eq. (4.15) together with Eqs. (4.12) and (4.13). In case of biaxial symmetry however, both sets Eqs. (4.15) and (4.16), must be solved simultaneously, which implies solving $N(N+1)$ equations iteratively. Obviously, the number of N depends on the degree of alignment of the nematic phase via the mole fraction and concentration. Following [80] we chose $N = 7$ as a minimum for weakly ordered nematic phases and we increased its value up to a maximum $N = 12$ for higher concentrations. The numerical integrations were performed using Gaussian quadrature. The initial trial ODFs were those in the perfectly aligned uniaxial (or biaxial) nematic phase. The solutions were iterated until the normalization factors Z_j had converged to within 10^{-6}.

Once the consistency equations have been solved, the entropic contributions σ_j and ρ_{jk} can be calculated from

$$\sigma_j = -\ln 4\pi Z_j + \sum_{n=1}^{N}\alpha_{2n}^{(j)}\langle P_{2n}\rangle_{f_j} + \sum_{n=1}^{N}\sum_{m=1}^{n}k_{nm}\beta_{2n}^{2m\,(j)}\left\langle P_{2n}^{2m}\cos 2m\phi\right\rangle_{f_j},$$

$$\rho_{jj} = 1 + \frac{4}{\pi}\sum_{n=1}^{N}d_{2n}\langle P_{2n}\rangle_{f_j}^2 + \sum_{n=1}^{N}\sum_{m=1}^{n}k_{nm}\left\langle P_{2n}^{2m}\cos 2m\phi\right\rangle_{f_j}^2,$$

$$\rho_{12} = 1 + 2\sum_{n=1}^{N}c_{2n}\langle P_{2n}\rangle_{f_1}\langle P_{2n}\rangle_{f_2} + \sum_{n=1}^{N}\sum_{m=1}^{n}k_{nm}\left\langle P_{2n}^{2m}\cos 2m\phi\right\rangle_{f_1}\left\langle P_{2n}^{2m}\cos 2m\phi\right\rangle_{f_2}. \tag{4.17}$$

4.3.2. Direct numerical solution

The main drawback of the series expansion is that the convergence becomes very sluggish when the nematic phase is strongly aligned. To obtain reasonable quantitative results, N should be taken very large ($N \gg 10$) in that regime, which makes the numerical procedure computationally awkward. To make headway, we may consider an alternative method, due to Herzfeld *et al.* [33], in which the integral equations Eq. (4.8) are solved directly by assuming a grid of angles Ω and Ω'. Taking the exponentiated form of Eq. (4.8) and eliminating the Lagrange multipliers using the normalization conditions of the ODFs we may rewrite Eq. (4.8) in an iterative form

$$f_1^{(n+1)}(\Omega) = \frac{\exp\left[-\frac{8c}{\pi}(1-x)\int |\sin\gamma(\Omega,\Omega')|\, f_1^{(n)}(\Omega')d\Omega' - 4cxq_{12}\int |\cos\gamma(\Omega,\Omega')|\, f_2^{(n)}(\Omega')d\Omega'\right]}{\int d\Omega \exp\left[-\frac{8c}{\pi}(1-x)\int |\sin\gamma(\Omega,\Omega')|\, f_1^{(n)}(\Omega')d\Omega' - 4cxq_{12}\int |\cos\gamma(\Omega,\Omega')|\, f_2^{(n)}(\Omega')d\Omega'\right]},$$

$$f_2^{(n+1)}(\Omega) = \frac{\exp\left[-4c(1-x)q_{12}\int |\cos\gamma(\Omega,\Omega')|\, f_1^{(n)}(\Omega')d\Omega' - \frac{8c}{\pi}xq_{22}\int |\sin\gamma(\Omega,\Omega')|\, f_2^{(n)}(\Omega')d\Omega'\right]}{\int d\Omega \exp\left[-4c(1-x)q_{12}\int |\cos\gamma(\Omega,\Omega')|\, f_1^{(n)}(\Omega')d\Omega' - \frac{8c}{\pi}xq_{22}\int |\sin\gamma(\Omega,\Omega')|\, f_2^{(n)}(\Omega')d\Omega'\right]}.$$

$$(4.18)$$

The integrations over the solid angles were carried out by Simpson's quadrature. We considered intervals of $[0, \pi/2]$ for the polar angle θ and $[0, 2\pi]$ for the azimuthal angle ϕ. The intervals were discretized into J_θ and J_ϕ equal parts. For the uniaxial nematic phases, the integrations over the azimuthal angle vanish so that we need only perform numerical integrations over the polar angle. Accurate results for highly ordered uniaxial nematic phases were obtained using $J_\phi = 1000$ and $J_\theta = 400$. Refining the grid size even further did not lead to significant changes in the ρ_{jk} and σ_j reported here. Initial guesses for $f_1(\Omega)$ and $f_2(\Omega)$ were used to solve the coupled set Eq. (4.18) iteratively. The solutions were iterated until the convergence criterion $\max\left|f_j^{(n+1)}(\Omega) - f_j^{(n)}(\Omega)\right| < 10^{-8}$ was satisfied. Once the equilibrium ODFs were obtained, the entropic contributions σ_j and ρ_{jk} could be calculated straightforwardly from Eqs. (4.4) and (4.5) using Simpson's quadrature.

4.4. Order parameters

In order to identify the isotropic and nematic phases, we introduce uniaxial (S_j) and biaxial (Δ_j) order parameters for each component j. Following [80] we define

$$S_j = \langle P_2(\cos\theta)\rangle_{f_j} = \frac{1}{2}\left\langle 3a_z^2 - 1\right\rangle_{f_j},$$

$$\Delta_j = \frac{1}{3}\left\langle P_2^2(\cos\theta)\cos 2\phi\right\rangle_{f_j} = \left\langle a_x^2\right\rangle_{f_j} - \left\langle a_y^2\right\rangle_{f_j}, \qquad (4.19)$$

where a_s is the projection of the particle orientation vector onto the s axis of the reference frame. The order parameter S_j describes the orientational ordering of the rods and plates with respect to the z axis whereas Δ_j describes the ordering of the species within the xy plane. For random orientations (isotropic phase) $\langle a_s^2\rangle = 1/3$

(with $s = x, y, z$), so that all order parameters are zero. In case of uniaxial order, the biaxial order parameters Δ_j are zero because there is no preferred direction in the xy plane ($\langle a_x^2 \rangle = \langle a_y^2 \rangle$). In the biaxial nematic phase all order parameters will generally be nonzero.

When $0 < S_j \leq 1$, the particle orientation vectors of component j are preferentially oriented along the z axis (polar alignment) whereas a negative value ($-0.5 \leq S_j < 0$) indicates that the particles lie preferentially in the xy plane (planar alignment). In the actual calculations we used two types of reference frames; a rod (N^+) reference frame in which the rods point along the z axis and the platelets' normal vectors lie in the xy plane and, secondly, a plate (N^-) reference frame in which the z axis is oriented along the preferred direction of the plates' normal vector in a discotic phase, while the rod vectors are oriented in the xy plane. Since the N^+ phase is characterized by polar alignment of the rods and planar alignment of the platelets we must have $S_R > 0$ and $S_P < 0$ (within the rod reference frame). In the N^- phase, the situation is reversed so that $S_P > 0$ and $S_R < 0$ (within the plate reference frame).

4.5. Bifurcation analysis

4.5.1. Isotropic-uniaxial nematic bifurcation

The isotropic ODF $f_j \equiv 1/4\pi$ is a trivial solution to Eq. (4.8) for any concentration and mole fraction. At higher concentrations however, the forms of the equilibrium ODFs will contain orientation dependent contributions indicating anisotropic phase solutions. These solutions will continuously split off from the isotropic branch at the $I - N$ bifurcation point. To find this point, we may assume that the nematic order is vanishingly small close to the $I - N$ bifurcation. Retaining only the first Legendre polynomial in Eqs. (4.9) and (4.12) and linearizing with respect to the coefficient $\alpha_2^{(j)}$ gives

$$f_j(\theta) = \frac{1}{4\pi} \left[1 + \alpha_2^{(j)} P_2(\cos\theta) \right], \qquad j = 1, 2. \tag{4.20}$$

Substituting this into the consistency equations Eq. (4.15) yields $\langle P_2 \rangle_{f_j} \equiv S_j = \alpha_2^{(j)}/5$. Consequently, the coefficients (Eq. (4.13)) for the uniaxial nematic phases read

$$\alpha_2^{(1)} = \frac{c}{4} \left[(1-x)\alpha_2^{(1)} - 2xq_{12}\alpha_2^{(2)} \right],$$

$$\alpha_2^{(2)} = \frac{c}{4} \left[-2(1-x)q_{12}\alpha_2^{(1)} + xq_{22}\alpha_2^{(2)} \right]. \tag{4.21}$$

These equations give (for a given mole fraction x) the bifurcation concentration as the root of the characteristic equation $\det \mathbf{M} = 0$ where

$$\mathbf{M} = \begin{pmatrix} 1 - \frac{c}{4}(1-x) & \frac{c}{2}xq_{12} \\ \frac{c}{2}(1-x)q_{12} & 1 - \frac{c}{4}xq_{22} \end{pmatrix}. \tag{4.22}$$

The characteristic equation thus reads

$$1 - \frac{c}{4}\left[(1-x) + xq_{22} \right] + \left(\frac{c}{4} \right)^2 \left[x(1-x)(q_{22} - 4q_{12}^2) \right] = 0. \tag{4.23}$$

The concentration at which a bifurcation from the isotropic to a uniaxial nematic phase can be expected is given by the lowest positive solution of Eq. (4.23).

4.5.2. Uniaxial-biaxial nematic bifurcation

The same analysis described above can be adopted to locate the onset of biaxial order from a uniaxial reference phase. Assuming the lowest order of biaxiality ($m = 1$) in Eq. (4.12) and linearizing with respect to $\beta_2^{2\,(j)}$ we may write the biaxial solution close to the $N - B$ bifurcation point as follows

$$
\begin{aligned}
f_j(\Omega) =& Z_j^{-1} \exp\left[\sum_{n=1}^{\infty} \alpha_{2n}^{(j)} P_{2n}(\cos\theta)\right]\left[1 + \sum_{n=1}^{\infty} k_{n1}\beta_{2n}^{2\,(j)} P_{2n}^2(\cos\theta)\cos 2\phi\right], \\
=& f_j^{\mathrm{N}}(\theta)\left[1 + \sum_{n=1}^{\infty} k_{n1}\beta_{2n}^{2\,(j)} P_{2n}^2(\cos\theta)\cos 2\phi\right],
\end{aligned}
\tag{4.24}
$$

where $f_j^{\mathrm{N}}(\theta)$ is the ODF of the uniaxial reference phase. Inserting Eq. (4.24) into Eq. (4.16) yields

$$
\left\langle P_{2n}^2 \cos 2\phi \right\rangle_{f_j} = \sum_{k=1}^{\infty} \beta_{2k}^2 W_{nk}^{(j)},
\tag{4.25}
$$

with

$$
\begin{aligned}
W_{nk}^{(j)} =& \frac{(2k-2)!}{(2k+2)!}\left\langle P_{2n}^2(\cos\theta)P_{2k}^2(\cos\theta)\right\rangle_{f_j^{\mathrm{N}}(\theta)}, \\
=& \frac{(2k-2)!}{(2k+2)!}\int_0^1 P_{2n}^2(\cos\theta)P_{2k}^2(\cos\theta)f_j^{\mathrm{N}}(\theta)d(\cos\theta).
\end{aligned}
\tag{4.26}
$$

Inserting Eq. (4.25) into the biaxial coefficients Eq. (4.14) then leads to the following linear set

$$
\begin{aligned}
\beta_{2n}^{2\,(1)} =& c\sum_{k=1}^{N}\left[-\frac{8}{\pi}(1-x)d_{2n}W_{nk}^{(1)}\right]\beta_{2k}^{2\,(1)} - c\sum_{k=1}^{N}\left[4xq_{12}c_{2n}W_{nk}^{(2)}\right]\beta_{2k}^{2\,(2)}, \\
\beta_{2n}^{2\,(2)} =& c\sum_{k=1}^{N}\left[-4(1-x)q_{12}c_{2n}W_{nk}^{(1)}\right]\beta_{2k}^{2\,(1)} - c\sum_{k=1}^{N}\left[\frac{8}{\pi}xq_{22}d_{2n}W_{nk}^{(2)}\right]\beta_{2k}^{2\,(2)}.
\end{aligned}
\tag{4.27}
$$

When we truncate the series after the N-th term, the characteristic determinant $\mathbf{M}$ for this set is a $2N \times 2N$ matrix. It is convenient to rewrite the matrix $\mathbf{M}$ in the form $\mathbf{I} - c\mathbf{A}$, where $\mathbf{I}$ is the unit matrix and $\mathbf{A}$ is a numerical matrix. The characteristic equation is then given by

$$
\det\mathbf{M} = \det\left[\mathbf{I} - c\mathbf{A}\right] = \det\left[\mathbf{A} - c^{-1}\mathbf{I}\right] = 0.
\tag{4.28}
$$

The bifurcation concentration is found by numerically determining the eigenvalues of the matrix $\mathbf{A}$. The concentration at which a bifurcation from a uniaxial to a biaxial symmetry can be expected is given by the inverse of the highest real and positive eigenvalue of $\mathbf{A}$. Since the parameters $W_{nk}^{(j)}$ in $\mathbf{A}$ are dependent on the concentration through the ODFs of the uniaxial nematic reference phase, the bifurcation points must be calculated self-consistently. The technique is to compute $W_{nk}^{(j)}$ (Eq. (4.25)) for a
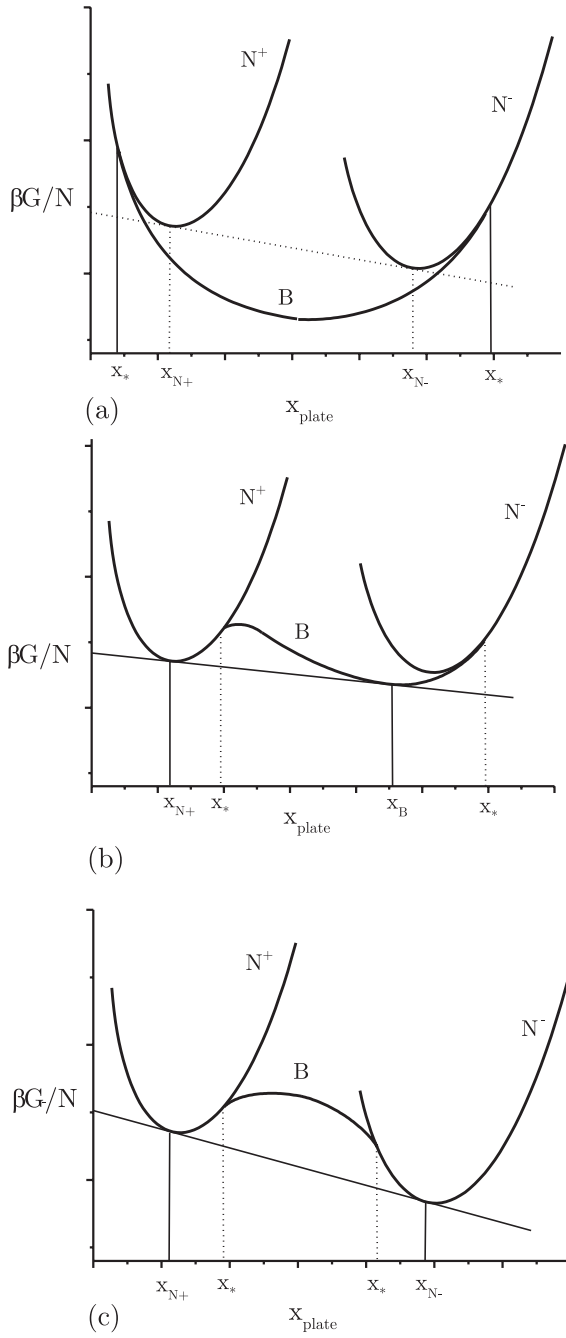
FIGURE 4.1. Schematic illustration of the common tangent construction to determine phase coexistence in a binary rod-plate mixture. (a) Stable biaxial nematic phase, the $N^+ - N^-$ equilibrium is metastable (dotted lines). (b) Uniaxial-biaxial $(N^+ - B)$ demixing. (c) Uniaxial-uniaxial $(N^+ - N^-)$ demixing. The biaxial nematic phase is metastable. The uniaxial-biaxial bifurcation points are indicated by x_*, all others denote binodal points. Stable phase points are indicated by solid lines, metastable ones by dotted lines.

given initial concentration (using either the series expansion method or a numerical grid, see Sec. 4.3) and then put it into the bifurcation equation Eq. (4.28) and find the desired root. For that concentration, new parameters $W_{nk}^{(j)}$ were calculated and inserted into Eq. (4.28) to find the new root. This procedure was repeated until the concentration had converged to within 10^{-6}.

4.6. Biaxiality and demixing

As already mentioned in the Introduction, the central issue in this Chapter is to assess the stability of the biaxial nematic phase in relation to the mixture's asymmetry. It is important to realize that the biaxial nematic phase may be metastable with respect to some demixing transition, e.g. a phase separation into two uniaxial nematic phases (N^+ and N^-). In this respect, it is instructive to consider the Gibbs free energy, defined as

$$\frac{\beta G}{N} = \frac{\beta F}{N} + c^{-1}\left(b\beta\Pi\right). \tag{4.29}$$

By plotting the Gibbs free energy as a function of the mole fraction at a constant osmotic pressure, all stable and metastable phase equilibria can be inferred graphically from the free energy by performing common tangent constructions. In our approach however we merely focus on the location of the binodal and bifurcation points rather than explicitly calculating the Gibbs free energy. In Fig. 4.1, we show that all information concerning the (meta)stability of the nematic phases can be obtained from the relative location of these points. In Fig. 4.1, we have sketched three scenarios. A close inspection reveals that the biaxial phase can only be stable when both uniaxial binodal points are located *in between* the uniaxial-biaxial bifurcation points (Fig. 4.1(a)). In the opposite case (Fig. 4.1(c)), the biaxial nematic phase is metastable with respect to demixing into the uniaxial nematic phases. In Fig. 4.1(b), we have depicted a possible transitional scenario in which one bifurcation point (from the N^- phase) is located "outside" the uniaxial binodal points (as in Fig. 4.1(a)) while the other one lies in between. Clearly, this scenario must give rise to a stable first order uniaxial-biaxial transition ($N^+ - B$ in this case). We will meet this scenario in our actual calculations, but it should be mentioned that other transitional scenarios are also conceivable, depending on the exact curvature of the biaxial branch. In particular, one can think of a biaxial-biaxial demixing scenario which may occur when the B-branch in Fig. 4.1(a) displays a local maximum. However, since we choose not to calculate the Gibbs free energy of the biaxial nematic phase, the exact shape of the biaxial branch remains largely unknown. This means that we cannot completely exclude other scenarios than the ones depicted in Fig. 4.1 to occur in our systems.

4.7. Phase Diagrams

As mentioned in Sec. 4.2, the input for our phase diagram calculations are the rod-plate isotropic excluded volume ratios, q_{12} and q_{22}, given by Eq. (4.3). To facilitate comparisons with the systems studied in the previous Chapter, we assume that the rods and plates have equal thickness, so that $L_P = D_R$. It is now convenient to rewrite Eq. (4.3) in terms of the particles' *aspect ratios* for rods $(L/D)_R$ and plates $(D/L)_P$

$$q_{12} = \frac{1}{4}\left(\frac{D}{L}\right)_P^2 \Big/ \left(\frac{L}{D}\right)_R, \qquad q_{22} = \frac{\pi}{4}\left(\frac{D}{L}\right)_P^3 \Big/ \left(\frac{L}{D}\right)_R^2. \tag{4.30}$$

Henceforth, we fix the aspect ratio of the rods at $(L/D)_R = 15$, which value matches the average aspect ratio of the colloidal rods used in experiment [73]. This means that we use the aspect ratio of the plates to tune the asymmetry of the mixture. Consequently, from Eq. (4.30) we see that the mixture is symmetric ($q_{22} = 1$) if $(D/L)_P = (900/\pi)^{1/3} \approx 6.59$. Increasing the platelets' aspect ratio from this value will make the mixture more and more asymmetric. When $(D/L)_P = 15$ we reach the case of the strongly asymmetric mixture studied experimentally in [73] and theoretically in Chapter 3.

4.7.1. Scenario I: stable biaxial nematic phase; bicritical point

In Fig. 4.2 we show the phase diagram for the case $(D/L)_P = 7$ which is slightly above the symmetric value. We have also constructed a volume fraction representation in Fig. 4.2(b). The topology of the $\Pi - x$ diagram is very similar to the symmetric case [84]: upon compressing the system from the isotropic phase, a first order transition takes place into a uniaxial phase with the symmetry of the majority component (the rod-rich N^+ phase or the plate-rich N^- phase). At higher pressures, continuous (second order) transitions from the uniaxial to the biaxial phase occur. Note that the uniaxial demixing binodals, also indicated in Fig. 4.2, are metastable because they lie "inside" the area marked out by the bifurcation lines. There is a special point, called a bicritical (or Landau) point where a second order transition occurs from the isotropic to the biaxial phase. In addition, the uniaxial phase boundaries come together in a sharp cusp at this point implying that all uniaxial order parameters must go to zero there (Fig. 4.3). Due to the asymmetry, the bicritical point is now located at lower mole fractions ($x = 0.41$) compared to the symmetric case ($x = 0.5$) whereas the minimum in the osmotic pressure has shifted to higher mole fractions ($x = 0.66$). This minimum now constitutes an azeotropic point marking equal mole fractions of the coexisting phases.

4.7.2. Scenario II: stable biaxial nematic phase; isotropic-biaxial equilibria

Increasing the asymmetry of the mixture leads eventually to a qualitatively different topology, as we see in Fig. 4.4. In this scenario, the bicritical point has disappeared which means that all transitions from the isotropic to the nematic phases have become first order. In particular, we can identify an intermediate two-phase region in which the isotropic phase coexists with the biaxial phase. The isotropic-biaxial nematic equilibria were calculated using the direct numerical solution approach, outlined in Sec. 4.3.2. In order to obtain reasonable quantitative results for the biaxial nematic phase, while minimizing the computational burden we used a limited grid-size $J_\theta = J_\phi = 40$. To illustrate the evolution of the nematic structures along the isotropic-nematic equilibria, we have plotted the order parameters in Fig. 4.5.

The biaxial order parameters rise from zero without a jump indicating that the symmetry of the coexisting nematic phase changes continuously from (rod-rich) uniaxial to biaxial back to (plate-rich) uniaxial as the mole fraction of plates is increased. The discontinuous jump around $x^I_{\text{plate}} = 0.075$ is artificial due to the fact that we used different reference frames in the actual calculations. The phase lines were calculated

(a)   (b)
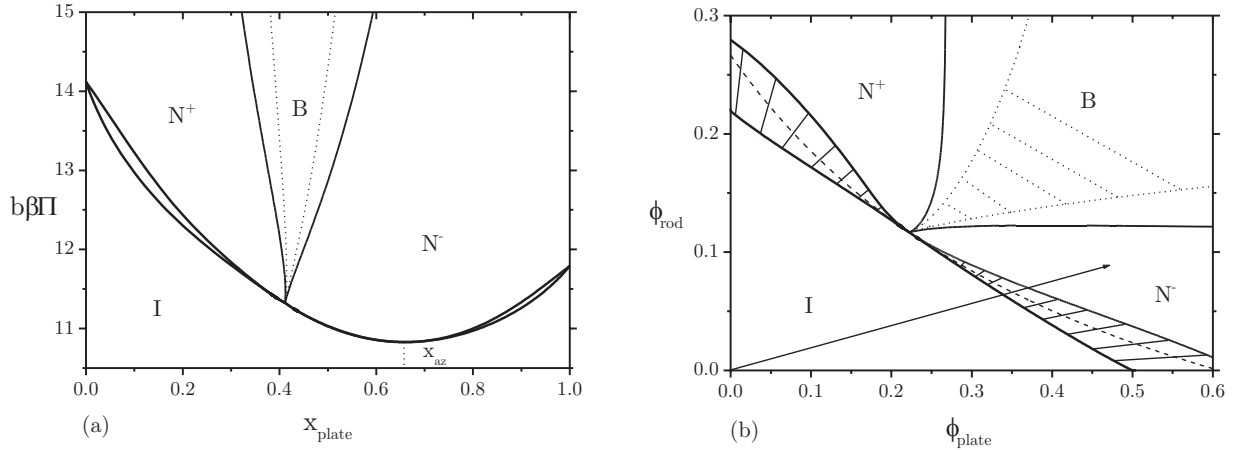
FIGURE 4.2. Scenario I: (a) Phase diagram in the pressure-composition plane for a slightly asymmetric mixture $[(D/L)_P = 7]$. Thick solid lines indicate stable phase transitions. The dotted lines represent metastable $N^+ - N^-$ binodals. An azeotropic point is present at $x_{az} = 0.66$. (b) Same diagram in the volume fraction representation. Coexisting phases are connected by tilted tie lines. The dashed line represents the $I - N$ bifurcation curve. The dilution line drawn corresponds to the azeotropic mole fraction.
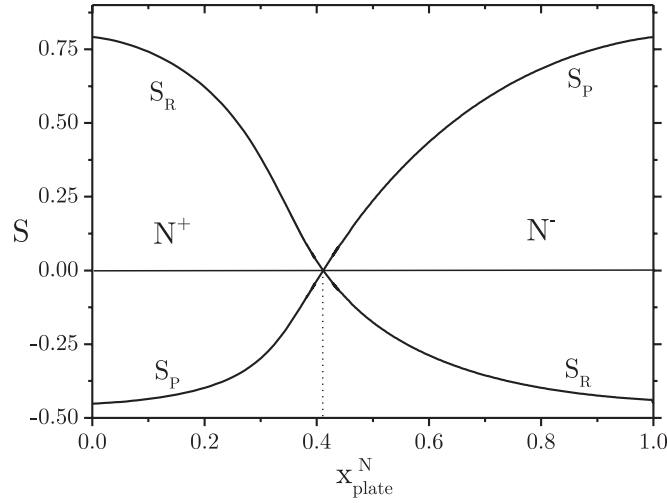
FIGURE 4.3. Scenario I: Evolution of the uniaxial order parameters S at $I - N$ coexistence as a function of x_{plate} in the nematic phase for the case $(D/L)_P = 7$. A critical point is located at $x_{plate} = 0.41$.

starting from either a pure system of rods ($x = 0$) using the rod reference frame or a pure system of platelets adopting the plate reference frame. Note that the artificial switching from one reference frame to the other only affects the order parameters. Of course, it does not influence the thermodynamic properties of the nematic phases, as we see from the biaxial binodal in Fig. 4.4 which does not show a discontinuity.

In Fig. 4.6, we present a detailed picture of all phase lines involved for the case $(D/L)_P = 9.5$. From this graph we clearly see that the uniaxial demixing is metastable
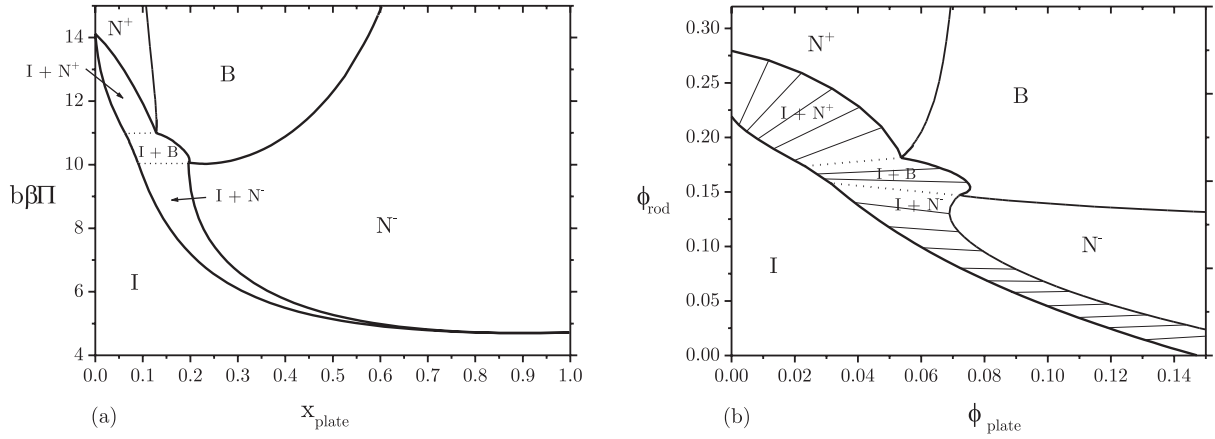
FIGURE 4.4. Scenario II: (a) Phase diagram in the pressure-composition plane for the case $(D/L)_P = 9.5$. The dotted lines mark the osmotic pressures where the nematic symmetry of the isotropic-nematic equilibria changes continuously from uniaxial to biaxial. (b) Same diagram in the volume fraction representation. Coexisting phases are connected by tilted tie lines.
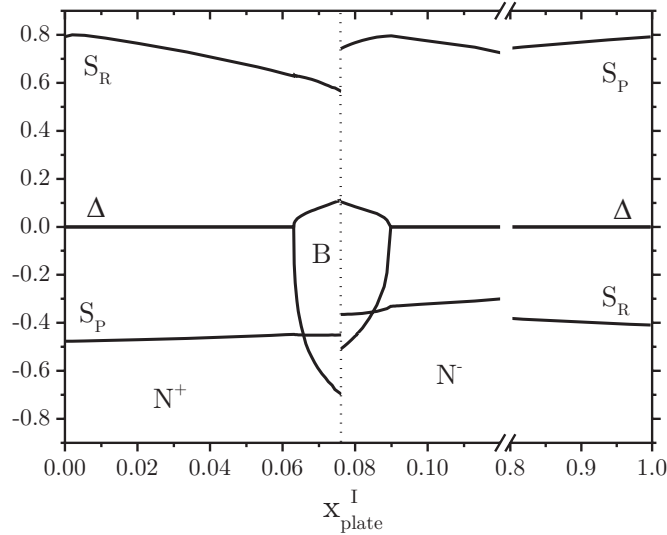
FIGURE 4.5. Scenario II: Evolution of the uniaxial (S) and biaxial (Δ) order parameters at isotropic-nematic coexistence as a function of x_{plate} in the isotropic phase for the case $(D/L)_P = 9.5$.

with respect to the biaxial nematic phase (the $N^+ - N^-$- binodals run in between the bifurcation lines). The absence of a bicritical point can also be inferred from this graph; the uniaxial binodals no longer meet the bifurcation lines in a single (bicritical) point, located on the $I - N$ bifurcation line, but merge into an azeotropic end point instead. Note that at this point the mole fractions of the uniaxial nematic phases are the same but the concentrations are not. Furthermore, the uniaxial order parameters are also nonzero at this point. Clearly, there must be a critical value for $(D/L)_P$ at which the bicritical point disappears by splitting into a critical point (where the $N - B$ bifurcation
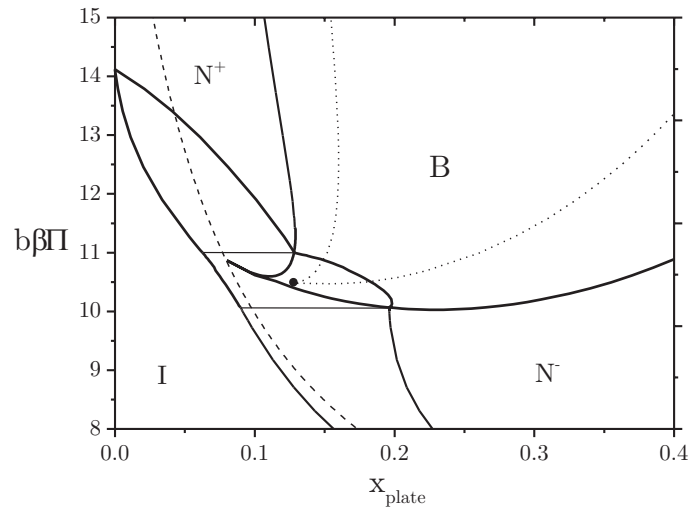
FIGURE 4.6. Detailed picture of the phase lines for the case $(D/L)_P = 9.5$. Dotted lines represent metastable $N^+ - N^-$ binodals, the dashed curve is the $I - N$ bifurcation curve. Note that the $N - B$ bifurcation curves coincide in a metastable critical point (on the $I - N$ bifurcation curve) whereas the $N^+ - N^-$ binodals meet in an azeotropic end point indicated by the black dot.
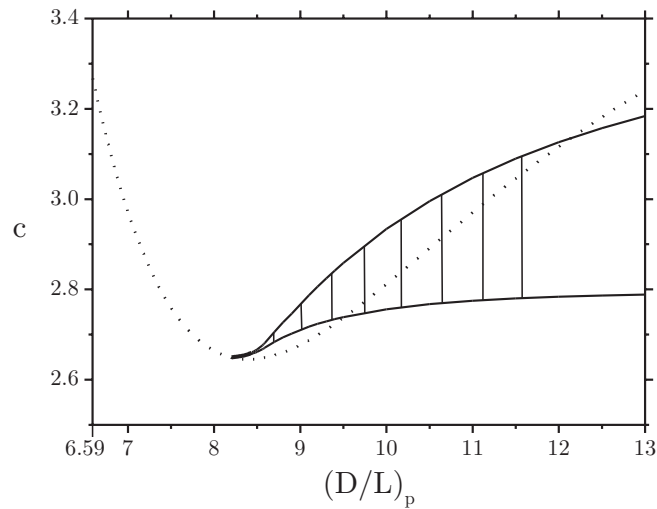
FIGURE 4.7. Location of the biaxial critical point (dotted line) and the concentrations of the coexisting uniaxial phases of the azeotropic end point (solid lines), connected by vertical tie lines, versus $(D/L)_P$. At $(D/L)_P \lesssim 8$ all lines collapse onto a single curve, describing the location of the bicritical point.

lines meet) and a corresponding azeotropic end point (where the uniaxial binodals meet) which simultaneously detaches from the isotropic-uniaxial nematic bifurcation line. In Fig. 4.7, we have plotted the location of these points as a function of the mixture's asymmetry. The location of the biaxial critical point can easily be determined algebraically by combining the $I - N$ and $N - B$ bifurcation equations assuming the lowest degree of nematic order of the uniaxial reference phase (Appendix). We observe
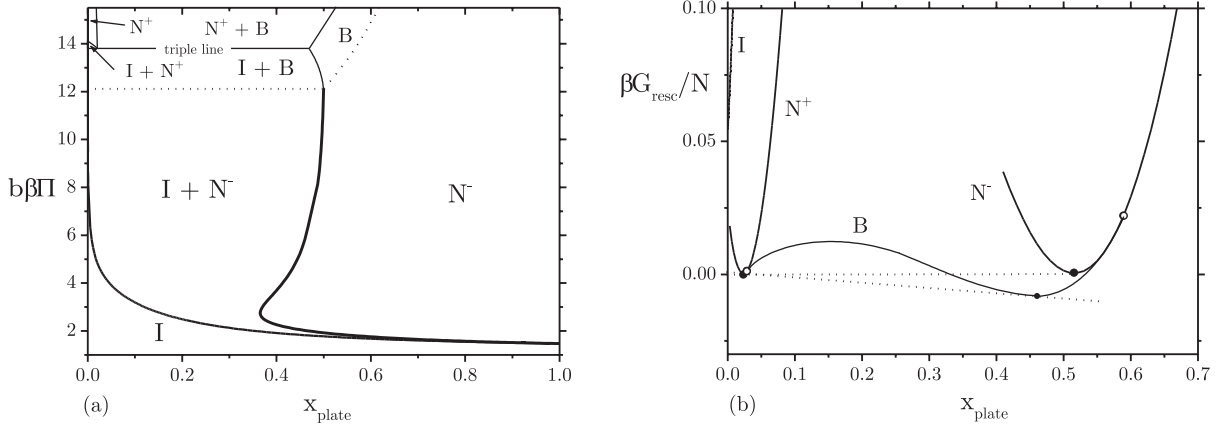
FIGURE 4.8. Scenario III: (a) Phase diagram in the pressure-composition plane for $(D/L)_P = 14$. Thick solid lines indicate stable phase boundaries. The $N^- - B$ bifurcation curve is indicated by the dotted line. The curves above the dotted ones are *sketched* (not calculated) outlining the qualitative phase behaviour at high densities. (b) Rescaled Gibbs free energy versus x_{plate} for the same mixture at constant pressure $b\beta\Pi = 14.5$. Binodal and bifurcation points are indicated by black and white dots, respectively. The curvature of the biaxial branch is given qualitatively by the sketched curve. A uniaxial-biaxial $(N^+ - B)$ demixing is evident.

that the concentrations corresponding to the azeotropic end point collapse onto the curve describing the biaxial critical point at some critical value $(D/L)_P \approx 8$ which means that the biaxial critical point and the azeotropic end point have merged into a bicritical point. We may therefore expect a change of scenario from I to II when the aspect ratio of the platelets exceeds 8.

4.7.3. Scenario III: uniaxial-biaxial demixing

When the asymmetry is enhanced even further, the phase behaviour of the rod-plate mixture changes dramatically. In Fig. 4.8, we have depicted the scenario for $(D/L)_P = 14$, which is close to the experimentally accessible case $((D/L)_P = (L/D)_R = 15)$ considered in Chapter 3. An essential difference with the previous scenario is that a nematic-nematic demixing occurs around $b\beta\Pi = 14$ at which a rod-dominated uniaxial nematic N^+ phase coexists with a biaxial phase roughly containing equal portions of each species. Furthermore, there is an associated triple point at which both N^+ and B coexist with an isotropic phase I. Upon compressing the system at higher mole fractions $(x > 0.5)$ a continuous transition occurs from the plate-dominated N^- phase to the biaxial phase which subsequently demixes by splitting off a fraction of the N^+ phase. Furthermore, a re-entrant phenomenon is present around $x = 0.4$ where the mixture displays a rich sequence of phases upon compression. To reduce the computational costs, we have not explicitly calculated the isotropic-biaxial equilibria for this case but merely sketched the qualitative topology of the phase diagram at higher pressures. The justification for the demixing scenario lies in the location of the uniaxial binodals

relative to the $N - B$ bifurcation lines. In Fig. 4.8(b) we have displayed the Gibbs free
energy at a particular osmotic pressure, in which the binodal and bifurcation points
are depicted explicitly. For the sake of clarity, we have rescaled the Gibbs free energy
by subtracting the linear common tangent to the uniaxial branches. We see that the
$N^+ - B$ bifurcation point now has shifted to the right of the N^+ binodal point whereas
the $N^- - B$ bifurcation is still located "outside" the N^- binodal point. As already
alluded to in Sec. 4.6, the only plausible scenario for this case is a demixing into N^+
and B, as indicated by the sketched biaxial branch in Fig. 4.8(b). Note that the shape
of this branch also suggests that the stable binodal point for B is located at slightly
lower mole fractions than the metastable one for N^-.

To limit computational effort, we have not attempted to find the specific aspect
ratio at which the $N^+ - B$ demixing first occurs and a change of scenario from type
II to III will take place. Obviously, from the results presented thus far, we know
that the transition must be somewhere in the range $10 < (D/L)_{\mathrm{P}} < 14$, which is an
experimentally accessible range.

4.7.4. Scenario IV: uniaxial-uniaxial demixing

Scenario III is not consistent with our previous calculations based upon the Gaussian
trial function approach. In particular, the surmised demixing transition into uniaxial
nematic phases, as observed experimentally and reproduced theoretic ally in Chapter
3 for strongly asymmetric rod-plate mixtures is not found in our numerical analysis of
the Euler-Lagrange equations. Instead, we observe a demixing into a rod-rich uniaxial
nematic phase and a biaxial nematic phase (containing approximately 50 % platelets)
for a mixture of rods and plates with aspect ratios around 15. The question now arises
whether or not a demixing into the uniaxial nematic phases (scenario IV) is recovered
when the aspect ratio of the platelets is increased beyond 15. Considering Fig. 4.8(b),
one can imagine that, upon increasing $(D/L)_{\mathrm{P}}$, the asymmetry may force the $N^- - B$
bifurcation point to shift in between the uniaxial binodal points such that the biaxial
nematic phase becomes completely metastable with respect to a $N^+ - N^-$ demixing,
according to Fig. 4.1(c). To verify this possibility we have calculated the location of
these points at a fixed osmotic pressure, namely the $I - N$ coexistence pressure for the
pure system ($b\beta\Pi = 14.12$) which is slightly above the triple pressure. In Fig. 4.9(a) we
have depicted the evolution of the N^--binodal (corresponding to the $I - N^-$ equilibria)
and the $N^- - B$ bifurcation point as a function of $(D/L)_{\mathrm{P}}$. The intersection point
around $(D/L)_{\mathrm{P}} = 17$ reveals that there must be a scenario IV such that the uniaxial
demixing is indeed recovered, albeit at a plate aspect ratio which is higher than the
one used in Chapter 3. For the sake of completeness, we have depicted the phase
diagram for the case $(D/L)_{\mathrm{P}} = 18$ in Fig. 4.9(b), which calculations were based upon
the Gaussian trial function approach, discussed in the previous Chapter. Note that this
diagram is qualitatively the same as Fig. 3.2 although the N^+ and $I - N^+$ coexistence
regions are hardly visible here due to the extremely low mole fractions of the coexisting
I and N^+ phases. Comparison with the numerical exact $I - N^-$-binodals shows that
the Gaussian approximation provides increasingly better quantitative results at high
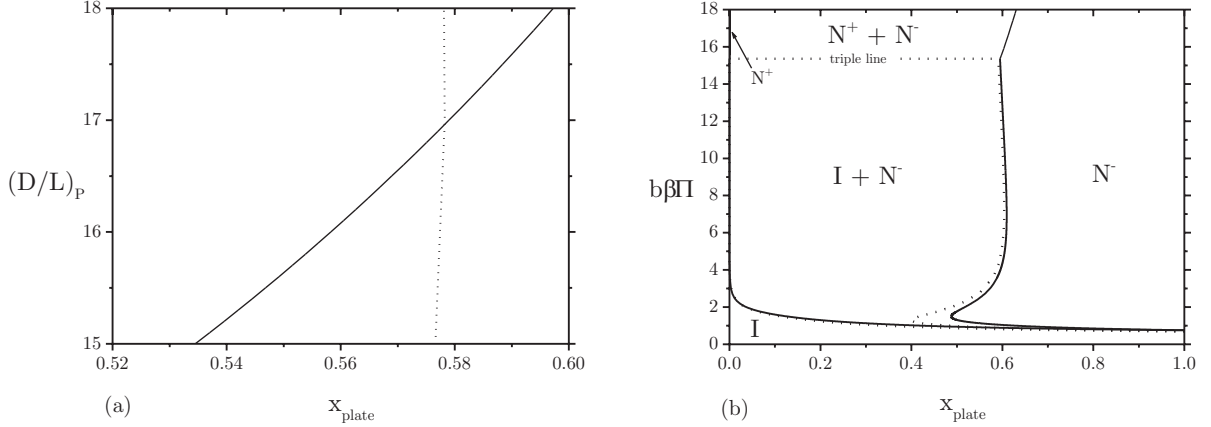
FIGURE 4.9. (a) Position of the N^- binodal point in terms of x_{plate} (solid) relative to the $N^- - B$ bifurcation point (dotted) at constant pressure $b\beta\Pi = 14.12$ as a function of $(D/L)_{\text{P}}$. Beyond the intersection (around $(D/L)_{\text{P}} = 17$) the biaxial nematic phase becomes metastable. (b) Scenario IV: Phase diagram in the pressure-composition plane for $(D/L)_{\text{P}} = 18$ calculated using Gaussian trials ODFs. The $I - N^+ - N^-$ triple line is represented by the horizontal dotted line. The numerically exact $I - N^-$-binodals are indicated by the dotted curves.

compressions where the alignment of the particles (in both polar and planar direction) is particularly strong. Deviations occur at lower osmotic pressure, in particular around $b\beta\Pi = 2$, showing that the re-entrant phenomenon is underestimated somewhat by the Gaussian approximation.

4.8. SUMMARY AND DISCUSSION

We have investigated the role of the rod-plate excluded volume ratio $(v_{\text{ex}}^{\text{PP}}/v_{\text{ex}}^{\text{RR}})$ in the phase behaviour of asymmetric mixtures of cylindrical rods and platelets (for which $v_{\text{ex}}^{\text{PP}} > v_{\text{ex}}^{\text{RR}}$). The phase diagrams were calculated from an exact numerical analysis of the Euler-Lagrange equations, obtained from formally minimizing the free energy, such that no simplifications were made *a priori* with respect to the ODF. Our particular interest was focussed on the stability of the biaxial nematic phase in relation to the mixture's asymmetry. Starting from the symmetric case we enhanced the asymmetry of the mixture by varying the platelet aspect ratio in the range $7 < (D/L)_{\text{P}} < 18$ while keeping the rod aspect ratio fixed at 15. Considering the role of the biaxial nematic phase in the overall topology of the phase diagram, we were able to distinguish four scenarios.

Upon increasing the plate aspect ratio from its symmetric value $((D/L)_{\text{P}} = 6.59)$ we observe that the characteristic bicritical point is retained initially (scenario I) but disappears around $(D/L)_{\text{P}} = 8$ and is replaced by a two-phase region marking first order transitions from the isotropic to the biaxial nematic phase (scenario II). At higher asymmetries (around $(D/L)_{\text{P}} = 15$) we found a uniaxial-biaxial $(N^+ - B)$ demixing

transition with an associated $I - N^+ - B$ triple equilibrium (scenario III). Increasing the aspect ratio beyond 17 gives a uniaxial-uniaxial $(N^+ - N^-)$ demixing with an associated $I - N^+ - N^-$ triple point (scenario IV). This indicates that the biaxial nematic phase may become completely metastable in highly asymmetric mixtures. To limit the computational burden, we have not explicitly calculated the isotropic-biaxial $(I - B)$ and uniaxial-biaxial $(N^+ - B)$ equilibria for scenario III. Therefore, it should be noted that due to the incertainty in the thermodynamic properties of the biaxial phase, other scenarios than the ones presented in this Chapter cannot be completely ruled out. Nevertheless, we believe that our scenarios are sufficiently plausible.

As mentioned several times before, there is experimental evidence of the uniaxial-uniaxial demixing transition (scenario IV) to occur in mixtures of colloidal rods and platelets, albeit at a slightly lower plate aspect ratio (of roughly 15). However, no detailed structure investigation on the nematic phases has been performed in [73] so that there are no conclusive results available as to whether the demixed nematic phases are really uniaxial or possibly have some degree of biaxiality. Therefore, considering our present theoretical predictions, it would be intriguing to verify the possibility of a uniaxial-biaxial demixing scenario to occur in these experimental systems. Of course, this would require a thorough reexamination of the experimental systems focussing on the optical properties of the nematic textures (particularly, for the plate-dominated nematic phase). Furthermore, our results also suggest that the formation of a biaxial nematic phase can be promoted experimentally by decreasing the diameter of the colloidal platelike colloids, thereby reducing the mixture's asymmetry. Finally, we remark that the effect of polydispersity and the influence of multi-particle correlations (both are not incorporated here) may give rise to qualitatively different scenarios from the ones predicted by our calculations.

In particular, one may question to what extent the stability of the biaxial nematic phase is affected by higher order terms in the virial expansion of the free energy. Recent calculations by Varga *et al.* [88], based upon a similar approach as ours, indicate that the stability of the biaxial nematic symmetry depends quite sensitively on the implementation of Parsons' approach and on the incorporation of higher order contributions to the rod-plate excluded volumes in Eq. (3.5) (which correct for the particles' finite thicknesses). However, we believe that resolving this issue in an appropriate way requires a systematic direct inclusion of many-body excluded volume terms into the free energy, rather than indirectly accounting for these via a rescaling of the two-particle excluded volumes. Since it is next to impossible to carry this out in a theoretical study, we consider it to be a future challenge for computer simulators and experimentalists to verify what is really happening in these mixtures.

APPENDIX: CALCULATION OF THE BIAXIAL CRITICAL POINT

Fig. 4.6 shows that the $N - B$ bifurcation curves emanate from the $I - N$ bifurcation curve at a critical point where the order parameters are necessarily zero. To calculate this point for a given asymmetry, we may perform a $N - B$ bifurcation analysis starting

from a weakly ordered uniaxial phase. Assuming the lowest degree of nematic order in the uniaxial reference phase, we may approximate the uniaxial ODFs by Eq. (4.20). Substitution into Eq. (4.26) yields for the coefficients $W_{11}^{(j)}$

$$
\begin{aligned}
W_{11}^{(j)} &= \frac{1}{4!} \int_0^1 \left[P_2^2(t) \right]^2 \left(1 + \alpha_2^{(j)} P_2(t) \right) dt, \quad (t = \cos\theta) , \\
&= \frac{1}{5} - \frac{2}{7} S_j ,
\end{aligned} \tag{4.31}
$$

in terms of the uniaxial order parameters $S_j = \alpha_2^{(j)}/5$. Using this together with $d_2 = -5\pi/32$ and $c_2 = 5/8$ (from Eq. (4.10)) we obtain, from (Eq. 4.27), the following linear set

$$
\begin{aligned}
\beta_2^{2\,(1)} &= \frac{c}{4}(1-x)\left(1 - \frac{10}{7}S_1\right)\beta_2^{2\,(1)} - \frac{c}{2}xq_{12}\left(1 - \frac{10}{7}S_2\right)\beta_2^{2\,(2)}, \\
\beta_2^{2\,(2)} &= -\frac{c}{2}(1-x)q_{12}\left(1 - \frac{10}{7}S_1\right)\beta_2^{2\,(1)} + \frac{c}{4}xq_{22}\left(1 - \frac{10}{7}S_2\right)\beta_2^{2\,(2)}.
\end{aligned} \tag{4.32}
$$

Setting $S_j = 0$ in Eq. (4.32) leads to the characteristic equation for the $I - N$ bifurcations Eq. (4.23) implying that the isotropic-biaxial bifurcation concentrations are *the same* as the isotropic-uniaxial bifurcation densities, for *any* mole fraction [79].

Since the bicritical point must be a solution of Eq. (4.23) we may subtract it from the characteristic equation corresponding to Eq. (4.32) to get the following equation

$$
0 = (1-x)S_1 + xq_{22}S_2 + \frac{c}{4}x(1-x)(4q_{12}^2 - q_{22})\left[S_1 + S_2 - \frac{10}{7}S_1 S_2\right]. \tag{4.33}
$$

Ignoring the $\mathcal{O}(S^2)$ term and eliminating S_j using the relation

$$
S_2 = S_1 \frac{\left[\frac{c}{2}(1-x) - 2\right]}{cxq_{12}}, \tag{4.34}
$$

from Eq. (4.21), we obtain

$$
0 = q_{22}x + \frac{c}{4}x(1-x)\left[4q_{12}^2 - 2(q_{12} + q_{22})\right] - \left(\frac{c}{4}\right)^2 x(1-x)\left[4q_{12}^2 - q_{22}\right]\left[2xq_{12} + (1-x)\right]. \tag{4.35}
$$

Solving this equation together with the $I - N$ bifurcation equation Eq. (4.23) uniquely determines the biaxial critical point (in terms of x and c) for any given set of parameters q_{jk}. The solutions for the symmetric case, discussed in [80], can be recovered by substituting $x = 1/2$ and $q_{22} = 1$ in Eq. (4.35) to obtain $c = 8/(2q_{12}+1)$ and $S_1 = -S_2$.

5

Demixing in binary mixtures of anisometric particles

ABSTRACT

In this Chapter we summarize the isotropic and nematic phase behaviour in binary mixtures of hard rods or plates with different lengths or diameters within the framework of the Onsager theory. On the basis of Gaussian trial functions the relative importance of different entropic contributions in the demixing of the isotropic and nematic phases is explained for various mixtures. The implications of Parsons' method are discussed in more detail and new results are given for mixtures of plates differing only in diameter or thickness.

5.1. INTRODUCTION

Mixing anisometric particles with different sizes or shapes gives rise to an entropy of mixing in addition to the common orientational and packing contributions. The subtle interplay of the three entropic contributions may give rise to a rich phase behaviour. Generalizations of Onsager's theory to binary mixtures have indeed revealed aspects that are not encountered in the monodisperse cases, such as a fractionation effect (redistributing the species among the coexisting phases) and reentrant phenomena [69, 87, 89].

The most important characteristic of these mixtures is the possibility of demixing transitions in both the isotropic and nematic phases. Depending on the concentration and size ratio of the species, a homogeneous isotropic or nematic phase may split into two phases with the same uniaxial symmetry but different densities and compositions. Moreover, the system can display associated triphasic equilibria, involving $I - N - N$ or $I - I - N$ coexistences. The demixing phenomenon was first encountered in nematic phases of rods differing only in length [66]. Later on, similar calculations based upon a generalized Onsager theory [36] revealed that the rod lengths should differ at least by a factor 3.167 in order to have a demixing of the nematic state.

In the last decade, a number of papers have appeared in which several other binary mixtures of hard anisometric colloids were studied within the Onsager treatment, including mixtures of rods or plates differing only in thickness [69, 90], rods differing both in length and thickness [70, 89, 91] and rod-plate mixtures [48, 79, 84, 87]. In this Chapter we summarize existing theoretical work along with new results (mainly for plate-plate mixtures) to present an overview of the isotropic and nematic phase stability in binary mixtures of rod- and platelike species. We shall restrict ourselves to binary mixtures

for which *only one* of the particle dimensions is unequal for both species while the other is common to all particles. In particular, we focus on the possibility of demixing transitions within the homogeneous isotropic and nematic phases and provide a theoretical underpinning for the associated demixing mechanisms.

5.2. Generalized Onsager theory

In this Chapter we present an alternative and concise formulation of the generalized Onsager theory for mixtures within the trial function approximation. A comprehensive derivation can be found in Chapter 1.

To treat a multi-component mixture of hard anisometric particles with total number density ρ and mole fractions x_i of species i, we now start from the following expression for the Helmholtz free energy:

$$\frac{F}{Nk_BT} \simeq \text{cst} + \ln\rho - 1 + \sum_i x_i \ln x_i - \sum_i x_i \frac{\Delta S_{\text{or,i}}}{Nk_B} + \frac{1}{2}\rho\tilde{f}_{\text{CS}}(\phi)\sum_i\sum_j x_ix_j \left\langle\langle v_{\text{excl}}\rangle\right\rangle_{ij}, \quad (5.1)$$

where $\ln\rho - 1$ is the ideal translational entropy and $\sum_i x_i \ln x_i$ the entropy of mixing. The last two terms are the orientational entropy and the (packing) entropy related to the excluded volume. The function $\tilde{f}_{\text{CS}}(\phi) = (1 - \frac{3}{4}\phi)/(1-\phi)^2$, arising from Parsons' method, partially accounts for the effect of higher virial terms. At vanishing volume fractions $\tilde{f}_{\text{CS}}(\phi) \to 1$ which gives back the expression for the second-virial approximation. Triangular brackets indicate (orientational) averages with respect to the distribution of species indicated by the subscript. In the remainder of this Chapter we will often implicitly use Gaussian trial functions [34] to describe the sharply peaked angular distributions of the particles in the nematic state. However, it will suffice to refer to these in terms of the width of the distribution for particle type i, characterized by the *typical* angle $\tilde{\theta}_i = \langle\theta^2\rangle_i^{1/2}$ with the nematic director. For the orientational entropy the isotropic phase is taken as the reference state. To estimate the orientational entropy for the nematic phase just consider the number of orientational states accessible to the particles. In the isotropic phase this is proportional to the surface of the full unit sphere, 4π, whereas in the nematic phase the particles have to remain within the typical angle $\tilde{\theta}_i$ around 0 or π. For small $\tilde{\theta}_i$ these are just two circular surfaces on the unit sphere with each an approximate surface of $\pi\tilde{\theta}_i^2$, as sketched in Fig. 5.1. This leads to the following entropy difference ΔS_{or}

$$\Delta S_{\text{or,i}} \simeq Nk_B\left[\ln(\# \text{ nematic states }) - \ln(\# \text{ isotropic states})\right] \qquad (5.2)$$
$$\simeq Nk_B\left[\ln(2\times\pi\tilde{\theta}_i^2) - \ln(4\pi)\right],$$

$$\frac{\Delta S_{\text{or,i}}}{Nk_B} \sim \ln(\tilde{\theta}_i^2/2) + 1. \qquad (5.3)$$

The term +1 follows from a full calculation within the Gaussian approximation, introduced in Sec. 1.3.1. Note that for the small widths $\tilde{\theta}_i$ of the distributions we shall encounter, $\Delta S_{\text{or,i}}$ is negative, which ought to be the case going from the random isotropic
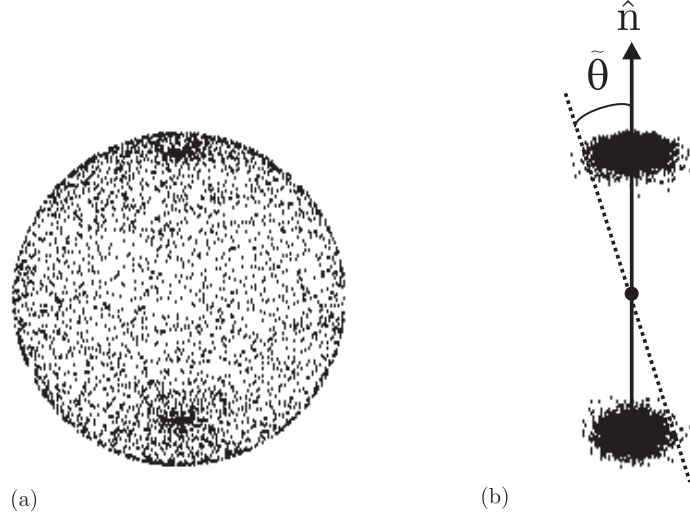
FIGURE 5.1. Impression of the orientation distribution (indicated by dots) on the unit sphere in the isotropic state (a) and the nematic state (b). The typical angle with the nematic director $\hat{\mathbf{n}}$ is indicated by $\tilde{\theta}$.

state to the more ordered nematic state. For two thin particles at mutual angle γ, we may only consider the leading order term for the excluded volume

$$\langle\langle v_{\text{excl}}\rangle\rangle_{ij} \sim \tilde{v}_{ij} \langle\langle \sin\gamma\rangle\rangle_{ij}, \tag{5.4}$$

where $\tilde{v}_{ij} = L_i L_j (D_i + D_j)$ for thin rods while the corresponding expression for platelets reads $\tilde{v}_{ij} = \frac{\pi}{4}D_i D_j (D_i + D_j)$ in terms of the particle lengths L_i and L_j and diameters D_i and D_j. Eq. (5.4) involves a two-particle average of $\sin\gamma$, which is always $\pi/4$ in the isotropic state, whereas in a highly ordered nematic state it is simply related to the typical angular widths of the distributions [34]:

$$\langle\langle \sin\gamma\rangle\rangle_{ij} \sim \langle\langle\gamma\rangle\rangle_{ij} \sim \frac{1}{2}\sqrt{\pi}\,(\tilde{\theta}_i^2 + \tilde{\theta}_j^2)^{1/2}. \tag{5.5}$$

5.2.1. Monodisperse systems

For monodisperse systems all this taken together results in a very simple expression for the Helmholtz free energy in the isotropic state:

$$\frac{F^{\text{iso}}}{Nk_BT} \simeq \text{cst} + \ln\rho - 1 + (\pi/8)\tilde{v}\rho\tilde{f}_{\text{CS}}(\phi) \simeq \text{cst}' + \ln c - 1 + c\tilde{f}_{\text{CS}}(\phi), \tag{5.6}$$

in terms of the dimensionless concentration $c \equiv (\pi/8)\tilde{v}\rho$ related to the volume fraction ϕ via $c = l\phi$ (rods) and $c = (\pi/4)l\phi$ (plates). Here, l is the aspect ratio, defined as the ratio of the largest to the smallest dimension of the particle (i.e. for rods $l = L/D$, plates have $l = D/L$). The corresponding expression for the nematic state is found

using the same ingredients:

$$\frac{F^{\text{nem}}}{Nk_BT} \sim \text{cst}' + \ln c - 1 - \ln(\tilde{\theta}^2/2) - 1 + c\tilde{f}_{\text{CS}}(\phi)\sqrt{\frac{8}{\pi}}\tilde{\theta}, \tag{5.7}$$

but this expression should still be minimized with respect to the unknown parameter $\tilde{\theta}$ giving

$$\tilde{\theta} \sim \sqrt{\frac{\pi}{2}}\frac{1}{c\tilde{f}_{\text{CS}}(\phi)} \propto \frac{1}{l\phi\tilde{f}_{\text{CS}}(\phi)}. \tag{5.8}$$

Here we see that the angular distribution adapts itself such that its width is inversely proportional to the volume fraction and also inversely proportional to l. If we substitute this form back into Eq. (5.7) and also refer to Eq. (5.1) a remarkable phenomenon appears for the interaction term: *the excluded volume contribution per particle,* $\frac{1}{2}\langle\langle v_{\text{excl}}\rangle\rangle\rho$, *in the nematic state equals the constant value of 2 irrespective of concentration.* This behaviour indicates that the narrowing of the distribution Eq. (5.8) exactly compensates the increasing probability of meeting other particles with increasing concentration. The final result for the free energy in the nematic state is now extremely simple:

$$\frac{F^{\text{nem}}}{Nk_BT} \sim \text{cst}' + 3\ln c \ \left[+2\ln\tilde{f}_{\text{CS}}(\phi)\right] + \ln\frac{4}{\pi}. \tag{5.9}$$

Due to the constancy of the excluded volume no linear contribution in c (as was found in Eq. (5.6)) is obtained. Using the thermodynamic relation $\Pi \equiv -(\partial F/\partial V)_{T,N} = k_BT\rho^2(\partial(F/Nk_BT)/\partial\rho)_{T,N}$ then gives 3 times the ideal (Van 't Hoff) osmotic pressure (setting $\tilde{f}_{\text{CS}}(\phi) = 1$ for the time being):

$$\frac{\Pi^{\text{nem}}}{k_BT} \sim 3\rho. \tag{5.10}$$

5.2.2. Multicomponent systems

For a multicomponent system the isotropic free energy is a straightforward extension of Eq. (5.6), while the ingredients for the nematic state substituted in Eq. (5.1) give

$$\frac{F^{\text{nem}}}{Nk_BT} \sim \text{cst} + \ln\rho - 1 + \sum_i x_i\ln x_i - \sum_i x_i\left[\ln(\tilde{\theta}_i^2/2) + 1\right]$$
$$+ \frac{1}{2}\rho\tilde{f}_{\text{CS}}(\phi)\sum_i\sum_j x_ix_j\tilde{v}_{ij}\frac{\sqrt{\pi}}{2}\sqrt{\tilde{\theta}_i^2 + \tilde{\theta}^2}, \tag{5.11}$$

where $\phi = \sum_i \phi_i$ now represents the *total* volume fraction. The set of parameters $\tilde{\theta}_i$ is as yet unknown and has to be determined by simultaneous solution of the following minimization equations:

$$-\frac{2x_i}{\tilde{\theta}_i} + \rho\tilde{f}_{\text{CS}}(\phi)x_i\sum_j x_j\tilde{v}_{ij}\frac{\sqrt{\pi}}{2}\frac{\tilde{\theta}_i}{\sqrt{\tilde{\theta}_i^2 + \tilde{\theta}_j^2}} \sim 0. \tag{5.12}$$

Multiplying this equation by $\tilde{\theta}_i$, summing over i and adding the resulting equation to the one obtained by interchanging i and j gives

$$\frac{1}{2}\rho\tilde{f}_{CS}(\phi)\sum_i\sum_j x_i x_j \tilde{v}_{ij}\frac{\sqrt{\pi}}{2}\sqrt{\tilde{\theta}_i^2+\tilde{\theta}_j^2}\sim 2. \tag{5.13}$$

Comparing this result to Eq. (5.11) we see that it is just the excluded-volume term within the free energy, so that we can state: *the excluded-volume contribution per particle in the nematic state equals the constant value of 2 irrespective of concentration or polydispersity* [92]. Although solving equations Eq. (5.12) for the set $\{\tilde{\theta}_i\}$ is only possible numerically, it can be easily verified that an inverse proportionality to $(\rho\tilde{f}_{CS}(\phi))$ is retained for every $\tilde{\theta}_i$ [93]. Using this information in Eq. (5.11) reveals the following structure for the free energy in the nematic state:

$$\frac{F^{nem}}{Nk_BT}\sim cst + 3\ln\rho\left[+2\ln\tilde{f}_{CS}(\phi)\right]+\mathcal{F}(\{x_i\}), \tag{5.14}$$

where concentration (ρ) and composition ($\{x_i\}$) dependence are in separate terms. The former leads again to the quasi-ideal osmotic pressure Eq. (5.10) (considering that $\tilde{f}_{CS}(\phi) = 1$), completely independent of the composition of the nematic state. The latter also contains a non-trivial contribution originating from the orientational entropy in Eq. (5.11). Consequently the chemical potentials of species i, obtained from $\mu_i = (\partial F/\partial N_i)_{N_{j\neq i},V,T}$ have a non-trivial composition dependence, which may drive phase separations as described later.

In Part II of thesis we show how the isotropic-nematic phase equilibria can be calculated for *polydisperse* systems of anisometric particles. Rather than containing a distinct number of particles types, these systems are characterized by a *continuous* spread in particle length or diameter. As examples we will consider systems of hard rod- and platelike cylinders with polydisperse lengths.

5.3. Gaussian approximation versus formal approach

A formal approach to the minimization of the free energy in the nematic state follows from realizing that there is a *continuous* spread of angles θ_i of particle type i with the director along the interval $0 < \theta_i < \pi$. The orientational averages in the free energy Eq. (5.1) can be rewritten in terms of continuous orientational distribution functions (ODFs). Thermodynamically consistent solutions for these functions are obtained by performing functional differentiations with respect to the ODFs and solving the resulting minimization equations. These equations constitute a coupled set of nonlinear integral equations which can be solved only by applying appropriate numerical techniques [33]. In the Gaussian approximation implicitly used above it is assumed that the ODFs obey a *prescribed* Gaussian form ($\sim \tilde{\theta}_i^{-2}\exp[-\theta_i^2/\tilde{\theta}_i^2]$) and the free energy minimization is then carried out by a simple differentiation with respect to the typical angle $\tilde{\theta}_i$ (See also Sec. 1.3.1.). In this respect, we may recall the inverse proportionality between the typical angle and the Gaussian variational parameter α_i for type i, indicating that small typical angles correspond to large α_i.

Unlike the formal approach, the Gaussian approximation allows us to obtain explicit asymptotic expressions for the orientational and packing entropies in the nematic state, at least for the monodisperse case [5]. Although the Gaussian ODF does not qualify as an exact thermodynamic equilibrium ODF it shows the correct high-density scaling behaviour such that the approximation is expected to be satisfactory for strongly aligned nematic states [94]. As to the binary mixtures to be considered in the following we may intuitively expect the Gaussian approach to work particularly well for mixtures with extreme size ratios where the degree of alignment of both species is usually very strong (due to their size difference).

5.4. Demixing instability

When considering binary mixtures, it is always important to verify the thermodynamic stability of the isotropic and nematic phases against a possible demixing into two phases with the same symmetry. A convenient thermodynamic variable to analyze the *local* stability of a homogeneous phase with respect to infinitesimal fluctuations in the density and composition (at constant osmotic pressure) is the Gibbs free energy $\beta G/N$ which can be obtained from the free energy by a Laplace transform: $G/N = F/N + \rho^{-1}\Pi$. The condition for local stability then follows from the second derivative of the Gibbs free energy with respect to the mole fraction [67, 95]

$$\left(\frac{\partial^2 \tilde{g}}{\partial x^2}\right)_{T,\Pi} > 0, \tag{5.15}$$

at constant temperature T and osmotic pressure Π. In practice, it is usually more convenient to rewrite this explicitly in terms of derivatives of the Helmholtz free energy with respect to density and composition

$$\left(\frac{\partial^2 \tilde{f}}{\partial x^2}\right)_{T,\rho} - \rho\left(\frac{\partial^2 \tilde{f}}{\partial x \partial \rho}\right)^2\left[2\frac{\partial \tilde{f}}{\partial \rho} + \rho\frac{\partial^2 \tilde{f}}{\partial \rho^2}\right]_{T,x}^{-1} > 0, \tag{5.16}$$

where $\tilde{g} = G/Nk_BT$ and $\tilde{f} = F/Nk_BT$ denote *intensive* free energies. The limit of stability of the mixed state is given by $(\partial^2 \tilde{g}/\partial x^2)_{T,\Pi} = 0$. The solutions $\rho_s(x)$ of this equation represent the socalled *spinodal* curve. The corresponding spinodal pressure Π_s can be obtained by inserting $\rho = \rho_s(x)$ into the osmotic pressure. The critical point (Π^*, x^*) of the demixing transition is then obtained from the condition $d\Pi_s(x)/dx = 0$. Corresponding demixing binodals can be calculated by requiring equal osmotic pressure and chemical potentials of both components in the demixed phases. This can be done either entirely numerically or by means of a (graphical) common tangent procedure as shown in Sec. 4.6.

5.5. Isotropic-nematic fractionation effects

For the sake of clarity let us now define the following binary mixtures. *R-I*: rods with different lengths (L) but equal thickness (D), *R-II*: rods with different diameters but equal length, and likewise for the platelets, *P-I*: platelets with equal thickness (L)
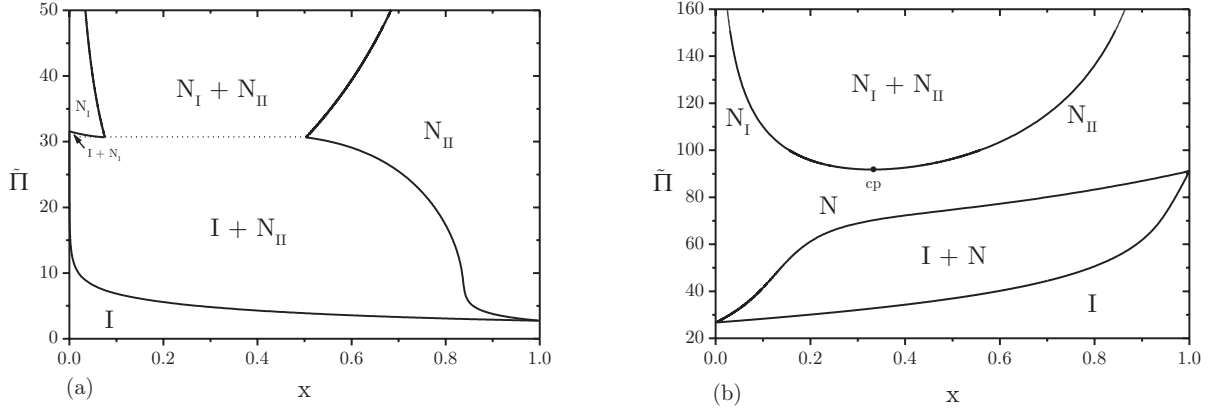
FIGURE 5.2. Phase diagrams in terms of osmotic pressure $\tilde{\Pi} = (1/2) \langle\langle v_{\text{excl}}\rangle\rangle_{11}^{\text{iso}} \Pi/k_B T$ plotted versus the mole fraction of the largest species $x = x_2$, obtained from the Onsager-Parsons free energy. (a) Case P-I: mixture of platelets with equal thickness but different diameters ($L_1 = L_2$, $l_1 = 10$, $l_2 = 20$). The dotted line represents an $I - N_I - N_{II}$ triple line. (b) Case P-II: binary mixture of thin and thick hard platelets with equal diameter ($D_1 = D_2$, $l_1 = 9$, $l_2 = 4$).

differing in diameter (D) and *P-II*: platelets with equal diameter but different thickness. To investigate the behaviour of the latter we need to include the next order (thickness dependent) contribution to the excluded volume of two platelets Eq. (5.4). The reason for this is that the plate's thickness does not enter into the leading order contribution of the excluded volume, cf. Eq. (2.2), so that retaining the leading term only does not allow to discriminate between plates differing only in thickness.

In Fig. 5.2 we show two phase diagrams which are representative for binary mixtures of platelets differing in thickness or diameter (i.e. cases P-I and P-II). From the osmotic pressure representations we can immediately infer a strong repartitioning of the species among the coexisting isotropic and nematic phases, i.e. the different phases are markedly enriched in either the large or the small species. However, the two scenarios depicted in Fig. 5.2 are quite distinct. For mixture P-I the largest species appear to preferentially occupy the nematic phase whereas in the other case the large platelets accumulate in the isotropic phase. Fractionation in binary mixtures of rods (both R-I and R-II) occurs in a way similar to that of plates with different diameters (P-I) as sketched in Fig. 5.2(a) with a preference of the longer/thicker rods for the nematic phase [65, 69].

The anomalous fractionation behaviour of platelet mixture P-II may lead to an *inversion of densities* of the isotropic and nematic phases involving an isotropic lower phase in coexistence with a nematic upper phase, as shown explicitly in Chapter 2. This behaviour can also be inferred from Fig. 5.2(b). Although the isotropic phase always has a lower number density than the nematic phase, its *mass* density, which also depends upon the average particle size in the phase, may become higher than that of

the nematic phase due to fractionation, the biggest particles migrating into the isotropic phase.

5.6. Demixing of the isotropic and nematic phases

5.6.1. Nematic-nematic demixing

As we can see from the phase diagrams depicted in Fig. 5.2, a homogeneous nematic system may under certain conditions demix into two nematic phases with the same uniaxial nematic symmetry but with different number densities and compositions. For all four mixtures considered in this Chapter, this demixing transition can occur if the corresponding length or thickness ratio exceeds some threshold value. However, the interplay of the different entropic contributions involved can lead to distinctly different demixing mechanisms for these mixtures.

Judging from the structure of the nematic free energy Eq. (5.11), it is obvious that the demixing must be driven by a competition between mixing, orientation and packing (i.e. excluded-volume) entropy. However, since the latter contribution is a constant independent of the composition for all cases (except for the plates with bidisperse thickness, P-II) it is clear that the excluded-volume effect plays no role and that the demixing involves a balance between mixing and orientational entropy. In case of rods with length bidispersity (R-I) the orientational entropy of the *short* rods favours demixing because of the strong alignment the long rods impose on the short ones in the mixed nematic phase [36]. Demixing occurs when the gain of orientational entropy outweighs the simultaneous loss of mixing entropy. A similar scenario applies to the other mixtures R-II and P-I, while case P-II is an exception because there the demixing is essentially driven by a competition between mixing and the excess packing entropy due to the plates' thickness (rather than their orientational entropy, as shown explicitly in Chapter 2).

The underlying mechanism may also have important implications for the topology of the nematic-nematic coexistence region. In particular, if the packing entropy is irrelevant all binodals can be shown to be completely independent of concentration and osmotic pressure*. This is easily understood by considering the Gibbs free energy of the nematic phase. Applying the appropriate Laplace transform of Eq. (5.14) and using the osmotic pressure Eq. (5.10) gives

$$\tilde{g}^{\text{nem}}(\Pi, x) \sim \text{cst} + 3\ln(\Pi/3) + \mathcal{F}(x, q). \tag{5.17}$$

Since the first terms are trivial contributions independent of the mole fraction, it is clear that the last contribution is solely responsible for the demixing and that the presence of an instability is only determined by the size ratio q. This means that the demixing binodals do *not* depend upon the concentration or the osmotic pressure of the nematic phase. Consequently, in a $\Pi - x$ representation, all binodals must be straight vertical lines [36]. The *threshold* value for q above which an instability occurs was

---

*Formally, this conclusion is only valid within the Gaussian trial function Ansatz we implicitly use here.

found at $q = 3.167$ for rods of type R-I [36] whereas the platelets of type P-I demix at considerably lower size ratios $q > 1.753$. Based on similar calculations, Hemmer [91] found that for the case R-II a diameter ratio larger than 4.258 is required.

As mentioned already, mixtures of thin and thick platelets (P-II) are governed by a different demixing scenario. There, the excluded-volume contribution (more precisely, the thickness-dependent correction term) is responsible for the demixing. The packing contribution of the Gibbs free energy (which favours demixing) for the case P-II reads

$$\tilde{g}_{\text{excl}}^{\text{nem}} = 2 + 8\phi = 2 + \frac{32}{\pi}c(\Pi, x) \sum_{i=1,2} x_i \frac{L_i}{D}, \tag{5.18}$$

where the concentration $c(\Pi, x)$ follows from inverting the equation of state Eq. (2.17). Due to its concentration dependence the latter term in Eq. (5.18) will always outweigh the mixing contribution at sufficiently high pressures, irrespective of the size ratio. Therefore, there is no threshold value in these mixtures and demixing occurs at any size ratio. However, in order for the critical pressure to attain physically acceptable values it is required that the thickness ratio is larger than 3 [90].

To assess the effect of Parsons rescaling on the shape of the demixing binodals we may analyze its additional contribution to the Gibbs free energy Eq. (5.17). The osmotic pressure of the nematic state within the Parsons' approach becomes

$$\frac{\Pi^{\text{nem}}}{k_B T} \sim c \left[3 + 2 \frac{\partial \ln \tilde{f}_{\text{CS}}(\phi(x, c))}{\partial \ln \phi(x, c)} \right]. \tag{5.19}$$

Inverting the pressure now yields a non-trivial mole-fraction dependence of the concentration $c(\Pi, x)$ (compared to a simple $c(\Pi) = \Pi/3$ for the case $\tilde{f}_{\text{CS}}(\phi) = 1$). This implies that all binodals become implicitly dependent upon the osmotic pressure so that they no longer form straight lines in a $\Pi - x$ phase representation, as we see in Fig. 5.2. As to the Gibbs free energy, the trivial second term in Eq. (5.17) should now be replaced by the following non-trivial contribution

$$\tilde{g}^{\text{P}}(\Pi, x) \sim 3 \ln c \left[\Pi(x) \right] + 2 \ln \tilde{f}_{\text{CS}}(x, c \left[\Pi(x) \right]). \tag{5.20}$$

To verify whether this contribution stabilizes or destabilizes the homogeneous nematic state we must know the sign of its second order derivative with respect to the mole fraction. This calculation can only be done in a numerical way since it is not possible to invert the osmotic pressure Eq. (5.19) analytically. It turns out that $(\partial^2 \tilde{g}^{\text{P}}/\partial x^2)$ is generally positive indicating that the correction due to the Parson rescaling always *favours the mixed state*. Consequently the critical values mentioned above need to be adapted slightly due to the rescaling. An interesting manifestation of the stabilizing effect of the Parson approach is the possibility of the demixing binodals closing off at a lower critical point. This would give a scenario similar to the one shown in Fig. 5.2(b) for the case P-II; although the size ratio is larger than the threshold value the nematic-nematic two-phase region only opens up when the pressure exceeds a certain value. Note that this scenario is not encountered without Parsons rescaling since the binodals then run vertically and therefore cannot meet in a critical point. At higher size

ratios, the critical point shifts to lower values of the pressures and the nematic-nematic demixing region eventually overlaps with the isotropic-nematic region. This gives rise to an isotropic-nematic-nematic triple equilibrium, comparable to the scenario shown in Fig. 5.2(a).

Calculations based upon the formal approach reveal the possibility of an *upper* critical or consolute point which marks the closing of the nematic-nematic region at high pressures and the reentrance of the homogeneous nematic state. These have been found in mixtures of rods with different lengths (R-I) [96] (albeit in an extremely small q interval at low size ratios) and in mixtures of thin and thick hard rods (R-II) [69]. The fact that this phenomenon is not observed in the Gaussian approach is probably related to the fact that the ODFs are not represented by their true equilibrium form. However, in both cases the consolute points are found to disappear at higher size ratios such that the high-q scenarios obtained within the formal approach are consistent with the ones sketched for the Gaussian approximation in Fig. 5.2.

5.6.2. Isotropic-isotropic demixing

Contrary to the nematic phase, a demixing of the isotropic phase is less common. So far, such an instability was only found in binary mixtures of thin and thick rods (R-II) [67, 69, 70]. However, by extending the simple spinodal analysis from [67] it can be easily verified that a similar demixing may take place in mixtures of platelets, both for P-I and P-II. Consider the free energy in the isotropic state

$$\tilde{f}^{\text{iso}} \sim \text{cst} + \ln \rho - 1 + \sum_{i=1,2} x_i \ln x_i + \frac{1}{2}\rho \tilde{f}_{\text{CS}}(\phi) B_2^{\text{iso}}, \tag{5.21}$$

with B_2^{iso} the excluded-volume dependent second virial coefficient:

$$B_2^{\text{iso}} = \frac{\pi}{4}\left((1-x)^2 \tilde{v}_{11} + 2x(1-x)\tilde{v}_{12} + x^2 \tilde{v}_{22}\right). \tag{5.22}$$

Inserting this into Eq. (5.16) (setting $\tilde{f}_{\text{CS}}(\phi) = 1$ for simplicity) and some rearrangements lead to the following stability condition [67]:

$$1 + \rho\frac{\pi}{4}\left((1-x)\tilde{v}_{11} + x\tilde{v}_{22}\right) - \left(\rho\frac{\pi}{4}\right)^2 x(1-x)\Delta > 0. \tag{5.23}$$

To arrive at Eq. (5.23) it is implicitly used that the system also fulfills the criterion for *mechanical* stability $\left(\partial^2 \tilde{f}/\partial v^2\right)_x > 0$, where $v = 1/\rho$ [95]. A demixing instability is only possible if $\Delta \equiv \tilde{v}_{12}^2 - \tilde{v}_{11}\tilde{v}_{22} > 0$ since only then the condition Eq. (5.23) is no longer satisfied for all $\rho > 0$. Substituting corresponding expressions for $\tilde{v}_{ij}$ (including the thickness dependent contribution for the case P-II) yields $\Delta > 0$ for all cases except for R-I, for which $\Delta = 0$. Hence, an isotropic-isotropic demixing may in principle be expected in all mixtures, except in binary systems of rods differing only in length.

Explicit results can be obtained by calculating spinodal curves (and its corresponding critical point) from Eq. (5.16) as a function of the size ratio. To illustrate this we have plotted in Fig. 5.3 the evolution of the isotropic-isotropic critical point for the binary plate mixtures P-I and P-II. Physical solutions are found for size ratios $q = D_2/D_1 > 1.95$ (P-I) and $q = L_2/L_1 > 1.42$ (P-II). However, considering the high osmotic pressures
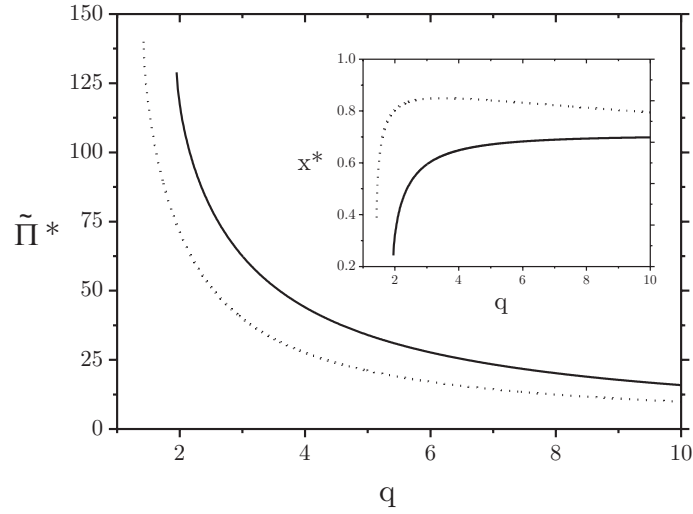
FIGURE 5.3. Locus of the isotropic-isotropic critical point, in terms of the critical pressure $\tilde{\Pi}^*$ and mole fraction x^* (inset), for binary plate mixtures P-I (solid curve, $q = D_2/D_1$) and P-II (dotted curve, $q = L_2/L_1$). Results are based on the Onsager-Parsons free energy using $l_1 = L/D_1 = L_1/D = 0.05$.

at low size ratios it is evident that the isotropic state (and therefore its demixing) will initially be *metastable* with respect to a transition to the nematic state. In order to estimate the minimum size ratio required for having *stable* demixing transitions we should compare the critical pressure in Fig. 5.3 with the maximum coexistence pressure pertaining to the isotropic-nematic transition. From this we obtain that $q > 7.4$ for P-I and $q > 2.85$ for P-II. Note that these values represent *lower* bounds to the metastable-stable transition and the exact transitions generally occur at higher size ratios. For the case R-II, the transition was predicted at $q > 8$ [69]. The fact that a demixing of the isotropic phase requires a considerably larger size ratio than the nematic phase is not surprising because the orientation entropy, which usually favours demixing, is not present in the isotropic state. Consequently, the demixing must be solely accomplished by excluded-volume effects, in particular the unfavourable excluded volumes between unlike particles, as we can infer from the condition $\Delta > 0$. We remark that the phase behaviour of platelets (P-I and P-II) can be surprisingly rich, with a possibility of both $N - N$ and $I - I$ two phase equilibria and their associated $I - N_I - N_{II}$ and $I_I - I_{II} - N$ triple equilibria, without having to go to extreme size ratios.

5.7. FINAL REMARKS

In this Chapter we have not treated the possibility of phase transitions from the nematic state to high-density liquid crystal symmetries with (partial) positional order, such as smectic and columnar phases. Since these phases are expected to appear in the high-pressure regime of the phase diagram, instabilities of the nematic state towards smectic/columnar ordering may interrupt the topology of the nematic-nematic demixing regimes in Fig. 5.2. So far such instabilities have only been analyzed theoretically for a

perfectly aligned nematic state of short and long rods (R-I) and thick and thin rods (R-II) [67]. There it was found that under certain conditions the demixing of the nematic phase is indeed pre-empted by transitions to smectic or columnar states. In Chapter 8 the stability of these liquid crystal states in *polydisperse* systems will be discussed by means of an analysis of the approximate model of perfectly aligned hard cylinders.

Part II

Polydisperse mixtures of anisometric particles

6

Isotropic-nematic phase behaviour of length-polydisperse hard rods

Abstract

The isotropic-nematic phase behaviour of length-polydisperse hard rods with arbitrary length distributions is obtained from a numerical treatment of the polydisperse Onsager formalism in the Gaussian approximation. We determine the onset of isotropic-nematic phase separation, coming from a dilute isotropic phase and a dense nematic phase, focusing on parent systems whose lengths can be described by either a Schulz or a "fat-tailed" log-normal distribution with appropriate lower and upper cutoff lengths. In both cases, very strong fractionation effects are observed for parent polydispersities larger than roughly 50 %. In these regimes, the isotropic and nematic phases are completely dominated by respectively the shortest and the longest rods in the system. Moreover, for the log-normal case, we predict triphasic isotropic-nematic-nematic equilibria to occur above a certain threshold polydispersity. By investigating the properties of the coexisting phases across the coexistence region for a particular set of cutoff lengths we show that the region of stable triphasic equilibria does not extend up to very large parent polydispersities but closes off at a consolute point located not far above the threshold polydispersity. The experimental relevance of the phenomenon is discussed.

6.1. Introduction

An important characteristic of systems of (anisometric) colloidal particles is their inherent polydispersity, i.e. the particles may differ in size and shape [7, 9]. The issue of polydispersity and its effect on the interpretation of experimental results has already been addressed by Onsager in his original paper [21]. Later on, extensions of the Onsager theory allowing for phase diagram calculations for bidisperse [34, 36, 65, 66, 69, 94] and tridisperse systems [97] of hard rods as well as binary mixtures of hard platelets [90] revealed a rich variety in behaviour, most notably a widening of the coexistence region, a fractionation effect (i.e. segregation of the species among the coexisting phases), a reentrant phenomenon and, most interestingly, the possibility of a demixing of the nematic phase which may give rise to isotropic-nematic-nematic triphasic equilibria.

So far, very few theoretical attempts have been made to study the isotropic-nematic phase behaviour of truly polydisperse systems, i.e. systems characterized by a *continuous* distribution in particle size. These studies however involve serious limitations such as discretizing the particle orientation vectors along the three Cartesian axes [98, 99]

–the so-called restricted-orientation or Zwanzig model [86]– or using perturbation theory to account for very narrow distributions in rod length [100, 101]. An important shortcoming of the restricted orientation models is that the orientational entropy is incorrectly described since the particles are not allowed to sample the entire orientational phase space. A concomitant effect is the overestimation of the probability of in-plane (or parallel) particle configurations which are relatively improbable in case of continuous orientations [102]. Very recently, it was shown that confining the orientational degrees of freedom may even give rise to spurious phase transitions which bear no physical justification [103]. All these considerations together confirm that the restricted-orientation models are inadequate for studying real liquid crystals. The perturbation theories based on the Onsager theory –which allows for *continuously* varying orientations– have been shown to qualitatively predict some generic features for polydisperse systems such as a broadening of the coexistence area and a fractionation effect, with the longest rod going preferentially into the nematic phase. However, other interesting phenomena which are expected to occur at much higher polydispersities –in particular polydispersity-induced nematic-nematic demixing transitions– cannot be studied appropriately within these approximations and therefore remain elusive.

Solving the phase equilibrium conditions for systems with arbitrary size distributions is by no means trivial and requires considerable numerical effort. In particular, the presence of almost infinitely many components in a polydisperse system requires an equally large number of coexistence conditions to be solved simultaneously which obviously is a formidable task [104]. Recently, a number of studies have appeared in which the polydisperse Onsager model, albeit in simplified form, was subjected to a numerical treatment. Speranza and Sollich [105, 106] investigated the so-called $\mathcal{P}_2$-approximation which consists of truncating an expansion of the orientation-dependent excluded-volume term (in terms of even Legendre polynomials $\mathcal{P}_{2n}$) after the first nontrivial term $\mathcal{P}_2$. A remarkable outcome of these calculations is that triphasic isotropic-nematic-nematic equilibria are predicted for *unimodal* rod length distributions with sufficiently fat tails (e.g. log-normal distributions). These equilibria occur in a small interval of polydispersities of the parent system. However, the simplified nematic ODF pertaining to the "$\mathcal{P}_2$-model" is only valid for the description of very weakly aligned nematic phases. The behaviour predicted from this model should therefore be considered with some care, particularly in those regions where the fractionation effect is strong and the phase behaviour is dominated by the effect of the longest rods in the system. The presence of very long rods in a nematic state may force the entire system into a strongly aligned nematic configuration, so that a more appropriate form for the nematic ODF is required in these cases.

In our approach, we use the Gaussian trial ODF approach to calculate the isotropic-nematic phase behaviour of hard rod systems which can be described by either a Schulz or a log-normal length distribution with arbitrary polydispersities. The benefit of using the Gaussian Ansatz is twofold. First, all necessary integrals for the monodisperse Onsager model are analytically tractable so that only numerical integrations over the

length distributions need to be considered for the polydisperse case. Second, the Gaussian ODF allows for a qualitatively better description of highly ordered nematic states compared to the $\mathcal{P}_2$-approximation which makes it a suitable tool for describing polydisperse systems, particularly the ones with a "fat-tailed" length distribution. While work on this subject was still in progress, Speranza and Sollich reported a numerical analysis of the exact Onsager model [107], i.e. using the numerically *exact* ODF. Also there, triphasic equilibria were predicted for both Schulz-type parent distributions and "fat-tailed" log-normal forms. However, due to the numerical complexity of the problem only the *onset* of nematic ordering from an isotropic reference phase was considered there so that no information could be obtained about the properties of the isotropic and nematic phases across the coexistence region. Consequently, no conclusive insight could be gained as to whether the triphasic equilibria constitute a significant part of the phase diagram. Within the Gaussian approximation it is possible to access the coexistence region with only limited additional numerical effort. An important consequence is that it enables us to gain insight in the extent of the isotropic-nematic-nematic stability region. Although we cannot calculate the binodal curves for these equilibria (which locate the precise onset), we are able to localize possible spinodal points for the coexisting nematic phase across the two-phase region, which indicate a local instability of the nematic phase. In that case, there must be an interval along the coexistence trajectory where a demixing of the nematic phase occurs and isotropic-nematic-nematic triphasic equilibria appear.

6.2. Polydisperse Onsager theory; starting equations

Let us consider a system of hard rodlike cylinders with equal diameters D but *different* lengths L, in a macroscopic volume V. To characterize the rod lengths in our polydisperse system we introduce the relative rod length $l = L/L_0$ (with L_0 some reference rod length) which is assumed to be a *continuous* variable. We may then take the limit $L_0/D \to \infty$ (infinitely thin rods) at constant values for the relative lengths l. Generalizing the original Onsager formalism to polydisperse systems leads to the following expression for the total Helmholtz free energy density f (in units $k_B T \equiv \beta^{-1}$)

$$f \equiv \frac{b\beta F}{V} \sim \int c(l)[\ln c(l) - 1]dl + \int c(l)\omega(l)dl + \int \int c(l)c(l')ll'\rho(l,l')dldl'. \qquad (6.1)$$

All irrelevant contributions linear in c arising from the standard chemical potentials of the particles are omitted since they only depend on the solvent chemical potential and the temperature. The concentrations c are rendered dimensionless by relating them to the orientationally averaged excluded volume per particle between two reference rods, $b = \pi D L_0^2/4$, via $c(l) = bN(l)/V$ where $N(l)dl$ is the number of particles with relative length between l and $l+dl$. The density distribution over lengths $c(l)$ can be decomposed according to $c(l) = c_0 p(l)$, with $p(l)$ the normalized length distribution ($\int dl p(l) \equiv 1$) and c_0 the total dimensionless rod concentration.

The free energy Eq. (6.1) consists of several entropic contributions. The first term represents the exact ideal free energy of the polydisperse system. The second term

contains the parameter ω as a measure for (the negative) of the orientational entropy [21]

$$\omega(l) \equiv \int \psi(l, \Omega) \ln[4\pi\psi(l, \Omega)]d\Omega, \tag{6.2}$$

where $\psi(l, \Omega)$ is the normalized ODF for species l describing the distribution of the particles' solid angle Ω. In the isotropic state, all orientations are equally probable so that ψ_{iso} is simply a constant $(1/4\pi)$ independent of l. In the nematic state, however, the ODFs are peaked functions (generally different for each species l), due to the fact that the rods are aligned along a nematic director. Note that ω (and hence the orientational free energy) attains its minimum ($\omega = 0$) in the isotropic state, whereas $\omega > 0$ in the nematic state.

The last term in Eq. (6.1) describes the excess free energy which accounts for the particle interactions. A measure for the average excluded-volume interaction between rods of relative length l and l' is given by the following angular average

$$\rho(l, l') \equiv \frac{4}{\pi} \int \int |\sin \gamma(\Omega, \Omega')| \, \psi(l, \Omega)\psi(l', \Omega')d\Omega d\Omega'. \tag{6.3}$$

Using the isotropic average $\langle\langle|\sin \gamma(\Omega, \Omega')|\rangle\rangle = \pi/4$ we obtain $\rho(l, l') \equiv 1$ for the isotropic state. This indicates that the excluded volume (or packing) free energy is indeed maximal in the isotropic phase but decreases as soon as the rods align to form a nematic phase.

We shall use Gaussian trial ODFs with variational parameter $\alpha(l)$ to describe the angular distribution of rods with relative length l in the nematic state [34]. The Gaussian Ansatz consists of supposing

$$\psi(l, \theta) \equiv \begin{cases} \frac{\alpha(l)}{4\pi} \exp[-\frac{1}{2}\alpha(l)\theta^2] & 0 \le \theta \le \frac{\pi}{2} \\[2mm] \frac{\alpha(l)}{4\pi} \exp[-\frac{1}{2}\alpha(l)(\pi - \theta)^2] & \frac{\pi}{2} \le \theta \le \pi \end{cases}, \tag{6.4}$$

where α is now a function of l. Note that, due to the uniaxial symmetry of the nematic phase, the ODF only depends upon the polar angle θ between the particle orientation vector and the nematic director. Inserting Eq. (6.4) in Eq. (6.2) and straightforward integration yields for the orientational entropy

$$\omega(l) \sim \ln \alpha(l) - 1. \tag{6.5}$$

For the excluded volume entropy in the nematic phase $\rho_{\mathrm{nem}}(l, l')$ only the leading order term of its asymptotic expansion for large α will be retained

$$\rho_{\mathrm{nem}}(l, l') \sim \sqrt{\frac{8}{\pi}\left(\frac{1}{\alpha(l)} + \frac{1}{\alpha(l')}\right)} + \mathcal{O}\left[\alpha^{-3/2}(l), \alpha^{-3/2}(l')\right]. \tag{6.6}$$

Substituting Eqs. (6.5) and (6.6) into Eq. (6.1) and minimizing the free energy density with respect to the non-conserved orientational degrees of freedom by means of a functional differentiation gives

$$\frac{\delta f}{\delta \alpha(l)} \sim \frac{c(l)}{\alpha(l)} - \left(\frac{8}{\pi}\right)^{1/2} \frac{lc(l)}{2\alpha^2(l)} \int l'c(l')\left(\frac{1}{\alpha(l)} + \frac{1}{\alpha(l')}\right)^{-1/2} dl'. \tag{6.7}$$

Applying the stationarity condition $\delta f/\delta\alpha(l) \equiv 0$ and some rearranging leads to the following self-consistency equation

$$\tilde{\alpha}(l) = 2l^2 \left\{ \int l' p^{(N)}(l') \left[1 + \frac{\tilde{\alpha}(l)}{\tilde{\alpha}(l')} \right]^{-1/2} dl' \right\}^2, \qquad (6.8)$$

Here, we have factorized the Gaussian variational parameter function $\alpha(l)$ into a concentration-dependent term and a contribution $\tilde{\alpha}(l)$ only related, via Eq. (6.8), to the normalized length distribution in the nematic phase $p^{(N)}(l)$. Hence we write

$$\alpha(l) = \tilde{\alpha}(l)\frac{4c_0^2}{\pi}. \qquad (6.9)$$

showing that for all l the variational parameter α depends quadratically on c_0 just as in the monodisperse case [5]. An approximate analytical solution to Eq. (6.8) valid for infinitely narrow distributions (denoted by subscript δ) can be obtained by substituting a delta function $p^{(N)}(l) = \delta(l-1)$ which gives [100]

$$\tilde{\alpha}_\delta(l) = \frac{1}{2}\left(\sqrt{8l^2+1}-1\right). \qquad (6.10)$$

This result may be interpreted as a measure for the nematic alignment of a *single* rod with relative length l added to a nematic bulk system of monodisperse rods with reference length L_0. Eq. (6.10) shows that $\tilde{\alpha}_\delta(l)$ and hence the order parameter S, defined as [5]

$$S(l) \equiv \int \mathcal{P}_2(\cos\theta)\psi(l,\theta)d(\cos\theta) \sim 1 - \frac{3}{\alpha(l)}, \qquad (6.11)$$

are in general increasing functions of the relative rod length, i.e. $\tilde{\alpha}_\delta(l) \propto l$ for large l, as we might have anticipated. Moreover, $\tilde{\alpha}_\delta(0) = 0$ which means that there is no ordering for rods of zero length, as formally must be the case. However, it should be pointed out that rods with lengths close to zero must be excluded from our model because the normalization factors for the Gaussian ODFs in Eq. (6.4) do not allow for a correct description of isotropically distributed or weakly aligned species in the nematic state. For consistency reasons we must therefore introduce a lower limit ($l_{\min} > 0$) in all length distributions.

6.3. I-N PHASE COEXISTENCE

6.3.1. Equilibrium conditions for polydisperse systems

The conditions for phase equilibrium are that the coexisting isotropic and nematic phases must have equal chemical potential $\mu(l)$ for all relative rod lengths l, as well as equal osmotic pressure Π. The chemical potential can be derived by functional differentiation of the free energy with respect to the length distribution $c(l)$

$$\beta\mu(l) = \frac{\delta f}{\delta c(l)}. \qquad (6.12)$$

Using Eqs. (6.5) and (6.6) together with the isotropic values $\omega \equiv 0$ and $\rho \equiv 1$ we obtain

$$\beta\mu_{\text{iso}}(l) = \ln c^{(I)}(l) + 2lc_1^{(I)}$$

$$\beta\mu_{\text{nem}}(l) = \ln c^{(N)}(l) + \ln\left[\frac{4}{\pi}(c_0^{(N)})^2\tilde{\alpha}(l)\right] - 1 + \tilde{\mu}_{\text{ex}}^{(N)}(l), \tag{6.13}$$

where c_1 denotes the first *moment density* following from the definition

$$c_k = c_0 m_k = \int dl\, l^k c(l), \qquad k = 0, 1, 2, \ldots \tag{6.14}$$

Here, m_k denotes the k-th moment of the (normalized) distribution. The excess chemical potential for the nematic phase $\tilde{\mu}_{\text{ex}}^{(N)}(l)$ is given by

$$\tilde{\mu}_{\text{ex}}^{(N)}(l) = 2^{3/2}l \int dl'\, p^{(N)}(l')l'\left(\frac{1}{\tilde{\alpha}(l)} + \frac{1}{\tilde{\alpha}(l')}\right)^{1/2}. \tag{6.15}$$

independent of the concentration of the nematic phase. Similar to Eq. (6.8) we can straightforwardly obtain an analytical solution for $\tilde{\mu}_{\text{ex}}^{(N)}(l)$ valid for near monodisperse distributions by substituting $p^{(N)}(l) = \delta(l-1)$. This yields the following scaling result

$$\tilde{\mu}_{\text{ex},\delta}^{(N)}(l) \propto l\sqrt{\frac{1}{\tilde{\alpha}_\delta(l)} + 1}. \tag{6.16}$$

Using Eq. (6.10) it then follows that $\tilde{\mu}_{\text{ex}}^{(N)}(l) \propto l$, for very large l, which is an *exact* scaling result. In the limit $l \to l_{\text{max}}$ the excess chemical potential is the reversible work required to insert a very long rod in a perfectly aligned configuration of reference rods (the inserted rod being parallel to the other rods). This quantity, which is simply the work required to create a (macroscopic) cavity of the scaled particle against the pressure exerted by the fluid, increases linearly with the volume (and hence the length) of the inserted rod. The osmotic pressure can be written in terms of the chemical potential and the free energy via

$$b\beta\Pi \equiv -f + \beta\int dl\, c(l)\mu(l), \tag{6.17}$$

which immediately yields for the isotropic phase

$$b\beta\Pi_{\text{iso}} \sim c_0^{(I)} + (c_1^{(I)})^2. \tag{6.18}$$

For the nematic phase this formally gives

$$b\beta\Pi_{\text{nem}} \sim c_0^{(N)} + f_{\text{ex}}^{(N)}. \tag{6.19}$$

However, this result can be simplified considerably by noting that the volume fraction of the average excluded volume (per particle) in the nematic phase is a constant, as shown in Sec. 5.2.2 of the previous Chapter. We thus have

$$N\frac{\langle\langle v_{\text{excl}}\rangle\rangle_{l,l'}}{V} \sim c_0^{(N)}\langle\langle ll'\rho(l,l')\rangle\rangle_{l,l'} = 2. \tag{6.20}$$

The brackets denote averages over the normalized length distribution. This result, which is due to Odijk [92], generally holds for both monodisperse and polydisperse

systems, independent of their composition. From the free energy Eq. (6.1) it then follows that $f_{\text{ex}}^{(N)} = 2c_0^{(N)}$ so that the osmotic pressure of the nematic phase reduces to

$$b\beta\Pi_{\text{nem}} \sim 3c_0^{(N)}, \tag{6.21}$$

like for a monodisperse system [5]. We can now state the conditions for the coexistence between the isotropic and nematic daughter phases into which a parent phase (henceforth denoted with superscript 0) with length distribution $c^{(0)}(l)$ is assumed to have split [98]. From Eq. (6.13), equality of chemical potentials of both phases is obeyed exactly if the distributions in the phases have the following form

$$c^{(a)}(l) = W(l)\exp[\xi^{(a)}(l)], \qquad a = I, N \tag{6.22}$$

where $W(l) \equiv \exp[\beta\mu(l)]$ must be a function common to both phases, since $\mu^{(I)}(l) = \mu^{(N)}(l) = \mu(l)$. The functions $\xi^{(a)}(l)$ are given by

$$\xi^{(I)}(l) = -2lc_1^{(I)}$$
$$\xi^{(N)}(l) = \left(1 - \ln\frac{4}{\pi}\right) - 2\ln c_0^{(N)} - \ln\tilde{\alpha}(l) - \tilde{\mu}_{\text{ex}}^{(N)}(l). \tag{6.23}$$

Furthermore, conservation of matter requires

$$c^{(0)}(l) = (1-\gamma)c^{(I)}(l) + \gamma c^{(N)}(l), \tag{6.24}$$

where γ denotes the fraction of the system volume occupied by the nematic phase. Using this, we can express $W(l)$ in terms of the parent distribution $c^{(0)}(l)$ giving

$$c^{(a)}(l) = c^{(0)}(l)\frac{\exp[\xi^{(a)}(l)]}{(1-\gamma)\exp[\xi^{(I)}(l)] + \gamma\exp[\xi^{(N)}(l)]}. \tag{6.25}$$

These functions represent the equilibrium rod length distributions for the coexisting phases. The phase equilibria can now, in principle, be obtained by solving a set of self-consistency equations for the moment densities of both phases and for the functions $\tilde{\alpha}(l)$ and $\tilde{\mu}_{\text{ex}}^{(N)}(l)$ pertaining to the nematic phase. These equations will be worked out below for a specific situation, namely the onset of isotropic-nematic phase separation.

6.3.2. The onset of I-N phase separation; cloud and shadow curves

In this section we aim at locating the onset of isotropic-nematic phase separation indicated by so-called cloud and shadow points [98, 104]. A cloud point marks the density where the parent phase has split off an infinitesimal amount of a new coexisting phase, called the shadow phase. Accordingly, at the isotropic cloud point only an infinitesimal amount of nematic phase (shadow phase) has emerged and so the distribution of the isotropic phase is only negligibly perturbed away from the parent. Hence, for the isotropic cloud point we may set $\gamma = 0$ in Eq. (6.25) so that,

$$c^{(I)}(l) = c^{(0)}(l), \tag{6.26}$$

implying that the distribution in the isotropic phase at the cloud point is equal to the parent distribution, hence $c_k^{(I)} = c_k^{(0)}$ with $k = 0, 1$. The (normalized) rod distribution

in the nematic shadow phase (with density $c_0^{(N)}$) is now given by

$$
\begin{aligned}
p^{(N)}(l) &= \frac{c^{(0)}(l)}{c_0^{(N)}} \exp\left[\xi^{(N)}(l) - \xi^{(I)}(l)\right] \\
&= \mathcal{K}_N \frac{p^{(0)}(l)}{\tilde{\alpha}(l)} \exp\left[2c_1^{(0)}l - \tilde{\mu}_{\text{ex}}^{(N)}(l)\right],
\end{aligned}
\tag{6.27}
$$

where $\mathcal{K}_N = \pi e c_0^{(0)}/4(c_0^{(N)})^3$ and $p^{(0)}(l)$ the normalized parent distribution. Note that Eq. (6.27) is an implicit expression for $p^{(N)}(l)$ because it still depends on the unknown functions for the variational parameter $\tilde{\alpha}(l)$ and the excess chemical potential $\tilde{\mu}_{\text{ex}}^{(N)}(l)$ for each species in the nematic shadow phase. Explicit solutions for these functions can be obtained by substituting Eq. (6.27) into Eqs. (6.8) and (6.15) and numerically solving the resulting self-consistency equations.

The concentrations of the isotropic cloud phase and the coexisting nematic shadow are found by imposing the normalization condition for the distribution in the nematic shadow phase,

$$
\int p^{(N)}(l) \equiv 1,
\tag{6.28}
$$

and the condition of equal osmotic pressure

$$
3c_0^{(N)} = c_0^{(0)} + (c_1^{(0)})^2.
\tag{6.29}
$$

Note that the ratio between the zeroth and first moment densities on the right-hand side of Eq. (6.29) is *fixed* by the parent distribution. Using the condition of equal pressure to eliminate e.g. $c_0^{(N)}$, we may conveniently combine Eqs. (6.28) and (6.29) into one self-consistency equation for the concentration of the isotropic cloud point, which we can solve in an iterative fashion. However, since $\tilde{\alpha}(l)$ and $\tilde{\mu}_{\text{ex}}^{(N)}(l)$ also depend on $c_0^{(0)}$ (via $p^{(N)}(l)$, Eq. (6.27)) this equation has to be solved along with the coupled set of self-consistency equations, Eqs. (6.8) and (6.15), so that we end up with a set of three coupled nonlinear equations. Obviously, solving this set is not a trivial task but requires some numerical effort. For this reason we have devoted an Appendix A to this issue where we describe some details of the numerical procedures adopted in this study.

We can now perform a similar analysis to obtain expressions for the *nematic* cloud point and the associated *isotropic* shadow point, which locate the onset of $I - N$ equilibrium coming from a dense nematic parent phase. Since the latter now coexists with an infinitesimal amount of an isotropic shadow phase we may set $\gamma = 1$ in Eq. (6.25) so that $c^{(N)}(l) = c^{(0)}(l)$ and $c_0^{(N)} = c_0^{(0)}$. The (normalized) rod distribution in the isotropic shadow phase (with density $c_0^{(I)}$) is then given by

$$
\begin{aligned}
p^{(I)}(l) &= \frac{c^{(0)}(l)}{c_0^{(I)}} \exp\left[\xi^{(I)}(l) - \xi^{(N)}(l)\right] \\
&= \mathcal{K}_I p^{(0)}(l)\tilde{\alpha}(l) \exp\left[-2c_1^{(I)}l + \tilde{\mu}_{\text{ex}}^{(N)}(l)\right],
\end{aligned}
\tag{6.30}
$$

where $\mathcal{K}_I = 4(c_0^{(0)})^3/\pi e c_0^{(I)}$. Since the functions $\tilde{\alpha}(l)$ and $\tilde{\mu}_{\text{ex}}^{(N)}(l)$ correspond to the nematic parent phase we may substitute $p^{(N)}(l) = p^{(0)}(l)$ in Eqs. (6.8) and (6.15).

Consequently, as the normalized parent distributions $p^{(0)}(l)$ have a predescribed form and do *not* depend on any concentration, the coupled self-consistency equations need to be solved only *once* for a given $p^{(0)}(l)$. The forms of the parent distributions will be specified in Sec. 6.3.4.

Once the solutions for $\tilde{\alpha}(l)$ and $\tilde{\mu}_{\mathrm{ex}}^{(N)}(l)$ have been obtained, the concentrations of the nematic cloud and shadow point can be calculated by requiring self-consistency for the zeroth moment (normalization condition) and the first moment of the isotropic shadow distribution

$$\int p^{(I)}(l) = 1,$$

$$\int l p^{(I)}(l) = m_1^{(I)} = \frac{c_1^{(I)}}{c_0^{(I)}}. \tag{6.31}$$

Similar to the previous case, we can rewrite these two conditions together with the equality of osmotic pressure Eq. (6.29) into a set of consistency relations from which the densities of the nematic cloud and isotropic shadow phases (*viz.* $c_0^{(0)}$, $c_0^{(I)}$ and $c_1^{(I)}$) can be obtained numerically (see also Appendix A).

6.3.3. Inside the coexistence region

We will now focus on the coexistence region between the isotropic and nematic cloud points, where both phases coexist in noninfinitesimal amounts, i.e. $0 < \gamma < 1$. According to Eq. (6.25), the equilibrium length distributions in the coexisting phases are then given by

$$c^{(I)}(l) = \frac{c^{(0)}(l)}{\gamma \exp\left\{\Delta\xi[\tilde{\alpha}(l), \tilde{\mu}_{\mathrm{ex}}^{(N)}(l)]\right\} + (1 - \gamma)},$$

$$c^{(N)}(l) = \frac{c^{(0)}(l)}{(1 - \gamma) \exp\left\{-\Delta\xi[\tilde{\alpha}(l), \tilde{\mu}_{\mathrm{ex}}^{(N)}(l)]\right\} + \gamma}. \tag{6.32}$$

with $\Delta\xi(l) = \xi^{(N)}(l) - \xi^{(I)}(l)$, given by Eq. (6.23). Note that both distributions are now different from the parental one. Solving the coexistence problem is done in a similar way to the one described previously for the isotropic cloud and shadow points. From an experimental point of view, we are only interested in results located on so-called physical dilution lines along which the overall system number density ($c_0^{(0)}$) is changed (e.g. by adding or evaporating solvent) while the overall composition of the species ($p^{(0)}(l)$) remains fixed. The parent distributions will be specified below.

6.3.4. Parent distributions

The numerical method described in the previous sections allows us to calculate the isotropic-nematic phase diagram for in principle arbitrary parent distributions. In our study we specify two types of distributions. The first one is the Schulz distribution which has the form

$$p^{(0)}(l) = N l^z \exp[-(z + 1)l], \tag{6.33}$$

with normalization factor N. In order to exclude rods with potentially zero length we truncate the distribution at some lower cutoff length $l_{\min}$. Henceforth we fix $l_{\min} = 0.01$. For calculational purposes (see Appendix A) we must also have some finite cutoff length $l_{\max}$ at large l. Of course, introducing cutoff lengths is also reasonable from a physical standpoint. The first and second moment (defined as $m_k = \langle l^k \rangle$, $k = 1, 2$) of the Schulz distribution are $m_1 = 1$ and $m_2 = (z + 2)/(z + 1)$ only for the *unbounded* case. However, in case of finite cutoff lengths the moments will deviate from these values. Although the corrections are generally small, in particular for large $l_{\max}$, they cannot be neglected. Therefore, we choose to calculate all relevant moments of the parent distribution numerically via $m_k = \int_{l_{\min}}^{l_{\max}} l^k p^{(0)} dl$. The polydispersity σ is defined as

$$\sigma^2 = \frac{\langle l^2 \rangle}{\langle l \rangle^2} - 1, \tag{6.34}$$

and would yield $\sigma^2 = (1 + z)^{-1}$ for the unbounded Schulz distribution.

The second distribution we consider is the log-normal one. The "fat-tailed" log-normal distribution decays much slower at large l than the Schulz one and therefore possesses a significantly larger contribution of long rods. The log-normal distribution reads

$$p^{(0)}(l) = N l^{-1} \exp\left[-\left(\frac{\ln l - \mu}{2w^2} \right)^2 \right]. \tag{6.35}$$

For the unbounded distribution, w is directly related to the polydispersity via $w^2 = \ln(1 + \sigma^2)$ and the parameter μ is chosen such that $m_1 = 1$, giving $\mu = -w/2$. The second moment is then given by $m_2 = 1 + \sigma^2$. Also here, truncation of the distribution at some values $l_{\min}$ and $l_{\max}$ leads to deviations for which we correct numerically.

6.4. Results for the onset of I-N phase separation

6.4.1. Schulz distributions

In Figs. 6.1 to 6.3 we have depicted the results for a Schulz parent distribution with cutoff lengths $l_{\min} = 0.01$ and $l_{\max} = 100$. The curves describing the densities of the cloud and shadow phases are shown in Fig. 6.1. A striking broadening of the coexistence gap can be detected, mainly due to a dramatic increase of the concentration of the nematic cloud phase. In Fig. 6.1(b) we see that the volume fraction of the nematic cloud phase increases by several orders of magnitude at $\sigma > 0.5$. Although the nematic shadow curve crosses the corresponding isotropic cloud curve at $\sigma \approx 0.5$ in Fig. 6.1(a), the volume fraction (and hence the mass density) of the nematic shadow remains higher than that of the isotropic cloud phase throughout the phase diagram as we see in Fig. 6.1(b). Fig. 6.2(a) shows the extent of fractionation, i.e. the repartitioning of the long and short rods, among the coexisting phases at the onset of phase separation. A marked feature is the rapid increase of the average length in the nematic shadow around some "transitional" polydispersity $\sigma_t \simeq 0.5$. This indicates that the nematic phase becomes preferably populated by the longest rods in the system. Note that there is a similar
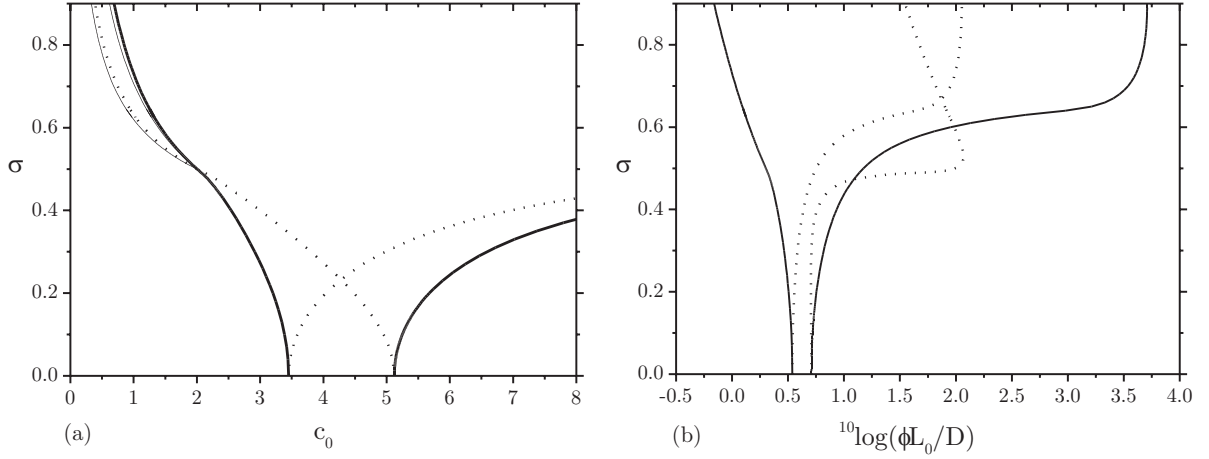
FIGURE 6.1. (a) Concentrations of the isotropic and nematic cloud phases (solid lines) and the corresponding shadow phases (dotted lines) plotted against (on the vertical axis) the polydispersity σ of a Schulz parent with $l_{\min} = 0.01$ and $l_{\max} = 100$. The isotropic cloud curve is the one with the lowest concentration. In the monodisperse limit ($\sigma = 0$) the isotropic cloud point meets the shadow of the nematic cloud point and vice versa. The thin solid lines are the limiting curves for $l_{\max} \to \infty$, given by Eq. (6.43) in Appendix B. (b) Logarithm of the scaled volume fraction $\phi L_0/D$ plotted versus the parent polydispersity σ on the vertical axis. Note the dramatic increase of the volume fraction of the nematic cloud phase.
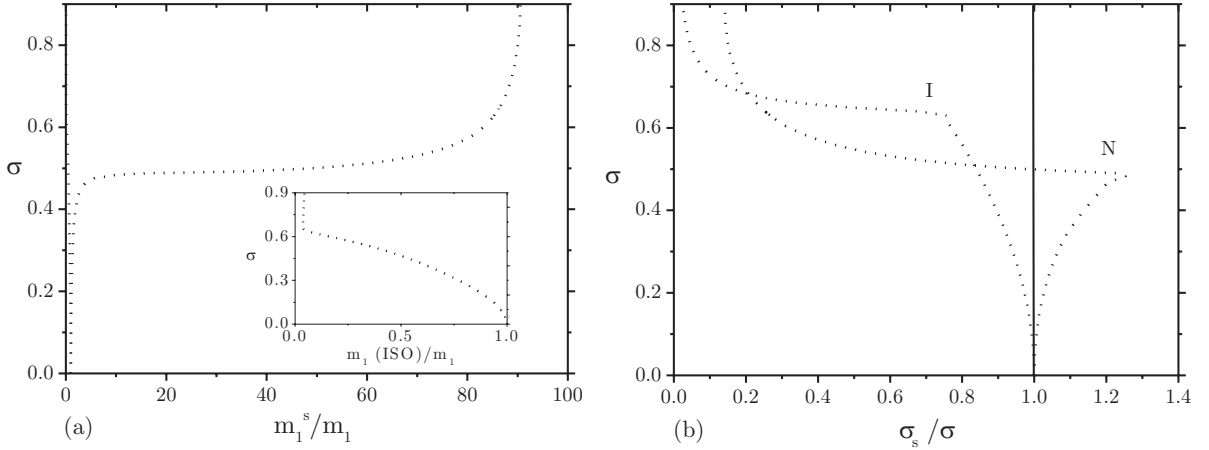
FIGURE 6.2. (a) Average length $\langle l \rangle = m_1^s$ in the isotropic and nematic shadow phases relative to the average length m_1 in the cloud phase plotted against (on the vertical axis) the polydispersity σ of a Schulz parent with $l_{\min} = 0.01$ and $l_{\max} = 100$. The inset shows the relative average length in the isotropic shadow phase (corresponding to the nematic cloud point). (b) Polydispersity of the isotropic and nematic shadow phases σ_s (relative to the parental one σ) plotted against σ. Note the kinks in the isotropic and nematic branches around $\sigma \approx 0.65$ and 0.5, respectively.

Figure 6.3. Normalized length distributions in the nematic shadow phases $p^{(N)}(l)$ for various parent polydispersities σ of the same Schulz parent as in the previous figures.

effect in the *isotropic* shadow phase around $\sigma_t \simeq 0.7$ where the *shortest* rods completely dominate the isotropic shadow phase at higher polydispersities. The same effects are reflected somewhat clearer in Fig. 6.2(b) showing the evolution of the polydispersity of the shadow phases. At $\sigma = \sigma_t$, the polydispersity of the shad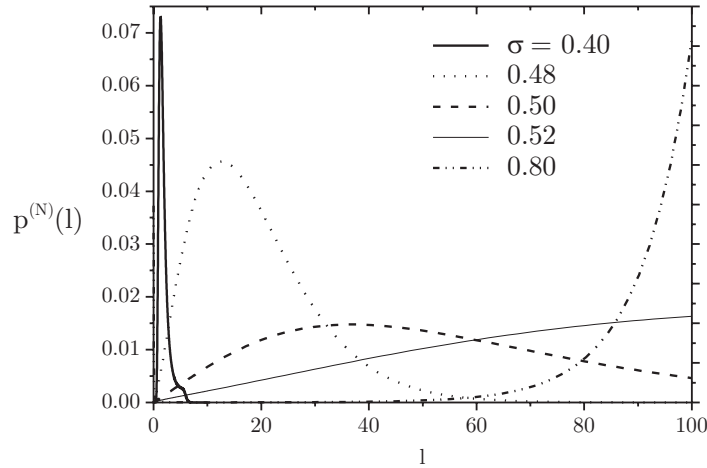ow phases show a kink. The strong decrease at higher σ is due to the effect that the shadow phases become more and more enriched in either the longest or the shortest rods in the distribution. The dramatic change of the composition across the σ-range is shown explicitly in Fig. 6.3 where we have depicted the normalized length distributions in the nematic shadow phase for various σ. A similar picture is obtained for the distributions in the isotropic shadow phase (not shown here) but with the peak of the distribution shifting rapidly towards the lower cutoff length $l_{\min} = 0.01$.

In summary, we can state that there are two fractionation regimes for the onset of phase separation. First, at low polydispersities ($\sigma < \sigma_t$) moderate fractionation is observed and the shadow phases are mainly populated by rods with slightly higher (or lower) than average length. Second, at higher polydispersity ($\sigma > \sigma_t$) strong fractionation occurs such that the shadow phases are completely dominated by the longest (or shortest) rods in the distribution. In a small interval around $\sigma = \sigma_t$ the location of the peak of the length distribution shifts rapidly, upon increasing σ, from a value slightly different from one (pertaining to the low-σ regime) to a value close to the the cutoff length (corresponding to the high-σ regime).

So far, we have only discussed the results for a single set of cutoff lengths. Although the results for different cutoff lengths can be significantly different, particularly in the "cutoff-dependent" regime $\sigma > \sigma_t$ [106], the global phase behaviour remains qualitatively the same. Therefore we conclude that the aforementioned fractionation scenario generally holds for any Schulz parent with sufficiently extreme cutoff lengths ($l_{\min} \ll 1$ and $l_{\max} \gg 1$). An interesting limiting case however is the behaviour for Schulz parents with infinitely large cutoff lengths. For this specific case, we could obtain simple scaling
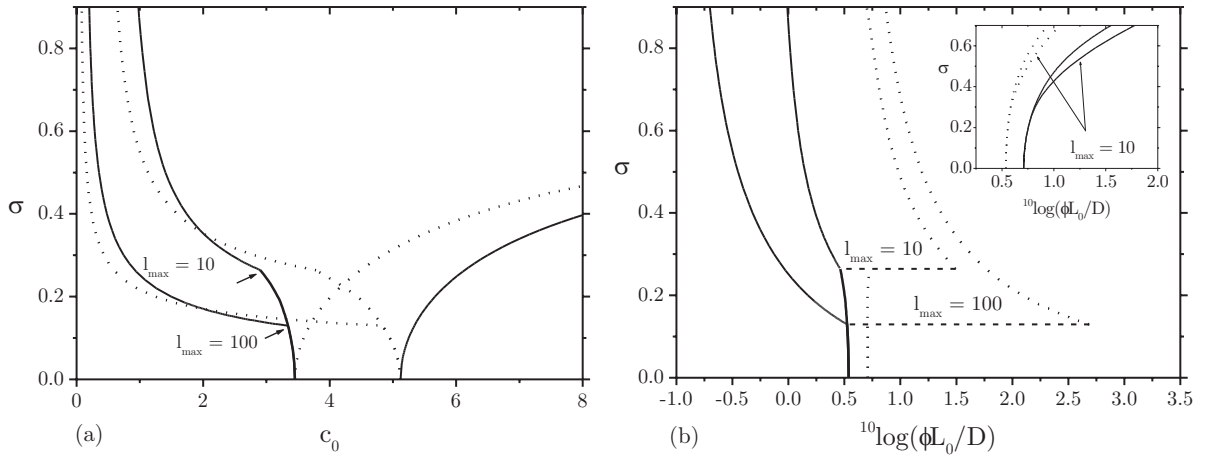
FIGURE 6.4. (a) Concentrations of the isotropic and nematic cloud phases
(solid lines) and the corresponding shadow phases (dotted lines) plotted against
(on the vertical axis) the polydispersity σ of a log-normal parent distribution
with the same lower cutoff length $l_{min} = 0.01$ but two different higher cutoff
lengths, $l_{max} = 10$ and 100. The isotropic cloud curve is the one with the lowest
concentration. The nematic cloud curve and the associated isotropic shadow
curve are insensitive to the value of l_{max} on this scale and therefore the results
for $l_{max} = 10$ and 100 overlap. At the kink in the isotropic cloud curve the
isotropic cloud phase coexists with two nematic phases differing in composition.
(b) Logarithm of the scaled volume fraction $\phi L_0/D$ plotted versus the parent
polydispersity σ on the vertical axis. The main graph shows the results for the
isotropic cloud and the nematic shadow phase, the inset for the nematic cloud
and its isotropic shadow phase.

relations which describe the global behaviour of the nematic shadow in the limit of an
unbounded Schulz parent, i.e. $l_{max} \rightarrow \infty$. The scaling analysis, worked out briefly in
Appendix B, is closely related to a more elaborate analysis presented in Ref. [107] for
the exact Onsager model. In particular, we show in Appendix B that the Gaussian
Ansatz must yield the *exact* high-cutoff scaling relations. The reason for this is that
our high-cutoff scaling form for $p^{(N)}(l)$ (for the nematic shadow phase) is completely
analogous to the exact scaling result.

Finally, we remark that we do not observe a real jump in the shadow curves (and a
kink in the associated cloud curves), as found in Ref. [107]. The presence of a jump in
the shadow curve indicates that, at some point, the isotropic cloud phase coexists with
two different nematic shadow phases and that a region of stable triphasic equilibria
develops. Therefore we conclude that, within the Gaussian Ansatz, the Schulz form
does not give rise to a three-phase separation, at least up to $l_{max} = 100$.

6.4.2. Log-normal distributions

The results for the log-normal case are presented in Figs. 6.4 and 6.5. The cloud
and shadow curves shown in these figures correspond to log-normal parent distributions
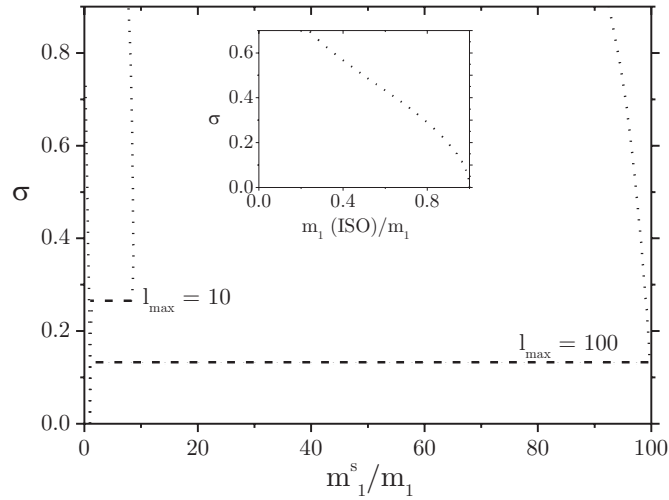with the same lower cutoff length $l_{min} = 0.01$ but two different higher cutoffs $l_{max} = 10$

FIGURE 6.5. Average length m_1^s in the shadow phases relative to the parental one m_1 for log-normal parent distributions with cutoff lengths $l_{\max} = 10$ and 100 as a function of the parent polydispersity σ. The inset shows the relative average length in the isotropic shadow phase (corresponding to the nematic cloud point). Also here, the results for $l_{\max} = 10$ and 100 overlap.

and 100. We see that the phase behaviour is globally the same as for the Schulz case. There is a generic broadening of the biphasic region (Fig. 6.4(b)) and a very pronounced fractionation effect, particularly among the isotropic cloud and nematic shadow phases, as visible in Fig. 6.5. At low polydispersities the distribution in the nematic shadow phase is very similar to the parent distribution (albeit with a higher average length). At higher polydispersities, however, we enter a regime characterized by extreme fractionation, i.e. the nematic shadow phase is dominated by the longest rods in the distribution. Remarkably, we do not see a similar transition in the isotropic shadow phase in Fig. 6.5, as we did in the Schulz case. This implies that fractionation from the nematic cloud phase is much weaker for log-normal distributions than for Schulz ones.

A crucial difference with the previous results is that the transition between the regimes occurs discontinuously. At the transition polydispersities σ_t the isotropic cloud curves show a kink and the associated nematic shadow curves exhibit a jump. Precisely at the kink, the isotropic cloud phase coexists with two different nematic phases, one containing mostly rods with slightly higher than average length (denoted by N_I) while the second one (N_{II}) is dominated by the longest rods in the distribution. Therefore, this special point indicates the presence of a stability region for $I - N_I - N_{II}$ triphasic equilibria for log-normal distributions. In Fig. 6.5 we see that the position of the kink (in terms of σ_t) rapidly shifts to lower polydispersities as $l_{\max}$ increases. From this, we anticipate that the triphasic equilibrium must set in at almost zero polydispersity (near monodisperse systems) for very large cutoff lengths.

Like for the Schulz case, we can obtain information about the global phase behaviour for parent distributions at infinite cutoff lengths $l_{\max}$ from the high-cutoff scaling results,

shown in Appendix B. The most important outcome is that the concentrations of the isotropic cloud and nematic shadow phases go to zero for large cutoff length rather than approaching asymptotic forms such as in the Schulz case. Furthermore, it is shown explicitly that fractionation between the isotropic cloud and nematic shadow phases is stronger than for the Schulz case.

So far, we have only looked at the onset of phase equilibrium by analyzing the properties of the cloud and shadow phases. The next step is to explore the coexistence region in more detail. An intriguing issue is to verify the region of stability for the isotropic-nematic-nematic triphasic region for the log-normal case. This will be dealt with in the next section, where we discuss the phase diagram for a log-normal parent with cutoff length $l_{\max} = 10$ in more detail.

6.5. Inside the I-N coexistence region

Across the coexistence region the equilibrium length distributions of the coexisting phases, which originate from a parent phase with a prescribed distribution $p^{(0)}(l)$, change continuously as the overall density of the parent $c_0^{(0)}$ is changed. In the actual calculations however it is more convenient to impose the fraction γ occupied by the nematic phase rather than $c_0^{(0)}$ and calculate the corresponding densities self-consistently. In Figs. 6.6 and 6.7 we show the properties of the coexisting isotropic and nematic phases for a log-normal parent distribution with polydispersities $\sigma = 0.4$ and $\sigma = 0.3$, respectively. Fig. 6.6(a) shows that the average length in the nematic daughter phase decreases rapidly in the regime $c_0^{(0)} \lesssim 3$ whereas only weak changes are notable at higher $c_0^{(0)}$. Furthermore, we see that the volume occupied by the nematic phase is extremely small in the former regime. The same feature is observed in the volume fraction representation in Fig. 6.6(b). In particular, the non-monotonicity of the nematic branch is reflected somewhat clearer here. The fact that the isotropic branch runs extremely close to the dilution line for $c_0^{(0)} < 3$ indicates that the fraction of nematic phase formed must indeed be very small. The rather exotic oscillations in the behaviour of the polydispersities of the daughter phases in Fig. 6.6(c) reflect a dramatic change of shape of the length distribution in the nematic phase in the first part ($\gamma < 10^{-2}$) of the dilution trajectory as shown in Fig. 6.6(d). Note that the distribution of the nematic shadow phase is in fact bimodal, with a small peak around $l = 1$ and a much larger one at $l = l_{\max}$. When the overall density is increased the second peak shifts to lower values of l and eventually coincides with the first peak. When the overall density has reached about $c_0^{(0)} = 4$ (corresponding to a nematic phase volume fraction of about 10 %) the distribution of the nematic phase resembles the parental one, albeit with a slightly higher average length. The phase behaviour scenario sketched above is qualitatively similar to the one reported in Ref. [106] for the $\mathcal{P}_2$-model.

In Fig. 6.7(a) we have plotted the evolution of the average length for a parent with polydispersity $\sigma = 0.3$. A peculiar behaviour is observed, which is also reflected in Fig. 6.7(b) where the coexistence pressure is plotted versus γ. Clearly, there is a region where the pressure decreases as a function of γ which suggests an instability (or van der
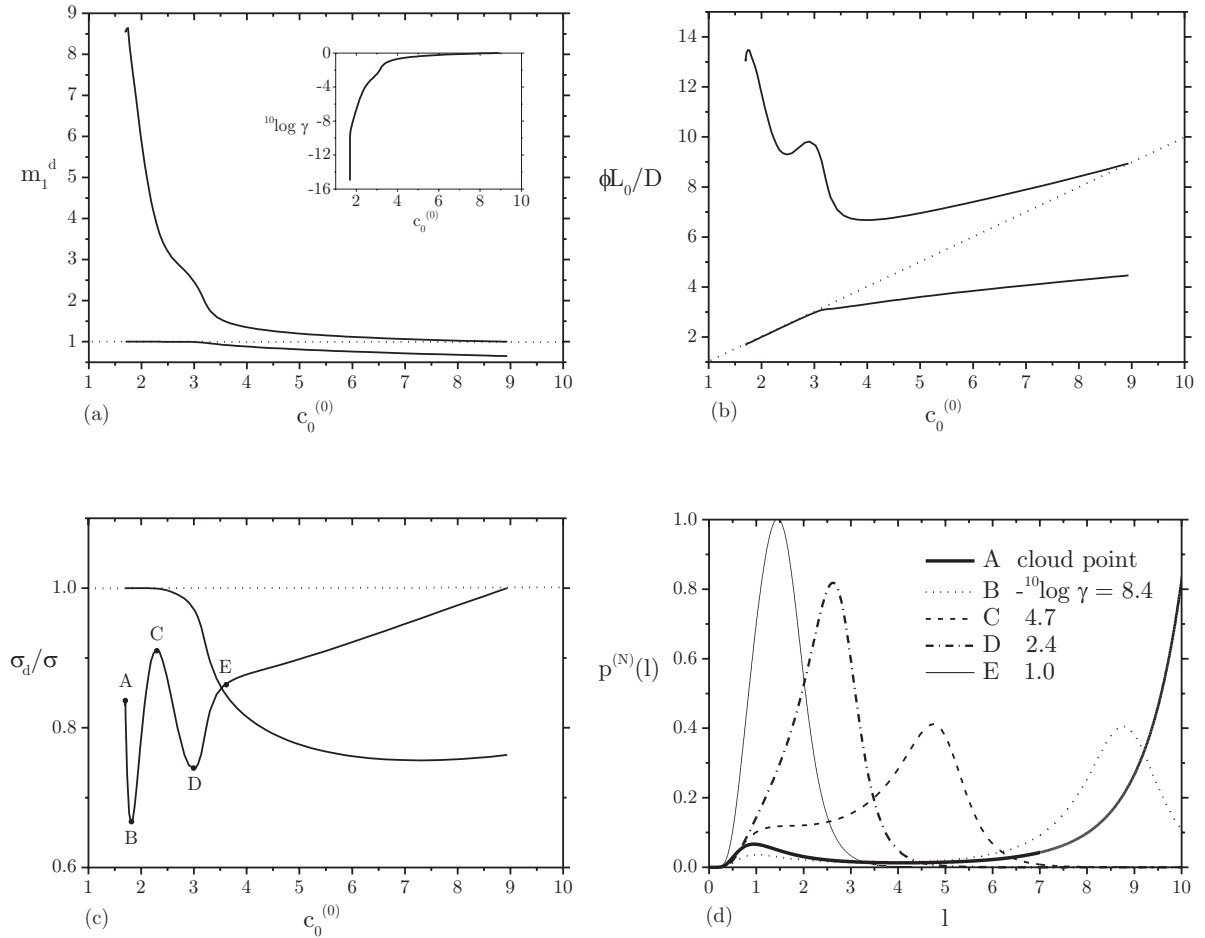
FIGURE 6.6. (a) Average rod length m_1^d in the coexisting daughter phases (solid lines) plotted versus the concentration $c_0^{(0)}$ of the parent across the coexistence region for a log-normal parent with $l_{min} = 0.01$ and $l_{max} = 10$ at fixed polydispersity $\sigma = 0.4$. The curve for which $m_1^d > 1$ is the nematic branch. The dotted line corresponds to $m_1 = 1$ for the parent phase. The inset shows the (logarithm of the) fraction γ of the system volume occupied by the nematic phase. Note that the amount of nematic phase is extremely small in the region $c_0^{(0)} < 3$. (b) Evolution of the scaled volume fraction $\phi L_0/D$ in the coexisting daughter phases across the coexistence region for the same parent. The nematic branch is the one with the highest volume fraction. The dilution line is indicated by the dotted line. (c) Relative polydispersity σ_d/σ of the coexisting daughter phases across the coexistence region for the same parent. By definition, the dilution line (dotted) is given by $\sigma_d/\sigma = 1$. (d) Plot of the normalized length distributions of the nematic phase across the coexistence region corresponding to the positions A through E in (c).

Waals) loop indicating a possible demixing of the nematic phase. In Appendix C we show that the local extrema in the osmotic pressure in Fig. 6.7(b) can be connected to spinodal points for the nematic phase which indicate that the coexisting nematic phase indeed becomes locally (and hence also globally) unstable. In the region between the
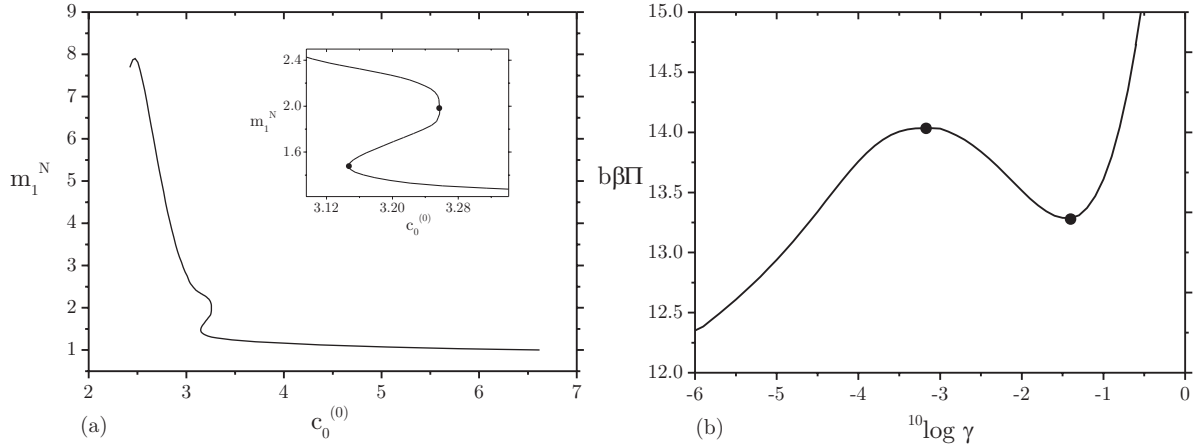
FIGURE 6.7. (a) Average rod length m_1^d in the nematic phase across the coexistence region for a log-normal parent with $\sigma = 0.3$ and cutoff lengths $l_{min} = 0.01$ and $l_{max} = 10$. The inset shows a hysteresis loop indicating a local instability of the nematic phase. (b) Coexistence pressure across the coexistence region for the same parent. In the region where $\delta(b\beta\Pi)/\delta\gamma < 0$ the nematic phase is locally unstable with respect to a nematic-nematic demixing.

stationary points $(\delta(b\beta\Pi)/\delta\gamma = 0)$, the coexistence between the isotropic and a single nematic phase also becomes unstable such that a triphasic isotropic-nematic-nematic $(I - N_I - N_{II})$ demixing occurs.

It should be stressed that the actual onset of the three-phase separation is marked by *binodal* points which we have not located in this study, except for the kink at σ_t. In general, binodal points are located at a lower concentration than the spinodal points so that the demixing usually occurs well before the point where the system becomes locally unstable. This becomes clear in Fig. 6.8 where we show the details of the phase diagram in the vicinity of the kink including the spinodal curves (in terms of $c_0^{(N)}$) for the coexisting nematic phase. At the kink $\sigma_t = 0.264$ the three-phase separation sets in right at the isotropic cloud point but the spinodal points are located at higher concentrations. An important feature in Fig. 6.8 is the presence of an upper consolute (or critical) point at $\sigma = 0.373 \pm 0.001$ where the spinodal curves meet. This means that the region of stable triphasic equilibria does not extend up to large parent polydispersities but closes off at the consolute point.

Another remarkable observation is that the spinodal curves have a lower consolute point $\sigma = 0.24 \pm 0.005$, located *below* the kink. This means that the three-phase region does not set in at the kink ($\sigma = \sigma_t$) as one may naively assume, but at a somewhat smaller parental polydispersity. Consequently, the phase behaviour we can infer from Fig. 6.8 becomes rather exotic. Several scenarios can be distinguished. At low polydispersities (up to the lower consolute point) there is a common isotropic-nematic phase separation involving a moderately fractionated N_I-phase. When the parental σ crosses the lower consolute point the coexisting N_I-phase demixes at some point on the dilution trajectory (called the onset density) and a second nematic N_{II} emerges.
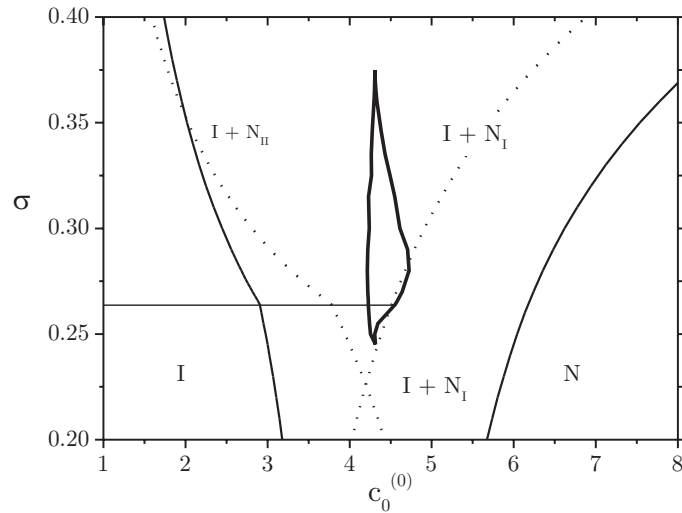
FIGURE 6.8. Phase diagram for log-normal parent distribution with cutoff lengths $l_{\min} = 0.01$ and $l_{\max} = 10$. The thick curves delimit the spinodal instability region for the coexisting nematic phase (in terms of the concentration of the *nematic* phase $c_0^{(N)}$). The region is bounded by a lower ($\sigma = 0.24 \pm 0.005$) and an upper ($\sigma = 0.373 \pm 0.001$) consolute point.

There will be a small density interval where all three phases coexist, but N_{II} eventually disappears and a regular biphasic $I - N_I$ is recovered. As we approach the kink, the onset density shifts towards the isotropic cloud curve. At the kink, two infinitesimal fractions of the two nematic phases are formed right at the cloud point. At $\sigma > \sigma_t$ a different scenario is encountered; a strongly fractionated N_{II}-phase (containing the longest rods) is split off first at the isotropic cloud point. At higher concentrations (when I and N_{II} coexist in finite amounts) a second nematic phase (N_I) is formed and an $I - N_I - N_{II}$ triphasic equilibrium develops. Upon slightly further concentrating the system, the N_{II}-phase eventually disappears and regular $I - N_I$ biphasic equilibria are recovered. Finally, at parent polydispersities above the upper consolute point $\sigma > 0.373$ the behaviour of the pressure as a function of γ does not show any stationary points (cf. Fig. 6.6(a)) so that we may assume that the isotropic-nematic equilibria remain stable throughout the region. Upon concentrating the isotropic phase a strongly fractionated nematic phase (reminiscent of the N_{II} phase) is formed initially but the composition of this phase evolves *gradually* towards a N_I-type nematic as the biphasic region is crossed.

6.6. SUMMARY AND DISCUSSION

We have numerically investigated Onsager's second virial theory for polydisperse hard rods within the Gaussian Ansatz. The onset of isotropic-nematic phase separation is obtained from the cloud and shadow curves, which delimit the coexistence region. Within the same numerical framework, we could also explore the properties of the coexisting phases across the coexistence region. In this work, we focussed on

systems of polydisperse hard rods whose lengths can be described by a Schulz or a log-normal distribution. The basic difference between these two forms is that the fat-tailed log-normal one contains a significantly higher fraction of longer rods. For numerical and consistency purposes we truncated the distributions at both ends at sufficiently low and high cutoff lengths. Using truncated distributions is also justifiable from an experimental point of view. For parent distributions of the Schulz type the phase diagram contains two fractionation regimes. First, at low parent polydispersities moderate fractionation occurs and the average rod lengths in the isotropic and nematic shadow phases are not much different from the average length in the parental cloud phase. Second, at higher parental σ fractionation effects are extremely strong and the isotropic and nematic shadow phases are completely dominated by respectively the longest and the shortest rods present in the system.

For the exact Onsager model, Speranza and Sollich [107] very recently predicted a kink in the isotropic cloud curve (and a jump in the corresponding nematic shadow curve) for Schulz parents with cutoff lengths $l_{max} > 50$. The presence of this kink indicates a region of stable isotropic-nematic-nematic triphasic equilibria. Here we do not find any indication for such a three-phase separation for Schulz parents at least up to $l_{max} = 100$. The discrepancy may be due to the Gaussian Ansatz, which implies that the ODFs are not represented by their correct equilibrium forms. Moreover, the Schulz form might be a borderline case since its tail is too modest to induce a strong demixing but too "fat" to suppress it completely so that the presence of a kink in the isotropic cloud curve depends quite sensitively on the precise representation of the ODF.

Although the Gaussian ODF is not a solution of the exact stationarity condition for the ODF, it does satisfy the exact high-density scaling relation [35]. This means that the properties of highly ordered nematic states are described very well by the Gaussian form. In fact, the description becomes *exact* for infinitely aligned states. A manifestation of this is the osmotic pressure for the nematic phase, Eq. (6.21), which is the *exact* high-density result [35]. Consequently, for our polydisperse systems, we expect the Gaussian Ansatz to work increasingly well both for highly concentrated nematic phases and ones that are dominated by the longest rods. In both cases, the nematic alignment of all species is expected to be very pronounced such that the use of the scaling ODF (for all l) is justified. To verify this notion, we have plotted the variational parameter as a function of length, for both the nematic shadow phase and the nematic cloud phase corresponding to a Schulz parent in Fig. 6.9. Since the Gaussian ODF is expected to be the least correct for the shortest rods (which show the weakest alignment), we focus on the interval $l < 1$. In order for the results to be self-consistent, the alignment must be strong enough and the variational parameter must therefore be sufficiently large (say $^{10}\log \alpha > 1$) for all lengths. Fig. 6.9(a) shows that this is not entirely the case; in the regime of low fractionation the shortest rods (with $l \lesssim 0.4$) are not sufficiently aligned by the longer rods so that the Gaussian description fails here. In the regime $\sigma > 0.5$, which is physically the most interesting one, the ordering of the short rods is much higher due to the presence of very long rods in the nematic shadow phase, and the
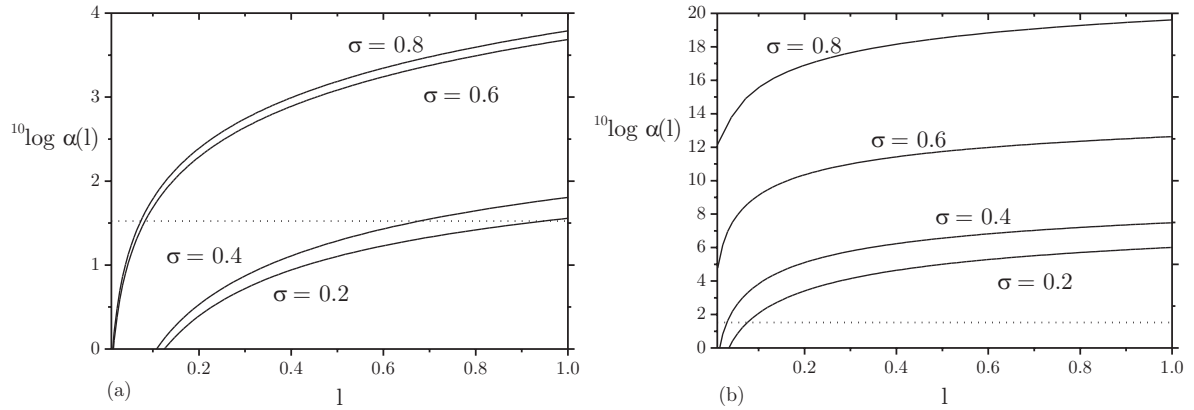
FIGURE 6.9. Behaviour of the Gaussian variational parameter $\alpha(l)$ for the shortest rods of a Schulz parent with $l_{\min} = 0.01$ and $l_{\max} = 100$ (see also Fig. 6.1(a)). (a) Results for the nematic shadow phase at various σ. (b) Same for the nematic cloud phase. For comparison the result for the monodisperse system ($\alpha = 33.4$) [5] is indicated by the dotted line.

Gaussian Ansatz is fully justified. Similar for the nematic cloud phase in Fig. 6.9(b) we see that the shortest rods are not well represented by the Gaussian ODF at low σ but much better at $\sigma > \sigma_t$ where the variational parameter increases several orders of magnitude due to a dramatic increase of the concentration of the nematic cloud phase (see also Fig. 6.1(b)). Obviously, for any rod length significantly larger than $l_{\min}$ the Gaussian ODF works very well because α generally becomes extremely large for any σ. Therefore we conclude that given the fact that the composition of the nematic phases is dominated by the longest rods, particularly in the physically relevant cutoff-dependent regimes, the Gaussian approximation is an appropriate tool in our study.

We now turn to the log-normal case. The fractionation scenario we observe there is qualitatively the same as the one for the Schulz case; weak fractionation occurs at low σ where the distributions in the shadow phases are reminiscent of the parental one, but dramatic segregation effects take place above some threshold σ, particularly between the isotropic cloud and the nematic shadow phase. A crucial difference with the results for the Schulz case however is that the transition between the two fractionation regions shows a discontinuity at $\sigma = \sigma_t$. At this point, the isotropic cloud curve shows a kink which corresponds to a jump in the nematic shadow phase. The jump indicates that an isotropic cloud phase must coexist with two different shadow phases, one containing mostly rods of slightly higher than average length (the N_I-phase) and the other one predominantly containing very long rods (the N_{II}-phase). For log-normal distributions with a moderate cutoff-length $l_{\max} = 10$ we found that the kink is located at a fairly low polydispersity $\sigma_t = 0.264$. This value will decrease for larger cutoff lengths and eventually go to zero when $l_{\max}$ approaches infinity. This indicates that adding a very small fraction of long rods to a weakly polydisperse system of much shorter rods can already induce a three-phase demixing. A similar effect is observed in binary mixtures of long and short hard rods with sufficiently large length ratios [36].

For the case $l_{max} = 10$ we could infer a spinodal instability of the nematic phase from analyzing the phase properties along the coexistence region, in particular the evolution of the coexistence pressure. The determination of the spinodal points has not been performed rigorously but merely indirectly by locating the stationary points in the osmotic pressure (see Appendix C for a discussion). The result of this analysis is that the triphasic area does not extend up to very large parent polydispersities but terminates at a consolute point located at $\sigma = 0.373 \pm 0.001$. A remarkable feature is that the spinodal boundaries have a lower consolute point located *below* the kink, namely at $\sigma = 0.24 \pm 0.005$, indicating that the isotropic-nematic-nematic triphasic region does not open up precisely at the kink but at a slightly lower parental polydispersity.

We have not been able to determine the corresponding binodal points, which mark the actual onset of three-phase separation from the isotropic-nematic biphasic equilibria. Considering the results for the approximate Onsager $\mathcal{P}_2$-model, as numerically analyzed by Speranza and Sollich [106], we expect these triphasic equilibria to be limited to a very small density interval across the coexistence region, which makes it very hard to observe the phenomenon in experiment. Another problem is that the fraction of the system volume occupied by the nematic phases is predicted to be at the most 0.1 %, so that it will be very difficult to distinguish (or even detect) the two different nematics. Therefore we must conclude that, although the log-normal distribution contains sufficient long rods to induce a demixing of the nematic phase, the (mole) fraction of these rods is too small to give rise to an observable fraction of the demixed nematic phases.

Experimentally, phenomena such as a broadening of the biphasic region and a fractionation effect have been observed unequivocally in a number of experimental studies [108–111]. Observations of triphasic isotropic-nematic-nematic equilibria were however only reported for systems whose length distributions appear to be more or less bimodal rather than unimodal. These bimodal shapes were either accomplished deliberately by mixing species with different lengths, as done by Itou [111] with semiflexible schyzophyllan rods or caused by the presence of large aggregates as found by Kajiwara *et al.* [112] in systems of rigid imogolite rods. Buining *et al.* [110] observed the formation of second nematic phase in systems of polymer-coated (hard) boehmite rods, albeit a long time after the two-phase isotropic-nematic phase separation had finished. Also there, the triphasic demixing is probably due to the presence of a small number of very long rods or aggregates present in the system causing the length distribution to be (slightly) bimodal [113]. The experimental results therefore seem to indicate that having a three-phase separation with observable fractions of all phases requires some degree of bimodality (with a sufficiently large length ratio between the short and long species) in the parental length distribution. Hence, an intriguing issue left open for future investigation is the question how the triphasic phenomenon predicted for the log-normal distributions changes for a parent distribution with a slightly bimodal shape (e.g. with a small second peak just below l_{max}). In particular, a bimodal distribution may give rise to enhanced fractionation behaviour and more pronounced triphasic equilibria than predicted for the unimodal log-normal form.

Appendix A: Numerical procedure

The self-consistency equations for $\tilde{\alpha}(l)$ and $\tilde{\mu}_{ex}^{(N)}(l)$, Eqs. (6.8) and (6.15), were solved using a numerical grid of lengths. The iterative scheme we used is analogous to the one described by Herzfeld *et al.* [33] for computing the numerically exact equilibrium ODF of the monodisperse Onsager model. The $l-$interval $[l_{\min}, l_{\max}]$ was discretized into N (not necessarily equal) parts. The mesh size must be chosen very carefully, particularly for large $l_{\max}$, because the distributions become considerably peaked at low polydispersities. Therefore, for parent polydispersities lower than approximately $\sigma = 0.25$ we chose to divide the integration interval into three regimes. The interval $[1-8\sigma^2, 1+8\sigma^2]$ in the vicinity of the peak, where the distribution changes rapidly, was discretized into $\frac{3}{5}N$ equal parts, and the intervals $[l_{\min}, 1-8\sigma^2]$ and $[1+8\sigma^2, l_{\max}]$, where the distribution is generally much smoother, were both discretized into $\frac{1}{5}N$ equal parts. For parent polydispersities larger than $\sigma = 0.25$ the entire interval was discretized into N equal parts. It proved to be sufficient to use $N = 150$ in order to obtain quantitatively reliable results. However, for the calculation of the full phase split (Sec. 6.3.3) a smaller mesh size ($N = 50$) was used to limit the computational burden. Increasing the number of mesh points led to only marginally different results in this case while the calculation time increased dramatically. For small polydispersities we used Eqs. (6.10) and (6.16) as initial guesses and the successive iteration was performed until the following convergence criteria were satisfied:

$$\max_{n=1,\dots N} |\tilde{\alpha}(l_{n+1}) - \tilde{\alpha}(l_n)| < 10^{-6},$$

$$\max_{n=1,\dots N} \left| \tilde{\mu}_{ex}^{(N)}(l_{n+1}) - \tilde{\mu}_{ex}^{(N)}(l_n) \right| < 10^{-6}. \tag{6.36}$$

After each iteration step 10% of the new solution had to be added to 90 % of the previous one for the next iteration step to ensure the convergence of the method.

The iteration algorithm we figured out to calculate the phase equilibria can be described as follows. First, the corresponding equilibrium forms for $\tilde{\alpha}(l)$ and $\tilde{\mu}_{ex}^{(N)}(l)$ were calculated for a given set of starting concentrations. These results were then put into the self-consistency equations for the cloud and shadow concentrations to obtain new values. These equations were obtained by recasting the self-consistency conditions for the moments (e.g. Eq. (6.28)) in an iterative form such that the concentrations could be calculated by a simple fixed-point iteration. Finally, for the new concentrations, corresponding forms for $\tilde{\alpha}(l)$ and $\tilde{\mu}_{ex}^{(N)}(l)$ were computed and substituted again into the self-consistency equations. This procedure was repeated until all concentrations had converged to within 10^{-5}. To ensure convergence of this iteration loop a damping percentage of 80 % was used, which means that only 20 % of the change was retained at each iteration step.

Appendix B: High-cutoff scaling results

In this Appendix we focus on the properties of the nematic shadow phase in the cutoff-dependent regime ($\sigma > \sigma_t$) for systems with infinite cutoff lengths. For the exact

Onsager model, Speranza and Sollich [107] made a detailed analysis of these properties based upon the high-density (and high-cutoff) scaling forms of the exact nematic ODF. Here, we will not reproduce the analysis but merely show that the scaling form for the length distribution in the nematic shadow phase in the limit $l_{max} \to \infty$ is *analogous* to the one obtained in Ref. [107]. Consequently, all scaling properties which follow from the Gaussian approximation must be *exactly the same* as the ones derived from the exact high-cutoff scaling results.

The first step is to solve the coupled set of consistency equations, Eqs. (6.8) and (6.15). In order to obtain analytic solutions for these nonlinear integral equations we exploit the fact that the nematic shadow phase is completely dominated by the longest rods in the system at $\sigma > \sigma_t$. When the cutoff length increases, the length distribution in the nematic shadow will be more and more peaked at $l = l_{max}$. In the limit of infinite l_{max} it is therefore justified to use the Ansatz $p^{(N)}(l) = \delta(l - l_{max})$ which suggests an effectively monodisperse nematic shadow phase only containing the longest rods in the system. Substituting the delta-function in Eqs. (6.8) and (6.15) allows us to obtain asymptotic forms for the Gaussian variational parameter $\tilde{\alpha}(l)$ and the excess chemical potential $\tilde{\mu}_{ex}^{(N)}(l)$ of the nematic shadow phase. These expressions now read

$$\tilde{\alpha}(l) = l_{max}^4 \mathcal{F}(l/l_{max}), \tag{6.37}$$

$$\tilde{\mu}_{ex}^{(N)}(l) = \frac{l}{l_{max}} 2^{3/2} \sqrt{1 + \mathcal{F}^{-1}(l/l_{max})}, \tag{6.38}$$

where $\mathcal{F}$ is given by

$$\mathcal{F}(l/l_{max}) = \frac{1}{2} \left[\sqrt{1 + 8 \left(\frac{l}{l_{max}} \right)^2} - 1 \right]. \tag{6.39}$$

Note that $\mathcal{F}(l/l_{max})$ always has a value between zero and unity. A close inspection reveals that the variational parameter $\tilde{\alpha}(l)$ scales as $\tilde{\alpha}(l) \propto l_{max}^4$ whereas the excess chemical potential $\tilde{\mu}_{ex}^N(l)$ remains of the order $\mathcal{O}(1)$ for all lengths. Using this in Eq. (6.27) we can write down a scaling expression for the length distribution in the nematic shadow phase, which in its general form reads

$$p^{(N)}(l) = \text{cst} \frac{c_0^{(0)}}{(c_0^{(N)})^3} l_{max}^{-4} p^{(0)}(l) \exp \left[2c_1^{(0)} l - \mathcal{W}(l/l_{max}) \right], \tag{6.40}$$

where $\mathcal{W}$ is a contribution of the order $\mathcal{O}(1)$:

$$\mathcal{W}(l/l_{max}) = \ln \mathcal{F}(l/l_{max}) + \tilde{\mu}_{ex}^{(N)}(l/l_{max}). \tag{6.41}$$

which attains its maximum $\mathcal{W} = 4$ for $l = l_{max}$. The scaling solution Eq. (6.40) is completely analogous to the one found in Ref. [107], the only differences being the exact form of $\mathcal{W}(l/l_{max})$ and the constant cst. However, since these contributions are both subleading in the limit $l_{max} \to \infty$ they are irrelevant for the rest of the analysis and hence do not influence the scaling results. The similarity between the exact high-density scaling analysis and the Gaussian approximation is also confirmed by the fact

that both theories predict the same scaling result for the nematic osmotic pressure, namely $b\beta\Pi = 3c_0^{(N)}$.

For the sake of completeness, let us now briefly outline the basic results of the high-cutoff scaling analysis. For a comprehensive treatment of this subject the reader is referred to Ref. [107]. For a Schulz parent, we may use Eq. (6.33) in Eq. (6.40) to obtain

$$p^{(N)}(l) = \mathcal{K}_N l_{\max}^{-4} l^z \exp\left[\varepsilon l - \mathcal{W}(l/l_{\max})\right], \tag{6.42}$$

where $\varepsilon = 2c_1^{(0)} - (z + 1)$ and $z = \sigma^{-2} - 1$. For very large l the exponent $\exp[\varepsilon l]$ will be the dominating contribution. At $\sigma > \sigma_t$, the nematic shadow is supposed to be dominated by the longest rods and the distribution $p^{(N)}(l)$ should therefore be an increasing function of length. This requires ε to be positive and yields the condition $c_0^{(0)} > \frac{1}{2}(z + 1)$. Since the concentration of the cloud phase appears to decrease with increasing $l_{\max}$ this then implies that the isotropic cloud curve (and hence the nematic shadow curve) has a finite lower bound for large cutoff lengths. The limiting solutions, for which $\varepsilon = 0$, therefore read

$$c_0^{(0)} = \frac{1}{2\sigma^2},$$
$$c_0^{(N)} = \frac{1}{6\sigma^2}\left(1 + \frac{1}{2\sigma^2}\right), \tag{6.43}$$

using Eq. (6.29) and setting $c_1^{(0)} = c_0^{(0)}$ for a Schulz parent (Sec. 6.3.4). These results are plotted in Fig. 6.1(a). To be consistent, let us now look for a solution for the transition polydispersity σ_t above which the nematic shadow phase for a Schulz distributed parent is completely dominated by the longest rods. We start with the concentration of the nematic shadow phase which is proportional to the integral over the normalized length distribution, i.e $c_0^{(N)} \propto \int p^{(N)}(l)dl$. From Eq. (6.42) we thus obtain

$$c_0^{(N)} \propto l_{\max}^{-4} \int_0^{l_{\max}} l^z \exp\left[\varepsilon l - \mathcal{W}(l/l_{\max})\right] dl. \tag{6.44}$$

For the sake of convenience we have set $l_{\min}$ equal to zero. Since the integrand is dominated by the exponent $\exp[\varepsilon l]$ for large l we may approximate the integral by bringing all slowly varying contributions in front of the integral sign and evaluating them at $l = l_{\max}$, which gives

$$c_0^{(N)} \propto l_{\max}^{-4} \left. |l^z \exp[-\mathcal{W}(l/l_{\max})]| \right|_{l=l_{\max}} \int_0^{l_{\max}} dl \exp[\varepsilon l]$$
$$c_0^{(N)} \propto l_{\max}^{z-3} \frac{\exp[\varepsilon l_{\max}]}{\varepsilon l_{\max}}. \tag{6.45}$$

The next step is to recast the latter equation into a scaling relation for ε. Taking the logarithm on both sides of Eq. (6.45) gives

$$\varepsilon \propto (3 - z)\frac{\ln l_{\max}}{l_{\max}} + \frac{\ln \varepsilon l_{\max}}{l_{\max}} + \mathcal{O}(l_{\max}^{-1}). \tag{6.46}$$

From the known limits $\varepsilon l_{\max} \to \infty$ and $\varepsilon \downarrow 0$ for $l_{\max} \to \infty$ we can deduce that $\varepsilon l_{\max}$ must increase more slowly than linearly with $l_{\max}$. Consequently, the second and third

terms in Eq. (6.46) are both subleading contributions so that we retain up to leading order

$$\varepsilon \propto (3 - z)\frac{\ln l_{\max}}{l_{\max}}, \tag{6.47}$$

which shows that $\varepsilon l_{\max}$ indeed increases logarithmically rather than linearly as we already anticipated. However, in order to make this result fully self-consistent it is also required that $z < 3$ (and correspondingly $\sigma > 0.5$) since ε must be positive. This means that $\sigma = 0.5$ is a lower bound for the cutoff-dependent regime in the limit $l_{\max} \to \infty$. In other words, the transition from the low fractionation regime to the regime where the nematic shadow is completely dominated by the longest rods occurs *exactly* at $\sigma_t = 0.5$ for Schulz parents with infinitely high cutoff lengths.

We now turn to the average length in the nematic shadow phase which is related to the first moment density $c_1^{(N)} \propto \int l p^{(N)}(l)dl$. Analogously to Eq. (6.45) it follows that $c_1^{(N)} \propto l_{\max}^{z-2} \exp[\varepsilon l_{\max}]/\varepsilon l_{\max}$ and that the average length hence scales as $\langle l \rangle \equiv c_1^{(N)}/c_0^{(N)} \propto l_{\max}$. Since the distribution in the nematic shadow phase is dominated by $\exp[\varepsilon l]$ we expect that only rods whose lengths are of the order $\mathcal{O}(1/\varepsilon)$ smaller than $l_{\max}$ contribute to the average length. We can therefore write

$$\langle l \rangle = l_{\max}\left[1 - \mathcal{O}\left(\frac{1}{\varepsilon l_{\max}}\right)\right], \tag{6.48}$$

and from Eq. (6.47)

$$\langle l \rangle = l_{\max}\left[1 - \mathcal{O}\left(\frac{1}{\ln l_{\max}}\right)\right]. \tag{6.49}$$

This result shows that the average length in the nematic shadow phase in principle diverges for $l_{\max} \to \infty$ but the logarithmic correction causes the actual $\langle l \rangle$ to be significantly lower than $l_{\max}$.

A similar treatment can be given for a log-normal parent distribution. However, the analysis for the log-normal case is even more involved and we will only present the basic results and refer to [107] for details. First, the concentration of the isotropic cloud phase appears to have the following $l_{\max}$-dependence

$$c_0^{(0)} = \frac{\ln^2 l_{\max}}{4\ln(1 + \sigma^2)l_{\max}} + \mathcal{O}\left(\frac{\ln l_{\max}}{l_{\max}}\right), \tag{6.50}$$

which is crucially different from the Schulz case because the concentration of the cloud and shadow phases now go to zero rather than approaching boundary values as in the Schulz case. Second, the average length can be shown to behave as

$$\langle l \rangle = l_{\max}\left[1 - \mathcal{O}\left(\frac{1}{\ln^2 l_{\max}}\right)\right]. \tag{6.51}$$

Similar to the Schulz distribution, the average length scales as $\langle l \rangle \propto l_{\max}$ but the correction term is now considerably smaller which implies that the fractionation effect is much more pronounced for log-normal distributions at $\sigma > \sigma_t$, as we already noticed by comparing Figs. 6.2(a) and 6.5.

Appendix C: Local stability of the nematic phase

In this Appendix we show that the anomalous behaviour of the coexistence pressure in Fig. 6.7(b) can be related to a local instability of the coexisting nematic phase. In particular, we show that the local extrema in the pressure curve correspond to spinodal points which indicate that the nematic phase becomes locally (and hence also globally) unstable across the coexistence region.

In general, a system is locally stable with respect to infinitesimal density fluctuations $(c(l) \rightarrow c(l) + \delta c(l))$ if the following stability criterion is satisfied:

$$\delta^2 f \equiv \int dl \int dl' \frac{\delta^2 f}{\delta c(l) \delta c(l')} \delta c(l') \delta c(l) > 0. \tag{6.52}$$

If $\delta^2 f < 0$ the free energy has negative curvature directions indicating local instability. With the aid of Eq. (6.12), we see that $\delta^2 f$ vanishes if

$$\int dl' \frac{\delta \beta \mu(l)}{\delta c(l')} \delta c(l') = 0, \tag{6.53}$$

which is the spinodal criterion generalized for polydisperse systems [114]. At a spinodal point there is an incipient instability direction $\delta c(l)$ along which the chemical potential functional does not change.

Let us now focus on the evolution of the length distribution of the nematic phase (in coexistence with an isotropic phase) across the coexistence region and denote this distribution by $c^*(l)$. The shape of $c^*(l)$ depends uniquely on the nematic fraction γ, so that the curves in Fig. 6.7 represent trajectories parametrized by γ. To verify the local stability of the nematic phase for a parent with a given polydispersity we have numerically probed small nematic density fluctuations (caused by a small increase $\Delta\gamma$) *along the dilution trajectory* and calculated the corresponding curvature $\delta^2 f^*$ from Eq. (6.52). In order to obtain sufficiently small density variations with adequate precision we enhanced the accuracy of the iteration schemes outlined in Appendix A by several orders of magnitude. The results are shown in Fig. 6.10. Clearly, the nematic phase does not remain locally stable throughout the coexistence region, as indicated by the behaviour of $\delta^2 f^*$. Moreover, we see that the spinodal points ($\delta^2 f^* = 0$), which confine the region of instability, coincide with the stationary points in the pressure as a function of $\log \gamma$.

The relation between the spinodal points and the local extrema in the pressure can easily be established explicitly. Consider an infinitesimal change of the coexistence pressure $\delta(b\beta\Pi)^*$ corresponding to an infinitesimal displacement $\delta c^*(l)$ on the trajectory in Fig. 6.10. The pressure change can be written as

$$\delta(b\beta\Pi)^* = \int dl' \left. \frac{\delta(b\beta\Pi)}{\delta c(l')} \right|_{c^*(l')} \delta c^*(l'). \tag{6.54}$$

We wish to express the pressure change in terms of the (change of the) chemical potential functional. Using the Gibbs-Duhem relation which, generalized to polydisperse systems,
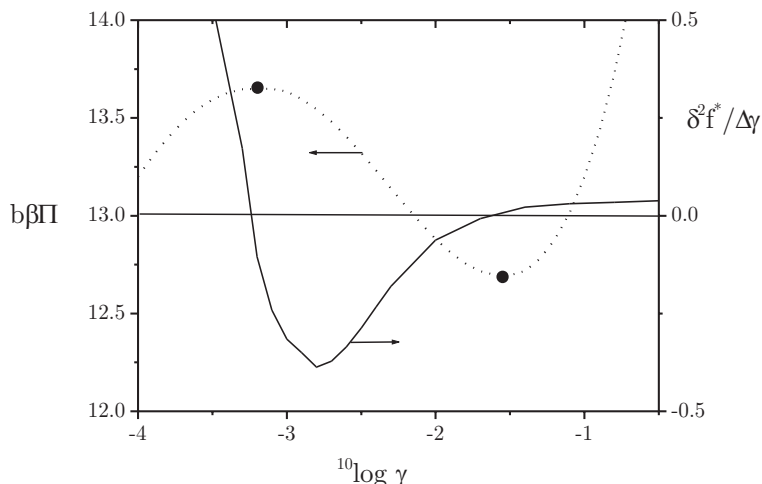
FIGURE 6.10. Coexistence pressure and normalized free energy curvature $\delta^2 f / \Delta\gamma$ of the nematic phase across the coexistence region plotted versus the (logarithm of the) system volume occupied by the nematic phase for a log-normal parent with $l_{\min} = 0.01$, $l_{\max} = 10$ and polydispersity $\sigma = 0.32$.

can be written in terms of functional derivatives

$$\frac{\delta(b\beta\Pi)}{\delta c(l')} = \int dl c(l) \frac{\delta\beta\mu(l)}{\delta c(l')}, \tag{6.55}$$

the pressure change Eq. (6.54) along the trajectory becomes

$$\delta(b\beta\Pi)^* = \int dl c^*(l) \int dl' \left. \frac{\delta\beta\mu(l)}{\delta c(l')} \right|_{c^*(l')} \delta c^*(l'). \tag{6.56}$$

If the system is at a spinodal point (with $\delta^* c(l)$ the instability direction), Eq. (6.53) holds and the pressure change must therefore vanish. Hence the local extrema in the coexisting pressure ($\delta(b\beta\Pi)^* = 0$) coincide with spinodal points indicating local instability of the coexisting nematic phase with respect to a small density fluctuation $\delta c^*(l)$ *along* the trajectory in Fig. 6.10. Although we established the aforementioned relation (at least numerically) only for a single dilution trajectory (*viz.* $\sigma = 0.32$) we assume that it holds for any local extrema in the pressure as a function of γ. Moreover, we stress that our attention is restricted to density fluctuations along the dilution trajectory. This means that we can not exclude the possibility of other spinodal points being present on the dilution trajectory which may have an "off-trajectory" instability direction (i.e. other than $\delta^* c(l)$). Resolving this issue however would require verification of infinitely many possible density deviations at each point on the trajectory, which clearly is an impossible task. We emphasize that our aim is not to obtain the exact spinodal (or binodal) boundaries associated with the three-phase equilibria but to provide global evidence of a demixing instability of the nematic phase.

7

Isotropic-nematic phase behaviour of length-polydisperse hard platelets

Abstract

We extend the binary model for thin and thick hard disks, described in Chapter 2, to a polydisperse one allowing for arbitrary polydispersity in thickness (i.e. the length of a flat cylinder). Strong fractionation effects are observed, with the thicker disks found preferentially in the isotropic phase. Due to this effect, the system may undergo an $I - N$ density inversion as observed explicitly in experiment. We also encounter a divergence of the $I - N$ coexistence region for Schulz-distributed parents with polydispersities larger than 46 %. An implication of this phenomenon is that the system cannot become fully nematic at high densities but will continue to split off a small fraction of a dilute isotropic phase predominantly containing very thick species.

7.1. Introduction

Recently, a novel model system for polydisperse disks has been developed consisting of sterically stabilized gibbsite platelets [11]. The particles are evidently polydisperse since the platelets strongly differ in both diameter and thickness. The polydispersity for each of the dimensions was estimated at 25 %. Quite unexpectedly, the phase behaviour of these platelike particles appeared to be more significantly affected by their polydispersity in thickness than by their polydispersity in diameter. While the fractionation in diameter between the isotropic and nematic phases was found to be rather weak [60,63], strong experimental evidence was found for a pronounced thickness fractionation in these systems [60]. The latter effect has led to a surprising phenomenon: the densities of the isotropic and nematic phases may invert upon concentrating a dilute sample in a test tube, indicating that an isotropic *bottom* phase coexists with a nematic *upper* phase [60]. This anomalous behaviour, referred to as the $I - N$ density inversion, can in principle be explained by the fractionation in thickness between the phases with the thicker platelets accumulating in the isotropic phase. The fractionation effect thus reduces the difference in mass densities between the coexisting phases. Consequently, an inversion occurs when the fractionation effect is strong enough to overrule the difference in thermodynamic number densities of the phases. In Chapter 2, we have verified the possibility of a density inversion in simple binary mixtures of thin and thick hard platelets with common diameter and showed that the inverted state is indeed found in a broad range of plate compositions.

117

In this Chapter, we extend our binary model (within the Onsager treatment) to a polydisperse one in which we allow for a *continuous* distribution in thicknesses. As in Chapter 2, we upgrade Onsager's original second virial approximation quantitatively by applying a rescaling of the second virial term according to Parsons' theory [23]. This approach allows us to incorporate higher virial terms into the free energy, albeit approximately, while requiring only specific knowledge of the two-body excluded volumes. To keep our model analytically tractable, we use Gaussian trial ODFs. In Chapter 2 it is shown that, with the Gaussian Ansatz, we may neglect the effect of the thickness on the equilibrium orientations of the platelets implying that the orientations are solely determined by their diameter, which is the same for all species. As a result, the distribution of orientations in the nematic phase can be characterized by a single ODF which holds for all species. This approach, referred to as the decoupling approximation, allows us to analytically minimize the free energy with respect to the orientational degrees of freedom and leads to an excess free energy obeying a simple moment structure, i.e. it only depends on the first two moments of the thickness distribution [114]. Applying the coexistence conditions for polydisperse systems then leads to a set of simple consistency equations which we can solve without having to perform numerical integrations over the length distributions.

7.2. Moment free energy

The theoretical description of the present system is largely analogous to the one given in the previous Chapter. Therefore, we shall only present the relevant expressions and refer the reader to Chapters 6 and 2 for details. Let us consider a system of hard disks with common diameter D but *polydisperse thickness* –such that there is a continuous distribution of lengths L– in a macroscopic volume V. We define, $l = L/L_0$ as the relative thickness with respect to some reference length L_0.

The free energy of the system is given by Eq. (6.1) in terms of of the normalized thickness distribution $c(l) = bN(l)/V$, with $b = \pi^2 D^3/16$ the excluded volume of two infinitely thin disks. Moreover, $c_0 = \int c(l)dl$ is the total dimensionless concentration of platelets. While the orientational part of the free energy is the same as the one derived in Sec 6.2 –again using Gaussian ODFs given by Eq. (6.4)– the excluded-volume part, however, is essentially different from the previous one. This is related to the thickness correction to the excluded volume of two platelike cylinders at mutual angle γ. Recall that (Eq. (2.2))

$$v_{\text{excl}}(\gamma) = \frac{\pi}{2} D^3 \sin\gamma + (l + l') L_0 D^2 \left\{ \frac{\pi}{4} + E(\sin\gamma) + \frac{\pi}{4} |\cos\gamma| \right\} + \mathcal{O}(L_0^2 D), \qquad (7.1)$$

involving the complete elliptic integral of the second kind $E(k)$. Consequently, the excluded volume integrals, defined as

$$\rho(l, l') \equiv (2b)^{-1} \int \int v_{\text{excl}}(\gamma) \psi(\theta, l) \psi(\theta', l') d\Omega d\Omega' \qquad (7.2)$$

have more intricate appearances. For the nematic phase we have

$$\rho_{\text{nem}}(l, l') = \frac{4}{\pi} \int \int |\sin \gamma| \, \psi(l, \theta) \psi(l', \theta') d\Omega d\Omega'$$
$$+ \frac{2}{\pi} \frac{L_0}{D}(l + l') \int \int \left[3 - \frac{1}{2} \sin^2 \gamma + |\cos \gamma| \right] \psi(l, \theta) \psi(l', \theta') d\Omega d\Omega' + \mathcal{O}[(L_0/D)^2]. \tag{7.3}$$

Inserting the Gaussian ODFs and performing an asymptotic expansion for large α yields up to leading order

$$\rho_{\text{nem}}(l, l') \sim \sqrt{\frac{8}{\pi} \left(\alpha^{-1}(l) + \alpha^{-1}(l') \right)} + \frac{8}{\pi} \frac{L_0}{D}(l + l') \left[1 + \mathcal{O}(\alpha^{-1}(l), \alpha^{-1}(l')) \right]. \tag{7.4}$$

Ignoring the $\mathcal{O}(\alpha^{-1})$ term is crucial since it leads to $\alpha(l)$ being *decoupled* from the thickness distribution, as explained in Chapter 2. A formal justification of this decoupling approximation will be given below. For the isotropic phase we have

$$\rho_{\text{iso}}(l, l') = 1 + \frac{L_0}{D}(l + l') \left(1 + \frac{3}{\pi} \right) + \mathcal{O}(L_0^2/D^2), \tag{7.5}$$

which diverges from Onsager's original description –where $\rho_{\text{iso}} \equiv 1$– because of the slightly different definition for $\rho(l, l')$ used here. Note that the expressions above are straightforward generalizations of Eqs. (2.13) and (2.5) in Chapter 2. Putting these results back into the free energy density Eq. (6.1) gives for the isotropic phase

$$f_{\text{iso}} \equiv \frac{b \beta F}{V} \sim \int c(l)[\ln c(l) - 1] dl + c_0^2 + \left(2 + \frac{6}{\pi} \right) \frac{L_0}{D} c_0 c_1, \tag{7.6}$$

where $c_k \equiv \int c(l) l^k dl$ define the (ordinary) moment densities (in terms of the weight function l^k) [114].

Inserting the entropic contributions Eqs. (6.5) and (7.4) into the free energy and performing a functional differentiation with respect to $\alpha(l)$ yields for the nematic phase

$$\frac{\delta f}{\delta \alpha(l)} \sim \frac{c(l)}{\alpha(l)} - \sqrt{\frac{8}{\pi}} \frac{c(l)}{\alpha^2(l)} \int c(l') \left(\frac{1}{\alpha(l)} + \frac{1}{\alpha(l')} \right)^{-1/2} dl'. \tag{7.7}$$

Applying the stationarity condition $\delta f/\delta \alpha(l) = 0$ gives after some rearrangements

$$\alpha^{1/2}(l) \sim \sqrt{\frac{8}{\pi}} \int \frac{c(l')}{[1 + \alpha(l)/\alpha(l')]^{1/2}} dl'. \tag{7.8}$$

Obviously, a similar expression is obtained for $\alpha(l')$. It is convenient to combine both expressions using the ratio $Q(l, l') \equiv \alpha(l)/\alpha(l')$ to obtain

$$Q^{1/2}(l, l') \sim \int \frac{\tilde{c}(l'')}{[1 + Q(l, l'')]^{1/2}} dl'' \bigg/ \int \frac{\tilde{c}(l''')}{[1 + Q(l', l''')]^{1/2}} dl''', \tag{7.9}$$

which is an implicit equation for $Q(l, l')$. Note that Q only depends on the normalized distributions $\tilde{c}(l) \equiv c(l)/c_0$ and not on the overall concentration c_0 of the nematic phase.

One readily concludes that $Q(l, l') = Q(1, 1) = 1$ is a solution of Eq. (7.9). Using this in Eq. (7.8) the stationarity condition within the decoupling approximation becomes

$$\alpha \sim \left(\sqrt{\frac{8}{\pi}} \int \frac{c(l')}{2^{1/2}} dl' \right)^2,$$

$$\alpha \sim \frac{4c_0^2}{\pi}, \qquad\qquad\qquad\qquad\qquad\qquad\qquad\qquad\qquad (7.10)$$

which is the same result as for the monodisperse system [5]. The physical interpretation of the decoupling approximation is that the orientation of the platelets is solely determined by the diameter –which is identical for all particles– and not by their thickness. Consequently, the orientational degrees of freedom are *decoupled* from the degrees of freedom which determine the shape of the thickness distribution. Using these results in Eq. (6.1) gives the following *explicit* expression for the free energy in the nematic phase

$$f_{\text{nem}} \sim \left(\ln \frac{4}{\pi} + 1 \right) c_0 + \int c(l)[\ln c(l) - 1]dl + 2c_0 \ln c_0 + \frac{16}{\pi}\frac{L_0}{D}c_0 c_1. \qquad (7.11)$$

7.2.1. Parsons rescaling

Like in Chapter 2 we apply Parsons' approach to correct for many-body correlations (see also Sec. 1.3.3). For a monodisperse system the rescaled Parsons free energy (denoted by P) reads

$$\frac{b\beta F_{\text{P}}^{\text{ex}}}{V} = \frac{(1 - \frac{3}{4}\phi)}{(1 - \phi)^2}c_0^2 \rho, \qquad\qquad\qquad\qquad\qquad\qquad (7.12)$$

with $\rho \equiv \rho(1, 1)$. Generalizing the above expression for a polydisperse system leads to

$$\frac{b\beta F_{\text{P}}^{\text{ex}}}{V} = \frac{(1 - \frac{3}{4}\phi)}{(1 - \phi)^2} \int \int c(l)c(l')\rho(l, l')dldl'$$

$$= \tilde{f}_{\text{CS}}(\phi)\frac{b\beta F_{\text{O}}^{\text{ex}}}{V}, \qquad\qquad\qquad\qquad\qquad\qquad (7.13)$$

where $b\beta F_{\text{O}}^{\text{ex}}/V$ is the excess free energy in the second virial approach, given by the last term in Eq. (6.1). Furthermore, ϕ is the total volume fraction of platelets, related to the thickness distribution $c(l)$ via

$$\phi = \frac{4}{\pi}\frac{L_0}{D} \int c(l)l\,dl = \frac{4}{\pi}\frac{L_0}{D}c_1. \qquad\qquad\qquad\qquad\qquad (7.14)$$

Replacing the last term in Eq. (6.1) by Eq. (7.13) gives

$$f_{\text{iso}}^{\text{P}} \sim \int c(l)[\ln c(l) - 1]dl + \tilde{f}_{\text{CS}}(\phi)\left[c_0^2 + \left(2 + \frac{6}{\pi} \right)\frac{L_0}{D}c_0 c_1 \right]. \qquad (7.15)$$

The stationarity condition pertaining to the nematic state Eq. (7.10) becomes $\alpha \sim (4/\pi)\left[c_0 \tilde{f}_{\text{CS}}(\phi) \right]^2$ resulting in the Onsager-Parsons free energy for the nematic state

$$f_{\text{nem}}^{\text{P}} \sim \left(\ln \frac{4}{\pi} + 1 \right) c_0 + \int c(l)[\ln c(l) - 1]dl + 2c_0 \ln \left[c_0 \tilde{f}_{\text{CS}}(\phi) \right] + \tilde{f}_{\text{CS}}(\phi)\frac{16}{\pi}\frac{L_0}{D}c_0 c_1. \quad (7.16)$$

Comparing both expressions above we see that the excess free energy of the isotropic and nematic states obey simple moment structures since they depend on a *finite* number of moments of the thickness density distribution $c(l)$ [114]. In fact only the zeroth and first moment densities are relevant*. Owing to their simple structure, the analysis of the isotropic-nematic coexistence equations will be considerably easier here than in Chapter 6, as we shall see later. Note that the present description stands in great contrast to the one formulated in the previous Chapter, where the free energy could not be expressed in closed form due to the analytically intractable self-consistency equation given by Eq. (6.8).

7.3. CONSISTENCY EQUATIONS

The chemical potentials of the isotropic and nematic states are given by the functional derivative of the free energy density with respect to $c(l)$. Within the second virial approximation we obtain

$$\beta\mu_{\text{iso}}(l) = \ln c(l) + 2c_0 + \left(2 + \frac{6}{\pi}\right)\frac{L_0}{D}(c_0 l + c_1),$$

$$\beta\mu_{\text{nem}}(l) = \ln c(l) + 2\ln c_0 + \frac{16}{\pi}\frac{L_0}{D}(c_0 l + c_1) + \left(\ln\frac{4}{\pi} + 3\right). \tag{7.17}$$

The osmotic pressure can be written in terms of the chemical potential and the free energy via $b\beta\Pi \equiv -f + \beta\int dlc(l)\mu(l)$ which yields

$$b\beta\Pi_{\text{iso}} \sim c_0 + c_0^2 + \left(2 + \frac{6}{\pi}\right)\frac{L_0}{D}c_0 c_1,$$

$$b\beta\Pi_{\text{nem}} \sim 3c_0 + \frac{16}{\pi}\frac{L_0}{D}c_0 c_1. \tag{7.18}$$

Similar but more complicated expressions can be derived straightforwardly from the Onsager-Parsons free energy, Eqs. (7.15) and (7.16). Imposing equality of chemical potentials leads to the following equilibrium thickness distributions

$$c^{(a)}(l) = W(l)\exp[\xi^{(a)}(l)], \qquad a = I, N, \tag{7.19}$$

with arguments

$$\xi^{(I)}(l) = -\left(2 + \frac{6}{\pi}\right)\frac{L_0}{D}(c_0^{(I)}l + c_1^{(I)}) - 2c_0^{(I)},$$

$$\xi^{(N)}(l) = -\frac{16}{\pi}\frac{L_0}{D}(c_0^{(N)}l + c_1^{(N)}) - 2c_0^{(N)}\ln c_0^{(N)} - \left(\ln\frac{4}{\pi} + 3\right). \tag{7.20}$$

The function $W(l) \equiv \exp[\beta\mu(l)]$ must be common to both phases. Exploiting conservation of matter $c^{(0)}(l) = \gamma c^{(I)}(l) + (1-\gamma)c^{(N)}(l)$ –with γ denoting the fraction of isotropic phase– we may reexpress $W(l)$ in terms of a fixed parent distribution $c^{(0)}(l)$ describing the thickness distribution in the homogeneous system, i.e.

$$c^{(a)}(l) = c^{(0)}(l)\frac{\exp[\xi^{(a)}(l)]}{\gamma\exp[\xi^{(I)}(l)] + (1-\gamma)\exp[\xi^{(N)}(l)]}, \qquad a = I, N. \tag{7.21}$$

---

*It can be shown that the formal (i.e. exact) polydisperse Onsager free energy depends on an infinite set of moment densities with complicated weight functions [107].

The moment densities (c_0 and c_1) involved in Eqs. (7.18) and (7.20) are obtained by integrations over these distributions

$$c_0^{(a)} = \int c^{(a)}(l)dl \quad \text{and} \quad c_1^{(a)} = \int l c^{(a)}(l)dl, \qquad a = I, N. \tag{7.22}$$

To specify the parent distribution $c^{(0)}(l)$ we assume that the thicknesses are distributed along a Schulz distribution

$$c^{(0)}(l) = c_0^{(0)} \frac{(1+z)^{1+z}}{\Gamma(1+z)} l^z \exp[-(z+1)l], \tag{7.23}$$

which is normalized according to $\int c^{(0)}(l)dl = c_0^{(0)}$, with $c_0^{(0)}$ the overall particle concentration in the parent phase and has an average thickness $m_1^{(0)} \equiv c_1^{(0)}/c_0^{(0)} = 1$. The latter implies that we may identify the ratio D/L_0 involving the reference length as the mean aspect ratio of the platelets. The polydispersity (defined as the relative standard deviation σ) is related to the parameter z via

$$\sigma \equiv \left([m_1]^{-2} \int l^2 \frac{c^{(0)}(l)}{c_0} dl - 1 \right)^{1/2} = (1+z)^{-1/2}. \tag{7.24}$$

We are now ready to investigate the coexistence between the isotropic and nematic phase in our polydisperse model. Before discussing the full coexistence problem, we will first derive simple expressions for the cloud and shadow curves which locate the onset of phase separation. For the isotropic cloud point we may set $\gamma = 1$ in Eq. (7.21) so that

$$c^{(I)}(l) = c^{(0)}(l),$$
$$c^{(N)}(l) = c^{(0)}(l) \exp[\xi^{(N)}(l) - \xi^{(I)}(l)]. \tag{7.25}$$

Substituting this into Eq. (7.22) gives $c_0^{(I)} = c_1^{(I)} = c_0^{(0)}$ showing that the isotropic phase is identified as the parent. The moment densities for the associated nematic shadow are then given by

$$c_0^{(N)} = c_0^{(0)} \frac{(1+z)^{1+z}}{\Gamma(1+z)} \exp\left[\Delta\xi''\right] \int l^z \exp\left[(\Delta\xi' - (z+1))l\right] dl,$$
$$c_1^{(N)} = c_0^{(0)} \frac{(1+z)^{1+z}}{\Gamma(1+z)} \exp\left[\Delta\xi''\right] \int l^{z+1} \exp\left[(\Delta\xi' - (z+1))l\right] dl, \tag{7.26}$$

where we have rewritten $\xi^{(N)}(l) - \xi^{(I)}(l)$ by splitting it into parts, according to

$$\xi^{(N)}(l) - \xi^{(I)}(l) \equiv \Delta\xi'l + \Delta\xi''. \tag{7.27}$$

Note that $\Delta\xi'$ and $\Delta\xi''$ are both independent of l. The integrals can be worked out straightforwardly to obtain the following coupled set of consistency equations

$$c_0^{(N)} = c_0^{(0)} \exp\left[\Delta\xi''\right] \left(\frac{z+1}{(z+1) - \Delta\xi'} \right)^{z+1},$$
$$c_1^{(N)} = c_0^{(0)} \exp\left[\Delta\xi''\right] \left(\frac{z+1}{(z+1) - \Delta\xi'} \right)^{z+2}. \tag{7.28}$$
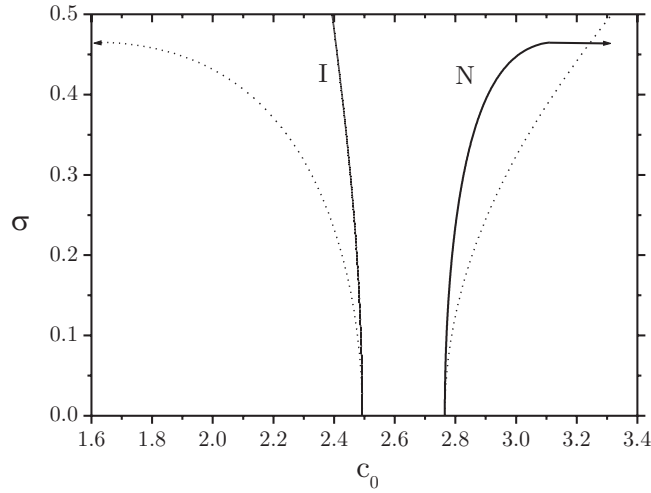
FIGURE 7.1. Isotropic and nematic cloud curves (solid) and the corresponding shadow curves (dotted) showing the concentrations of the coexisting phases c_0 as a function of the parent polydispersity σ. At $\sigma = 0$, the isotropic cloud point meets the shadow of the nematic cloud point and vice versa, as it should.

The same analysis can be done for the nematic cloud and shadow curves by setting $\gamma = 0$ so that the nematic phase is identified as the parent phase, i.e. $c_0^{(N)} = c_1^{(N)} = c_0^{(0)}$. The densities of the shadow phase ($c_0^{(I)}$ and $c_1^{(I)}$) are given by similar equations as Eq. (7.28). To track down the cloud and shadow curves we must solve the coupled set under the condition of equal osmotic pressures $\Pi_{\text{iso}} = \Pi_{\text{nem}}$.

In the coexistence region, which is bounded by the isotropic and nematic cloud points, both phases coexist in finite amounts, implying $0 < \gamma < 1$. From an experimental standpoint, the results must be restricted to lie on a physical dilution-line along which the shape of the parent distribution, $c^{(0)}(l)/c_0^{(0)}$, is kept fixed while the overall parent concentration $c_0^{(0)}$ is subject to variation. To calculate the evolution of the densities inside the coexistence region we have to solve the four integral equations Eq. (7.22) along with the condition of equal osmotic pressures. For a given polydispersity of the parent, there appear six variables in these equations –the five density variables $c_0^{(I)}, c_1^{(I)}, c_0^{(N)}, c_1^{(N)}, c_0^{(0)}$ plus γ– implying that one variable can be freely chosen. Numerically, rather than changing the overall parent density $c_0^{(0)}$, it has proven to be more convenient to construct a scheme in which γ is varied between 0 and 1 and the corresponding densities are calculated self-consistently [98].

7.4. Cloud and shadow curves

The results for the cloud and shadow curves are shown in Figs. 7.1 to 7.3. These curves are calculated from the Onsager-Parsons free energy, Eqs. (7.15) and (7.16). In all calculations we used $D/L_0 = 7.7$, which value is in close agreement with the average aspect ratio of the gibbsite platelets used in experiment [60]. From Fig. 7.1 we see that the coexistence region broadens significantly when the polydispersity of the parent
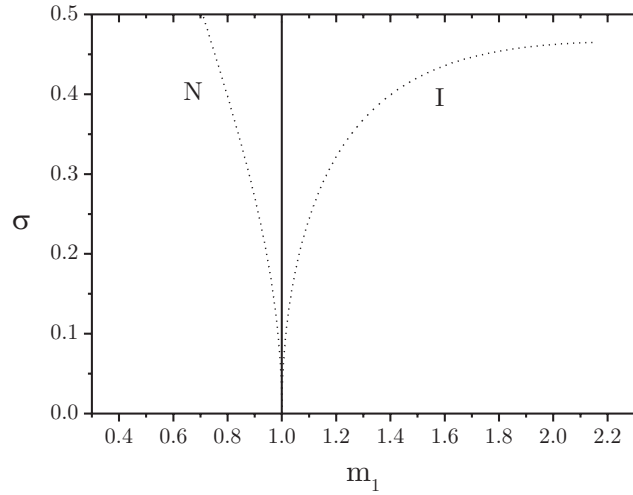
Figure 7.2. Average platelet thickness m_1 in the isotropic and nematic shadow phases as a function of the parent polydispersity σ. Note that both cloud curves are identical to the parent and therefore have $m_1 = m_1^{(0)} = 1$.
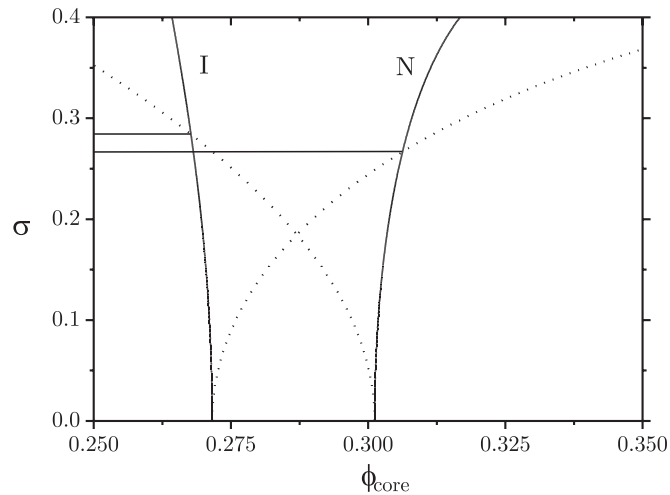

Figure 7.3. Isotropic and nematic cloud curves (solid) and the corresponding shadow curves (dotted) in terms of the core volume fractions ϕ_{core} of the coexisting phases as a function of the parent polydispersity σ. The horizontal lines denote the points where the cloud and shadow phases have equal mass densities. Above the "threshold" value $\sigma = 0.267$ (indicated by the lower horizontal line) the inverted state will be found *throughout* the coexistence region. In the small interval between the two horizontal lines ($0.267 < \sigma < 0.284$) a density inversion occurs *inside* the coexistence region.

becomes higher, in particular, at $\sigma > 0.4$. A notable feature is the divergence of the two-phase region at $\sigma > 0.46$ indicating that the concentration of the nematic cloud shifts to infinity while the concentration of the corresponding shadow rapidly moves to zero. This divergent behaviour is not observed for the isotropic cloud and shadow phases.

Although the concentration of the isotropic shadow increases rapidly with increasing polydispersity, it remains finite even at $\sigma \gg 0.5$. In Fig. 7.2 we show the average thickness of the platelets in the isotropic and nematic phases. A strong fractionation effect is observed, with the thicker platelets going preferentially into the isotropic phase. At high polydispersities ($\sigma > 0.4$) the effect becomes very pronounced since the average thickness in the isotropic phase may rise up to twice that in the nematic phase. Again we observe a divergence in the isotropic shadow phase at $\sigma > 0.46$ indicating that the average plate thickness rapidly shifts to infinity.

To verify the possibility of a density inversion, we have to calculate the mass density of the phases. In Chapter 2, rather than calculating the mass density itself, we considered the core volume fraction ϕ_{core} of the platelets to be a more convenient density variable. It is easy to show that ϕ_{core} is linearly proportional to the mass density of the gibbsite platelets used in experiment [60]. The core volume fraction can be calculated from

$$\begin{aligned}\phi_{\mathrm{core}} &= \frac{\pi}{4}\frac{N}{V}D^2\int c(l)(L-2\delta)dl \\ &= \frac{4}{\pi}\frac{L_0}{D}c_1 - \frac{8}{\pi}c_0\frac{\delta}{D},\end{aligned} \tag{7.29}$$

where δ/D is the thickness of the stabilizing polymer layer grafted onto the gibbsite platelets relative to the average diameter of the platelets. From the experimental results we estimate $\delta/D = 4/180$ [60]. The resulting plot is shown in Fig. 7.3. We indeed observe an inverted state (i.e. the isotropic phase being more dense than the nematic phase) at polydispersities roughly above 30 %. This implies that, at these polydispersities, the fractionation effect is strong enough to overcome the difference in number densities between the coexisting phases. In particular, we can identify a small interval $0.267 < \sigma < 0.284$ where a density inversion takes places inside the two-phase region, in accordance with the experimental observations[†]. In these cases, the normal state will be found at the beginning of the coexistence region (close to the isotropic cloud point) but an inverted state will be found near the nematic cloud point. Clearly, there must be a point $0 < \gamma < 1$ somewhere in the two-phase region where a density inversion takes place. To find this point, we have to resort to the full coexistence problem.

7.5. Inside the coexistence region

In Fig. 7.4 we show the evolution of the densities and average thicknesses across the coexistence region for a fixed polydispersity of the parent phase. As expected, both the densities and the averages m_1 vary smoothly between the isotropic and nematic cloud points which delimit the two-phase coexistence region. We see that the average

---

[†]The results in this Chapter only hold for Schulz-distributed parents within the Onsager-Parsons formulation. Different results might be obtained when adopting a different quantitative upgrade for the original second virial theory or a different parent distribution. However, our objective in this Chapter is to present a general framework allowing for arbitrary adaptations to be made with respect to these matters. A discussion of the effect of Parsons' approach on the isotropic-nematic transition densities can be found in Sec 2.5.
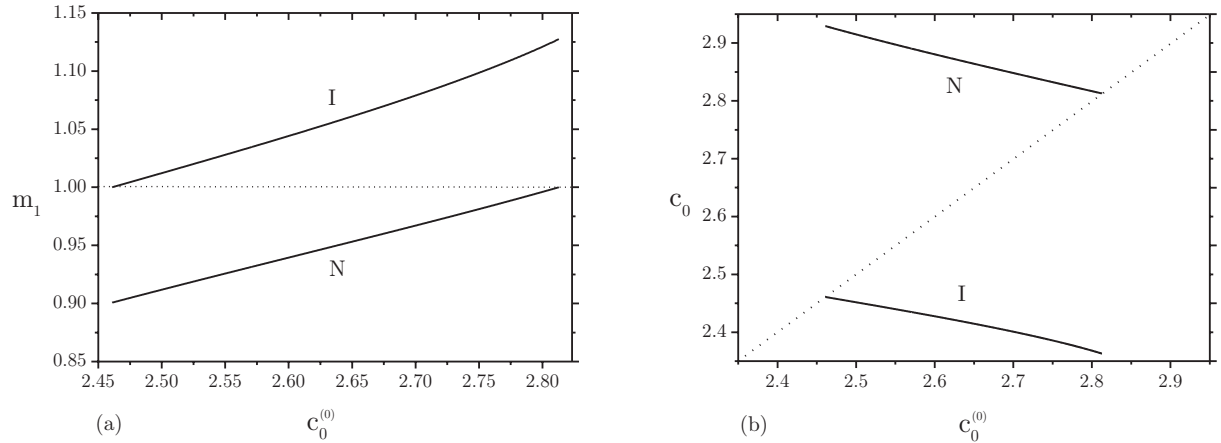
Figure 7.4. (a) Average thickness m_1 in the coexisting phases as a function of the concentration of the parent phase $c_0^{(0)}$ for $\sigma = 0.27$. The isotropic and nematic cloud points, which delimit the coexistence region, are located at the points where the curves meet the dilution line $m_1^{(0)} = 1$ (dotted line). (b) Evolution of the concentrations of the coexisting phases across the two-phase region for the same polydispersity. The dotted line represents the dilution line $c_0 = c_0^{(0)}$.

thickness is always higher in the isotropic phase than in the nematic phase, as we expect from Fig. 7.2. A more detailed picture of the fractionation effect can be found in Fig. 7.5 where we have depicted the thickness distributions in the coexisting phases.

In Fig. 7.6 we have plotted the variation of the core volume fractions for a parent with $\sigma = 0.27$ as the coexistence region is crossed. According to Fig. 7.3, this parent should undergo a density inversion somewhere inside the coexistence region. Fig. 7.6 shows that there is indeed an inversion, albeit very close to the nematic cloud point in this case. The inversion occurs at a parent volume fraction $\phi = 0.461$ which corresponds to $\gamma = 0.073$. So the inversion takes place when the volume occupied by the isotropic phase has decreased to about 7 % of the total system volume. Finally, in Fig. 7.7, we show the polydispersities of the daughter phases inside the coexistence region for the same parent as in Fig. 7.6. At coexistence, both daughter phases have a lower polydispersity than the parent phase due to the fractionation effect. However, the deviations are very small ($\Delta\sigma < 0.006$) for this particular parent polydispersity. Note that the polydispersities of the daughter phases reach their minimum around $\gamma = 0.5$ i.e. when the isotropic and nematic phases coexist in approximately equal amounts.

7.6. Summary and discussion

We have studied $I - N$ phase equilibria in the Onsager-Parsons model for hard disks allowing for polydispersity in thickness. The onset of phase separation is analyzed by calculating the cloud and shadow curves –which delimit the two-phase coexistence region– as a function of the polydispersity of the parent system. A significant broadening of the coexistence region is observed for moderately high polydispersities ($\sigma < 0.3$). We
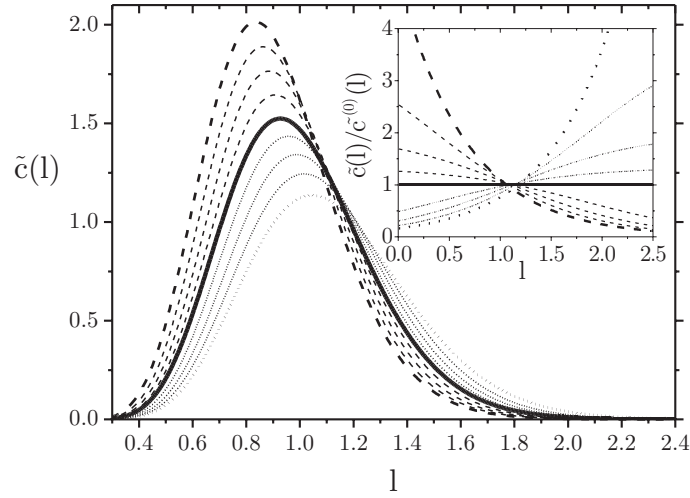
Figure 7.5. Normalized thickness distribution $\tilde{c}(l) \equiv c(l)/c_0^{(0)}$ in the isotropic and nematic phases at polydispersity $\sigma = 0.27$ for various γ. Upper dashed curve (bold): distribution in the nematic shadow at the isotropic cloud point ($\gamma = 1$). Lower dotted curve: distribution in the isotropic shadow at the nematic cloud point ($\gamma = 0$). The corresponding distributions in the cloud phases are given by the parental one (bold solid curve). The intermediate curves represent, from top to bottom, the distributions of the coexisting isotropic (dotted) and nematic (dashed) phases for $\gamma = 0.75$, 0.5 and $\gamma = 0.25$, respectively. The inset shows the ratio of the thickness distributions to that of the parent.
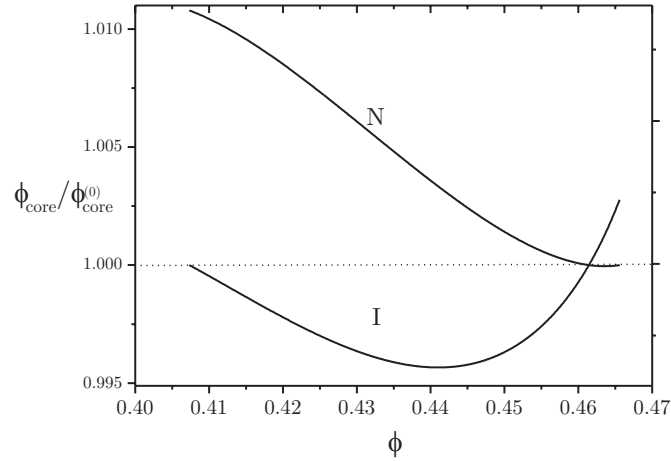
Figure 7.6. Ratio of the core volume fraction of the isotropic and nematic phases relative to the parental one for $\sigma = 0.27$ plotted versus the volume fraction of platelets ϕ in the parent phase. The dotted line represents the dilution line ($\phi_{core}/\phi_{core}^{(0)} = 1$). The intersection at $\phi = 0.461$ indicates the onset of a density inversion.

also see a strong fractionation effect with the thick species preferentially occupying the isotropic phase. Although the biphasic widening and fractionation effect are generic properties observed in many polydisperse systems [5, 104], it is rather surprising that

Figure 7.7. Evolution of the polydispersities σ_d of the coexisting isotropic and nematic daughter phases across the coexistence region for a parent with $\sigma = 0.27$ plotted versus the fraction γ of the system volume occupied by the isotropic phase. The solid horizontal line indicates the "threshold" polydispersity $\sigma = 0.267$ (see also Fig. 7.3). A parent phase with a polydispersity below this value will not exhibit a density inversion during phase separation.
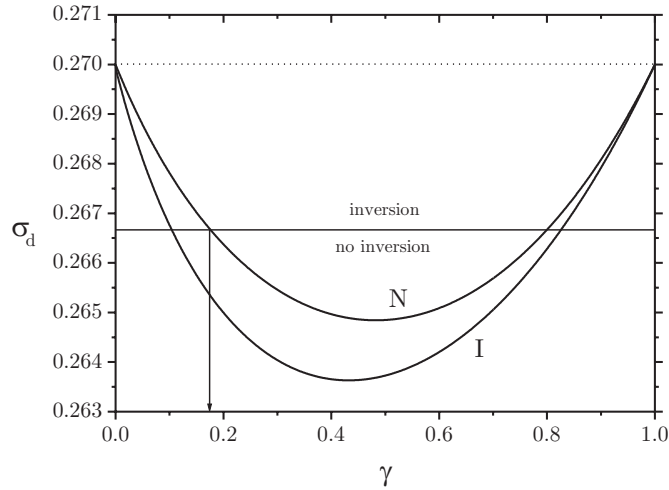
these effects occur so strongly in mixtures of disks which only differ in thickness. Eq. (7.1) shows that the plate thickness only marginally contributes to the excluded volume, provided that the inverse aspect ratios L_0/D are small parameters. Hence, one might have anticipated that the effect of thickness on the phase behaviour of disks is unlikely to be significant.

Even more striking is the infinite broadening of the coexistence region at polydispersities $\sigma > 0.46$ due to a divergence of the nematic cloud and shadow curves (see Figs. 7.1 and 7.2). This phenomenon can be interpreted as follows. When a dilute parent phase with $\sigma > 0.46$ is concentrated it starts to phase separate at the isotropic cloud point, initially splitting off an infinitesimal amount of nematic phase (the shadow). The fraction of nematic phase increases upon further concentrating the parent sample. However, as we see from Fig. 7.1, the parent will never reach the associated nematic cloud point. Regardless of the concentration of the parent phase, the system always splits off a tiny fraction of an (increasingly dilute) isotropic phase which, according to Fig. 7.2, will accommodate increasingly thicker platelets. This means that the system never becomes fully nematic, irrespective of the concentration of the parent. The question now arises whether this is a realistic picture. It may be possible that the anomalous behaviour stems from the fact that the thickness distribution adopted here is unbounded, meaning that there is a nonzero probability of finding species with very large (potentially infinite) thicknesses for which the inverse aspect ratio is no longer a small parameter. Therefore, different results might be obtained by introducing a finite cutoff value $l_\mathrm{max} \gg 1$ which might be more realistic from an experimental point of view.

In Chapter 2 we made a theoretical investigation of the experimentally observed $I - N$ density inversion by considering a simple binary mixture of platelets with differing thickness. Although the density inversion could readily be accounted for within this model, we were not able to explain another peculiar observation encountered in the experimental work [60]. As part of their experimental survey, Van der Kooij *et al.* performed an additional fractionation experiment in which a suspension was brought to a volume fraction ($\phi = 0.29$) close to the nematic cloud point ($\phi = 0.30$) and left to phase separate. The nematic upper phase was separated from the isotropic bottom phase and subsequently diluted. A remarkable observation was that this system did not exhibit a density inversion at any point in the isotropic-nematic coexistence region. This striking observation could however not be explained, for fundamental reasons, on the basis of the binary model for these systems, as discussed in Chapter 2.

In the present study we have extended our binary model to a polydisperse one, meaning that we allow for a continuous distribution in thickness instead of just two different species. We may now consider the polydispersities of the coexisting isotropic and nematic daughter phases for a given parent distribution. In Fig. 7.7 these results are plotted for a parent with $\sigma = 0.27$. As noted in the previous paragraph, the daughter phases have $\sigma < 0.27$ which is a direct consequence of the fractionation in thickness during phase separation. In this figure we also indicated the "threshold" polydispersity (see Fig. 7.3) below which the fractionation effect is too weak to accomplish an inversion of densities. So any daughter phase with a polydispersity below the threshold will probably not show an $I - N$ density inversion if this phase were to be isolated and subsequently diluted or concentrated (as the new parent phase). Despite the fact that the distributions in the daughter phases no longer exactly obey the Schulz form, the deviations will generally be very small close to the isotropic and nematic cloud points. Since the polydispersity of the parent may be chosen arbitrarily, we can make a reasonable account for the experimental observations by picking a parent polydispersity which is just above the "threshold" as indicated in Fig. 7.7. In that case, the polydispersities of the daughter phases will cross the threshold close to the nematic cloud point (i.e. when the system is almost fully nematic). Subsequent isolation and dilution of the near-Schulz nematic parent would then give a phase separation into an isotropic phase which is less dense than the nematic phase and hence the density inversion has disappeared.

An issue which is not addressed in this Chapter is the possibility of a demixing transition in the nematic phase. For binary mixtures of thin and thick platelets a stable demixing transition of the nematic phase could readily be established in Sec. 2.4. It was shown there that the transition occurs for any thickness ratio provided that the osmotic pressure is sufficiently high. In the present study, we have not found any indication for a such demixing instability, at least for the Schulz parents considered here.

8

Smectic versus columnar order in length-polydisperse mixtures of parallel hard rods

ABSTRACT

By means of a bifurcation analysis within the Onsager-Parsons formalism we study the stability of the nematic phase with respect to the spatially inhomogeneous smectic and columnar liquid crystal states in systems of perfectly aligned hard rodlike cylinders with arbitrary length polydispersity. It appears that polydispersity suppresses the smectic phase in favour of columnar ordering. At high polydispersities, the nematic to smectic transition, as found in monodisperse systems, is preempted by a transition from the nematic to a columnar state. Our predictions are in qualitative accordance with recent simulation results for freely rotating polydisperse rods.

8.1. INTRODUCTION

In the previous two Chapters we have extensively studied the implications of (length) polydispersity on the isotropic-nematic transition of cylindrical rods and plates. However, the possible stability of inhomogeneous liquid crystals in these mixtures was not considered there. Since the pioneering simulation studies of Frenkel *et al.* [16, 18] it is known that a nematic phase of hard anisometric particles becomes unstable with respect to a smectic (in case of rods) or a columnar phase (platelets) if the packing fraction exceeds a certain value. Theoretically, the stability of the smectic phase in systems of hard spherocylinders (i.e. rods) has been studied extensively within a number of density functional approximations [100, 115–120] while in some cases the stability of a crystalline solid state at high densities was also included in the framework [121–123]. For parallel cylinders, Mulder [115] showed that the simplest density functional i.e. a second virial approximation already suffices to establish an instability of a nematic phase against a smectic density modulation. The alternative possibility, a transition from a nematic to a columnar phase was shown to be metastable with respect to the nematic-smectic transition, at least for the parallel cylinders considered there.

Similar calculations for freely rotating hard spherocylinders within more elaborate DFT frameworks revealed the same behaviour indicating that the smectic order is not destroyed by the rotations of the rods [116, 117]. However, the nature of the nematic-smectic transition –in terms of a continuous or first order phase transition– did not

follow unambiguously from these theories. Later, computer simulations for freely rotating short [42, 46] and infinitely thin hard rods [124] revealed that the transition from a nematic to a smectic phase is in fact first order over the entire range of aspect ratios.

As to *mixtures* of rods, efforts have mainly been focussed on binary mixtures of long and short parallel rods [67, 125, 126] or length-polydisperse mixtures of parallel rods treated within a second-virial perturbation theory, valid for infinitely narrow size distributions [100]. It is our aim in this Chapter to qualitatively assess the effect of polydispersity on the nematic to smectic/columnar bifurcations by considering systems of parallel cylinders with *arbitrarily broad* length distributions described within a simple Onsager-Parsons density functional. As such, the model presented in this Chapter can be regarded as an extension of Sluckin's approach [100] in which both the effects of multi-particle correlations and (full) polydispersity are taken into account in a qualitative manner. The results from our approximate description will be compared with recent simulations by Bates and Frenkel [127] and elaborate DFT calculations by Bohle *et al.* [128], both aimed at polydisperse mixtures of freely rotating thin rods.

8.2. Bifurcation analysis

The general background of the bifurcation analysis to probe possible instabilities of the homogeneous nematic state towards inhomogeneous phases has been outlined in Sec. 1.3.4. The description there was aimed at monodisperse systems of freely rotating anisometric particles. In this Chapter we shall however focus on cylinders that are perfectly aligned along a nematic director $\hat{\mathbf{n}}$ so that the ODF formally reads $f(\Omega) = \delta(\Omega - \hat{\mathbf{n}})$. Moreover the lengths of the cylinders are assumed to be distributed continuously according to some fixed normalized length distribution $x(l)$, with $l = L/L_0$ the relative length of the cylinder with respect to the average length L_0. For these systems, we consider the following smectic density modulations[*]

$$
\begin{aligned}
\rho(\mathbf{r}; l) &= \rho x(l) + \delta\rho(\mathbf{q}; l)\cos(\mathbf{q}\cdot\mathbf{r}) \\
&= \rho x(l) + \delta\rho(\mathbf{q})x_{(1)}(l)\cos(\mathbf{q}\cdot\mathbf{r}),
\end{aligned} \tag{8.1}
$$

where $x_{(1)}(l)$ is a "new" length distribution reflecting the possibility that infinitesimal fluctuations in the length distribution, i.e. small fractionation effects, may also contribute to the loss of nematic instability. The natural thermodynamic variable to consider in this respect is the (intensive) grand canonical potential $\omega = \Omega/V$ (per unit volume). Generalized to polydisperse system the grand potential is given by

$$
\beta\omega[\rho(\mathbf{r}; l); \mu(l)] = \beta f_{\text{int}}[\rho(\mathbf{r}; l)] - \rho \int \beta\mu(l)x(l)dl, \tag{8.2}
$$

where the (intensive) Helmholtz free energy density $f_{\text{int}} = F/V$ can be expressed analogously to Eq. (1.43) in terms of the generalized density $\rho(\mathbf{r}; l)$. Note that Eq. (8.2) formally implies that the system must be kept in osmotic equilibrium with a reservoir at fixed values $\mu(l)$ of the chemical potentials.

---

[*]Similar to Eq. (1.45), the modulations for the columnar state are represented by a superposition of three cosines reflecting the (two-dimensional) hexagonal order.

Similar to the description in Sec. 1.3.4, the condition for marginal stability of the homogeneous nematic phase is obtained by inserting the perturbations Eq. (8.1) into the grand potential and performing an expansion up to second order in the amplitude $\delta(\mathbf{q})$. The bifurcation condition ($\beta\delta^2\omega = 0$) then leads to the following self-consistency equation for the length distribution $x_{(1)}(l)$:

$$x_{(1)}(l) = \rho x(l) \int dl' x_{(1)}(l') \hat{c}(\mathbf{q}; l, l'), \qquad (8.3)$$

analogous to Eq. (1.49). A close inspection of the latter reveals that the condition in fact represents an eigenvalue problem in terms of the *eigenfunctions* $x_{(1)}(l)$.

If we assume that the length distribution does *not* change at the transition we may substitute $x_{(1)}(l) = x(l)$ which gives the divergence criterium for the structure function, similar to Eq. (1.48):

$$S(\mathbf{q}; \rho) = \left[1 - \rho \iint dl dl' x(l) x(l') \hat{c}(\mathbf{q}; l, l')\right]^{-1}. \qquad (8.4)$$

Contrary to systems of freely rotating particles, the cosine-transformed correlation function $\hat{c}(\mathbf{q}; l, l')$ for parallel cylinders, represented within the rescaled second virial approximation by

$$\hat{c}(\mathbf{q}; l, l') = -\tilde{f}_{\mathrm{CS}}(\phi) \int_{v_{\mathrm{excl}}(l,l')} d\Delta\mathbf{r} \cos(\mathbf{q} \cdot \Delta\mathbf{r}), \qquad (8.5)$$

can easily be calculated in closed form for an aligned fluid since the excluded volume body is a perfect cylinder. The result for two parallel cylinders with lengths lL_0, $l'L_0$ and diameter D explicitly reads [115]:

$$\hat{c}(Q_\parallel, Q_\perp; l, l') = -\pi L_0 D^2 \tilde{f}_{\mathrm{CS}}(\phi) j_0\left(Q_\parallel \frac{l + l'}{2}\right) \frac{J_1(Q_\perp)}{\frac{1}{2}Q_\perp}, \qquad (8.6)$$

where $j_n(x) = \sin x / x$ denotes a spherical Bessel function and $J_n(x)$ a standard one [129]. Moreover, $Q_\parallel = 2\pi L_0 / \lambda_{\mathrm{SmA}}$ and $Q_\perp = 2\pi D / \lambda_{\mathrm{C}}$ represent the dimensionless wave numbers for the smectic and columnar density waves, directed parallel and perpendicular to the symmetry axes of the cylinders, respectively. Following Chapter 6 we will use a truncated *log-normal* form (Eq. (6.35)) with appropriate lower and higher cutoff lengths, l_{min} and l_{max}, to specify the distribution of particle lengths $x(l)$ in the nematic state.

8.3. Results

In Fig. 8.1. we have collected the results of the bifurcation analysis for a log-normal distribution with appropriate cutoff lengths. The bifurcation from a nematic to smectic or columnar phase at a given polydispersity is given by the lowest density (and corresponding wave-vectors) which gives rise to physical solutions of Eq. (8.4) and Eq. (8.3). Examples of the eigenfunctions $x(l)$ pertaining to the latter condition are depicted in Fig. 8.2. For the sake of clarity we have plotted its relative contribution compared to the normalized length distribution $x(l)$.
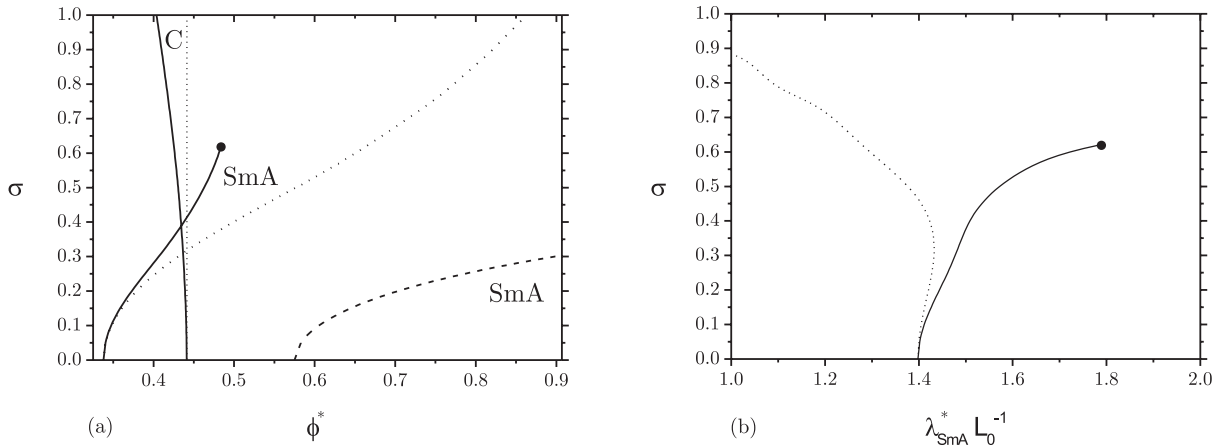
FIGURE 8.1. (a) Bifurcation diagram in terms of volume fractions ϕ^* for parallel hard cylinders with a log-normal length distribution (cutoff lengths, $l_{\min} = 0.1$ and $l_{\max} = 50$) obtained from the Onsager-Parsons free energy. Dotted curves represent solutions of Eq. (8.4) whereas solid ones are the results of the exact bifurcation equation given by Eq. (8.3). The dashed curve is analogous to Sluckin's [100] result within the pure second-virial approximation using the condition Eq. (8.4). In that case the nematic-columnar bifurcation is located beyond the volume fraction of closest packing $\phi_{cp} = \pi/2\sqrt{3} \approx 0.9069$. (b) Smectic layer spacing λ_{SmA}^* relative to the average rod length L_0 corresponding to the nematic-smectic bifurcation curves in (a). The two-dimensional hexagonal spacing at the N-C bifurcation is insensitive to σ (for both conditions) and remains at a constant value $\lambda_C^*/D = 1.223$.

First of all, from Fig. 8.1(a) we note the drastic effect of Parsons' rescaling which brings about a major downward shift of the bifurcation densities, leading to more realistic results. In particular, for $\sigma = 0$ we observe that the metastable nematic-columnar bifurcation which occurs beyond the volume fraction of closest packing within the second virial approximation, is now located in the physical regime. At higher polydispersities the bifurcation to the smectic phase is postponed to higher ϕ whereas the transition to the columnar state is completely unaffected according to the structure factor condition Eq. (8.4) or only marginally stabilized as predicted from the self-consistent method Eq. (8.3). This is a manifestation of the fact that the cylinder length and diameter represent completely *independent* length scales. Note that a similar indifference would be observed for the nematic-smectic bifurcation in case of *diameter* polydispersity.

The fact that Eq. (8.3) leads to systematically lower bifurcation densities compared to Eq. (8.4) is due to the additional composition fluctuations which are not allowed by the socalled *constrained eutectic* condition of Eq. (8.4) [130]. A more surprising discrepancy however is the trend of the smectic layer spacing in Fig. 8.1(b). Although both conditions predict an initial grow of the layer spacing upon increasing σ, the structure factor condition yields an unexpected and rather unphysical *decrease* of the spacing at
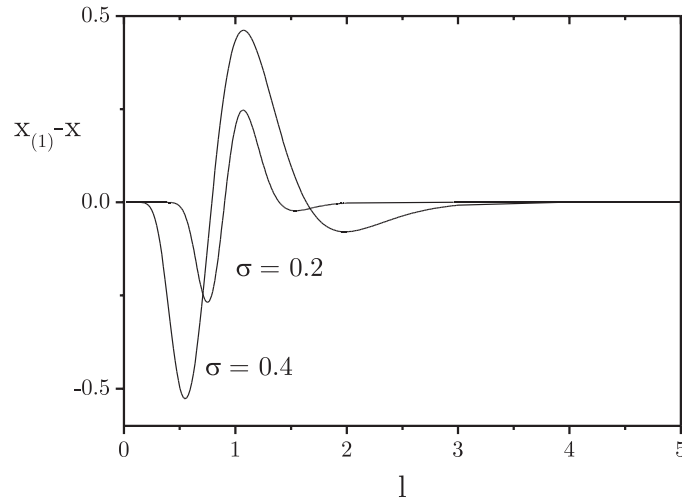
Figure 8.2. Relative eigenfunctions $x_{(1)}(l) - x(l)$ corresponding to the N-SmA bifurcation for the same system as in Fig. 8.1. at two different parent polydispersities.

higher polydispersities. This behaviour does not follow from the self-consistent condition which predicts an increase up to some *terminal* polydispersity at $\sigma = 0.623$. Beyond this point the wave-vector which minimizes the bifurcation density has jumped to zero, which formally corresponds to a macroscopic density modulation no longer reflecting a genuine smectic symmetry. We thus expect the smectic order to be entirely destroyed above the terminal value. However, we also see that the smectic phase becomes metastable with respect to a N-C transition considerably below the terminal value; at $\sigma > 0.434$ the nematic-smectic bifurcation is pre-empted by a transition from the nematic to a columnar state. This mechanism is essentially different from the one reported by Sluckin. Based on analytical results (which are reproduced by the dashed curve in Fig. 8.1(a)) it was argued that the destruction of the smectic phase occurs at the terminal polydispersity where ϕ^* reaches its close packing value, i.e. at $\sigma \simeq 0.3$.

The length distributions depicted in Fig. 8.2 suggest that there must be a strong coupling between fluctuations in the spatial density and the length distribution. The system shows a clear propensity to expel particles with below-average lengths from the emerging smectic phases whereas rods of average (or slightly higher than average) length are favoured. The coupling between composition and density fluctuations is probably responsible for the unphysical results obtained from the constrained eutectic bifurcation condition Eq. (8.4).

8.4. Discussion and outlook

Results from Monte Carlo simulations by Bates and Frenkel [127] and DFT calculations by Bohle *et al.* [128] for freely rotating polydisperse rods reveal a scenario which is similar to ours; there is a crossover from a smectic to a columnar state upon increasing length polydispersity. Quantitatively, these crossovers were predicted around $\sigma \simeq 0.25$

(DFT) and $\sigma \simeq 0.18$ (simulations) which is about half the value found in this study. A comparable phenomenon was found in binary mixtures of short and long parallel hard cylinders at certain intermediate mole fractions [67]. These results imply that the columnar phase becomes a thermodynamically stable high-density phase in highly polydisperse systems of rods.

The key issue which prevents our description from being quantitatively reliable is the neglect of orientations. Although one might argue that the rods are almost perfectly aligned at high packing fractions, it turns out that the orientational free energy remains an essential ingredient in the regime where smectic or columnar phases appear. We can illustrate this notion by comparing the nematic-smectic bifurcation for infinitely thin parallel rods, shown in Fig. 8.1(a) at $\sigma = 0$, to the one obtained for *freely rotating* rods. The latter is calculated within Onsager-Parsons theory using the self-consistent condition, given by Eq. (1.49). The required transformed Mayer function, Eq. (1.50), for a freely rotating infinitely thin rod is obtained from an explicit analysis for sphero-cylinders by Van Roij [58]. This yields $\phi^* = 0.4037$ with corresponding dimensionless smectic spacing $\lambda^*/L = 1.293$ in close agreement with the simulation result $\phi^* = 0.418$ from Bolhuis and Frenkel [42]. Comparing this with the present results $\phi^* = 0.338$ and $\lambda^*/L = 1.398$ we conclude that introducing orientational freedom causes a significant upward shift of the bifurcation density while simultaneously giving a *smaller* value for the layer spacing. These findings were in fact already reported by Poniewierski [120] using a similar asymptotic analysis. Moreover, allowing for orientational degrees of freedom leads to a first-order nematic-smectic transition –compared to a *continuous* transition for the aligned fluid[†]– irrespective of the aspect ratio [124]. In this case, the bifurcation analysis is no longer an appropriate tool to locate the onset of the phase transition since the amplitudes of the smectic density waves then suddenly jump to finite values (rather than raising continuously from zero) at the onset of the transition.

Another deficiency of the parallel-cylinder model is that it does not discriminate between a slender rodlike and a thin platelike cylinder, as the results are completely independent of the aspect ratio. Formally, the results presented here should therefore also apply to thin parallel disks. However, the model does not give a realistic description of plate systems since these do not exhibit a nematic-smectic transition but a first order nematic-columnar one at all aspect ratios [18, 131].

Extending the present approach to polydisperse mixtures of freely rotating rods poses serious technical difficulties. Although progress has been made for the nematic-smectic bifurcation for polydisperse thin rods by performing an asymptotic expansion of the orientationally averaged correlation function (i.e. the transformed excluded-volume body) using Gaussian trial ODFs [59], a similar expansion for the columnar symmetry however could not be performed analytically.

[†]The effect of polydispersity on the nature of the nematic-smectic and nematic-columnar transitions could in principle be verified by considering higher-order bifurcation equations emerging from a Landau-type expansion of the free energy [115]. We shall leave this issue untouched in this Chapter.

As to platelets the situation is even more cumbersome, as already noted in the Chapter 1. The reason for this is that the excluded-volume body of a thin disk is an intricate and hence difficult to parametrize geometrical object, in particular, when the mutual angles between two platelets is comparable to the internal angle L/D and edge-edge correlations start to play a role. These near-parallel configurations must be described properly since they are largely responsible for driving a nematic phase into a columnar structure.

Part III

Epilogue

9

Sedimentation and multi-phase equilibria in mixtures of platelets and ideal polymer

ABSTRACT

The role of gravity in the phase behaviour of mixtures of hard colloidal plates without and with non-adsorbing ideal polymer is explored. By analyzing the (macroscopic) osmotic equilibrium conditions we show that sedimentation of the colloidal platelets is significant on a height-range of even a centimeter. Gravity enables the system to explore a large density range within the height of a test tube which may give rise to the simultaneous presence of multiple phases. As to plate-polymer mixtures it is shown that sedimentation may lead to a coexistence of four phases including an isotropic gas and liquid phase, nematic and columnar phase. The phenomenon has been observed experimentally in systems of colloidal gibbsite platelets mixed with PDMS-polymer.

9.1. INTRODUCTION

It is well known that adding non-adsorbing polymer to a colloidal dispersion induces an attractive depletion potential of mean force between the colloidal particles. For colloidal spheres, the attractive potential has been shown to give rise to a phase separation in a colloid-poor "gas" and colloid-rich "liquid" or "solid" phase at sufficiently high concentrations of the colloid and the polymer [132–136]. Compared to colloidal spheres the behaviour of dispersions of rod- and platelike colloids mixed with polymer is richer due to their possibility to form liquid crystal phases, i.e. nematic (N), smectic (SmA) and columnar (C). Recent experiments on mixtures of colloidal gibbsite platelets and non-adsorbing polymer have uncovered the phase behaviour of plate-polymer mixtures [75]. A manifestation of the rich phase behaviour of these mixtures is the observation of a four-phase equilibrium involving both isotropic gas and liquid phases along with nematic and columnar states. The appearance of this multi-phase coexistence seems to conflict with the phase rule of Gibbs which states that the number of coexisting phases is limited to three for an athermal binary mixture. One of the possible explanations conjectured by the authors [75] is that the observation might be due to the polydispersity in particle size since the presence of many components (i.e. platelets with different diameters and thicknesses) in principle allows for a coexistence of arbitrarily many phases.

Another possibility to reconcile the experimental results with Gibbs' phase rule is by accounting for an external gravitational field. Sedimentation of particles leads to a

density gradient which facilitates the formation of multiple phases in a vessel of sufficient height. In this Chapter we scrutinize the effect of sedimentation in systems of colloidal platelets with and without added polymer from a simple osmotic equilibrium treatment. We will first consider a one-component system of colloidal platelets and then study the influence of the polymer-induced depletion attraction using a mean-field free-volume theory [137, 138].

9.2. Sedimentation equilibrium: one-component system

Let us consider a vessel containing colloidal particles (platelets) in osmotic equilibrium with a dispersing solvent with a chemical potential μ_0 subject to a gravitational field along the z-direction of the vessel. We assume that the concentration profile of the colloids is sufficiently smooth so that the system is *locally* in a homogeneous equilibrium state between z and $z + dz$. This is usually the case if the particles are not too large and heavy and if the dispersion is not too close to a critical point. The (macroscopic) condition for sedimentation equilibrium reads

$$-\left(\frac{\partial \Pi}{\partial \rho}\right)_{T,\mu_0} \frac{d\rho}{dz} = m^* g \rho \tag{9.1}$$

in terms of the osmotic compressibility $(\partial \rho / \partial \Pi)_{T,\mu_0}$ of the dispersion and the buoyant mass m^* of the colloidal particle (g is the gravitational acceleration). The concentration profile $\rho(z)$ of the colloids can be obtained from Eq. (9.1) if the osmotic pressure as a function of ρ, i.e. the equation of state (EOS), is known.

In the present study we will encounter phase-separated samples which contain a number of coexisting phases. Since these phases are generally described by *different* equations of state it is convenient to treat each daughter phase i separately and assign a phase height H_i to each of them. Recasting Eq. (9.1) in dimensionless form by introducing the height parameter $\zeta = z/H_{(i)}$ (with $0 < \zeta < 1$) and dimensionless plate concentration $c_i = \rho_i D^3$ (with D the plate diameter) corresponding to phase i yields

$$-\frac{1}{c_i(\zeta)} \frac{dc_i(\zeta)}{d\zeta} \left(\frac{\partial(\beta \Pi_i D^3)}{\partial c_i(\zeta)}\right)_{T,\mu_0} = \tilde{H}_i \tag{9.2}$$

with $\beta = 1/k_B T$ and $\tilde{H}_i = H_i/\xi$ the height of phase i rendered dimensionless by relating it to the *gravitational length* $\xi = k_B T/m^* g$ which is on the order of 10^{-3} m for the colloidal dispersions of gibbsite platelets we consider here.

The average concentration $c_{0,i}$ in phase i follows from

$$\int_0^1 c_i(\zeta) d\zeta = \int_{c_{b,i}}^{c_{t,i}} c_i'(\zeta) \frac{d\zeta}{dc_i'} dc_i' = c_{0,i} \tag{9.3}$$

where $c_{t,i}$ and $c_{b,i}$ denote the concentrations at the top and the bottom of the phase, respectively. The average concentration c_0 of the *sample* then follows from a simple linear combination $c_0 = \sum_i c_{0,i} \tilde{H}_i / \tilde{H}$ with $\tilde{H} = \sum_i \tilde{H}_i$ the dimensionless sample height.

Note that in an experimental situation these concentrations are to be determined from a *given* average sample concentration c_0. In order to solve Eq. (9.2) for colloidal platelets
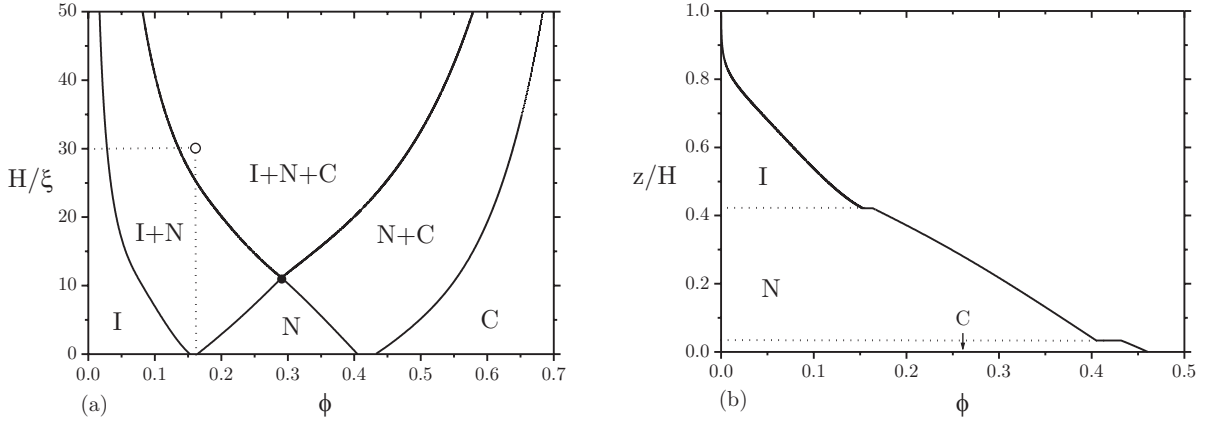
FIGURE 9.1. (a) Phase diagram for colloidal platelets with $L/D = 0.05$ in a gravitational field. Plotted is the reduced *sample* height $\tilde{H} = H/\xi$ versus the overall plate volume fraction ϕ_0. The three-phase region opens up at $H = 11.15\xi$. (b) Concentration profile of a sample with overall volume fraction $\phi_0 = 0.157$ and vessel height $H = 30\xi$ (corresponding to the open dot in (a)). Plotted is the relative height z/H versus ϕ. The $I-N$ and $N-C$ phase boundaries are indicated by the horizontal dotted lines.

we must known the EOS $\Pi_i(c_i)$ for the different liquid crystal states (*viz.* isotropic (I), nematic (N) and columnar (C)) encountered upon densifying these systems. As a quantitative input we use fits to the EOS obtained from Monte-Carlo simulations of hard platelets performed by Zhang *et al.* [43]. A polynomial of the K-th order was used as a fitting function so that $\beta\Pi_i D^3 = \sum_{n=1}^{K} a_{n,i}c_i^n$, with $i = I, N, C$. The coefficients $a_{n,i}$ pertaining to state i can be found in Ref. [43]. The polynomial form of the EOS allows for a simple analytic solution of the concentration profile from Eq. (9.2) in the different phases.

The effect of gravity on the phase behaviour of the colloidal platelets is presented in Fig. 9.1. The curves represent so-called *cloud curves* which indicate the minimum sample height (and associated overall volume fraction) needed to induce the formation of an infinitesimal amount of a new phase at the top and/or the bottom of the vessel due to sedimentation of the particles. On the horizontal axis we find the coexistence densities for the $I-N$ and $N-C$ transitions at zero gravity, which would correspond to a vessel with zero height. Fig. 9.1(a) shows that a vessel height of about 10 gravitational lengths already leads to significant changes in the phase diagram. A large three-phase isotropic-nematic-columnar region is encountered which opens up at the state point indicated by the black dot. At the associated volume fraction ($\phi_0 = 0.291$) the system is fully nematic at short sample heights but as soon as the height exceeds 11.15 gravitational lengths two additional fractions of an isotropic and columnar phase are split off *simultaneously* at the top and bottom of the sample, respectively. To compare with actual sample heights we use the following expression for the gravitation length, $\xi = k_B T/(g v_{\text{plate}} \rho^*_{\text{plate}})$ with $v_{\text{plate}} = \frac{\pi}{4}LD^2$ the colloid volume. Using experimental data for the colloidal gibbsite platelets dispersed in toluene (plate dimensions $D = 180$ nm, $L = 12$ nm and buoyant

density $\rho^*_{\text{plate}} = 1.5 \ 10^3$ kg/m^3) we obtain $\xi = 0.9$ mm. This means that the three-phase isotropic-nematic-columnar equilibria in Fig. 9.1 may be expected in samples larger than a centimeter, which is comparable to the typical height of a test tube. Fig. 9.1(b) shows an example of a concentration profile one may encounter experimentally in a sample with overall plate volume fraction of 15.7 % and height of 2.7 cm. The scenario is that the system initially phase separates into equal portions of an isotropic and nematic phase. At a later stage, a columnar fraction will be formed at the bottom of the vessel due to slow sedimentation of the platelets. At sedimentation equilibrium, the I, N and C phases respectively occupy 58, 39 and 3 % of the system volume.

9.3. Plate-polymer mixtures

We now turn to systems of colloidal platelets (component "1") mixed with non-adsorbing ideal polymers (denoted by "p") in a solvent. The gravitational length of the polymer is much larger than that of the colloidal particles ($\xi_p >> \xi_1$) due to its negligible buoyant mass. We may therefore assume that there is no external force acting on the polymer coil and that the chemical potential of the polymer can be considered *constant* throughout the system. The mixture can thus be treated as an *effective* one-component system of colloidal platelets in a gravitational field and the osmotic pressure balance now reads analogously to Eq. (9.1)

$$-\left(\frac{\partial \Pi}{\partial \rho_1}\right)_{T,\mu_0,\mu_p} \frac{d\rho_1}{dz} = m^*_1 g \rho_1, \tag{9.4}$$

at constant μ_p. Similar to Eq. (9.2) we can rewrite this equilibrium condition in dimensionless form. Substituting the EOS for a colloid-polymer mixture from a free-volume treatment of the Asakura-Osawa model (see Appendix) yields the following differential equation describing the colloid density profile $c_{1,i}(\zeta)$ in the daughter phase i

$$-\frac{1}{c_{1,i}(\zeta)} \frac{dc_{1,i}(\zeta)}{d\zeta} \left[\left(\frac{\partial(\beta\Pi_i^{(0)}D^3)}{\partial c_{1,i}}\right)_{T,\mu_0,\mu_2} - z_p D^3 \left(\frac{d^2\alpha_i}{dc_{1,i}^2}\right) c_{1,i}(\zeta) \right] = \tilde{H}_i, \tag{9.5}$$

which must be solved along with the auxiliary condition for the overall concentration Eq. (9.3). Comparing with Eq. (9.2) we see that the terms between square brackets now represent an *effective* (inverse) osmotic compressibility. The first contribution is the inverse compressibility of the one-component plate system whereas the second term accounts for the effective depletion attraction between the platelets due to the presence of the polymer. The strength of the depletion attraction can be varied by changing the fugacity z_p of the polymer, related to the chemical potential via $z_p = \exp[\beta\mu_p]/V$. Note that the result for a one-component system (Eq. (9.2)) is recovered for $z_p = 0$, as it should. The effective compressibility also depends on the fraction of *free volume* α_i available to the polymer in the liquid crystal state i. Explicit expressions for α_i are given in the Appendix. It is easily verified that $d^2\alpha_i/dc_{1,i}^2$ is generally positive for all states $i = I, N, C$ implying that the effective osmotic compressibility is *larger* than
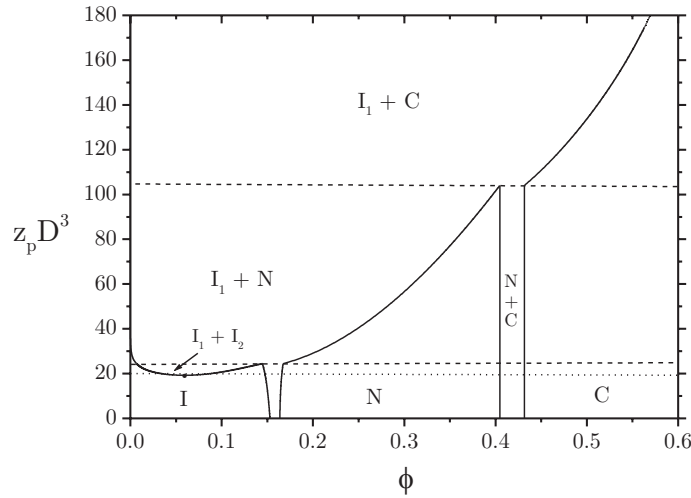
FIGURE 9.2. Phase diagram of a plate-polymer mixture with $L/D = 0.05$ and $q = 0.355$ in the fugacity - volume fraction plane, reproduced from Ref. [43]. On the vertical axis, the region of stable isotropic gas-liquid $(I_1 - I_2)$ equilibria is confined between a lower critical point at $z_pD^3 = 19.233$ (dotted line) and the $I_1 - I_2 - N$ triple line at $z_pD^3 = 24.454$ (lower dashed line). The upper dashed line at $z_pD^3 = 104$ represents the $I_1 - N - C$ triple line.

that of a pure system of plates due to the attractive depletion forces, as we intuitively expect.

In Fig. 9.2 we have depicted a phase diagram for the zero-gravity case reproduced from Ref. [43]. The values for the plate aspect ratio and the polymer to plate size ratio $q = 2R_g/D$ (with R_g the polymer radius of gyration) are chosen such as to match the experimental values for the gibbsite-PDMS mixtures studied by Van der Kooij *et al.* [75]. The volume fractions in the coexisting phases can be deduced from tie lines given by horizontal lines in this representation. At low reservoir fugacity the phase behaviour of the mixture differs only marginally from that of the pure system. At $z_pD^3 > 19.233$ the isotropic phase becomes unstable with respect to a demixing into an isotropic gas phase (I_1) and a liquid phase (I_2). The gas phase is poor in colloid but rich in polymer, vice versa for the liquid phase. The nematic-columnar transition is virtually unaffected by the presence of the polymer up to the $I_1 - N - C$ triple line located at $z_pD^3 = 104$. At higher fugacities the depletion attraction is strong enough to induce a transition from an isotropic gas (I_1) to a columnar solid (C) phase, without the intervention of a nematic phase.

In Fig. 9.3 we have depicted a phase representation, analogous to Fig. 9.1, of the same mixture in a gravitational field at fixed reservoir fugacity $z_pD^3 = 20$. Also here, we see that sedimentation leads to remarkably rich phase behaviour; several multi-phase equilibria appear that are not present in the zero-gravity case in Fig. 9.2. Most notably, a four-phase region opens up at $H/\xi = 11.70$ which, recalling that $\xi = 0.9$ mm, is again about a centimeter. An equilibrium involving isotropic gas, liquid, nematic and columnar phases has also been observed in the gibbsite-PDMS mixtures [75]. We stress
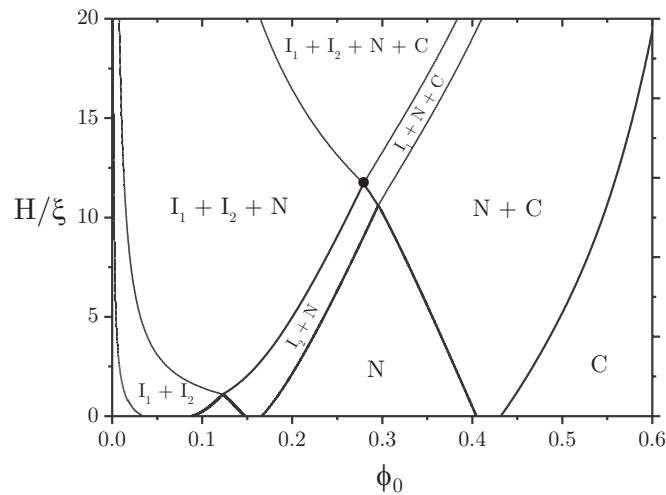
Figure 9.3. Phase diagram of the same mixture as in Fig. 9.2 in a gravitational field at (constant) fugacity $z_p D^3 = 20$. Plotted is the relative sample height $\tilde{H} = H/\xi$ versus the overall plate volume fraction. The four-phase region opens up at $H = 11.70\xi$ (black dot).
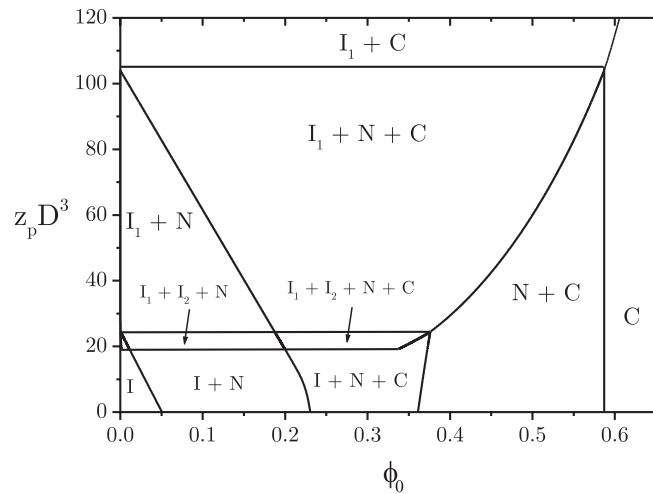

Figure 9.4. Same as Fig. 9.3 in a reservoir fugacity - volume fraction representation at fixed vessel height $H = 1.5$ cm ($H/\xi = 16.67$).

that the experimental observation of four distinct phases in a tube of a few centimeters is related in a fortuitous way to the platelets' size (and hence their gravitational length). If the platelets were much larger, they would rather have formed a dense, quasi-uniform sediment at the bottom of the tube. If they were smaller, gravity might not have been strong enough to enforce a four-phase sedimentation equilibrium.

From an experimental standpoint it is more appropriate to fix the total sample height rather than the reservoir fugacity. In Fig. 9.4 we show a representation in terms of the fugacity versus the overall volume fraction at fixed sample height $H = 1.5$ cm, which is the typical length of the test tubes used in experiment [75]. Unlike Fig. 9.2 this representation does *not* provide information about the composition of the coexisting
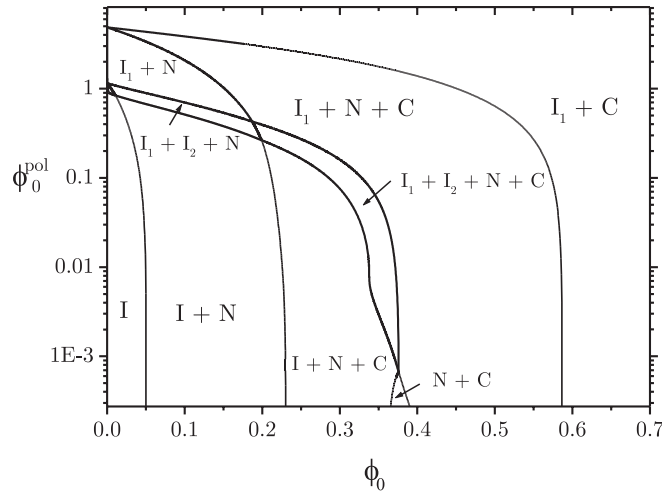
Figure 9.5. Phase diagram corresponding to Fig. 9.4 in terms of the overall polymer concentration ϕ_0^{pol} in the system (plotted on a logarithmic scale) versus ϕ_0. The monophasic region for the columnar phase is not visible on this scale due to extremely low polymer concentrations.

phases, it merely indicates which phases can be expected in a sample with a fixed height and a given overall density and reservoir fugacity. Comparing with Fig. 9.2 we see that the four-phase region in Fig. 9.4 must be confined within the range $19.233 < z_p D^3 < 24.454$ since only there both stable $I_1 - I_2$ and $N - C$ two-phase equilibria occur at low and high densities, respectively.

In Fig. 9.5 we have depicted the same phase diagram in terms of the overall volume fractions of polymer and colloid in the system. The polymer volume fraction in phase i is obtained straightforwardly from $\phi_i^{\text{pol}} = (\pi/6)q^3 z_p D^3 \langle \alpha \rangle_i$ where $\langle \alpha \rangle_i$ is the average free-volume fraction in phase i. This diagram is probably more appealing from a practical point of view than the previous ones since it directly shows which phases can be expected when polymer and platelets are mixed at known concentrations. Clearly, the four-phase region extends over a considerable region of polymer and colloid concentrations showing that a four-phase equilibrium may be expected in a broad range of plate-polymer compositions.

In conclusion, we state that gravity enables the colloidal platelets to scan a large density range within the range of a few centimeters. Since mixtures of plates and ideal polymer display a number of phase transitions within a relatively small range of concentrations, sedimentation may thus lead to the presence of multiple phases in a test tube. It is important to note that the *maximum* number of phases that can appear simultaneously in the tube is governed solely by the effective interactions between the colloids. In the present system these interactions are tuned directly by the polymer chemical potential in the reservoir. Gravity can therefore only induce the formation of those phases that are allowed at a particular interaction strength, as becomes evident from comparing Fig. 9.3 to Fig. 9.2.

9.4. Final Remarks

The theoretical results obtained thus far prompt us to reconsider experimental observations in other colloidal mixtures. For instance, mixtures of hard rod- with platelike colloids also display rich phase behaviour with a possibility of even five coexisting phases [82]. The five-phase coexistence involves (from top to bottom) an isotropic, rod-rich nematic (N^+), X-phase (its symmetry has not been identified yet), plate-rich nematic (N^-) and a columnar phase. Also in these mixtures, the polydispersity in particle size (both plate-diameter and rod-length) is appreciable. Although the phase behaviour is certainly influenced by polydispersity the effect of gravity should not be neglected. Given the present results one may question to what extent these multi-phase equilibria are induced by an external gravitational field acting on the particles. This issue will be deferred to future investigation. However, we can already point out that both components will generally be subject to the gravitational field in these mixtures so that the effective one-component approach, described in Sec. 9.3, cannot be applied for binary mixtures of colloids. Consequently, the chemical potentials of the species are coupled and therefore cannot be varied independently (as we could do for μ_p in this study) [139]. Clearly, the coupling leads to more complicated equilibrium conditions than the ones formulated here.

Appendix: Mean-field description of the Asakura-Oosawa model

To study the thermodynamic properties of colloid-polymer mixtures it is advantageous to consider a so-called *semi-grand canonical ensemble* comprising a system of N colloidal particles in osmotic equilibrium with a reservoir containing polymer solution at fixed chemical potential for the polymer μ_p and the solvent μ_0 [137, 140]. In the derivations below we shall ignore the "background" solvent for notational convenience. Note that, unlike the colloids, the polymer coils are allowed to exchange between the system and the reservoir. In the Asakura-Oosawa model [141–143] the interactions between the colloids U_{cc} are considered hard whereas the polymers are modeled as penetrable hard spheres. The latter implies that the polymers have no interaction with each other ($U_{pp} = 0$) but a hard-body interaction with the colloids. Therefore, $U_{cp} = \infty$ if any polymer sphere overlaps with a colloid and $U_{cp} = 0$ otherwise. Let us denote the positions and orientations of the N colloidal platelets collectively by $\{\mathbf{r}^N, \mathbf{\Omega}^N\}$ and the positions of the M polymers by $\{\mathbf{r}^M\}$. The semi-grand canonical partition function Ξ of the system can be written as [144]

$$
\Xi(N, V, T, \mu_p) = \frac{1}{N! \mathcal{V}_c^N} \sum_{M=0}^{\infty} \frac{1}{M! \Lambda_p^{3M}} \int d\mathbf{r}^N d\mathbf{\Omega}^N d\mathbf{r}^M
$$
$$
\times \exp\left[-\beta \mu_p M - \beta U_{cc}(\mathbf{r}^N, \mathbf{\Omega}^N) - \beta U_{cp}(\mathbf{r}^N, \mathbf{\Omega}^N, \mathbf{r}^M) \right], \tag{9.6}
$$

where Λ_p^3 and $\mathcal{V}_c$ represent the thermal volumes of the polymer sphere and the platelet, obtained by performing integrations over the kinetic degrees of freedom for the polymer

and (both translational and orientational ones) for the platelet. We may now carry out the integrations over the polymer degrees of freedom for a fixed colloidal configuration $\{\mathbf{r}^N, \mathbf{\Omega}^M\}$. The outcome of this integration is simply the *free volume* in which a polymer sphere does not overlap with any colloid, i.e

$$\int d\mathbf{r}^M \exp\left[-\beta U_{cp}(\mathbf{r}^N, \mathbf{\Omega}^N, \mathbf{r}^M)\right] = \left(\int d\mathbf{r}_1 \exp\left[-\beta U_{cp}(\mathbf{r}^N, \mathbf{\Omega}^N, \mathbf{r}^M)\right]\right)^M$$

$$= \left[V_{\text{free}}(\mathbf{r}^N, \mathbf{\Omega}^N)\right]^M. \tag{9.7}$$

Using this in Eq. (9.6) we can express the semi-grand canonical partition function in a more convenient form after some rearrangements. Introducing the polymer *fugacity* $z_p = \exp\left[\beta\mu_p\right]/\Lambda_p^3$ we may write

$$\Xi(N, V, T, \mu_p) = \frac{1}{N!\mathcal{V}_c^N} \int d\mathbf{r}^N d\mathbf{\Omega}^N \exp\left[-\beta U_{cc}(\mathbf{r}^N, \mathbf{\Omega}^N)\right] \sum_{M=0}^{\infty} \frac{1}{M!} \left[z_p V_{\text{free}}(\mathbf{r}^N, \mathbf{\Omega}^N)\right]^M$$

$$= \frac{1}{N!\mathcal{V}_c^N} \int d\mathbf{r}^N d\mathbf{\Omega}^N \exp\left[-\beta W_{cc}(\mathbf{r}^N, \mathbf{\Omega}^N)\right], \tag{9.8}$$

where W_{cc} is the potential of mean force between the platelets accounting for the depletion effect of the polymer:

$$\beta W_{cc}(\mathbf{r}^N, \mathbf{\Omega}^N) = \beta U_{cc}(\mathbf{r}^N, \mathbf{\Omega}^N) - z_p V_{\text{free}}(\mathbf{r}^N, \mathbf{\Omega}^N). \tag{9.9}$$

We will now apply a mean-field approximation to this exact result by replacing the configurationally dependent free volume with a *mean free volume*, averaged over all colloidal configurations of a pure system of platelets [137]. Introducing the configurationally averaged free-volume fraction α we thus substitute $V_{\text{free}}(\mathbf{r}^N, \mathbf{\Omega}^N) = \alpha V$ so that Eq. (9.8) becomes

$$\Xi(N, V, T, z_p) = Q_c^{(0)}(N, V, T) \exp\left[z_p \alpha V\right], \tag{9.10}$$

in terms of the canonical partition function $Q_c^{(0)}(N, V, T)$ for a pure system of hard platelets. The semi-grand canonical potential of the mixture now follows from $\beta\Omega = -\ln\Xi$ so that

$$\beta\Omega(N, V, T, z_p) = \beta F^{(0)}(N, V, T, z_p = 0) - z_p \alpha V, \tag{9.11}$$

with $F^{(0)}$ the reference (Helmholtz) free energy of the colloidal system without polymer. Note that z_p is equal to the reservoir polymer concentration $\rho_p = N_p/V$ for an ideal polymer. The average number of polymers in the system $\langle N_p \rangle$ follows from the standard derivative $\langle N_p \rangle = -z_p \left(\partial\beta\Omega/\partial z_p\right)_{N,V,T}$. Combining this with Eq. (9.11) we can establish the straightforward relation, $\langle N_p \rangle/V = \rho_p \alpha$, stating that the average polymer concentration in the system $\langle N_p \rangle/V$ is simply the reservoir polymer concentration times the free-volume fraction.

The osmotic pressure of the colloid-polymer mixture follows from Eq. (9.11) using the standard derivative $\Pi = -\left(\partial\Omega/\partial V\right)_{N,T,\mu_p}$:

$$\tilde{\Pi} = \tilde{\Pi}^{(0)} + z_p D^3 \left[\alpha - \rho\frac{d\alpha}{d\rho}\right], \tag{9.12}$$

in terms of the dimensionless pressure $\tilde{\Pi}^{(0)} \equiv \beta\Pi^{(0)}D^3$ of the reference platelet system. An expression for the free-volume fraction α can be obtained from scaled particle theory [145, 146]. Zhang *et al.* [138] derived expressions for *cut spheres* with diameter D and thickness L. The general expression for the free volume reads

$$\alpha = (1 - \phi)\exp\left[-\left(Ay + By^2 + C\tilde{\Pi}^{(0)}\right)\right], \tag{9.13}$$

with $y \equiv \phi/(1 - \phi)$ and ϕ the plate volume fraction. The expression still depends on the pressure $\Pi^{(0)}$ of the reference cut sphere system, for which no analytical expression is available yet. Specific expressions α_i for the different liquid crystal states i can be obtained by inserting the corresponding EOS $\tilde{\Pi}_i^{(0)}$ from the simulation fits. The coefficients are given by

$$A = \frac{q\left(1 + 2l - l^2\right) + q^2\left[2l + \left(\frac{\pi}{2} - \arcsin l\right)\right]\sqrt{1 - l^2}}{(l - l^3/3)},$$

$$B = \frac{q^2\left(1 + 2l - l^2\right)^2}{2\left(l - l^3/3\right)^2}, \qquad C = \pi q^3/6, \tag{9.14}$$

with $l = L/D$ the inverse plate aspect ratio and $q = 2R_g/D$ the size ratio of the ideal spherical polymer and the platelet. The volume fraction follows from

$$\phi = \frac{\pi}{4}\rho D^3\left(l - l^3/3\right). \tag{9.15}$$

ACKNOWLEDGEMENT

10

On the equation of state of a dense columnar liquid crystal

ABSTRACT

We present an accurate description of a columnar liquid crystal of hard disks at high packing fractions using an improved free-volume theory. We find that the orientational entropy plays a crucial role and leads to a different high-density scaling pressure compared to the traditional cell model. Our predictions are quantitatively tested against recent Monte-Carlo simulations on hard cut spheres showing that the pressures agree within 1% at packing fractions $\phi > 0.8$. The inter- and intracolumnar spacings are found to match the simulations within 1% over the entire columnar stability range.

10.1. INTRODUCTION

The lyotropic columnar liquid crystal state, characterized by a two-dimensional hexagonal stacking of columns each with a liquidlike internal structure, has received considerable attention in recent years both in experiment [147, 148] and computer simulations [18, 43]. The recently developed systems of polymer-grafted polydisperse gibbsite colloids are known to show a first order phase transition from the homogeneous nematic state to an inhomogeneous columnar phase upon densification [148]. The columnar signature of the latter is evidenced by its bright Bragg-reflections for visible light and it has also been confirmed on a more rigorous basis using Small-Angle X-ray Scattering (SAXS). Future efforts can, for instance, be put into purifying these systems (to reduce its polydispersity) and manipulating the columnar texture by means of a magnetic field, both aimed at making high-quality single-domain columnar structures, which may serve as candidates for the production of e.g. colloidal photonic crystals [149, 150].

Recent simulation work by Zhang *et al.* has led to accurate numerical results for the various thermodynamic properties of the columnar state, e.g. pressure, chemical potential and the free-volume fraction (see Chapter 9), which pose a challenge for theoretical interpretation. In this Chapter we shall consider a simple but accurate description for a columnar state inspired by cell theory, which was first applied to spatially ordered liquid crystals by Taylor, Hentschke and Herzfeld [151, 152]. To describe the properties in the positionally ordered dimensions the particles are assumed to be confined within discrete compartments according to the classical free-volume approach [153, 154]. For the columnar phase, these compartments are represented by hexagonal tubular cells which form a close-packed structure. In the non-correlated version of the cell model

151

the disks may take any position within the cell but they may not share the cell with another particle or penetrate an adjacent one. The cell model will be combined with an appropriate description of the one-dimensional fluid behaviour of the disks inside the columnar cells, which we will discuss first.

10.2. Modified Tonks fluid

We start from the traditional Tonks model [155] applied to a one-dimensional fluid of N hard disks with diameter D and thickness L whose centres of mass can move freely on a line with length ℓ. Since the disks are allowed to rotate freely around their centres of mass, the effective excluded thickness $\tilde{L}_{i,j}$ between two adjacent disks i and j is an orientation-dependent quantity, i.e. $\tilde{L}_{i,j}(\Omega_i, \Omega_j) > L$, in terms of the solid angle Ω. We assign x_k to the position of particle k on the line and fix the first and last particle at $x_1 = 0$ and $x_N = \ell$, respectively. The configurational integral for this system in the macroscopic limit $L/\ell \to 0$ is then formally written as

$$Q_N = \frac{1}{\mathcal{V}^N N!} Q_N^{\text{or}} \left\langle \left(\ell - \tilde{L}_{\text{tot}}(\Omega_1, \ldots, \Omega_N) \right)^N \right\rangle_{f(\Omega)}, \qquad (10.1)$$

with $\mathcal{V}$ the thermal volume pertaining to the translational and orientational kinetic degrees of freedom. The brackets denote an orientational average according to some unknown orientation distribution function (ODF) $f(\Omega)$ which is normalized according to $\int f(\Omega) d\Omega \equiv 1$. Note that Q_N is proportional to an N-dimensional free volume with $\tilde{L}_{\text{tot}}$ the total occupied length for a given orientational configuration, expressed in terms of the following sum

$$\tilde{L}_{\text{tot}}(\Omega_1, \ldots, \Omega_N) = \sum_{k=1}^{N} \tilde{L}_{k,k+1}(\Omega_k, \Omega_{k+1}). \qquad (10.2)$$

Eq. (10.1) is difficult to analyze rigorously so we shall approximate it as follows

$$Q_N \simeq \frac{\ell^N}{\mathcal{V}^N N!} Q_N^{\text{or}} \left(1 - \frac{1}{\ell} \left\langle \tilde{L}_{\text{tot}}(\Omega_1, \ldots, \Omega_N) \right\rangle_{f(\Omega)} \right)^N, \qquad (10.3)$$

which is assumed to be justified for the strongly aligned orientational configurations we expect in a concentrated columnar state. Further simplification in this respect can be achieved by neglecting the azimuthal dependency of the excluded length between two adjacent disks. To this end we shall consider an *effective* thickness of the disks, which is determined solely by the polar deflection angle. For small angles this quantity is given by

$$\tilde{L}_{\text{eff}} = L \left[1 + \frac{1}{2} \frac{D}{L} |\theta| + \mathcal{O}(\theta^2) \right], \qquad (10.4)$$

up to leading order in θ. To account for the azimuthal correlations we have included the prefactor '1/2' in Eq. (10.4). In this way we partially correct for the fact that the excluded length between two disks at fixed polar angles becomes minimal when

the azimuthal orientations are the same. The orientationally averaged total occupied length is now approximated by the following mean-field expression

$$\left\langle \tilde{L}_{\text{tot}} \right\rangle_{f(\Omega)} \simeq N \left\langle \tilde{L}_{\text{eff}} \right\rangle_{f(\theta)}. \tag{10.5}$$

where the ODF obeys common uniaxial symmetry and depends only on the polar angle θ. The configurational integral then simply becomes

$$Q_N = \frac{\ell^N}{\mathcal{V}^N N!} Q_N^{\text{or}} \left(1 - \rho \left[1 + \frac{D}{2L} \langle |\theta| \rangle_{f(\theta)} \right] \right)^N, \tag{10.6}$$

in terms of the linear density $\rho = NL/\ell$. The orientational configurational integral Q_N^{or} reads (cf. Eq. (1.9))

$$Q_N^{\text{or}} = \exp \left[-N \langle \ln[4\pi f(\theta)] \rangle_{f(\theta)} \right]. \tag{10.7}$$

and the total Helmholtz free energy $\beta F = -\ln Q_N$ of the modified Tonks fluid is given by a superposition of the ideal, orientational and configurational entropic contributions:

$$\frac{\beta F_{\text{fluid}}}{N} = \ln[\rho \mathcal{V}] + \int f(\theta) \ln[4\pi f(\theta)] d\Omega - \ln \left[1 - \rho \left(1 + \frac{D}{2L} \int f(\theta) |\theta| d\Omega \right) \right], \tag{10.8}$$

with $\beta = 1/k_B T$. The thermodynamic equilibrium ODF can be obtained by a functional minimization of the free energy with respect to the orientational distribution under the normalization restriction. After some algebra we arrive at the following *closed* expression for the normalized ODF:

$$f(\theta) = \frac{\alpha^2}{4\pi} \exp[-\alpha|\theta|], \tag{10.9}$$

where α depends on the density and the disk aspect ratio D/L via

$$\alpha = \frac{3}{2} \frac{D}{L} \left(\frac{\rho}{1 - \rho} \right), \tag{10.10}$$

Since $\alpha \gg 1$ for sufficiently anisometric disks ($D/L \gg 1$) the ODF is sharply peaked around $\theta = 0$, as we expect. The divergence of α at close packing ($\rho = 1$) indicates that the disks are forced to orient parallel to the director in this limit. Inserting Eq. (10.9) and straightforward integration yields an explicit free energy in terms of the density ρ. Taking the standard derivative with respect to the density then gives the (dimensionless) pressure βPL of the one-dimensional fluid:

$$\beta PL = \frac{3\rho}{1 - \rho}, \tag{10.11}$$

which is exactly three times the original Tonks pressure. This result implies that the orientational confinement of the disks inside the columns gives rise to an additional entropic contribution $2\rho/(1 - \rho)$ to the total pressure. Note that the derivation of Eq. (10.11) closely resembles the origin of the quasi-ideal pressure of the nematic state $\beta P \sim 3N/V$ within the asymptotic (Gaussian) analysis described in Sec. 5.2, although both have a different physical basis.

10.3. Cell model

The description of the columnar phase in the two positionally ordered dimensions is analogous to that of a two-dimensional (hexagonally) ordered configuration of N disks. According to the non-correlated version of the cell model the configurational integral of the N particle-system can be approximated by [156]

$$
\begin{aligned}
Q_N^{\text{cell}} &= \int d\mathbf{r}^N \exp[\beta U(\mathbf{r}^N)] \\
&\simeq \left(\int d\mathbf{r} \exp\left[-\frac{\beta}{2} u_{\text{cell}}^{\text{nn}}(\mathbf{r}) \right] \right)^N ,
\end{aligned} \tag{10.12}
$$

where $u_{\text{cell}}^{\text{nn}}(\mathbf{r})$ is the potential energy between the particle and its nearest neighbours. For hard interactions the second phase space integral is simply the (2-D) *free volume* of the particle in the cell. Assuming that the nearest neighbours constitute a perfect hexagonal cage, the free volume is given by $V_{\text{free}} = \sqrt{3}(\Delta_c - D)^2/2$ with Δ_c the nearest neighbour distance. The configurational integral then becomes (ignoring all irrelevant contributions)

$$
Q_N^{\text{cell}} \simeq (V_{\text{free}})^N \propto \left(1 - \bar{\Delta}_c^{-1} \right)^{2N} , \tag{10.13}
$$

in terms of the dimensionless spacing $\bar{\Delta}_c = \Delta_c/D$. Applying the condition of single-occupancy (i.e. one array of disks per column) we can use $\bar{\Delta}_c$ to relate the linear density ρ to the three-dimensional volume fraction via

$$
\rho = \phi^* \bar{\Delta}_c^2, \tag{10.14}
$$

with $\phi^* = \phi/\phi_{\text{cp}}$ the volume fraction normalized to its close-packing value $\phi_{\text{cp}} = \pi/2\sqrt{3}$.

The total excess Helmholtz free energy of the columnar state is obtained by adding the cell contribution to the Tonks excess free energy. Omitting all constant terms we arrive at

$$
\frac{\beta F_{\text{tot}}^{\text{ex}}}{N} \sim -2 \ln \left[\frac{\rho}{1 - \rho} \right] - \ln \left[1 - \rho \right] - 2 \ln \left[1 - \bar{\Delta}_c^{-1} \right] , \tag{10.15}
$$

representing the orientational, 'Tonks' and cell contributions, respectively. Inserting Eq. (10.14) and minimizing* the free energy with respect to the cell spacing $\bar{\Delta}_c$ yields a third-order consistency equation with complicated solutions. Expanding the physical solution near close-packing in terms of $1 - \phi^*$ up to leading order yields

$$
\bar{\Delta}_c = 1 + \frac{1}{5}(1 - \phi^*) + \mathcal{O}[(1 - \phi^*)^2]. \tag{10.16}
$$

Inserting the exact expression into the free energy Eq. (10.15) and taking the appropriate derivative gives a similar expansion for the total dimensionless pressure $\tilde{P} = \beta P v_0/\phi_{\text{cp}}$ (with v_0 the disk volume), i.e.

$$
\tilde{P} = \frac{5}{1 - \phi^*} + 6.4 + 1.128(1 - \phi^*) + \mathcal{O}[(1 - \phi^*)^2], \tag{10.17}
$$

---

*By definition, the ideal free energy ($\sim \ln \rho$) does not depend on the cell spacing and therefore drops out of the free energy minimization.
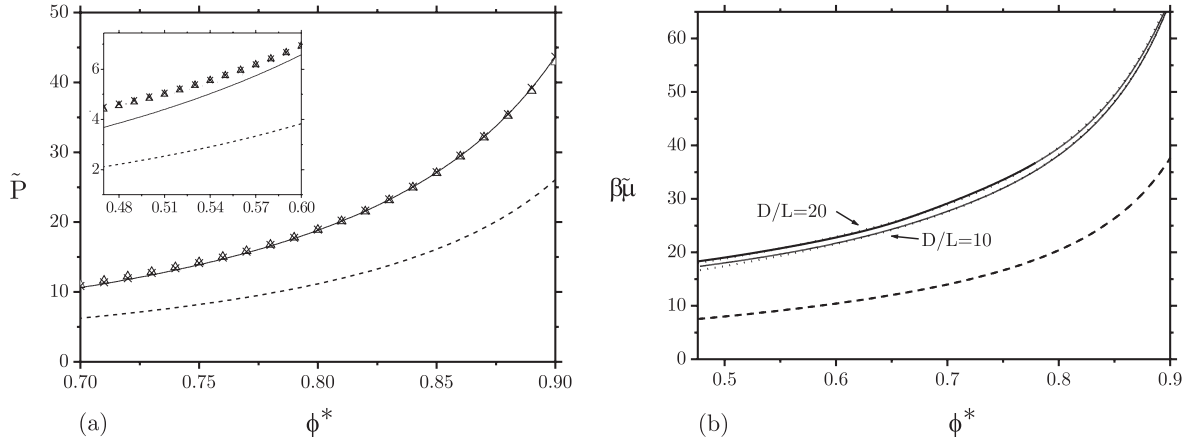
FIGURE 10.1. (a) Equations of state for the columnar phase. The solid curve is the prediction from the present cell model, the dashed curve follows from the traditional cell pressure, Eq. (10.18). The symbols correspond to the simulation data from Zhang *et al.* [43] for $D/L = 10$ (crosses) and $D/L = 20$ (triangles). The inset shows the pressure in the dilute regime near the columnar-nematic transition at $\phi^* \approx 0.48$. (b) Dimensionless chemical potential $\beta\tilde{\mu} = \beta\mu - \ln\left[v_0/\mathcal{V}\phi_{\mathrm{cp}}\right]$ from simulations (dotted curves) and cell-theory (solid curves). The prediction from the traditional cell model, indicated by the dashed curve, is independent of D/L.

indicating that the high-density scaling pressure, i.e. the leading order contribution, is essentially different from the classical cell prediction $3/(1-\phi^*)$ for hard spheres [157]. The latter result is completely analogous to our result for *perfectly aligned* disks and can be reproduced directly from Eq. (10.15) by omitting the orientational contribution given by the first term. The "traditional" cell pressure is given by

$$\tilde{P} \equiv \frac{\phi^*}{1-(\phi^*)^{1/3}} = \frac{3}{1-\phi^*} + 4 + \mathcal{O}(1-\phi^*). \tag{10.18}$$

10.4. Results and discussion

In Fig. 10.1(a) we have plotted the abovementioned cell equations of state, i.e. Eq. (10.18) and the closed-form analogue of Eq. (10.17) which we do not show here, along with ones obtained from Monte-Carlo simulations on cut-spheres by Zhang *et al.* [43], as discussed in the previous Chapter. The quantitative agreement between the present cell description and the simulations significantly improves upon densification. Above $\phi^* \approx 0.8$ the agreement is found to be smaller than 1%. Obviously, the discrepancy is much larger in the dilute regime ($\phi^* < 0.6$) where the cell model, at least the simplest version considered here, is no longer quantitatively reliable.

The chemical potentials are depicted in Fig. 10.1(b). These are readily obtained from the absolute free energy and pressure of the cell model via the Legendre transform $\mu = (F + PV)/N$ and by means of a Gibbs-Duhem integration of the pressure fits obtained from the simulation data [43]. Again, close agreement is found between both.
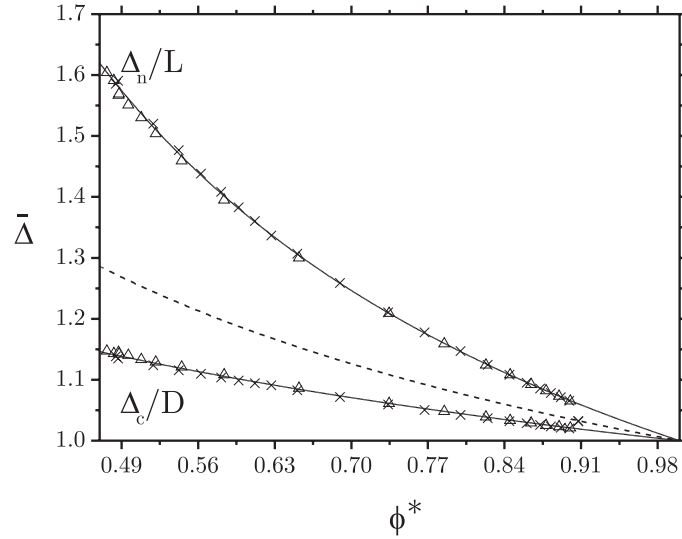
FIGURE 10.2. Normalized inter- and intracolumnar spacings, Δ_c/D and Δ_n/L respectively, as a function of ϕ^*. Solid lines are theoretical predictions, the symbols follow from simulations for $D/L = 10$ (crosses) and $D/L = 20$ (triangles). The dotted curve follows from the traditional cell model and denotes *both* spacings.

The values at melting are found to differ only by $0.3k_BT$ and $0.6k_BT$ for $D/L = 20$ and $D/L = 10$ respectively, indicating that the cell prediction is indeed surprisingly accurate throughout the ϕ^*-range. The "splitting" of the curves for both aspect ratios is simply due to the orientational entropy (second term in Eq. (10.8)):

$$\frac{\beta F_{\text{or}}}{N} = 2\ln\alpha - 2, \tag{10.19}$$

which depends explicitly on D/L via Eq. (10.10) and therefore gives rise to a different intercept at the melting volume fraction.

Let us now focus on the spacings between the columns $\bar{\Delta}_c$ and the average disk spacing inside the columns $\bar{\Delta}_n \equiv \Delta_n/L$. The latter is given by

$$\bar{\Delta}_n \equiv \rho^{-1} = 1 + \frac{3}{5}(1 - \phi^*) + \mathcal{O}[(1 - \phi^*)^2], \tag{10.20}$$

Comparing with Eq. (10.16) we see that the relative intracolumnar distance between the disks grows faster than the intercolumnar spacing between the columns, i.e. the expansion of the columnar structure is highly anisometric. This behaviour is quite different from the classical model for which $\bar{\Delta}_n \equiv \bar{\Delta}_c = \phi^{*-1/3}$ indicating an *isometric* expansion upon lowering ϕ^*. In Fig. 10.2 the predicted spacings, given by the closed-form analogues of Eqs. (10.16) and (10.20), are compared with simulation results. Unlike the pressure, the prediction for the columnar spacings remains surprisingly accurate even in the regime close to the columnar-nematic transition. Quantitatively, theory and simulation are found to agree within 1% over the entire columnar stability range.
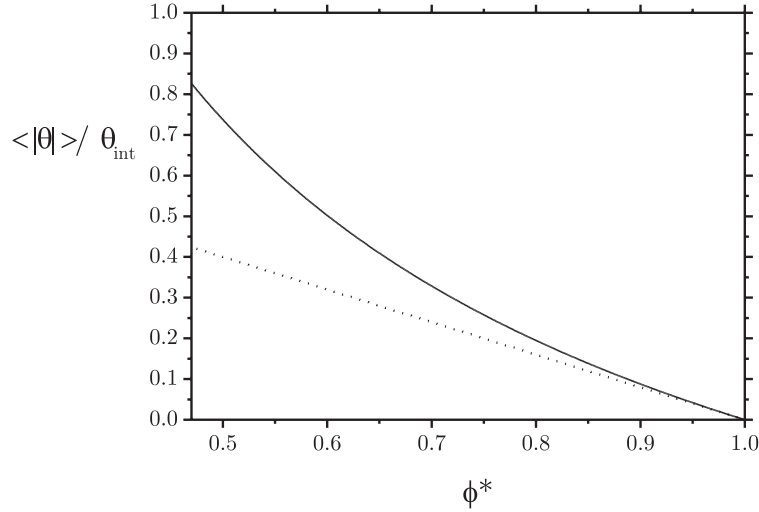
FIGURE 10.3. Average polar angle relative to the internal angle ($\theta_{\text{int}} \sim L/D$) plotted versus ϕ^* (solid curve). The dotted line shows the asymptotic result given by Eq. (10.21).

To assess the degree of orientational order in the dense columnar state we consider the ratio of the average polar angle $\langle |\theta| \rangle$ to the *internal* angle $\theta_{\text{int}} \sim L/D$. The leading order contribution of this ratio near close packing is given by (cf. Eq. (10.10))

$$\frac{\langle |\theta| \rangle}{\theta_{\text{int}}} \simeq \frac{D}{L} \left(\frac{2}{\alpha} \right) \sim \frac{4}{5}(1 - \phi^*), \tag{10.21}$$

showing that the disks are only marginally perturbed away from their parallel orientations since the average "off-parallel" deflection angle does not exceed the internal angle of the disk. The full result, depicted in Fig. 10.3, shows rather surprisingly that this situation remains up to volume fractions close to the columnar-nematic transition, located around $\phi^* \approx 0.48$. This indicates that the orientational freedom of the disks is extremely small throughout the *entire* columnar stability regime. We conclude that the dominance of near-parallel configurations also gives an *a posteriori* justification for the mean-field asymptotic analysis presented here.

10.5. CONCLUDING REMARKS

The present model constitutes a significant improvement over the traditional one which appears to be far from accurate even in the regime near close packing. Contrary to the case of a hard-sphere crystal [157] the traditional cell model clearly does not work accurately for a columnar liquid crystal. Future work on the model could be aimed at refining the present description in the regime close to the melting transition by introducing more advanced cell theories which include e.g. cooperative motion of the columns [158]. The fact that the simulation pressures in Fig. 10.1(a) remain insensitive to the aspect-ratio throughout the entire columnar stability range is surprising and

supports the notion that the columnar phase is dominated by cell-behaviour up to the melting transition, albeit in more sophisticated fashion than we described here.

Bibliography

[1] H. Zocher. *Z. Anorg. Allg. Chem.*, 147:91, 1925.

[2] I. Langmuir. *J. Chem. Phys.*, 6:873, 1938.

[3] F. C. Bawden, N. W. Pirie, J. D. Bernal, and I. Fankuchen. *Nature*, 138:1051, 1936.

[4] J. D. Bernal and I. Fankuchen. *J. Gen. Physiol.*, 25:111, 1941.

[5] G. J. Vroege and H. N. W. Lekkerkerker. *Rep. Prog. Phys.*, 55:1241, 1992.

[6] J. C. P. Gabriel and P. Davidson. *Top. Curr. Chem.*, 226:119, 2003.

[7] P. A. Buining, C. Pathmamanoharan, J. B. H. Jansen, and H. N. W. Lekkerkerker. *J. Am. Ceram. Soc.*, 74:1303, 1991.

[8] M. P. B. van Bruggen, F. M. van der Kooij, and H. N. W. Lekkerkerker. *J. Phys.: Condens. Matter*, 8:9451, 1996.

[9] A. Wierenga, T. A. J. Lenstra, and A. P. Philipse. *Colloids Surfaces A*, 134:359, 1998.

[10] M. P. B. van Bruggen, J. K. G. Dhont, and H. N. W. Lekkerkerker. *Macromolecules*, 32:2256, 1999.

[11] F. M. van der Kooij and H. N. W. Lekkerkerker. *J. Phys. Chem. B*, 102:7829, 1998.

[12] F. M. van der Kooij. *Phase behaviour and dynamics of suspensions of hard colloidal platelets*. PhD thesis, Utrecht University, 2000.

[13] B.J. Alder and T.E. Wainwright. *J. Chem. Phys.*, 27:1208, 1957.

[14] W. W. Wood and J. D. Jacobson. *J. Chem. Phys.*, 27:1207, 1957.

[15] W. G. Hoover and F. H. Ree. *J. Chem. Phys.*, 49:3609, 1968.

[16] D. Frenkel, H. N. W. Lekkerkerker, and A. Stroobants. *Nature*, 332:822, 1988.

[17] D. Frenkel. *Liq. Cryst.*, 5:929, 1989.

[18] J. A. C. Veerman and D. Frenkel. *Phys. Rev. A*, 45:5632, 1992.

[19] D. Frenkel. *Physica A*, 313:1, 2002.

[20] P. Bartlett, R. H. Ottewill, and P. N. Pusey. *J. Chem. Phys.*, 93:1299, 1990.

[21] L. Onsager. *Ann. N.Y. Acad. Sci.*, 51:627, 1949.

[22] M. A. Cotter. *Hard particle theories of nematics*. In G. R. Luckhurst and G. W. Gray, editors, *The molecular physics of liquid crystals*. Academic Press, New York, 1979.

[23] J. D. Parsons. *Phys. Rev. A*, 19:1225, 1979.

[24] W. G. MacMillan and J. E. Mayer. *J. Chem. Phys.*, 13:276, 1945.

[25] T. L. Hill. *Statistical mechanics*. McGraw-Hill, New York, 1956.

[26] J. P. Hansen and I. R. McDonald. *Theory of Simple Liquids*. Academic Press, London, 1986.

[27] N. G. van Kampen. *Physica*, 27:783, 1961.

[28] M. A. Cotter and D. E. Martire. *J. Chem. Phys.*, 53:4500, 1970.

[29] H. Löwen et al. *Special issue on density functional theory of liquids. J. Phys; Condens. Matt.*, 14:11897, 2002.

[30] R. F. Kayser and H. J. Raveche. *Phys. Rev. A*, 17:2067, 1978.

[31] G. Lasher. *J. Chem. Phys.*, 53:4141, 1970.

[32] K. Lakatos. *J. Stat. Phys.*, 2:121, 1970.

[33] J. Herzfeld, A. E. Berger, and J. W. Wingate. *Macromolecules*, 17:1718, 1984.

[34] T. Odijk and H. N. W. Lekkerkerker. *J. Phys. Chem.*, 89:2090, 1985.

[35] R. van Roij and B. M. Mulder. *Europhys. Lett.*, 34:201, 1996.

[36] G. J. Vroege and H. N. W. Lekkerkerker. *J. Phys. Chem.*, 97:3601, 1993.

[37] D. Frenkel. *J. Phys. Chem.*, 91:4912, 1987.

[38] D. Frenkel. *J. Phys. Chem.*, 92:5314, 1988.

[39] N. F. Carnahan and K. E. Starling. *J. Chem. Phys.*, 51:635, 1969.

[40] D. Frenkel and B. M. Mulder. *Mol. Phys.*, 55:1171, 1985.

[41] B. Tjipto-Margo and G. T. Evans. *J. Chem. Phys.*, 93:4254, 1990.

[42] P. Bolhuis and D. Frenkel. *J. Chem. Phys.*, 106:666, 1997.

[43] S. D. Zhang, P. A. Reynolds, and J. S. van Duijneveldt. *J. Chem. Phys.*, 117:9947, 2002.

[44] S. D. Lee. *J. Chem. Phys.*, 87:4972, 1987.

[45] S. D. Lee. *J. Chem. Phys.*, 89:7036, 1989.

[46] S. C. McGrother, D. C. Williamson, and G. Jackson. *J. Chem. Phys.*, 104:6755, 1995.

[47] P. J. Camp, C. P. Mason, M. P. Allen, A. A. Khare, and D. A. Kofke. *J. Chem. Phys.*, 105:2837, 1996.

[48] P. J. Camp and M. P. Allen. *Physica A*, 229:410, 1996.

[49] P. J. Camp, M. P. Allen, P. G. Bolhuis, and D. Frenkel. *J. Chem. Phys.*, 106:9270, 1997.

[50] B. Barboy and W. M. Gelbart. *J. Chem. Phys.*, 71:3053, 1979.

[51] T. V. Ramakrishnan and M. Yussouf. *Solid State Commun.*, 21:389, 1977.

[52] T. V. Ramakrishnan and M. Yussouf. *Phys. Rev. B*, 19:2775, 1979.

[53] R. Evans. *Adv. Phys.*, 28:143, 1979.

[54] M. Baus. *Mol. Phys.*, 50:543, 1983.

[55] H. Löwen. *Phys. Rep.*, 237:249, 1994.

[56] M. P. Allen, C. P. Mason, E. de Miguel, and J. Stelzer. *Phys. Rev. E*, 52:25, 1995.

[57] B. M. Mulder. *Phys. Rev. A*, 39:360, 1987.

[58] R. van Roij. *Simple theories of complex fluids*. PhD thesis, Utrecht University, 1996.

[59] H. H. Wensink and G. J. Vroege. *unpublished results*.

[60] F. M. van der Kooij, D. van der Beek, and H. N. W. Lekkerkerker. *J. Phys. Chem. B*, 105:1696, 2001.

[61] J. C. P. Gabriel, C. Sanchez, and P. Davidson. *J. Phys. Chem.*, 100:11139, 1996.

[62] A. Mourchid, A. Delville, J. Lambard, E. Lecolier, and P. Levitz. *Langmuir*, 11:1942, 1995.

[63] M. A. Bates and D. Frenkel. *J. Chem. Phys.*, 110:6553, 1999.

[64] M. A. Bates. *J. Chem. Phys.*, 111:1732, 1999.

[65] H. N. W. Lekkerkerker, Ph. Coulon, R. van der Hagen, and R. Deblieck. *J. Chem. Phys.*, 80:3427, 1984.

[66] T. M. Birshtein, B. I. Kolegov, and V. A. Pryamitsin. *Polym. Sci. U.S.S.R.*, 30:316, 1988.

[67] R. van Roij and B. Mulder. *Phys. Rev. E*, 54:6430, 1996.

[68] M. Dijkstra and R. van Roij. *Phys. Rev. E*, 56:5594, 1997.

[69] R. van Roij, B. Mulder, and M. Dijkstra. *Physica A*, 261:374, 1998.

[70] P. C. Hemmer. *J. Stat. Phys.*, 100:3, 2000.

[71] I. S. Gradshteyn and I. M. Ryzhik. *Table of Integrals, Series and Products*. Academic Press, San Diego, 1994.

[72] F. M. van der Kooij. *personal communication*.

[73] F. M. van der Kooij and H. N. W. Lekkerkerker. *Phys. Rev. Lett.*, 84:781, 2000.

[74] F. M. van der Kooij and H. N. W. Lekkerkerker. *Langmuir*, 16:10144, 2000.

[75] F. M. van der Kooij, M. Vogel, and H. N. W. Lekkerkerker. *Phys. Rev. E*, 62:5397, 2000.

[76] R. Alben. *J. Chem. Phys.*, 59:4299, 1973.

[77] A. Saupe, P. Boonbrahm, and L. J. Yu. *J. Chim. Phys.*, 80:7, 1983.

[78] Y. Rabin, W. E. Mc Mullen, and W. M. Gelbart. *Mol. Cryst. Liq. Cryst.*, 89:67, 1982.

[79] A. Chrzanowska. *Phys. Rev. E*, 58:3229, 1998.

[80] A. Stroobants and H. N. W. Lekkerkerker. *J. Phys. Chem.*, 88:3669, 1984.

[81] P. Bartlett. *J. Phys.: Condens. Matter*, 2:4979, 1990.

[82] F. M. van der Kooij and H.N.W. Lekkerkerker. *Langmuir*, 16:10144, 2000.

[83] P. F. Byrd and M. D. Friedman. *Handbook of Elliptic Integrals for Engineers and Physicists*. Springer Verlag, Berlin, 1954.

[84] S. Varga, A. Galindo, and G. Jackson. *Phys. Rev. E*, 66:011707, 2002.

[85] R. van Roij and B. Mulder. *J. Phys. (France) II*, 4:1763, 1994.

[86] R. Zwanzig. *J. Chem. Phys.*, 39:1714, 1963.

[87] H. H. Wensink, G. J. Vroege, and H. N. W. Lekkerkerker. *J. Chem. Phys.*, 115:7319, 2001.

[88] S. Varga, A. Galindo, and G. Jackson. *J. Chem. Phys.*, 117:10412, 2002.

[89] S. Varga, A. Galindo, and G. Jackson. *Mol. Phys.*, 101:817, 2003.

[90] H. H. Wensink, G. J. Vroege, and H. N. W. Lekkerkerker. *J. Phys. Chem. B*, 105:10610, 2001.

[91] P. C. Hemmer. *Mol. Phys.*, 96:1153, 1999.

[92] T. Odijk. *Liq. Cryst.*, 1:97, 1986.

[93] H. H. Wensink and G. J. Vroege. *J. Chem. Phys.*, 119:6868, 2003.

[94] R. van Roij and B. Mulder. *J. Chem. Phys.*, 105:11237, 1996.

[95] H. B. Callen. *Thermodynamics and an Introduction to Thermostatistics.* John-Wiley and Sons Inc., New York, 1985.

[96] S. Varga and I. Szalai. *Phys. Chem. Chem. Phys.*, 2:1955, 2000.

[97] G. J. Vroege and H. N. W. Lekkerkerker. *Colloids Surf., A*, 130:405, 1997.

[98] N. Clarke, J. A. Cuesta, R. P. Sear, P. Sollich, and A. Speranza. *J. Chem. Phys.*, 113:5817, 2000.

[99] Y. Martinez-Raton and J. A. Cuesta. *J. Chem. Phys.*, 118:10164, 2003.

[100] T. J. Sluckin. *Liq. Cryst.*, 1:111, 1989.

[101] Z. Y. Chen. *Phys. Rev. E*, 50:2849, 1994.

[102] J. P. Straley. *J. Chem. Phys.*, 57:3694, 1972.

[103] K. Shundyak and R. van Roij. *Phys. Rev. E*, 69:041703, 2004.

[104] P. Sollich. *J. Phys.; Condens. Matter*, 14:79, 2002.

[105] A. Speranza and P. Sollich. *J. Chem. Phys.*, 117:5421, 2002.

[106] A. Speranza and P. Sollich. *J. Chem. Phys.*, 118:5213, 2003.

[107] A. Speranza and P. Sollich. *Phys. Rev. E*, 061702, 2003.

[108] S. Fraden, G. Maret, and D. L. D. Caspar. *Phys. Rev. E*, 48:2816, 1993.

[109] N. Donkai, K. Kajiwara, M. Schmidt, and T. Miyamoto. *Makromol. Chem.*, 14:611, 1993.

[110] P. A. Buining and H. N. W. Lekkerkerker. *J. Phys. Chem.*, 97:11510, 1993.

[111] T. Itou and A. Teramoto. *Macromolecules*, 17:1419, 1984.

[112] K. Kajiwara, N. Donkai, Y. Hiragi, and H. Inagaki. *Makromol. Chem.*, 187:2883, 1986.

[113] P. A. Buining, Y. S. J. Veldhuizen, C. Pathmamanoharan, and H. N. W. Lekkerkerker. *Colloids Surf.*, 64:47, 1992.

[114] P. Sollich, P. B. Warren, and M. E. Cates. *Adv. Chem. Phys.*, 116:265, 2001.

[115] B. M. Mulder. *Phys. Rev. A*, 35:3095, 1987.

[116] A. Poniewierski and R. Holyst. *Phys. Rev. Lett.*, 61:2461, 1988.

[117] A. M. Somoza and P. Tarazona. *Phys. Rev. A*, 41:965, 1990.

[118] A. Poniewierski and R. Holyst. *Phys. Rev. A*, 41:6871, 1990.

[119] A. Poniewierski and T. J. Sluckin. *Phys. Rev. A*, 43:6837, 1991.

[120] A. Poniewierski. *Phys. Rev. A*, 45:5605, 1992.

[121] R. Holyst and A. Poniewierski. *Mol. Phys.*, 71:561, 1990.

[122] H. Xu. *Mol. Phys.*, 77:311, 1992.

[123] H. Xu, H. N. W. Lekkerkerker, and M. Baus. *Europhys. Lett.*, 17:163, 1992.

[124] J. M. Polson and D. Frenkel. *Phys. Rev. E*, 56:6260, 1997.

[125] A. Stroobants. *Phys. Rev. Lett.*, 69:2388, 1992.

[126] S-M Cui and Z. Y. Chen. *Phys. Rev. E*, 50:3747, 1994.

[127] M. A. Bates and D. Frenkel. *J. Chem. Phys.*, 109:6193, 1998.

[128] A. M. Bohle, R. Holyst, and T. Vilgis. *Phys. Rev. Lett.*, 76:1396, 1996.

[129] M. Abramowitz and I. A. Stegun. *Handbook of mathematical functions.* Dover, New York, 1973.

[130] R. McRae and A. D. J. Haymet. *J. Chem. Phys.*, 88:1114, 1988.

[131] M. A. Bates and D. Frenkel. *Phys. Rev. E*, 57:4824, 1998.

[132] C. F. Vester. *Kolloid-Z.*, 84:63, 1938.

[133] H. de Hek and A. Vrij. *J. Colloid Interface Sci.*, 84:409, 1981.

[134] B. Vincent, J. Edwards, S. Emmet, and R. D. Groot. *Colloids Surf.*, 31:267, 1988.

[135] A. P. Gast, W. B. Russel, and C. K. Hall. *J. Colloid Interface Sci.*, 109:161, 1986.

[136] S. M. Illet, A. Orrock, W. C. K. Poon, and P. N. Pusey. *Phys. Rev. E*, 51:1344, 1995.

[137] H. N. W. Lekkerkerker, W. C. K. Poon, P. N. Pusey, A. Stroobants, and P. B. Warren. *Europhys Lett.*, 20:559, 1992.

[138] S. D. Zhang, J. S. van Duijneveldt, and P. A. Reynolds. *Mol. Phys.*, 100:3041, 2002.

[139] A. Vrij. *J. Chem. Phys.*, 72:3735, 1980.

[140] H. N. W. Lekkerkerker. *J. Colloid Interface Sci.*, 51:419, 1990.

[141] S. Asakura and F. Oosawa. *J. Chem. Phys.*, 22:1255–1256, 1954.

[142] S. Asakura and F. Oosawa. *J. Pol. Sci.*, 33:183–192, 1958.

[143] A. Vrij. *Pure Appl. Chem.*, 48:471, 1976.

[144] H. N. W. Lekkerkerker and G. J. Vroege. *Phase transitions in colloidal dispersions*. In H. van Beijeren and M. H. Ernst, editors, *Fundamental problems in statistical mechanics VIII*. Elsevier, 1994.

[145] H. Reiss, H. L. Frisch, and J. L. Lebowitz. *J. Chem. Phys.*, 31:369, 1959.

[146] J. L. Lebowitz, E. Helfand, and E. Praestgaard. *J. Chem. Phys.*, 43:774, 1965.

[147] A. B. D. Brown, C. Ferrero, T. Narayanan, and A. R. Rennie. *Eur. Phys. J. B*, 11:481, 1999.

[148] F. M. van der Kooij, K. Kassapidou, and H. N. W. Lekkerkerker. *Nature*, 406:868, 2000.

[149] V. L. Colvin. *MRS Bull.*, 26:637, 2001.

[150] K. P. Velikov, T. van Dillen, A. Polman, and A. van Blaaderen. *Appl. Phys. Lett.*, 81:838, 2002.

[151] M. P. Taylor, R. Hentschke, and J. Herzfeld. *Phys. Rev. Lett.*, 62:800, 1989.

[152] R. Hentschke, M. P. Taylor, and J. Herzfeld. *Phys. Rev. A*, 40:1678, 1989.

[153] H. Eyring and J. Hirschfelder. *J. Phys. Chem.*, 41:249, 1937.

[154] J. E. Lennard-Jones and A. F. Devonshire. *Proc. Roy. Soc. (London)*, page 53, 1937.

[155] L. Tonks. *Phys. Rev.*, 50:955, 1936.

[156] J. G. Kirkwood. *J. Chem. Phys.*, 18:380, 1950.

[157] B. J. Alder, W. G. Hoover, and D. A. Young. *J. Chem. Phys.*, 49:3688, 1968.

[158] B. J. Alder, W. G. Hoover, and T. E. Wainwright. *Phys. Rev. Lett.*, 11:241, 1963.

Summary

Mixing colloidal particles differing in size or shape may lead to enriched phase behaviour involving aspects that are not encountered in pure systems. Examples are repartitioning of the species among the coexisting phases, referred to as fractionation, re-entrant phase transitions and demixing transitions which may give rise to multi-phase coexistence. Recent experimental work on polydisperse mixtures of colloidal platelets as well as binary systems of rod- and platelike colloids and platelets and polymer have revealed many intriguing phenomena left open for theoretical considerations. The objective of this thesis is to theoretically account for the experimentally observed features starting from simple Onsager-type descriptions generalized to binary and polydisperse mixtures.

In Chapter 2 we provide a theoretical underpinning for the recently observed inversion of isotropic and nematic mass densities in polydisperse systems of hard platelets by investigating fractionation behaviour in simple binary mixtures of thin and thick hard platelets with equal diameter. It turns out that the phenomenon is a *direct* consequence of anomalous thickness fractionation such that the thickest i.e. heaviest species are expelled to the isotropic phase. Owing to the accumulation of the heavier particles in the isotropic phase its mass density may become higher than that of the nematic phase. We also find a stable nematic-nematic demixing transition in these mixtures as a result of a competition between entropy of mixing and the excess excluded-volume entropy pertaining to the platelets' finite thicknesses. The underlying demixing mechanism is compared in Chapter 5 with those found in related binary mixtures reported in literature. There we also establish a demixing of the isotropic phase in systems of platelets with either diameter of thickness bidispersity, provided that the size ratio exceeds some critical value.

Chapters 3 and 4 are devoted to the isotropic-nematic (I-N) phase behaviour of asymmetric rod-plate mixtures characterized by highly dissimilar excluded volumes of two rods and two platelets, the latter being the largest. These mixtures are representative of the experimental boehmite rod - gibbsite plate mixtures studied in experiment. Focussing first on uniaxial nematic phases, characterized by a single axis of alignment, we show by means of approximate Gaussian nematic orientation distributions that many features of the low-density part of the experimental phase diagram can be reproduced semi-quantitatively. In particular, a large isotropic-nematic-nematic triphasic region and a dominating appearance of the plate-rich uniaxial nematic phase are found, in accordance with experimental results. Next, within a formal approach to Onsager's second-virial theory, we consider the stability of the *biaxial* phase in these asymmetric mixtures. In this particular liquid crystal state the azimuthal symmetry of the uniaxial nematic states is broken since the rods and plates are aligned along two mutually perpendicular axes. Starting from the symmetric case and increasing the mixture's asymmetry gradually we find that the biaxial phase remains stable up to surprisingly high asymmetries. For highly asymmetric mixtures resembling the experimentally studied mixtures we find a scenario involving an isotropic - uniaxial nematic - biaxial nematic

triphasic equilibrium. These results open up the possibility of finding biaxial nematic textures in the aforementioned boehmite-gibbsite mixtures, which remains to be verified in future experiments.

In the next two chapters the challenging issue of calculating I-N phase equilibria in polydisperse systems are dealt with. First, in Chapter 6 we present a numerical study of these equilibria in systems of length-polydisperse hard rods described with Gaussian trial orientational distribution functions. Very pronounced fractionation effects are observed with the longest rods preferentially occupying the nematic phase and the shortest ones the isotropic phase. If the overall unimodal length distribution is sufficiently "fat-tailed" a spinodal instability of the nematic phase was established implying possible triphasic I-N-N equilibria, albeit in a marginally small interval along the dilution trajectory. By explicitly tracking down the spinodal curves we could reveal that the fractionation scenario in systems of polydisperse hard rods is surprisingly complicated. To justify the use of the Gaussian trial function approximation for these systems we show that the approach predicts the correct asymptotic behaviour for distributions with infinite cutoff lengths, compared to exact Onsager theory. In Chapter 7 we give a similar treatment for platelets with length (i.e. thickness) polydispersity. An important difference with the description in the previous Chapter is that this model, being an extension of the binary model from Chapter 2, gives a tractable moment structure for the excess free energy which poses less computational difficulties. We find that the I-N density inversion mentioned above is retained in polydisperse systems in a small window around a polydispersity of 27 %, in good agreement with the value found for the polydisperse gibbsite platelets. The generalized polydisperse model also allows for a correct description of the fractionation properties of the coexisting isotropic and nematic phases along the dilution trajectory compared to experimental results. These aspects of the phase behaviour could not be explained from the binary model for fundamental reasons.

Having focussed on the spatially homogeneous isotropic and nematic phases thus far, in Chapter 8 we briefly assess the stability of a polydisperse nematic phase with respect to the inhomogeneous smectic and columnar states. By means of a bifurcation analysis applied to a simple artificial system of parallel cylindric rods we indicate that the nematic-smectic transition, as found in monodisperse systems, is postponed upon increasing polydispersity in favour of the columnar phase. At high polydispersities a transition from the nematic to the smectic phase is pre-empted by a nematic-columnar transition, indicating that sufficient length polydispersity may give a thermodynamically stable columnar phase for colloidal rods. We also show that composition fluctuations play a crucial role at higher polydispersities. Allowing the size distribution to "fluctuate" at the bifurcation gives a qualitatively different outcome compared to the so-called 'constrained eutectic' approach in which case a fixed size distribution is assumed.

The aim of Chapter 9 is to illustrate the drastic influence of gravity on the phase behaviour of colloidal mixtures. In experiment, mixtures involving gibbsite platelets may build up a considerable concentration gradient inside a test tube due to sedimentation.

For mixtures of platelets and non-adsorbing polymer we show that sedimentation enables the formation of a four-phase equilibrium involving both isotropic gas and liquid phases, a nematic and a columnar phase, as observed in experimental plate-polymer mixtures.

Finally, in Chapter 10 we set up an improved free-volume theory for a columnar phase of hard platelets at high packing fractions. We combine the traditional cell model with an appropriate fluid description in the (one-dimensional) direction of the phase while accounting for the rotational freedom of the particles in a mean-field way. Excellent quantitative agreement with simulation results is found for the pressure, chemical potential and the inter- and intracolumnar spacings along the entire columnar stability range.

Samenvatting voor iedereen

Colloïdale systemen bestaan uit zeer kleine deeltjes met een afmeting kleiner dan éénduizendste millimeter. Een vloeistof waarin zulke deeltjes onophoudelijk rondzweven wordt een colloïdale dispersie of suspensie genoemd. Vele natuurlijke en alledaagse stoffen zoals bloed, melk, inkt en verf zijn in feite colloïdale dispersies. Een belangrijke fysische eigenschap van deze systemen is hun zogenaamde fasegedrag. Deze beschrijft de stabiliteit van de verschillende verschijningsvormen van een dispersie onder bepaalde omstandigheden zoals temperatuur of deeltjesconcentratie. Een bekende uiting van het fasegedrag van een dispersie is bijvoorbeeld het schiften van melk of mayonnaise, waarbij twee vloeistoflagen met duidelijk verschillende eigenschappen ontstaan uit een homogene vloeistof. Het begrijpen en verklaren van het fasegedrag van colloïdale dispersies is niet alleen belangrijk voor de toegepaste colloïdwetenschap, denk bijvoorbeeld aan het verbeteren van de houdbaarheid van melkproducten, maar ook voor de fundamentele natuurwetenschap omdat het gedrag van colloidale systemen in zekere zin analoog is aan dat van niet-colloïdale, oftewel moleculaire systemen. De fenomenologie van colloïdale systemen is daarom representatief voor een zeer breed scala aan materievormen.

Een aspect dat een cruciale rol speelt in het fasegedrag van colloïdale dispersies is de *interactie* tussen de colloïden. Deze interactie wordt bepaald door de manier waarop de deeltjes elkaar afstoten of aantrekken doordat ze bijvoorbeeld elektrisch geladen kunnen zijn. Een ander belangrijk aspect dat hiermee samenhangt en centraal staat in dit proefschrift, is de *vorm* van de deeltjes. Vele colloïdale systemen, bijvoorbeeld klei of bloed, bestaan namelijk niet uit simpele bolletjes maar uit plaat- of staafvormige deeltjes. Deze systemen hebben de bijzondere eigenschap dat ze zogenaamde *vloeibare kristallen* kunnen vormen. Deze verschijningsvormen van de materie, die we aantreffen in bijvoorbeeld digitale displays, worden gekarakteriseerd door structuren waarin de deeltjes min of meer in dezelfde richting wijzen (ze zijn orientationeel geordend) terwijl ze geen vaste positie in de ruimte innemen zoals in een normale kristallijne stof, denk bijvoorbeeld aan ijs. Uiterlijk zullen deze stoffen dus nog steeds het karakter van een vloeistof hebben, vandaar de naam. In Figuur 1.1 op pagina 2 staat een schematische weergave van de verschillende (vloeibaar-kristallijne) structuren die we kunnen tegenkomen in dispersies van colloïdale damschijfjes. Belangrijk hierbij is dat de stabiliteit van de vloeibare kristallen volledig bepaald worden door de *concentratie* van de colloïden in de vloeistof waarin ze rondbewegen. In de *isotrope* fase (I), stabiel bij lage deeltjesconcentraties, zijn de plaatjes volledig willekeurig georiënteerd. Als we de totale deeltjesconcentratie geleidelijk verhogen zal op een zeker punt fasescheiding (schifting) optreden waarbij het onderste gedeelte van bijvoorbeeld een buisje met dispersie ingenomen wordt door een *nematische* fase (N), waarin de schijfjes zijn opgelijnd langs een bepaalde voorkeursrichting. De nematisch fase heeft een iets hogere concentratie dan de isotrope fase en zal hierdoor zwaarder zijn. Merk op dat zowel de isotrope als de nematische fase positioneel *ongeordend* zijn doordat de deeltjes zich vrij kunnen verplaatsen over het gehele systeemvolume.

Bij nog hogere totaalconcentraties kunnen meer ingewikkelde vloeibaar-kristallijne structuren ontstaan met een hogere ordeningsgraad dan de nematische fase. Deze worden in het bijzonder gekarakteriseerd door positionele of kristallijne ordening, langs één of twee richtingen van het systeem. De *smectische* fase (SmA) wordt gekarakteriseerd door een lagenstructuur zodanig dat de plaatjes wanordelijk kunnen bewegen in de laag maar niet of nauwelijk van de ene naar de andere laag kunnen gaan. Welbeschouwd kan deze structuur dus worden opgevat als een kristal in één richting. In de *columnaire* fase (C) zijn de plaatjes gerangschikt in regelmatige verticale kolommen waarlangs ze wanordelijk op en neer kunnen bewegen. Aangezien de plaatjes zich niet of nauwelijks kunnen verplaatsen van de ene naar de andere kolom is de columnaire fase kristallijn in de twee horizontale richtingen. In het laatste hoofdstuk van dit proefschrift laten we zien dat de columnaire fase heel goed beschreven kan worden met een zogenaamd 'cel-model'. In dit eenvoudige model nemen we aan dat de deeltjes zijn opgesloten in celkolommen waarbinnen ze vrij op en neer kunnen bewegen maar waaruit ze niet "zijwaarts" kunnen ontsnappen, met andere woorden ze kunnen niet van de ene naar de andere cel gaan. Het blijkt dat vele eigenschappen van de columnaire fase, zoals de druk uitgeoefend door de deeltjes op een wand en de gemiddelde afstand tussen de schijfjes, voorspeld door ons simpele model verbluffend goed overeenkomen met de "exacte" resultaten verkregen uit nauwkeurige maar ingewikkelde computerberekeningen.

Een belangrijke eigenschap van vele colloïdale systemen is dat ze zijn opgebouwd uit deeltjes met een *verschillende* vorm en grootte, bijvoorbeeld grote en kleine bolletjes of (klei)plaatjes met verschillende dikten en diameters. Het zijn dus veelal *mengsels* van twee of meer verschillende deeltjestypen. De theoretische beschrijving van vloeibaar-kristallijne fase-overgangen in deze mengsels is het centrale thema van dit proefschrift. De beschrijving en analyse van het fasegedrag van mengsels is lastiger dan voor zuivere systemen, vooral wanneer er veel meer dan twee soorten deeltjes bij betrokken zijn. In dit laatste geval spreken we van *polydisperse* systemen. Desalniettemin zijn deze complexe mengsels het bestuderen meer dan waard omdat ze interessant en rijk fasegedrag kunnen vertonen, zoals ook uit experimenteel werk aan colloïdale modelsystemen van plaatjes of staafjes blijkt.

In het eerste deel van het proefschrift beperken we ons tot "simpele" *binaire* mengsels bestaande uit twee deeltjesvormen. In hoofdstuk 2 laten we zien dat het mengen van dikke en dunne schijfjes aanleiding geeft tot aanzienlijke *vorm-segregatie* bij het I-N fasescheiden. Hiermee wordt bedoeld dat het ene type deeltje (in dit geval de dikke schijfjes) zich ophopen in de isotrope fase terwijl het ander type (de dunne schijfjes) de voorkeur geeft aan de nematische fase. Onder bepaalde omstandigheden kan dit effect leiden tot een merkwaardige *dichtheidsinversie* waarbij de isotrope fase zwaarder wordt dan de nematische fase, ondanks de lagere deeltjesconcentratie in de isotrope fase. Experimenteel manifesteert dit verschijnsel zich in het omklappen van de onder- en bovenfasen in een buisje met een colloïdale plaatjesdispersie zoals in Figuur 2.1 op pagina 24 is te zien (hierbij is de donkere laag de isotrope en de lichte de nematische fase).
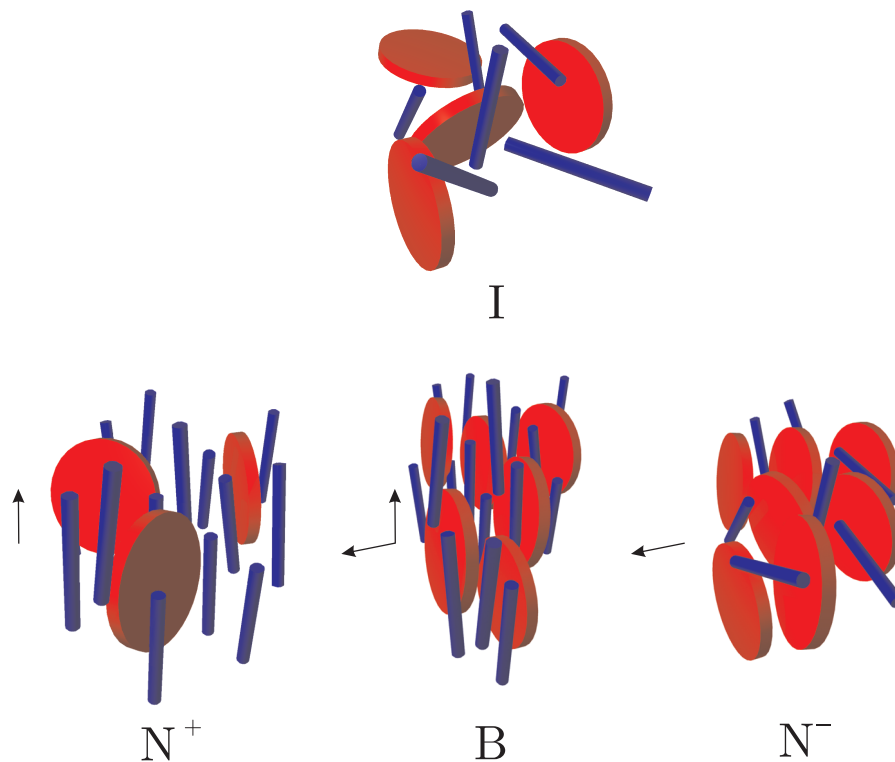
In de volgende twee hoofdstukken bekijken we het rijke fasegedrag van mengsels van plaatjes en staafjes. Karakteristiek voor deze mengsels is dat door het grote vormverschil van de deeltjestypen verschillende nematische fasen gevormd kunnen worden, zoals geschetst in de figuur. De onderlinge stabiliteit van deze nematische fasen hangt van vele factoren af waaronder de lengte tot diameter verhouding van de deeltjes en de verhouding tussen het aantal plaatjes en het aantal staafjes. Als de staafjes in de meerderheid zijn zal de nematische structuur eruit zien zoals geschetst voor de N^+ fase; de staafjes zijn opgelijnd langs de pijl en de plaatjes liggen er *willekeurig* georiënteerd tussen (ze hebben dus geen voorkeursrichting in het vlak loodrecht op de pijl). In mengsels gedomineerd door plaatjes vinden we een soortgelijke structuur aangegeven met N^- waarin de plaatjes sterk zijn opgelijnd langs een voorkeursas (zie pijl) met de staafjes willekeurig georiënteerd ertussen. In de *biaxiale* (B) fase zijn zowel de plaatjes als de staafjes opgelijnd langs twee onderling loodrechte assen. Het bestaan van de biaxiale fase is het meest interessante (en wetenschappelijk omstreden) aspect van deze mengsels. Deze structuur is namelijk nog nooit waargenomen in colloïdale systemen. Recent experimenteel onderzoek aan mengsels van plaatjes en staafjes met ongeveer dezelfde afmetingen (zoals in de figuur) lijkt te hebben aangetoond dat de biaxiale fase niet stabiel is en dat het mengsel zich liever opdeelt in de twee uniaxiale, dat wil zeggen enkel-assige, nematische fasen, N^+ en N^-. In hoofdstuk 4 laten we zien dat de biaxiale fase vanuit een theoretisch standpunt, tegen de experimentele verwachtingen in, toch verrassend stabiel is in deze mengsels en dat de mogelijkheid om deze exotische vloeibaar-kristallijne structuur in echte colloïdale mengsels waar te nemen niet moet worden uitgevlakt. Verder experimenteel onderzoek zal dit moeten uitwijzen.

In het tweede gedeelte van dit proefschrift breiden we de theoretische beschrijving uit naar polydisperse systemen, en wel naar afzonderlijke systemen van staaf- en plaatvormige cilindertjes met (schier oneindig) veel verschillende lengtes of diktes. In hoofdstuk 6 staan de volgende twee vragen centraal. (1): Hoe zullen de korte en lange staafjes in een polydispers systeem zich verdelen over de isotrope en nematische fasen, met andere woorden hoe ziet het vorm-segregatiegedrag eruit? en (2): Kan lengtepolydispersiteit (lees: een *continue* variatie in staaflengten) leiden tot twee of meerdere nematische fasen met verschillende samenstelling? Het opsplitsen van de nematische fase in tweeën is tot nu toe alleen experimenteel (en theoretisch) waargenomen in binaire mengsels van korte en lange colloïdale staafjes maar nog niet in de (meer gebruikelijke) gevallen waarin de staafjes een continue lengteverdeling hebben.

Het antwoord op de eerste vraag luidt dat lengtesegregatie een sterke invloed heeft op de isotroop-nematische fase-overgang. Het blijkt dat de allerkortste staafjes zich in hoge mate ophoopt in de isotrope fase terwijl de allerlangste liever in de nematische fase gaan zitten. Dit effect wordt des te sterker naarmate de variatie aan staaflengtes groter wordt. Dit laatste kan bijvoorbeeld worden bewerkstelligd door de lengteverhouding tussen het kortste en het langste staafje aanwezig in het systeem te verhogen. Het antwoord op de tweede vraag is positief. Het blijkt dat indien de lengtevariatie voldoende groot is, de nematische fase zich inderdaad opsplitst in tweeën. Hierbij zal de ene fase vrijwel uitsluitend de allerlangste staafjes bevatten terwijl de andere hoofdzakelijk bestaat uit staafjes met een gemiddelde lengte. Helaas laten de berekeningen ook zien dat het waarschijnlijk erg moeilijk zal zijn om dit exotisch verschijnsel experimenteel waar te nemen omdat er slechts een zeer geringe en dus nauwelijks waarneembare hoeveelheid van de tweede "lange-staven nemaat" gevormd zal worden.

In hoofdstuk 7 geven we een soortgelijke analyse van schijfjes met variërende dikte. We beperken ons hier tot aspecten met betrekking tot vorm-segregatie. De vraag is of we de experimenteel waargenomen isotroop-nematische dichtheidsinversie zoals besproken in hoofdstuk 2 voor een simpel systeem van dikke en dunne plaatjes, ook tegenkomen bij plaatjes met een continu variërende dikte. Deze polydisperse beschrijving staat dichter bij de experimentele situatie omdat de colloïdale deeltjes zelden in twee soorten (bijvoorbeeld dikke en dunne) zijn onder te verdelen maar eerder uit een veelheid aan verschillende deeltjesvormen bestaan. Het blijkt dat de dichtheidinversie inderdaad gehandhaafd blijft in polydisperse systemen en dus niet een artefact is van de simpele "binaire" aanpak in hoofdstuk 2. Uit de berekeningen volgt bovendien dat de minimale diktespreiding die nodig is om een inversie tot stand te brengen goed overeenkomt met de experimenteel gevonden waarde.

In hoofdstuk 8 bespreken we de stabiliteit van de smectische en columnaire fasen in systemen van staafjes met lengtepolydispersiteit. In Figuur 1.1 op pagina 2 staan deze fasen geschetst voor plaatvormige cilindertjes, maar de structuren voor staafjessystemen zijn hieraan volledig analoog. Beschouwen we een zuiver *nematisch*, d.w.z. opgelijnd, systeem van staafjes dan geldt dat de eerstvolgende stabiele structuur bij toenemende

concentratie de smectische fase is[†]. Introduceren we verschillende staaflengten dan is het evident dat de staafjes minder goed in de lagen van een smectische fase zullen passen vergeleken met een zuiver systeem van even lange staven. De columnaire structuur daarentegen zal relatief ongevoelig zijn voor een spreiding in lengte omdat de pakkingsefficiëntie hierbij grotendeels bepaald wordt door de staafdikte en deze is immers voor alle deeltjes gelijk. De verwachting is dan ook dat de smectische fase in sterke mate gedestabiliseerd wordt door lengtepolydispersiteit ten opzichte van de columnaire fase. Bij een voldoende grote lengtespreiding zou de smectische fase weleens volledig van het toneel kunnen verdwijnen om plaats te maken voor de columnaire fase. In het verleden is aangetoond dat dit vermoeden inderdaad correct is voor binaire mengsels van korte en lange staafjes. De vraag is natuurlijk of dit ook geldt voor polydisperse mengsels. In hoofdstuk 8 laten we zien dat hetzelfde scenario opgaat voor polydisperse systemen; bij een voldoende grote lengtespreiding zal de columnaire fase de eerstvolgende stabiele fase zijn na de nematische fase. We laten tevens zien dat vorm-segregatie effecten een belangrijke rol spelen bij de overgang van de nematische naar de smectisch fase. Net als bij de isotroop-nemaat overgang zullen de lange staven de voorkeur geven aan de meer geordende fase, in dit geval dus de smectische fase.

In hoofdstuk 9 bekijken we de invloed van zwaartekracht op het fasegedrag van colloïdale mengsels. Uit experimenteel werk is gebleken dat colloïdale plaatjes een sterke neiging hebben om naar de bodem van het buisje te zakken doordat de plaatjes aanzienlijk zwaarder zijn dan het oplosmiddel waarin ze rondzweven. Het gevolg is dat de concentratie onderin de buis hoger zal zijn dan bovenin zodat er sprake is van een *concentratiegradiënt*. Aan de hand van mengsels van plaatjes en polymeren[‡] illustreren we dat deze gradiënt een drastische invloed heeft op het fasegedrag. Een bijzondere manifestatie van het effect van zwaartekracht in deze mengsels is dat een *vierfasenevenwicht* gevormd kan worden. Dit houdt in dat er een schifting plaatsvindt waarbij vier afzonderlijke lagen met elk een aparte structuur ontstaan, te weten een polymeerrijke isotrope fase, een polymeerarme isotrope fase, een nematische en een columnaire fase. Een soortgelijk vierfasenevenwicht is ook experimenteel waargenomen.

[†]Voor plaatjes is dit de columnaire fase. We beperken ons in hoofdstuk 8 echter tot staafjes. Bovendien beschouwen we een eenvoudig systeem van *perfect opgelijnde* staafvormige cilindertjes.

[‡]Dit zijn flexibele, ketenvormige moleculen. In een geschikt oplosmiddel nemen deze lange ketens de gedaante aan van "zachte", bolvormige kluwens met ongeveer dezelfde omvang als een colloïdaal deeltje.

Nawoord

Aangekomen aan het eind van het boekje wilde ik graag diegenen bedanken die direct of indirect aan de totstandkoming van dit proefschrift hebben bijgedragen.

Allereerst dank ik mijn promotor Henk Lekkerkerker. Je aanstekelijke geestdrift en doortastend inzicht hebben me de afgelopen vier jaar zeer goed gedaan. Dat het van belang is om niet alleen over de theorie zelf na te denken maar vooral ook over de (experimentele) relevantie ervan is waarschijnlijk het belangrijkste inzicht dat je me hebt gegeven. Ook denk ik met tevredenheid terug aan de vele, altijd uitlopende, discussies en "fasediagram duidsessies" waarbij de 'kippevleugeltjes', 'puntmutsen', 'Goudse pijpen' en 'kerkramen' me nog lang zullen bijblijven.

Dat een goede buur beter is dan een verre vriend bewijst mijn co-promotor Gert Jan Vroege. Zonder jou, Gert Jan, zou dit proefschrift nooit zijn geworden wat het nu is. Je grondige analyse van al mijn "notities" is van essentiële betekenis geweest voor de kwaliteit die ze uiteindelijk in de vorm van wetenschappelijke publicaties (en natuurlijk dit boekje) hebben gekregen. Het was prettig om met je samen te werken en ik ben blij dat onze coalitie nog even blijft voortbestaan.

De Audiovisuele Dienst Chemie ben ik erkentelijk voor het leveren van gegarandeerd strakke posters en andere grafische output. Hierbij wilde ik vooral Ingrid van Rooijen bedanken voor het maken van de omslag van dit boekje.

In geval van computernood kon ik als partiële digibeet altijd worden getroost door Carel, David, Dirk of Tinus. Bedankt !

Voorts spreek ik mijn dankbaarheid uit aan alle leden van het Van 't Hoff lab. voor de prettige werkatmosfeer en de vele zinnige en (vooral ook) onzinnige discussies, al dan niet gezeten aan de koffie- of lunchtafel. Ik denk met warmte terug aan al die conferentiebezoeken, uitstapjes en culinaire uitspattingen die we de afgelopen jaren hebben meegemaakt. Ik ben blij dat ik nog even bij jullie mag blijven !

Tenslotte dank ik mijn ouders en familie voor hun niet-aflatende steun en belangstelling gedurende de afgelopen 10 Utrechtse jaren.

Curriculum vitae

De auteur van dit proefschrift werd geboren op 31 januari 1976 in Lichtenvoorde. Vanaf 1988 bezocht hij de R.K.S.G. Marianum te Groenlo, waaraan hij in 1994 het VWO-diploma behaalde. Aansluitend studeerde hij scheikunde aan de Universiteit Utrecht. Het doctoraal examen (cum laude) werd behaald in 2000 met als hoofdvak fysische en colloïdchemie en bijvakken wiskunde en fysische chemie. Het afstudeeronderzoek, uitgevoerd onder leiding van Prof. dr. J.K.G. Dhont, betrof een experimentele studie naar de vorming van stromingsgeïnduceerde bandenstructuren ('shear banding') in geconcentreerde colloïdale systemen. Sinds maart 2000 is de auteur als assistent in opleiding verbonden aan het Van 't Hoff Laboratorium voor Fysische en Colloïdchemie van de Universiteit Utrecht, waar hij in samenwerking met Dr. G.J. Vroege en Prof. dr. H.N.W. Lekkerkerker het in dit proefschrift beschreven onderzoek uitgevoerd heeft. De auteur zal tot 1 januari 2005 als post-doctoraal medewerker aan het Van 't Hoff laboratorium verbonden blijven.